UNIVERSIDAD DE MÁLAGA

FACULTAD DE CIENCIAS

DEPARTAMENTO DE INGENIERÍA QUÍMICA

TESIS DOCTORAL

PREPARACIÓN DE NANOFIBRAS DE CARBONO Y CERÁMICA PARA APLICACIONES EN INGENIERÍA QUÍMICA

Autor: Ramiro Rafael Ruiz Rosas

Directores: Prof. Dr. D. Tomás Cordero Alcántara

Prof. Dr. D. José Rodríguez Mirasol

Málaga, Enero 2012

UNIVERSIDAD DE MÁLAGA

SPICUM
servicio de publicaciones

AUTOR: Ramiro Rafael Ruiz Rosas

EDITA: Servicio de Publicaciones de la Universidad de Málaga

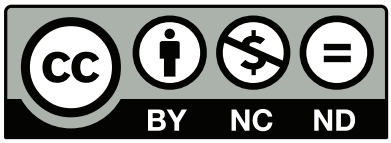

D. TOMÁS CORDERO ALCÁNTARA, Catedrático de Ingeniería Química de la Universidad de Málaga,

D. JOSÉ RODRÍGUEZ MIRASOL, Catedrático de Ingeniería Química de la Universidad de Málaga,

CERTIFICAN: Que el trabajo de investigación recogido en la presente Memoria ha sido realizado bajo su dirección en el Departamento de Ingeniería Química de la Universidad de Málaga por el Ingeniero D. Ramiro Ruiz Rosas, y reúne, a su juicio, contenido científico suficiente y las condiciones necesarias para ser presentado y defendido ante el Tribunal correspondiente para optar al Grado de Doctor en el marco de un Doctorado Europeo.

Málaga, Enero de 2012

Fdo.: Tomás Cordero Alcántara Fdo.: José Rodríguez Mirasol

For Ignatz

Pow!

Overview

Electrospinning has proven to be an effective method to obtain carbon and ceramic nanofiber fibers from conductive solutions of the corresponding precursor. In this technique, one or more of these solutions, held in one needle or several concentric capillary tubes, are subjected to an external electric field. Under suitable conditions, a jet of fluid is propelled from the capillary tip, getting stretched and solidifying while it flies towards a metallic collector, forming a rather long and small fiber. Electrospun fibers are usually collected as membranes. These are easy to handle, show very small resistance to diffusion because the small size of the fibers, and show low pressure drops when applied as filters due to high void porosity, i.e. void to fiber ratio, of the membrane.

The results in this work seem to point out that electrospinning is a suitable technique for the production of nanofibers destinated to chemical engineering applications, as catalytic or adsorption ones. The self-supported (zirconium oxide, alumina) or the metal doped (platinum over silica or carbon) fiber catalysts has been tested in several reaction process. In this sense, platinum-doped silica nanotubes have been successfully tested in NOx abatement. Zirconia nanofibers can be used in methanol decomposition to syngas or dimethyl ether production. Carbon-ceramic composites show acid properties and highly developed textural properties, as those required in alcohol dehydration. The reported platinum-doped carbon fibers could be used in hydrogen storage, and the high specific surface are of pure carbon fiber can be useful for adsorption of small molecules.

For carbon nanofiber production, lignin, a highly available, renewable and cheap biopolymer, has been proven as a suitable raw material. On the other hand, ceramic fibers can be synthetized ageing a sol precursor (thus obtaining a spinnable xerogel). Subsequent thermal treatments are necessary to obtain carbon and ceramic nanofibers; chemistry and textural surface properties are related to the temperature of such treatments.

Both kinds of nanofibers have been produced using co-axial electrospinning devices, which renders a higher stability of the ejecting area of the device (the Taylor cone), reflected in continuous production of fibers with high length-to-diameter ratios

and smooth surfaces. Co-axial electrospinning has been also used to obtain ceramic-carbon composite fibers, just spinning the adequate precursor for the inner or outer needle. This particular case also allows preparation of carbon fibers saving the lignin stabilization step. Finally, coelectrospinning the carbon or ceramic precursor with a metallic salt has been proved as an efficient method to prepare metal-doped fibers.

This Ph. D. thesis is divided into 7 chapters. The first one, introduction, is writing in Spanish, whereas the rest of the thesis is presented in English. The data provided in Chapters 2 to 6 is adapted from already published, accepted or submitted papers. Those chapters are devoted to preparation of lignin-based carbon fibers, platinum doped carbon fibers, ceramic-carbon composite fibers, zirconia nanofibers for methanol decomposition and platinum doped silica tubes for NO abatement. Each one has their own conclusions. The final chapter will give a small insight in the remaining and future work coming as a result of this thesis.

This work is a compendium of the following publications:

l. Lallave M., Bedia J., Ruiz-Rosas R., Rodríguez-Mirasol J., T. Cordero, Otero J.C., Márquez M., Barrero A., Loscertales I.G. Filled and hollow carbón nanofibers by coaxial electrospinning of Alcell lignin without binder polymers. Advanced Materials 2007; 19: 4292–4296.

2. R. Ruiz-Rosas, J. Bedia, M. Lallave, I.G. Loscertales, A. Barrero, J. Rodríguez-Mirasol, T. Cordero. Carbon Submicro-fibers by electrospinning of lignin. Carbon 2010, 48, 696-705.

3. R. Ruiz-Rosas, J. Bedia, M. Lallave, I.G. Loscertales, J. Rodríguez-Mirasol, T. Cordero. Methanol decomposition on electrospun zirconia nanofibers. Catal. Today 2011. DOI: 10.1016/j.cattod.2011.10.031.

4. R. Ruiz-Rosas, M. Lallave, I.G. Loscertales, J. Rodríguez-Mirasol, T. Cordero. Electrospun lignin-ceramic microfibers and tubes. Submitted to: Chemistry of Materials.

5. J. M. Rosas, R. Ruiz-Rosas, J. Bedia, M. Lallave, I.G. Loscertales, J. Rodríguez-Mirasol, T. Cordero. Electrospinning of silica sub-microtubes with platinum nanoparticles for the catalytic NO abatement. Submitted to: Chemistry of Materials.

This work has also generated the following congress and workshop contributions:

1. R. Ruiz-Rosas, J. Bedia, J. Rodríguez-Mirasol, T. Cordero, M. Lallave, I.G. Loscertales, A. Barrero. Preparation and characterization of lignin-based carbón nanofiber and nanotubes (Oral). Carbon, Seattle (USA), 2007.

2. R. Ruiz-Rosas, J. Bedia, M. Lallave, I.G. Loscertales, A. Barrero, J. Rodríguez-Mirasol, T. Cordero. Influencia de la temperatura de carbonización en las propiedades físico-químicas de las nanofibras de lignina (Oral). IX reunión del grupo español del carbón, Teruel (Spain), 2007.

3. R. Ruiz-Rosas, J. Bedia, M. Lallave, I.G. Loscertales, A. Barrero, J. Rodríguez-Mirasol, T. Cordero. Preparation and characterization of lignin-based Pt-carbon nanofibers (Poster). Carbon, Nagano (Japan), 2008.

4. R. Ruiz-Rosas, J.M. Rosas, J. Bedia, M. Lallave, I.G. Loscertales, A. Barrero, J. Rodríguez-Mirasol, T. Cordero. Preparation and characterization of lignin-based carbon submicrofibers and submicrotubes (Poster). ERA CHEMISTRY 6, Krakow (Poland), 2008.

5. R. Ruiz-Rosas, J. Bedia, M. Lallave, I.G. Loscertales, A. Barrero, J. Rodríguez-Mirasol, T. Cordero. Lignin-based electrospun carbon submicrotubes and submicroforms (Oral). Carbon, Biarritz (France), 2009.

6. J.M. Rosas, R. Ruiz-Rosas, M. Lallave, I.G. Loscertales, A. Barrero, J. Rodríguez-Mirasol, T. Cordero. Pt/Silica Nanotubes for selective catalytic reduction of NO (Poster). Europacat IX, Salamanca (Spain), 2009.

7. R. Ruiz-Rosas, J. Bedia, M. Lallave, I.G. Loscertales, A. Barrero, J. Rodríguez-Mirasol, T. Cordero. Lignin-based electrospun carbon microforms (Poster). COST Chemistry D36 Workshop, Benahavis (Spain), 2009.

8. R. Ruiz-Rosas, J. Bedia, M. Lallave, A. Barrero, I.G. Loscertales, J. Rodríguez-Mirasol, T. Cordero. Preparation and characterization of lignin-based carbón microtubes (Poster). Carbons for Energy Storage and Enviromental Protection (CESEP ‘09), Torremolinos (Spain), 2009.

9. R. Ruiz-Rosas, J. Bedia, M. Lallave, A. Barrero, I.G. Loscertales, J. Rodríguez-Mirasol, T. Cordero. Preparation and characterization of co-electrospun lignin-alumina microfibers and tubes (Oral). Carbon, Clemson (USA), 2010.

10. R. Ruiz-Rosas, J. Bedia, M. Lallave, A. Barrero, I.G. Loscertales, J. Rodríguez-Mirasol, T. Cordero. Methanol decomposition on electrospun zirconia nanofibers (Poster). COST Chemistry 36D Final Workshop. Fuengirola (Spain), 2011.

Acknowledges

Gracias es una de mis palabras favoritas.

Soy un tipo con suerte. Estoy rodeado de gente maravillosa y generosa. Derrida dice que para que un regalo sea completo, no debiera esperarse nada a cambio. Añade que un regalo así es imposible. El continuo intercambio, el reconocimiento y la comprensión mutuos, aquello que compartimos y que nos regalamos a diario, es interesado, y ese interés en el otro es lo que lo hace valioso. Es la única riqueza que llena.

Por eso, todos los días, gracias

A Mario y a Laura, por ser conmigo

A mis padres, por todo lo que tengo

A Tomás y a Pepe, por todas las puertas a un futuro mejor que me han abierto

A Nani, Olga, Jorge, María, Luis, Mari, Aurora, Fran y todos los que han pasado y pasan por el laboratorio, por hacer que cada día no vaya a trabajar, sino a aprender y a disfrutar

To Isabel and Inês, and Semih, Sesser, John and Ari, you gave me a warm home when I was abroad

A Bea, Merce, Elio, Elías, David, Juan, Paco, Álvaro, Martos, Jose Félix, Javi, Nieves, Marisa, Elisa, Marta, Sergio, Lucía, Elena, Marina, Alex, Rocío, Daviti y algunos otros, por todo lo que hemos vivido juntos estos años

R.R.R. acknowledges the assistance of the Ministry of Science and Education of Spain for the award of a FPI grant.

CONTENTS

0. OBJECTIVES

Electrospinning has emerged in recent years as a promising thecnique to prepare continuous fibers with sizes below the micron. A wide range of polymeric and ceramic precursors, even many apparently non-spinnable, can be casted in such a way. For instance, cheap biomass residues could be used as carbon fiber precursor, and sol-gel strategies to obtain porous alumina or silica can be also adapted to electrospinning production of ceramic fibers.

The main purpose behind this work is extending the current electrospinning applications to chemical engineering ones. The usual fate of these fibers is to be used in biomedicine, filter membranes or in thin films applications. But we could take advantage of the properties of these materials to improve the performance of heterogeneous catalysts and adsorption systems. Their small size and their usual conformation in non-woven membranes can overcome mass transport limitations and high pressure drops in the reacting system and can be easily handled. Moreover, the flexibility of the technique could allow cleverly modifying the electrospinning setup to achieve control of the active phase emplacement and particle size.

Consequently, this thesis reports the use of electrospinning in the preparation, as well as the characterization and test in chemical engineering applications, of:

a) Porous carbon fibers for catalytic and adsorption applications, and

b) Composite or ceramic heterogeneous catalysts that could be used in gas reaction systems, such as alcohol dehydration or air pollutant abatement.

1. INTRODUCCIÓN

1.0. Abstract

This chapter presents fiber production, in particular those made of carbon, by traditional methods. Next, electrospinning technique is explained. A brief history of the process, a detailed phenomenology of the technique and the most actual applications of electrospun fibers are developed in this section. Moreover, the coaxial electrospinning, one of the most interesting modifications used in electrospinning devices, is also defined. This chapter also contains a small introduction to catalysis and adsorption process, which are the intended application fields of the materials presented in this thesis. The reasons for using such electrospun fibers in these applications are also assessed. Usual catalyst synthesis processes are described. Materials for supports, as zeolites, nanostructured mesoporous materials, alumina or carbon; support preparation methods, such as sol-gel, hydrothermal treatment or nanocasting; impregnation methods of active phase, such as electrodepostion, incipient wetness and so on; as well as processing techniques for production of conformed solid catalysts are provided. Lignin-based carbon catalysts are also included. Finally, a methodology section, where additional equipments for thermal treatment and the reaction systems are described, closes the chapter.

1.1.Fibras

Por estructura fibrilar se entiende una forma maciza o hueca que es continua en una dimensión. Los materiales fibrilares son conocidos desde hace siglos. Las primeras fibras usadas por el hombre fueron de origen vegetal, principalmente aquellas provenientes del lino, el algodón o el cáñamo, siendo destinadas al hilado de textiles. También las fibras de origen animal, como la lana o la seda, fueron así empleadas.

Las primeras patentes para producir fibras de celulosa, conocidas como rayón, aparecen en el siglo XIX. Aunque el primer uso que ideó el químico inglés Joseph W. Swan para sus fibras fue el de filamento de carbono para las lámparas eléctricas incandescentes de Edison, en cuestión de años su invención fue aplicada a la producción a gran escala de “seda artificial”, destinada a uso textil. El siguiente gran avance vino de la mano del descubrimiento de los polímeros sintéticos en los años treinta del siglo XX.

Hasta ese momento, las fibras se obtenían a partir de polímeros naturales como la mencionada celulosa. Con la llegada del nylon, producido por polimerización de la caprolactama, las principales materias primas para la fabricación de fibras pasan a ser los derivados del petróleo.

Hoy en día se producen fibras de toda índole para usos muy variados a partir de multitud de polímeros. Las de mayor importancia siguen siendo las textiles, aunque las novedosas aplicaciones de las fibras de carbono las convierten en productos muy atractivos y de alto valor añadido, por lo que adquiere gran importancia el conseguir nuevas formas de fabricación de las mismas.

1.1.1. Producción de fibras por extrusión

La vía más habitual para el hilado de fibras. Consta de los siguientes puntos:

- Disolución o fundido del precursor deseado, a veces añadiendo fundentes para dar plasticidad a la mezcla resultante.
- Extrusión de la mezcla en una hiladora. Según si el precursor requiere una simple solidificación o una polimerización, esta etapa se llevará a cabo sometiendo al extrusado a un tratamiento en seco o en baño.
- En las fibras de carbono, es común un paso de estabilización de las fibras precursoras mediante pre-oxidación con disoluciones ácidas o estabilización térmica, lo que modifica la termoplasticidad de la fibra, evitando que esta se funda en la etapa siguiente.
- Para las fibras de carbono se hace necesario una carbonización de la fibra estabilizada, que se lleva a cabo en atmósfera inerte y normalmente a temperaturas comprendidas entre 1000 y 1400 ºC.
- Además, en aras de conseguir unas determinadas propiedades químicas superficiales, ya sea para aumentar su mojabilidad o para usar la fibra como soporte catalítico, se añade una etapa de tratamiento superficial de oxidación usando para ello distintos agentes oxidantes.

El diámetro final de las fibras preparadas de esta forma puede ser de hasta 10 μm, aunque cabe la posibilidad de conseguir mejoras en estas cifras con los últimos avances en los equipos de extrusados.

1.1.2. Producción de fibras por otros métodos mecánicos

Además de la extrusión tradicional, los métodos más usados hoy día para la producción de fibras por métodos mecánicos son:

1.1.2.1.Hilado de bicomponentes

En este caso, las fibras son hiladas por extrusión usando dos materiales [1]. Los avances tecnológicos en los sistemas de hilado permiten conformar fibras en estructuras corteza/núcleo, de cebra, en porciones de tarta y otras muchas formas. Las aplicaciones de estas conformaciones permiten, por ejemplo, retirar a posteriori uno de los componentes para obtener una fibra de menor tamaño o de aspecto segmentado. También, utilizando un polímero de bajo punto de fusión en la corteza de la fibra y otro de mayor punto de fusión en el interior, se pueden producir textiles que se fusionan por diversos puntos de su superficie formando redes más resistentes.

1.1.2.2.Soplado fundido

Este proceso permite producir redes fibrosas a partir de polímeros o resinas fundidos, usando para ello flujos de aire a gran velocidad o algún otro sistema para atenuar los filamentos [2]. Las fibras así obtenidas no son ordenadas y alcanzan tamaños alrededor de 3 µm, habiéndose registrado tamaños entre los 0.1 y los 15 µm. Aunque su módulo de Young no suele ser elevado, los textiles así obtenidos tienen una elevada opacidad, y su reducido tamaño hace que gocen de una elevada área específica externa, posibilitando su uso en adsorbentes y en aislantes.

1.1.3. Producción de fibras de reducido tamaño por métodos químicos

Además de los métodos basados en extrusión o inyección, existen métodos químicos, del tipo bottom-up, para producir nanofibras. El principal problema que se encuentra a la hora de usar estos métodos es la baja velocidad de producción que poseen y el elevado precio de las fibras así producidas. Entre estos métodos se cuentan:

1.1.3.1.Autoensamblaje

Hace referencia a la producción de nanofibras a partir de la correcta disposición de las moléculas que la componen. Las moléculas se disponen en estructuras ordenadas por interacciones de tipo no covalente. Las dimensiones de las fibras obtenidas por esta

vía son difíciles de controlar, y el método es complicado de transladar a la industria por problemas en su escalado. Se han producido nanotubos de pared múltiple de anchuras de pared por debajo de los 500 nm usando esta vía [3].

1.1.3.2.Nanomoldeo

En esta técnica se utiliza un material nanoestructurado poroso como molde o negativo con el que obtener las fibras [4]. El precursor del material del que se quiere fabricar la fibra es infiltrado en la red porosa del molde, para lo cual el precursor debe hallarse en fase líquida o gaseosa. Es necesario que el molde y el precursor o la disolución en la que viaja se encuentren en contacto íntimo para asegurar una infiltración que aproveche al máximo el molde escogido. Para asegurar un completo mojado de los poros, la química superficial del molde debe poseer una polaridad similar a la del disolvente; a veces se añaden surfactantes que ayudan a facilitar el contacto. Además, para evitar bloqueos de la red porosa, la velocidad de deposición debe ser menor que el tiempo de difusión del precursor a través de la red porosa. Por último, la temperatura, el pH y en general las condiciones de trabajo deben ser cuidadosamente escogidas para evitar un colapso del molde, como ocurre por ejemplo con las zeolitas al ser usadas en atmósferas húmedas o al trabajar a temperaturas elevadas. Una vez se asegura la correcta infiltración del molde, se procede a una segunda etapa de lavado en la que se retira el molde, habitualmente destruyéndolo, quedando libre la nanoestructura ordenada. Entre los métodos de infiltración del precursor disponibles se cuentan:

- *Deposición.* En ella el poro es infiltrado por el precursor en forma de disolución. El precursor se adsorbe en las paredes de los poros. Controlando los tiempos de contacto y la concentración de la disolución, es posible obtener nanotubos en tiempos cortos y bajas concentraciones, y nanofilamentos cuando la infiltración de la red porosa es completa [5].
- *Deposición electroquímica.* En ella el molde es en primer lugar anodizado con una capa metálica muy fina, con el objeto de hacerlo conductor. A continuación, los poros se rellenan por completo con un precursor que puede ser metálico o un polímero conductor, produciéndose nanofilamentos de metal o de carbono [6].
- *Polimerización.* El molde se sumerge en una disolución que contiene un monómero. A continuación, se añade el agente de polimerización. El

polímero resultante nucleará preferencialmente sobre las paredes de los poros del molde, creciendo a lo largo del radio del mismo. Nuevamente, tiempos cortos producirán nanotubos, mientras que tiempos largos conllevarán infiltración completa de la red porosa y formación de nanofilamentos [7].

• *Sol-gel.* De forma análoga a la polimerización, es posible preparar un sol en el que se dispersen partículas del molde. Las micelas del sol y posteriormente los agregados de partículas del gel se formarán dentro de los poros. Tras los tratamientos térmicos correspondientes, se obtendrá un xerogel que retendrá la morfología de la red porosa del molde [8].

1.1.4. Tipos de fibras atendiendo a su composición

Además de las fibras orgánicas, como las de carbono para refuerzo en materiales compuestos o las poliméricas del sector textil, es posible conformar en filamentos algunos materiales inorgánicos, siendo el caso más aplicado comercialmente el del óxido de silicio, del que se producen las fibras ópticas utilizadas en telecomunicaciones y las fibras de vidrio usadas como refuerzo. En cuanto a la aplicación de fibras en ingeniería química, las telas de fibra de carbón activado aventajan en uso a las fibras compuestas por otros materiales. A continuación se presentan las fibras de carbono y los nanotubos de carbono, un tipo de material carbonoso relativamente reciente que ha despertado el interés investigador, entre otras razones, por su posible uso como soporte catalítico.

1.1.4.1. Fibras de carbon

Las fibras de carbono son, hoy en día, un material de elevada importancia tecnológica y económica. Estos materiales se distinguen por su morfología filamentosa y un alto contenido en carbono, superior al 90% en peso. Sus propiedades químicas, mecánicas y eléctricas las hacen idóneas para multitud de aplicaciones avanzadas en campos tan dispares como la industria aeroespacial, la catálisis heterogénea o el material deportivo. Desde que se ideara un método de preparación de fibras de carbono a partir de la carbonización de filamentos de bambú (celulosa) a finales del siglo XIX, han aparecido una amplia gama de materiales carbonosos que son susceptibles de ser usados como precursores de estas fibras. En la década de los sesenta, la Union Carbide

ideó un método en el que se usaba rayón (celulosa purificada) para obtener fibras de alto módulo de Young. Más adelante hizo su aparición el poliacrilonitrilo (PAN), precursor más utilizado en la actualidad. Las fibras fabricadas a partir de éste tienen unas propiedades mecánicas excelentes, pero al ser caro, eleva el coste de producción. El uso de breas de petróleo o resinas fenólicas como materias primas para la preparación de fibras de carbono abarata el coste, pero empeoran sus propiedades. En las últimas dos décadas se ha investigado el uso de breas como precursores [9,10]. También se investiga en este campo el uso de fuentes renovables o recicladas de carbón [11]. Según el método de preparación que se haya seguido, el precursor utilizado, así como las propiedades obtenidas, las fibras comerciales se clasifican en:

- *Fibras de carbono de altas prestaciones.* Preparadas a partir de breas de mesofase (ultra-alto módulo) o poliacrilonitrilo (alto módulo). Se necesitan tratamientos térmicos adicionales a 2000-3000 ºC para su preparación. Por su elevado coste, estas fibras se dedican a aplicaciones muy limitadas que requieren fibras de muy altas prestaciones, como la industria aeroespacial, material deportivo, refuerzo en los materiales compuestos, etc.
- *Fibras de carbono conductoras/grafíticas.* Se preparan a partir de fibras de carbono, siempre que sean grafitizables, con un tratamiento térmico a 2400-3000 ºC. A esas temperaturas, los microcristales de carbón se ordenan tridimensionalmente en forma de carbono grafito, obteniéndose excelentes propiedades conductoras.
- *Fibras de carbono de uso general.* Se preparan a partir de breas de carbón y petróleo y resinas fenólicas. Su precio y propiedades mecánicas son inferiores que las de altas prestaciones. Entre ellas se cuentan las fibras de carbono activadas y las fibras de carbono crecidas en fase vapor. Las fibras de carbono activadas se distinguen por su elevada área superficial y distribución de tamaño de poros muy uniforme. Se preparan a partir de cualquiera de los precursores ya mencionados, añadiendo una etapa de activación, ya sea física o química, tras la carbonización. Estas fibras se pueden obtener en forma de telas o fieltros. Las fibras de carbono crecidas en fase vapor, en cambio, se obtienen mediante un proceso catalítico de depósito químico en fase vapor. Por este procedimiento se pueden preparar

fibras de reducido diámetro. Este método es análogo a la deposición química en fase vapor por el cual se preparan los nanotubos de carbono.

1.1.4.2.Nanotubos de carbono

Los nanotubos de carbono o CNT son estructuras de carbono grafito dispuestas en forma de lámina enrollada helicoidalmente a lo largo de un eje. Estos tubos pueden estar compuestos por una lámina (nanotubos de carbono de pared única o SWCNT, [12]) o por varias (nanotubos de carbono de pared múltiple o MWCNT [13]). Sus diámetros oscilan entre los 0,4 nanómetros del nanotubo de pared única hasta unas pocas decenas de nanómetros. Estos materiales están dotados de propiedades muy interesantes, como una estructura mesoporosa unidimensional a lo largo de su eje, altas áreas superficiales específicas, bajas resistividades eléctricas, alta estabilidad química y excelentes propiedades mecánicas. Desde que en 1991 Iijima publicó un método para preparar nanotubos de carbono por arco de descarga eléctrica [13], estos materiales han estado en el centro de atención de la comunidad científica internacional, contándose por miles las publicaciones referidas a métodos de síntesis, modificaciones estructurales, enaltecimiento de propiedades y novedosas aplicaciones de estos materiales carbonosos. Por citar algunos ejemplos de entre los muchos disponibles, se ha postulado el uso de CNT para la adsorción de H_2 [14], en la fabricación de transistores y circuitos lógicos [15], para reforzar materiales compuestos [16], en la preparación de sensores de VOCs multiseñal [17], como electrodos de supercondensadores [18] o como soportes catalíticos [19]. Los métodos de síntesis de CNT más usados son:

- *Descarga de arco eléctrico.* Fue la vía por la que Iijima produjo accidentalmente nanotubos de carbono como coproducto en la producción de fullerenos [13]. Consiste en la aplicación de un voltaje en torno a los 20V y de una corriente del orden de la centena de amperios en dos electrodos de grafito enfrentados, separados a una distancia de unos 5 mm y en una atmósfera de presión relativamente baja e inerte, siendo de helio habitualmente, Figura 1.1. En esas condiciones, se forma un plasma de carbono sublimado entre los electrodos que alimentará el crecimiento de los MWCNT sobre el ánodo, mientras el cátodo se va consumiendo durante el proceso. El ánodo puede ser dopado con catalizadores como níquel o cobalto para producir SWCNT [20]. La selectividad de este procedimiento ronda el 40%.

- *Ablación de plasma con láser*. Desarrollada por el grupo de Richard Smalley en la Rice University [21]. En ella, una porción de grafito es colocada en el centro de un horno tubular, mientras que en uno de los extremos se posiciona el láser que incidirá sobre el grafito vaporizándolo, y en el extremo contrario una punta de cobre refrigerada donde se depositarán los nanotubos formados, Figura 1.2. El horno se lleva a temperaturas de 1200 ºC en condiciones cercanas al vacío, y durante la operación se hace pasar una corriente de argón a una presión moderada, que será la que arrastre el carbono para que se deposite en forma de nanotubo en la punta de cobre [22]. La temperatura del horno puede controlar el diámetro de los CNT formados. Son mayoritariamente SWCNT, y su selectividad llega al 70%, aunque es un método costoso.

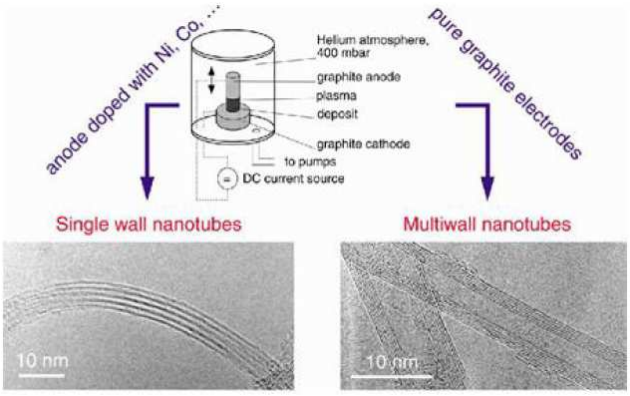

Figura 1.1. Descarga de arco eléctrico para la producción de CNT

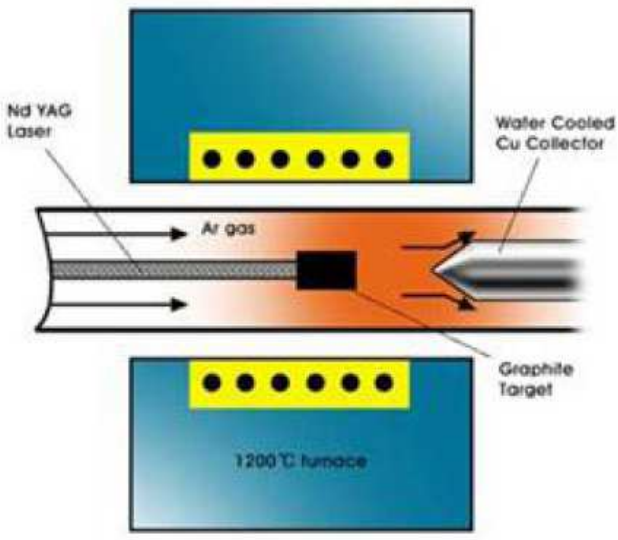

Figura 1.2. Método de ablación con láser para la producción de CNT

- *Deposición química en fase vapor (CVD).* Aunque reportado en fechas tan tempranas como los años 50, este método no regresó a la palestra hasta después de los trabajos de Iijima. La CVD consiste en un crackeo controlado de un hidrocarburo sobre un soporte catalítico dopado con metales de transición como el níquel [23], Figura 1.3. El catalizador es llevado a la temperatura de reacción en una atmósfera reductora para aumentar su actividad. Posteriormente, se hace pasar una corriente gaseosa compuesta por el gas de síntesis escogido, como puede ser el acetileno, el metano o el benceno, junto con hidrógeno. El hidrocarburo crackea sobre las partículas metálicas de catalizador, depositándose el carbono de forma ordenada sobre ella. El carbono grafítico difunde hacia el soporte, disponiéndose sobre la capa anterior de grafito y haciendo crecer la fibra, mientras que la partícula de catalizador se distancia de la superficie del sustrato. Por lo tanto, el tamaño de la partícula metálica dictará el diámetro del CNT preparado. Además, la relación de caudal entre el gas del precursor y el hidrógeno, así como la temperatura del horno y el metal escogido influirán tanto en la forma como en la longitud y en la pureza de los nanotubos obtenidos. Es el método que más se utiliza en la actualidad para la producción de CNT comerciales, así como el que más atención recibe por parte de los investigadores, como demuestra el número de artículos sobre CVD publicados en el último lustro, superando los 5000 artículos (SCOPUS, Septiembre de 2011.

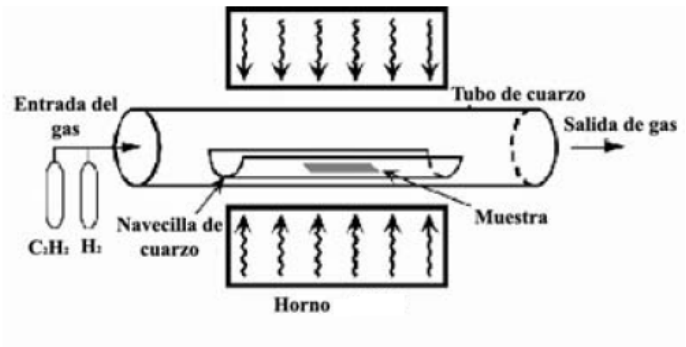

Figura 1.3. Reactor tubular para CVD

1.2.Electrospinning

La técnica de producción de fibras derivada de la aplicación de fuerzas electrohidrodinámicas (EHD) a un líquido conductor es denominada como electrospinning o electrohilado. Aunque tradicionalmente los materiales usados para la producción de fibras se limitan a polímeros, esta técnica para preparar fibras a partir de cualquier material en disolución o mezcla fundida gracias a una cuidadosa selección de disolventes y de la configuración del equipo de electrohilado. La principal característica de estas fibras es su reducido tamaño, siendo posible alcanzar diámetros en las decenas de nanómetros usando componentes de mucho mayor tamaño y disponibilidad. En consecuencia, desde que fue redescubierto en los noventa el electrohilado ha despertado un interés creciente en la comunidad científica, que ha motivado miles de publicaciones de temática dispar, y los numerosos avances cosechados en los últimos veinte años han hecho de la simple enumeración de las posibilidades de la técnica una ardua tarea que queda pronto desfasada. Por ello, aquí sólo se pretende presentar la técnica y describir aquellos de sus apartados que tienen un mayor grado de implicación en el trabajo desarrollado en esta tesis doctoral. Para obtener una panorámica más concreta sobre los aspectos más importantes del electrohilado sería recomendable acudir a algunas de las revisiones bibliográficas más destacadas, como aquellas que versan sobre aplicaciones [24-26], configuraciones del equipo [27], materiales electrohilables [28], la escalabilidad y la recolección de fibras [29], la descripción y modelado de las fuerzas EHD que hacen posible la técnica [30] y otras muchas sobre el estado del arte, disponibles en la literatura científica.

1.2.1. Historia

Aunque sería posible remontarse mucho más atrás en el tiempo si se considera como parte de su historia los descubrimientos en el campo del estudio de las fuerzas electrohidrodinámicas que se hayan detrás del funcionamiento de la técnica, el electrospinning tal y como es estudiado hoy día aparece por primera vez en una patente de Anton Formhals en la década de los 30 del siglo pasado [31]. En este documento se menciona ya que la acción de un campo eléctrico sobre disoluciones conductoras permite producir hilos de reducido tamaño o gotas. Formhals no es el único que estudia este fenómeno, habiendo incluso patentes anteriores como las de Cooley y Morton, aunque sí es el inventor más destacado de este grupo de precursores. Años más tarde,

Simm et al también proponen la producción de fibras de reducido para filtros usando este sistema.

De cualquier forma, ninguna de estas patentes se traducen en un uso comercial del electrospinning, hecho que tendría que esperar hasta la década de los ochenta en el mundo occidental, cuando la compañía Donaldson comienza a producir masivamente fibras electrohiladas como componente adsorbente de sus filtros [32]. En el otro lado del telón de acero, los científicos soviéticos Rozenblum y Petryanov-Sokolov también publicaron la fabricación de fibras electrohiladas, a las que buscaron como aplicación la captura de aerosoles. A partir de los años 40, el gobierno comunista puso en funcionamiento algunas fábricas que producían fibras de acetato de celulosa electrohiladas en disoluciones de etanol y dicloroetano, siendo usadas en unos filtros, usados como equipo de protección en plantas nucleares, que se dieron a conocer como "Filtros Petryanov". A finales de los años 60, el gobierno de la URSS proclamaba producir 20 millones de metros cuadrados por años de estos materiales.

Más allá de estos casi anecdóticos casos de comercialización de la técnica, ésta fue ignorada por la comunidad científica hasta los años 90, momento en que, con los trabajos del grupo de Reneker [33], Rutledge [34] y algunos otros, entre los que se cuenta el grupo de Loscertales en la Universidad de Málaga [35], el electrospinning fue revalorizado como una fuente potencial de fibras continuas de reducido tamaño y de una vasta variedad de compuestos poliméricos y precursores cerámicos. A modo de ejemplo del enorme interés captado por la técnica, a fecha de Septiembre de 2011, es posible encontrar más de 6400 trabajos bajo la acepción electrospinning y 261 reviews en la base de datos Scopus.

Hoy día, las principales compañías productoras de fibras mediante electrospinning se agrupan en la página web www.spinrati.com, contándose por decenas las universidades donde hay grupos entre cuyas líneas de investigación está el electrospinning. Cabe destacar en este sentido a la empresa española YFLOW, fundada en 2001 por científicos de las Universidades de Málaga y Sevilla. Esta empresa es pionera en el uso de técnicas electrohidrodinámicas para la producción de fibras, destacando sobretodo su crucial aporte en el desarrollo de equipos de electrospinning coaxial o co-electrospinning, cuya configuración de agujas coaxiales permite producir materiales fibrilares encapsulados o fibras huecas en un único paso.

1.2.2. Descripción de la técnica

El electrospinning se vale de un uso preciso de las fuerzas electrostáticas para abordar la producción de fibras submicrométricas. Estas fuerzas ya han sido usadas con anterioridad en los precipitadores electrostáticos o en los sprays para las emulsiones de pesticidas. Se puede definir el electrospinning como un proceso en el que una disolución de un polímero, un sol o una mezcla fundida, todas ellas conductoras, son hiladas en fibras de pequeño diámetro usando un campo eléctrico de elevado potencial. Las ventajas más evidentes de esta técnica son su simplicidad y flexibilidad.

1.2.2.1. Equipo básico

Aunque las interacciones físicas, químicas y eléctricas que rigen en este proceso son complejas, el aparato usado para electrohilado resulta de construcción sencilla, Figura 1.4. El montaje suele consistir en una fuente électrica de alto voltaje, que se usa para cargar eléctricamente una disolución de precursor de fibra, que se encuentra en una bomba de jeringa, en cuya boquilla se coloca la hiladora, normalmente una aguja metálica. En frente de la jeringa y a una distancia de no más de un metro, se emplaza un colector metálico también cargado eléctricamente con polaridad inversa a la de la disolución de precursor. El colector será una placa de aluminio, un tambor giratorio, una bandeja llena de líquido u otro sistema que permita la recolección de las membranas compuestas por fibras enmarañadas u orientadas según el tipo de colector empleado.

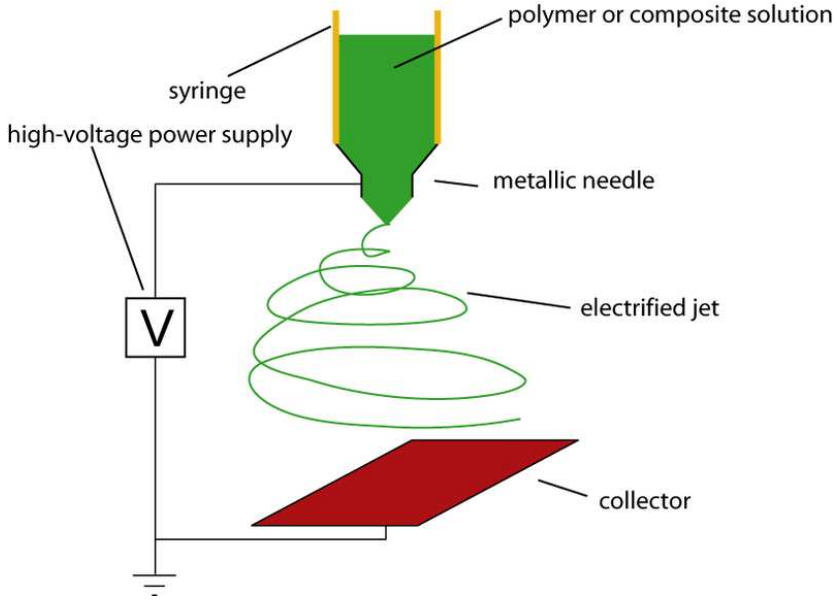

Figura 1.4. equipo básico de electrospinning (wikimedia commons).

1.2.2.2. Cono de Taylor

La disolución del precursor del material al que queremos dotar de forma fibrosa se bombea desde la jeringa a baja velocidad. Una gota de la disolución aparece en la punta de la aguja de la hiladora. La fuente de alto voltaje conectada a la misma induce la carga de la disolución. Los iones cargados que se producen se desplazan en la disolución hacia el punto más cercano al colector, que ha sido cargado a distinta polaridad para atraerlos. Ese punto es la gota en el extremo de la aguja. En ella, el equilibrio de fuerzas viscosas, de tensión superficial y eléctricas de repulsión entre cargas en la superficie de la gota causan que ésta se deforme, adoptando forma cónica, Figura 1.5. Este cono es conocido por "cono de Taylor". Más allá de una determinada carga crítica de la disolución, este cono se vuelve inestable, venciendo las fuerzas eléctricas a las de tensión superficial, produciéndose la eyección de líquido desde el cono hacia el colector. La estabilidad de este cono es crítica si se quiere mantener el proceso de electrospinning en funcionamiento durante un tiempo prolongado. Por ejemplo, una velocidad de evaporación alta o un líquido muy viscoso podrían inducir la solidificación del cono de Taylor, lo que detendría el proceso de electrospinning.

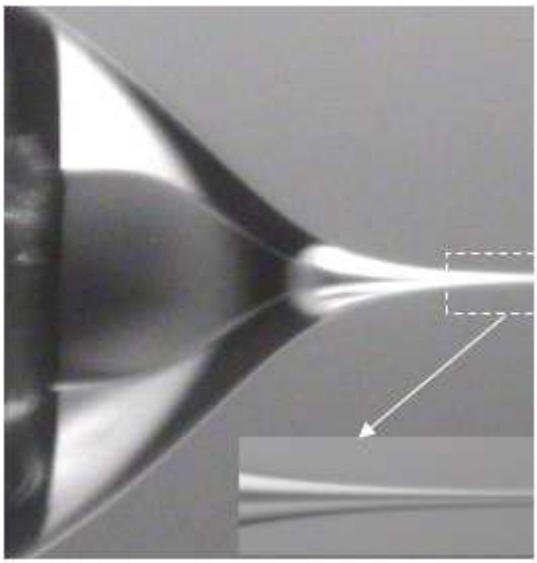

Figura 1.5. Cono de Taylor compuesto[35].

1.2.2.3. Eyección del chorro

Más allá de la carga crítica, un chorro de líquido es eyectado del cono de Taylor. Según es emitido del cono, el chorro de fluido forma un filamento continuo que va

estrechándose según se aleja de la aguja. Este fluido está cargado, y la acción del campo eléctrico entre la aguja y el colector hace que se acelere en sentido aguja-colector. En este sistema, para una disolución de una conductividad dada, el flujo impuesto de líquido en la bomba de jeringa y el potencial de campo eléctrico dictarán la dinámica de eyección de ese chorro a través de la resultante intensidad de corriente, siendo posible escoger unos valores de estos parámetros que mantengan estable el sistema durante un largo periodo de tiempo [30]. Además, de ellos dependerá el grosor del chorro, estrechamente relacionado con el tamaño final de la fibra. La figura 1.6 muestra este efecto.

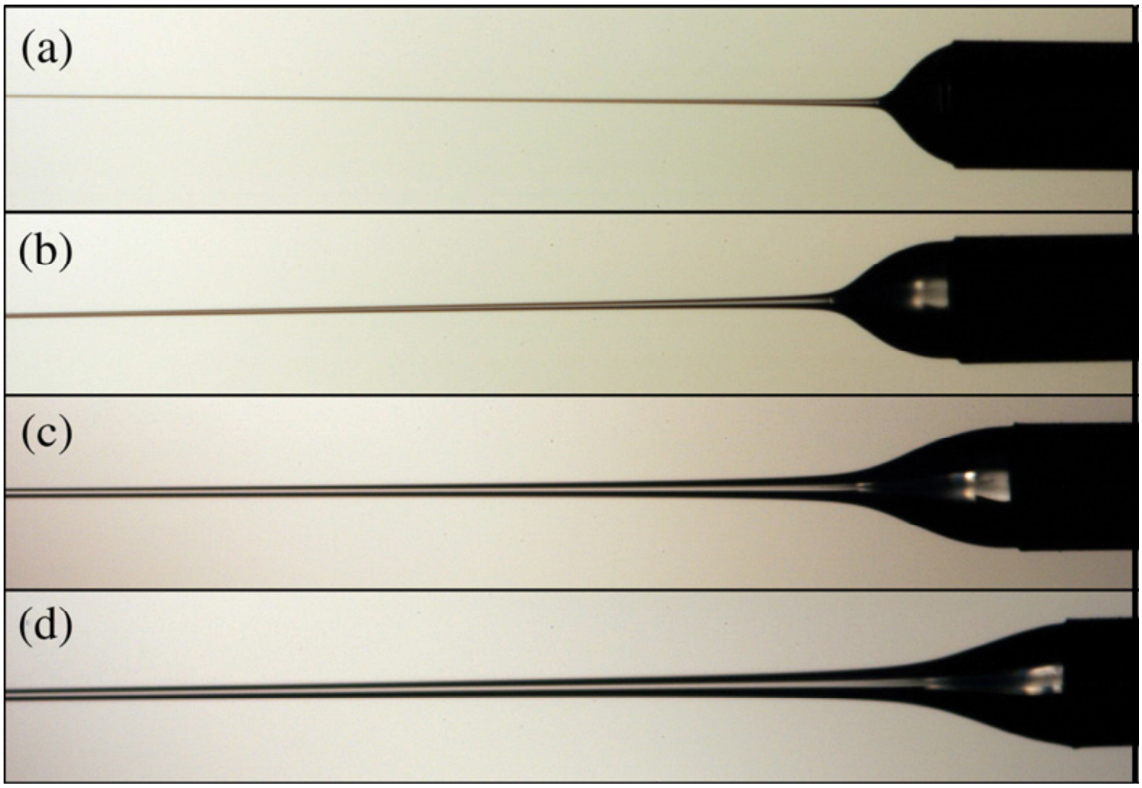

Figura 1.6. Imágenes de chorro hilado a partir de disoluciones de polietilenóxido en agua (a) Q=0.02 ml/min, E=0.282 kV/cm; (b) Q=0.10 ml/min, E=0.344 kV/cm; (c) Q=0.50 ml/min, E=0.533 kV/cm; (d) Q=1.00 ml/min, E=0.716 kV/cm [30].

1.2.2.4. Inestabilidades

En el vuelo del chorro hacia el colector, alguna de las fuerzas que están actuando simultáneamente sobre el filamento de fluido se impondrá, causando la aparición de las llamadas inestabilidades, responsables de cambios en la trayectoria, forma e incluso estabilidad del chorro. Se ha de considerar que, para conseguir mantener el

electrospinning operativo, durante el vuelo hacia el colector el chorro debe, en primer lugar, ser continuo. En segundo lugar, el disolvente que lo mantiene como líquido debe tener tiempo suficiente para evaporarse, dejando un filamento sólido que será el recogido en forma de membrana tras impactar en el colector. Las inestabilidades pueden acabar con la morfología fibrilar del chorro y/o hacer más largo el recorrido del chorro hasta el colector, incrementando el tiempo de vuelo y con ello el de evaporación de disolvente. El estudio de las inestabilidades es, por lo tanto, primordial para poder favorecer la acción de aquellas que nos interesen, y suprimir otras que pongan en peligro la estabilidad del sistema.

- *Inestabilidades de Rayleigh y variceal.* Aunque la primera se derivó para líquidos no conductores, ambas son equivalentes en cuanto a su funcionamiento. Deforman el chorro de forma axisimétrica, lo que quiere decir que causan ensanchamiento y estrechamiento radiales a lo largo de la longitud del chorro. Vienen causadas por la tensión superficial del líquido, y si se le da el tiempo suficiente, causa la rotura del chorro en gotas, obteniéndose el aerosol característico de la técnica de electrospray [36]. Zuo et al. [37] estudiaron el efecto de esta inestabilidad sobre la forma del chorro, y encontraron que si aparece de forma controlada, el chorro solidificará antes de que se rompa en gotas, obteniéndose es una fibra perlada. En ellas se observan protuberancias esféricas encastadas en el cuerpo de la fibra y separadas entre ellas a una distancia regular, como las presentadas en la micrografía de la figura 1.7.
- *Inestabilidad de latigueo.* Consiste en una oscilación lateral del chorro causada por la repulsión resultante entre los iones en su seno [38]. Aunque hace años se consideraba que el chorro se rompía en varios de menor diámetro a consecuencia de esta inestabilidad, se ha demostrado que el chorro es continuo, y el latigueo es el responsable del estrechamiento del diámetro del chorro [34]. El perímetro que alcanza este latigueo radialmente, esto es, la distancia del chorro hasta el eje de tiro de la aguja, va incrementándose según el chorro avanza hacia el colector, cubriendo un volumen con forma de cono invertido. El modelo propuesto por Reneker et al. [39] demuestra que esa elongación es responsable del estrechamiento del chorro, por lo que la aparición de esta inestabilidad se hace muy importante. En un trabajo reciente de Loscertales et al. [40] se demuestra que son tres los números adimensionales que gobiernan la

aparición de esta inestabilidad: los números capilar, el Bond eléctrico y el cociente entre la relajación eléctrica y el tiempo de residencia. La determinación de los valores mínimos y máximos de estos parámetros permitiría ajustar las variables de operación para obtener el latigueo deseado.

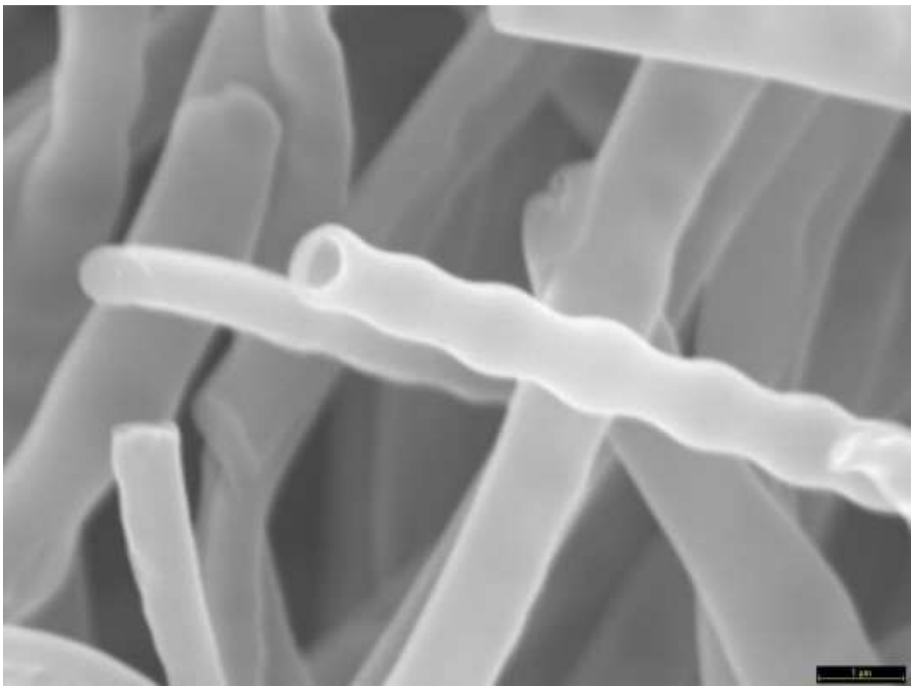

Figura 1.7. Fibra perlada de exterior de lignina e interior de aceite electrohilada mediante electrospinning coaxial. Escala: 1000 nm.

- *Inestabilidad de multichorro.* En ella el chorro se divide en varios filamentos de menor tamaño debido al exceso de densidad de carga superficial. La Figura 1.8 muestra la imagen TEM de una membrana de fibras de óxido de zirconio donde esta inestabilidad lleva a la aparición de tamaños de fibra muy variados.

1.2.2.5.Recolección de la fibra

Cuando las fibras impactan sobre el colector, van acumulándose una sobre otra formando una película de fibras enmarañadas. Estas fibras pueden ser recogidas en forma de membrana, la más habitual de las conformaciones en las que se presentan las nanofibras electrohiladas. En el caso de querer obtener fibras con la misma orientación, es posible aplicar varias estrategias. La más habitual es el uso de un tambor rotatorio como colector [41]. También se pueden usar colectores con formas tan variadas como puntas [42], barras paralelas o simples hatillos de cables conductores para dirigir la

recolección de la fibra en una orientación preferencial. Las fibras tienden a formar puentes entre las puntas o las barras si les le da el espacio adecuado entre ellas. Otra opción es rotar un par de discos o anillos paralelos [43]. Si no hay inestabilidades operando en el electrospinning, lo cual no es habitual, se pueden recolectar fibras orientadas simplemente escribiendo con el chorro sobre la cara del colector [44]. Por último, se pueden utilizar líquido conductores inmiscibles con las fibras que se están hilando en una especie de variante del hilado húmedo tradicional. Esto ayuda a la producción de fibras en las que el disolvente tiene poca volatilidad [45].

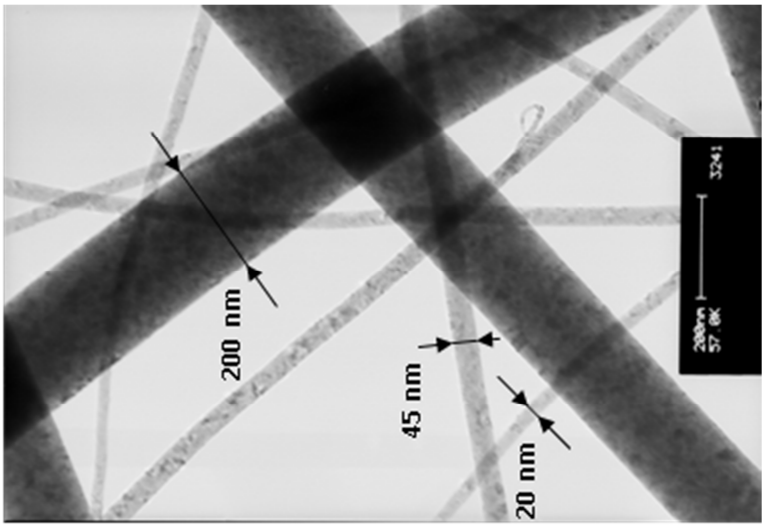

Figura 1.8. Imagen de microscopio electrónico de transmisión (TEM) de fibras de óxido zirconio calcinadas a 500 ºC. Escala: 200 nm.

1.2.3. Variables de operación

Los principales parámetros que controlan la estabilidad del proceso de electrospinning son aquellos que participan en las fuerzas eléctricas, de tensión superficial y viscoelásticas puestas en juego en este sistema. Estos parámetros se reparten en dos grupos; los pertenecientes a la disolución a hilar y los que corresponden al equipo de electrospinning.

Los parámetros del equipo que más influyen en la formación de la fibra son:

- *Voltaje.* El voltaje es responsable de la carga eléctrica del fluido. Como se indicó antes, será necesario un valor mínimo de voltaje para iniciar la eyección del chorro desde el cono de Taylor, mientras que un valor

demasiado alto llevará a la aparición de la inestabilidad de multichorro, descrita con anterioridad. Será necesario trabajar en el umbral marcado por estos dos valores [46]. Por lo demás, se sabe que el aumento del voltaje aplicado conlleva una velocidad de deposición de fibra más alta por una mayor transferencia de masa desde la punta de la aguja [47]. El incremento de la fuerza del campo eléctrico también hace disminuir el tamaño de la fibra al acelerarla, pero reduce el tiempo de vuelo, lo que puede llevar a menos evaporación de disolvente y conducir a fibras mayores [48].

- *Distancia del hilador al colector.* Afecta a la estructura y morfología de las fibras electrohiladas a través de su relación con el tiempo de vuelo, alterando los tiempos de latigueo y de evaporación. Mayores distancias favorecen la eliminación de la inestabilidad variceal, llevan a más tiempo de evaporación y el mayor latigueo reduce el diámetro de la fibra, pero se hace necesario un mayor voltaje para mantener la fuerza del campo eléctrico.
- *Velocidad de bombeo de la disolución.* Aunque favorece la producción de más cantidad de fibra, un mayor bombeo de líquido a la aguja lleva a mayores diámetros de fibra, e incluso puede detener el proceso de electrohilado si la máxima velocidad a la que se transfiere masa a través de la eyección de chorro es menor que la velocidad de bombeo de disolución [47].

Por otro lado, los parámetros de la disolución de mayor importancia son:

- *Concentración del precursor.* La concentración de la disolución es un parámetro de gran importancia porque afecta a la viscosidad y a la tensión superficial. Un valor bajo de concentración favorece la aparición de electrospray debido a la acción de la tensión superficial, mientras que una concentración elevada lleva a mayores viscosidades, hasta tal punto que puedan hacer que la disolución sea imposible de electrohilar. Por norma general, el diámetro de la fibra aumenta con la concentración de la disolución. En cuanto a la viscosidad y a la tensión superficial, la relación entre una y otra es determinante a la hora de obtener fibras de aspecto perlado, ya que la tensión superficial tiende a deformar el chorro en gotas, mientras que las fuerzas viscosas dan cohesión al chorro de líquido; la solidificación del chorro antes de que el chorro se rompa en gotas dará lugar

a tales fibras [49]. Es posible usar aditivos para modificar uno de estos dos parámetros para obtener la morfología deseada. Es el caso del uso de surfactantes en la producción de fibras de poli-vinil-alcohol para reducir la tensión superficial, acabando así con la formación de fibras perladas [37].

- *Conductividad de la disolución.* La disponibililidad de iones cargados en la disolución es un requisito indispensable para hacer electrohilable una disolución. Una mayor conductividad permite incrementar la capacidad de carga del líquido, incrementando el efecto del campo eléctrico. Baumgarden et al [50] demostraron que el radio del chorro varía inversamente con la raíz cúbica de la conductividad eléctrica de la disolución. Es posible añadir electrolitos a una disolución para hacerla más conductora y, por ende, más electrohilable, como se demuestra en el trabajo de Zong et al. en la producción de fibras de PDLA [51]. En cuanto a las inestabilidades, el aumento de la conductividad conlleva la supresión de la inestabilidad variceal, produciendo fibras de superficies más regulares.
- *Volatilidad del disolvente.* La importancia de esta propiedad es obvia, al determinar el tiempo necesario de vuelo para que el disolvente se evapore del chorro, solidificando en forma de fibra. Por otro lado, si el disolvente es muy volátil puede sobrevenir la solidificación del chorro antes de que se inicie la inestabilidad de latigueo, produciendo fibras demasiado gruesas al no haberse visto elongadas por el latigueo. Incluso puede ocurrir la solidificación del cono de Taylor, deteniéndose el proceso [52]. Aunque la volatilidad es una propiedad de la disolución, es posible modificar su efecto actuando sobre el ambiente en el que se lleva a cabo el electrospinning; por ejemplo, la humedad ambiental afecta a la hidrólisis de fibras de alcóxidos, y un control de la misma puede usarse para modificar la velocidad de solidificación de esas fibras.

1.2.4. Electrospinning co-axial

En 2002, los fundadores de Yflow publicaron en Science un método para generar conos de Taylor compuestos a partir del bombeo simultáneo de dos líquidos a través de dos agujas concéntricas. Esto permitía encapsular un líquido en otro siempre que fueran inmiscibles [35]. Como puede apreciarse en la figura 1.9, el montaje es análogo al

previamente detallado del electrospinning. En él, se han duplicando las bombas y se ha añadido una segunda aguja concéntrica a la boquilla de hilado. Sin necesidad de variar el montaje usado para tal fin, los autores extendieron el uso del cono de Taylor compuesto al electrospinning, obteniendo fibras huecas cerámicas a partir de una disolución no electrohilable, para lo que usaron el líquido bombeado por la aguja interna para arrastrar al precursor cerámico [53]. Aunque Barrero et al. patentan este sistema en 2002 [54], entre 2003 y 2004 varios grupos centrados en el estudio de las fuerzas electrohidrodinámicas reportan el uso de electrospinning co-axial para producir fibras compuestas [55-57].

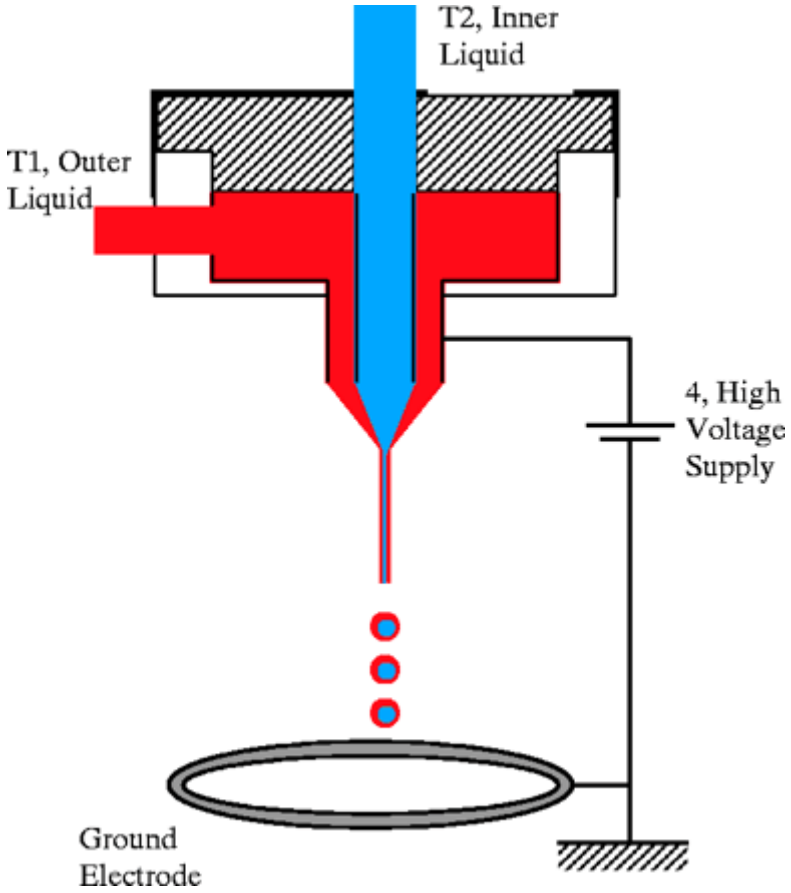

Figura 1.9. Montaje co-axial para encapsular líquidos, fácilmente extensible a electrospinning [35].

Este sistema de electrospinning puede ser usado para producir nanocápsulas de líquidos inmiscibles e hilar líquidos inmiscibles, tal y como se ha descrito en el párrafo anterior. También se pueden obtener fibras compuestas con distinta composición entre el interior y la superficie y fibras huecas extrayendo el líquido bombeado por la aguja interna, temas a los que se dedican dos de los capítulos de esta tesis.

En cuanto a las variables de operación en el eletrospinning co-axial, además de los parámetros descritos con anterioridad, aparecen tres nuevas variables [58]:

- La tensión superficial entre ambos líquidos, los cuales son no miscibles, es grande, y debe ser reducida al mínimo para obtener un cono de Taylor estable. Se suele conseguir añadiendo surfactantes u otros aditivos que sean miscibles en ambos líquidos.
- La viscosidad de ambos líquidos debe ser suficientemente elevada como para que el movimiento impuesto por el líquido de arrastre o conductor (en nuestro caso, el líquido bombeado por la aguja interna) se transmita hacia el otro líquido gracias al rozamiento en la interfase, venciendo además las fuerzas de tensión superficial que podrían acabar con el cono de Taylor compuesto.
- Por último, los cocientes de velocidad de bombeo externo e interno son controlados para evitar la aparición de un modo de goteo (si el caudal interno es muy bajo respecto al externo) o la desaparición de la capa de líquido externo, que podría verse arrastrada en gotas disueltas en el elevado flujo bombeado por la aguja interna.

1.2.5. Aplicaciones de los materiales electrohilados

Las fibras de reducido tamaño ya contaban con aplicaciones potenciales antes del redescubrimiento del electrospinning, y los últimos años han visto una explosión de publicaciones en las que se añaden nuevos campos donde aprovechar el pequeño tamaño y las excelentes propiedades de estos materiales. Si hubiese que escoger el campo donde las fibras electrohiladas han encontrado un mayor número de aplicaciones, seguramente sería la biomedicina el elegido, seguido de la separación en aguas cuando se usan como filtros. Cabe destacar también las aplicaciones como sensores, almacenamiento de energía, catalíticas e incluso como refuerzo estructural.

1.2.5.1. Aplicaciones en filtros

Esta fue la primera aplicación en la que se usaron fibras electrohiladas. Con ellas, es posible filtrar partículas de tamaño submicrométicо [59]. Las membranas de fibras poliméricas así preparadas tienen la ventaja de causar bajas pérdidas de presión en operación, y al estar cargadas eléctricamente pueden ejercer también de filtros

electrostáticos [60]. Si el material es poroso, puede ser usado como adsorbente en procesos de eliminación de contaminantes, tanto en fase acuosa como gaseosa, caso de las fibras de nylon para la eliminación de cadmio o de fibras de carbono para la adsorción de dióxido de azufre [61,62]. En cuanto a separación, la rugosidad o la morfología superficial de la fibra, así como la distancia entre las fibras, pueden ser aprovechadas para producir membranas superhidrofóbicas, capaces de separar rápida y selectivamente agua y otro líquido disuelto en ella, o, usando una fibra de un polímero transparente, es posible depositar capas del mismo sobre un cristal para volver la superficie hidrofóbica [63]. Es también posible crear textiles multicapas, donde se depositen películas electrohiladas de distintos materiales, aprovechando la capacidad para filtrar y adsorber de cada uno de ellos.

1.2.5.2. Aplicaciones en biomedicina

Hoy día es el área de aplicación que atrae un mayor esfuerzo investigador. La gran versatilidad del electrospinning hace posible electrohilar disoluciones de polímeros sintéticos que sean biocompatibles con el cuerpo humano. Este hecho se aprovecha principalmente en la producción de tejidos y en la dosificación controlada de medicamentos. En el primero de estos campos, la maraña de fibras electrohiladas conforma nanoarmazones que las células del tejido a crecer pueden utilizar como soporte para reproducirse rápidamente, permitiendo una regeneración más rápida del mismo [64,65]. Las ventajas de usar nanofibras incluyen un cociente muy elevado entre área y volumen ocupado, porosidad idónea, maleabilidad y posibilidad de obtener distinta rugosidad sobre la cara de la fibra. También es posible electrohilar disoluciones de las proteínas propias del cuerpo humano, obteniéndose un ambiente más favorable a, por ejemplo, la adhesión, proliferación y diferenciación de osteoblastos [66].

En cuanto a la dosificación de medicamentos, la encapsulación dentro de las nanofibras los protege de posible degradación en el flujo sanguíneo, pudiéndose liberar en la zona a tratar mediante un estímulo adecuado. De esta forma se han encapsulado antibióticos, tratamientos contra el cáncer o proteínas [67-69]. El electrospinning coaxial también puede usarse para conseguir este encapsulamiento. Para ello, la envoltura debe contar con una estructura porosa que permita la difusión del medicamento hacia el exterior mediante una cinética bien definida. Así, por ejemplo Zhang et al. [70] demostraron que la velocidad de dosificación dependía del tamaño de

la fibra, siendo menor a mayor tamaño de diámetro; de cualquier forma, la velocidad de dosificación disminuía suavemente, sin registrar cambios súbitos. Otros estudios demuestran que altas cargas de medicamento y envolturas de polímeros de bajo peso molecular favorecen velocidades de dosificación mayores [71,72].

1.2.5.3. Aplicaciones en sensores

Los materiales semiconductores como los óxidos de titanio, estaño, wolframio, molibdeno y otros, poseen la capacidad de detectar concentraciones de gases en el nivel de traza [73]. Al ser electrohilados, la elevada área específica junto con su elevada conductividad hacen de estos materiales productos idóneos para preparar nanosensores. Cuando el gas contaminante a analizar se adsorbe en una nanofibra de un metal semiconductor, la resistividad de este se ve alterada, produciendo un cambio de voltaje que puede ser relacionado con la presencia del gas. Así se han preparado fibras eficientes para la detección a nivel molecular [74,75]. De forma análoga pueden emplearse como sensores ópticos [76]. Por último, también cabe la posibilidad de usar las fibras como soporte y cargarlas con metales nobles sensibles a la presencia de determinados gases, por ejemplo depositando paladio sobre fibras de óxido de titanio [77]. Así se dota al metal de una mayor área específica, consiguiéndose un mayor aprovechamiento del mismo.

1.2.5.4. Aplicaciones en almacenamiento de energía

Nuevamente, las propiedades de los materiales electrohilables, junto con la morfología que se obtiene al electrohilarlos hacen de las nanofibras resultantes productos que pueden emplearse como fotoelectrodos en células fotovoltaicas (como en el trabajo de Song et al. [78] donde fibras de óxido de titanio nanoporoso alcanzan una generación de fotocorriente cercana al 90% de la de electrolitos líquidos de tintas sensibles, con la evidente ventaja de encontrarse en estado sólido). También se pueden usar como ánodos en baterías de litio, al contar con propiedades electroquímicas superiores a los materiales en polvo. Así, Chen et al. [79] han publicado la producción de fibras de LiCoO2-MgO mediante electrospinning coaxial con elevadas capacidades de carga y descarga y crecimientos de impedancia muy pequeños con el uso. Por último, se pueden aplicar como soporte catalítico de platino en los ánodos de las células de combustible para transformación directa de metanol [80], o bien para el almacenaje de hidrógeno a elevada presión [81].

1.2.5.5.Aplicaciones catalíticas

Como se desarrolló ya en el primer apartado de esta introducción, las propiedades que hacen de un material un soporte atractivo son una elevada área específica, una química superficial fácilmente modificable, elevada estabilidad térmica, química y mecánica, fácil manejo y baja pérdida de presión en operación. Mientras que las primeras propiedades se pueden satisfacer mediante el uso de un determinado material, la conformación del mismo es la que dicta la ausencia o presencia de las últimas. Las membranas de fibras electrohiladas dotan a los materiales tradicionalmente usados de soporte, como las alúminas, sílicas mesoporosas o el carbono, de una forma excelente para su aplicación en catálisis heterogénea. Así, es posible encontrar en la bibliografía artículos donde se postula el uso de fibras de óxido de titanio, zirconio o estaño para soportar metales nobles [82,83], el uso de fibras de titanio en reacciones fotocatalíticas [84] o la inmovilización de enzimas en el interior de las fibras, de forma que sigan teniendo actividad catalítica pero sin riesgo de que sean lavadas durante su uso [85]. Una estrategia común para generar porosidad en estos sistemas es añadir un aditivo de sacrificio, que al ser eliminado deje el negativo de su forma en el cuerpo de la fibra, obteniéndose una estructura porosa de un tamaño más o menos controlado [86].

1.3. Aplicaciones de fibras electrohiladas en ingeniería química

La presente tesis doctoral está dedicada a la preparación y caracterización de materiales electrohilados susceptibles de ser usados como catalizadores o soportes de catalizadores. Por otro lado, es habitual que un buen soporte sea también un buen adsorbente; por ello, estos materiales electrohilados presentados también pueden ser usados en aplicaciones que requieran de elevadas capacidades de adsorción, como el almacenamiento de energía o el tratamiento de aguas.

La preparación de estos materiales ha sido posible gracias a la colaboración establecida entre el grupo de investigación TERMA, del departamento de Ingeniería Química, de la Universidad de Málaga y YFLOW S.L., empresa surgida como spin-off de las universidades de Málaga y Sevilla. Es una empresa referente a nivel nacional y europeo en el empleo de las fuerzas electrohidrodinámicas para producir nanoestructuras.

1.3.1. Catálisis

Los catalizadores juegan un papel clave en los procesos industriales, permitiendo producir más cantidad con menor requerimiento de energía [87,88]. Se distingue dentro de ella la catálisis homogénea y la heterogénea, que hace referencia a si el catalizador se encuentra en la misma o en distinta fase que los reactivos, respectivamente. En este trabajo se propone el empleo de nuevos materiales como catalizadores heterogéneos, por lo que serán estos los que acaparen nuestra atención de aquí en adelante.

La importancia de la catálisis heterogénea difícilmente puede ser sobreestimada. En 2005, los productos obtenidos mediante reacciones catalizadas alcanzaron un valor de 900 mil millones de dólares en todo el mundo. Además de en la producción, la catálisis también juega un papel esencial en el control medioambiental y la obtención de energía [89].

El catalizador se compone normalmente de fase activa y soporte, que suele ser un material inerte, estable química, mecánica y térmicamente, de elevada área superficial específica y estructura porosa desarrollada [87,90]. De la interacción soporte-fase activa dependerá que se consiga una elevada dispersión del catalizador sobre la superficie, aprovechándose al máximo la fase activa [91,92]. A veces, el soporte es también capaz de promocionar la actividad catalítica y modificar, debido a sus propiedades texturales, la selectividad de la reacción catalizada. La conformación del soporte deviene en tema crucial, al poder afectar a la difusión de reactivos y productos hacia la superficie catalítica. Problemas de transferencia de materia en la película en torno a la partícula o de difusión en la partícula de catalizador producirían un bajo aprovechamiento del catalizador [93,94]. A nivel de proceso, la conformación del catalizador determina la pérdida de presión en el reactor, y la facilidad en el manejo del conformado simplifica la operación del reactor. Es sencillo inferir de todo esto que la mejora de los sistemas de soporte y el desarrollo de nuevos soportes y conformados son tareas de notable interés científico y económico.

1.3.2. Adsorción

La adsorción es una de las operaciones de separación más importantes en la industria química. En este sistema, el adsorbente, un sólido poroso de elevada superficie específica, es puesto en contacto con una corriente gaseosa o líquida en la que hay un

compuesto, adsorbato, cuyas moléculas presentan elevada afinidad por la superficie del adsorbente. Por lo tanto, las moléculas se adsorben en la superficie de la misma mediante interacciónes de naturaleza física o química, purificando la corriente de ese compuesto. Es así posible purificar o concentrar efluentes industriales. Si las fuerzas de interacción son de naturaleza física, son suficientemente débiles como para permitir la regeneración del adsorbente, desorbiendo el gas o líquido retenido. El adsorbente más frecuente es el carbón activo, aunque a veces se emplean la alúmina, el gel de sílice o los tamices moleculares.

1.3.3. Ventajas del uso de membranas de fibras en catálisis y adsorción

El afrontamiento de los problemas de transferencia de materia, tanto en catálisis como en adsorción, es esencial a la hora de optimizar las condiciones de operación de los reactores y adsorbedores. En el caso de la catálisis heterogénea, es sabido que los problemas difusivos en las conformaciones más habituales de los catalizadores, como los pellets, pueden causar una pérdida de rendimiento considerable, al ser menor la velocidad de difusión en el interior de las partículas que la velocidad de la reacción química. Para evitar el control difusional interno, es habitual acudir al uso de menores tamaños de partícula. Las ventajas de la reducción de la partícula catalítica se hacen ostensibles al estudiar el módulo de Thiele, que compara la velocidad de difusión en los poros con la velocidad de reacción.

$$\varphi = \frac{R}{3} \cdot \sqrt{\frac{k}{D}}$$

Donde R es el radio de la partícula, k la constante cinética, y D la difusividad en el seno de la partícula. Otra forma de enfocar este problema es que, al reducir el tamaño de partícula, se hace posible operar a mayor temperatura sin encontrar problemas difusionales. Esto se debe a que la constante cinética varía exponencialmente con la temperatura, mientras que la difusividad es tan solo proporcional a ella.

El problema habitual al que se enfrenta, por ejemplo, un reactor de lecho fijo al reducir el tamaño de partícula es el consiguiente aumento de la pérdida de carga. La

aproximación de Ergun es frecuentemente aceptada como válida para estimar el factor de fricción en lechos:

$$\frac{\Delta P}{L} = \frac{37{,}5 \cdot \mu \cdot u}{R^2 \cdot \rho} \cdot \frac{(1-\varepsilon)^2}{\varepsilon^3} + \frac{0{,}875 \cdot u^2}{R} \cdot \frac{(1-\varepsilon)}{\varepsilon^3} \quad \left[\frac{J}{kg \cdot m}\right]$$

Donde

ρ: densidad del fluido

μ: viscosidad del fluido

$\frac{\Delta P}{L}$: pérdida de carga por metro de lecho

ε: porosidad del lecho

u: velocidad superficial del fluido.

Por lo que cabe esperar un considerable aumento de la pérdida de carga al reducir el tamaño de la partícula. Además, para partículas esféricas, la porosidad del lecho disminuye con el tamaño de partícula, con lo que la pérdida de carga será mayor, aumentando consecuentemente la presión de trabajo del sistema. La necesidad de una capacidad de bombeo mayor conlleva un aumento considerable del coste de operación, lo que neutralizará el beneficio obtenido en la conversión al reducir el tamaño de partícula.

El mismo problema se observa en los adsorbedores. El balance de materia para un adsorbato a lo largo de un lecho de adsorción, considerando control difusional en la partícula y ausencia de dispersión axial y radial, es el siguiente:

$$\frac{\partial C}{\partial t} = u \cdot \frac{\partial C}{\partial z} + \frac{(1-\varepsilon)}{\varepsilon} \cdot \frac{15 \cdot D}{R^2} \cdot \left(q_p - q_B\right)$$

Donde *z* es la posición en la dirección longitudinal dentro del lecho y q_p, q_B es la concentración de adsorbato adsorbida en el seno de la partícula y en su superficie, respectivamente. Un menor tamaño de partícula conlleva un aumento en el el segundo término del lado derecho del balance, aquél que representa la velocidad de flujo hacia el interior de la partícula. Esto produce una disminución de la zona de transferencia de

masa del lecho. Por lo tanto, a igualdad de altura de lecho y de capacidad de adsorción del mismo, disminuir el tamaño de partícula lleva a curvas de ruptura con menor pendiente, es decir, a tiempos de ruptura mayores y, por lo tanto, a un mayor aprovechamiento del lecho. El problema al que se enfrenta el adsorbedor es, nuevamente, un aumento de carga similar al previamente presentado para los lechos catalíticos.

El uso de membranas de fibras producidas por electrospinning permite reducir notoramiente el radio de la partícula catalítica, que se ve disminuida en cuatro o cinco órdenes de magnitud, sin que la porosidad de la membrana se vea excesivamente mermada. Este hecho conlleva que, aunque la pérdida de carga aumente en estos sistemas, sus pérdidas de cargas sean menores de lo esperable. Matsumoto y Tanioka han estimado las pérdidas de carga para filtros de aire compuestos por fibras electrohiladas de poliacrilonitrilo. Observaron que las pérdidas de carga aumentaban al disminuir el tamaño de las nanofibras. Aun así, el valor de pérdida de carga que obtuvieron fue desde 10 hasta 50 veces menores que el estimado para esos radios de fibra por la ecuación de Pich para filtros fibrosos [95]. La ya demostrada reducción de los problemas de transferencia de masa en estos sistemas, unido a los aumentos de pérdidas de cargas mucho menores de los esperables, junto con la ventaja de ser materiales más manejables para el transporte y la operación, hacen de estas membranas una conformación de materiales adsorbentes y catalíticos muy prometedora.

1.3.4. Materiales para soporte

Los soportes de mayor implementación en la industria son la alúmina y la sílica, aunque otros materiales como los óxidos de zirconio y titanio o el carbono, ya sea como carbón activo o como nanotubos, han ganado popularidad en los últimos tiempos. Como ya se ha mencionado, estos materiales tienen en común su elevada porosidad, su estabilidad química y térmica y su capacidad para interaccionar con fases activas.

1.3.4.1. Alúmina

La alúmina u óxido de aluminio es un material cerámico de elevada estabilidad térmica y excelentes propiedades mecánicas debido a su elevada dureza. Para su uso como soporte catalítico se suele utilizar la fase cristalina amorfa o gamma-alúmina, siempre a temperaturas menores de 800 ºC, temperatura a la que se forma el alfa-

alúmina, que carece de porosidad. La actividad catalítica propia de la alúmina y su interacción con posibles fases activas viene determinada por los hidroxilos terminales y las vacantes en la red cristalina, los cuales se ven modificados mediante tratamientos en distintas atmósferas a temperaturas elevadas [96]. Son ampliamente utilizadas en reacciones de deshidratación de alcoholes, gracias a su estabilidad en atmósfera húmeda. También se emplean, como soporte, en reacciones de crackeo, isomerización, deshidrogenacion, desfluoración y desulfuración [97]. Su principal inconveniente es su baja área superficial específica cuando se compara con otros soportes.

1.3.4.2. Materiales Mesoporosos de sílice

Los materiales mesopororos ordenados de sílice fueron sintetizados por primera vez en 1969 y patentados por Mobil Oil Corporation en 1992 [98]. Su acrónimo significa Mobil Composition of Material (MCM). Consisten en largos canales hexagonales de tamaño regular con paredes de silica amorfa, aunque la técnica de producción empleada permite también obtener aluminosilicatos. Aunque inicialmente se idearon para ser usados en las unidades de craqueo catalítico (FCC) de las refinerías, como en el caso de los estudios de Corma [99], la falta de acidez superficial y la baja estabilidad hidrotermal los han reconducido como soporte catalítico, mediante substitución de elementos en la red cristalina, impregnación de la fase activa o inmovilización de catalizadores homogéneos. Aun así, se ha demostrado su utilidad como catalizadores autosoportados en reacciones de Friedel-Craft, acetilización, condensación aldólica y esterificación entre muchas otras. También se ha intentado funcionalizar la superficie de los canales usando técnicas de capado superficial o tratamientos con compuestos orgánicos hidrofóbicos [100]. De esta manera, se consiguen materiales híbridos orgánicos/inorgánicos con una mayor diversidad de usos. Además de aplicaciones en el área de catálisis, se ha postulado el uso de los materiales mesoporosos ordenados como tamices moleculares para, por ejemplo, adsorber dióxido de carbono o separar mezclas de alcoholes, resolviendo problemas ambientales o reduciendo costes energéticos al eliminar etapas de destilación [101].

1.3.4.3. Zeolitas

Las zeolitas son aluminosilicatos porosos usados habitualmente como adsorbentes. Su importancia es tal que se producen del orden de tres millones de tonelada al año [102]. En las refinerías se emplean en las unidades FCC, y son activas en reacciones de

isomerización, alquilación y craqueo gracias a su elevada acidez de Lewis y a las modificaciones de selectividad relacionadas con impedimentos estéricos dentro de sus cristales. Además de en reacciones catalizadas por ácidos, las zeolitas también funcionan como catalizadores básicos y redox. Su principal inconveniente viene dado por su reducido tamaño de poros, que causa severas limitaciones cuando se emplean reactantes de gran tamaño molecular. Algunas investigaciones se centran en mejorar la diffusion de los reactantes hacia los centros activos, ya sea incrementando el tamaño de los poros de las zeolitas [103], disminuyendo el tamaño del cristal [104], o añadiendo un sistema mesoporoso (es decir, de tamaños de poro medios entre 2 y 50 nm) junto con la microporosidad propia de estos cristales [105,106].

1.3.4.4. Otros óxidos metálicos

Además de los aluminosilicatos, es posible usar otros óxidos metálicos de bajo coste como soporte. Las propiedades texturales de estos materiales suelen ser menos interesantes que los de los soportes porosos descritos en los puntos anteriores, aunque las técnicas de síntesis desarrolladas en los últimos años han ayudado a aumentar las áreas superficiales y volúmenes de estos óxidos. En este caso, son la capacidad autocatalítica o la promoción del catalizador soportado sobre los mismos los que hacen interesante su uso. Entre estos óxidos encontramos los de titanio, los de zirconio o las arcillas.

Los catalizadores de titanio, usualmente en forma de anatasa, son usados habitualmente en reacciones fotocatalizadas como la oxidación por aire húmedo para el tratamiento de efluentes industriales [107]. También se usa como soporte catalítico en mezclas con sílica [108] u óxido de zirconio, pudiéndose usar en este último caso para, por ejemplo reacciones de deshidrogenación, descomposición de clorofluorocarbonos, o producción de caprolactama [109]. Estos catalizadores se pueden obtener en forma de aerogel, por ejemplo a partir de alcóxidos de titania, como se detalla en la revisión de Schneider y Baiker [110]. Tsevis et al. [111] han estudiado detalladamente la precipitación de anatasa en polvo a supersaturación constante. Esto se consiguió a velocidad de agitación constante e inyectando a pH controlado $TiOSO_4$ y sosa a relación volumétrica constante. Así se consiguieron áreas superficiales de entre 60 y 250 m^2/g, en función de la presencia de determinados iones en la disolución.

El óxido de zirconio es frecuentemente utilizado como soporte e incluso como catalizador en reacciones que precisen de relativa acidez superficial. Posee centros que catalizan reacciones ácido-base, de oxidación y de reducción. Su carácter ácido-básico depende de la fase cristalina, sea tetragonal o monoclínica, y de la temperatura de calcinación, de la que dependerán la cantidad y fortaleza de enlace de los grupos hidroxilos y las vacantes cristalinas presentes en su superficie. Aunque normalmente son poco porosas, es posible encontrar en la bibliografía más reciente catalizadores de óxido de zirconio de considerable mesoporosidad. Así, por ejemplo Chuah y Jaenicke [112], obtuvieron zirconias tetragonales de más de 170 m^2/g mediante digestión en agua a 100 ºC del óxido hidratado de zirconio y su posterior calcinación a 800 ºC. Cuando son sulfatadas, el óxido de zirconio se convierte en el sólido superácido de mayor fortaleza conocida, aumentando su actividad catalítica [113]. Por ejemplo, Corma et al [114] han reportado que la zirconia sulfatada es más activa que las zeolitas para reacciones de isomerización y alquilación a bajas temperaturas. La actividad de estos centros sulfanados depende de si se sulfata el óxido de zirconia hidratado o una vez ha sido calcinado, del precursor para la zirconia y del agente sulfatante, además de las condiciones de sulfatación [115]. El principal problema de estos óxidos de zirconio sulfatado es su baja resistencia a la desactivación, hecho que trata de solucionarse modificando el catalizador con metales de transición como platino, hierro y manganeso, por ejemplo en el primer caso hidrogenando el coque formado en la reacciones de isomerización de alcanos [116]. La zirconia se usa también en óxidos mixtos con cerio y platino como fase activa en los catalizadores de tres vías de los automóviles [117].

1.3.4.5. Materiales carbonosos

Los materiales de carbón, además de ser grandes adsorbentes, presentan una serie de ventajas en su uso para soporte de fases activas, como son su estabilidad química, resistencia mecánica, elevada porosidad y superficie [119,120]. El coste de estos materiales es generalmente menor que el de otros soportes tradicionales como la alúmina o la sílice. Otra gran ventaja de los catalizadores soportados sobre carbón es que la fase activa se puede recuperar fácilmente de los catalizadores agotados mediante combustión o gasificación del soporte carbonoso, lo cual es una gran ventaja cuando la fase activa es un metal precioso. El principal problema para la utilización de carbono en algunas reacciones catalíticas es su baja resistencia a la oxidación. La presencia de materia inorgánica procedente, bien del precursor o bien introducida durante el proceso

de preparación del carbón activo, es otra desventaja, aunque actualmente es posible preparar carbones porosos con contenidos muy bajos en materia mineral mediante la elección de un precursor adecuado.

Existe una gran variedad de materiales carbonosos que pueden ser utilizados como soporte de catalizadores. En un extremo se sitúa el grafito, que es un material muy puro, cristalino, inerte, no poroso y con superficie específica baja. En el extremo opuesto se encuentran los carbones activos, que son esencialmente amorfos, contienen impurezas y grupos funcionales, alta superficie y una porosidad muy heterogénea. Entre ambos extremos existe una amplia variedad de productos manufacturados a partir de distintos precursores con diferentes propiedades finales. Los productos resultantes cubren, por tanto, un amplio abanico de propiedades físicas y químicas.

En cuanto al uso del carbón activo en catálisis, aunque su superficie se puede considerar como inerte, si se compara con la de otros soportes catalíticos como la alúmina y la sílice, ésta posee una proporción significativa de sitios activos, constituidos por insaturaciones en los defectos y en los bordes de las capas de grafenos. La cantidad de estos sitios activos aumenta con la porosidad y el área superficial. La presencia de heteroátomos (principalmente, oxígeno, hidrógeno y nitrógeno) también introduce sitios activos en la superficie del carbón. El origen de estos sitios depende del precursor y del proceso de activación empleado. Aunque las superficies grafíticas son esencialmente hidrofóbicas, la química de la superficie se puede modificar para aumentar su carácter hidrofílico e, incluso, se pueden obtener carbones con propiedades de intercambio iónico.

La distribución del metal sobre la superficie del carbón cuando éste es usado como soporte depende en gran medida del disolvente utilizado en el proceso de impregnación. Como la superficie del carbón es esencialmente hidrofóbica, tiene poca afinidad por los disolventes de carácter polar como el agua y elevada afinidad por disolventes no polares como la acetona. En el caso concreto del Pt, Macheck et al [121], afirmaron que cuando el precursor metálico, ácido cloroplatínico, se disuelve en agua, el metal se localiza fundamentalmente sobre la superficie externa de las partículas de carbón, mientras que si se usa acetona como disolvente, esta penetra más fácilmente hasta el interior de los microporos, obteniéndose una distribución del metal más uniforme sobre la superficie interna de la partícula.

Por el lado del carbón, la porosidad y la química superficial rigen la correcta distribución de la fase activa sobre el carbón [119], pero no del área superficial. Así, Rodríguez-Reinoso et al [122] no apreciaron ninguna relación entre el área superficial y la dispersión del metal (Fe) con la actividad catalítica para la hidrogenación de CO en carbones con diferentes áreas superficiales. Además, la microporosidad de los carbones activos puede dificultar la movilidad de las partículas de metal depositado, facilitando su dispersión y evitando la sinterización.

El efecto de los grupos oxigenados superficiales sobre la dispersión del Pt sobre carbón fue examinado por Derbyshire et al. [123] y Prado-Burguete et al. [124,125]. Los últimos emplearon un negro de carbón de elevada área superficial, al que trataron a alta temperatura en hidrógeno, para eliminar la mayor parte de grupos oxigenados superficiales. Posteriormente, se oxidó con H_2O_2 en distintas condiciones con el objetivo de obtener diferentes soportes con la misma porosidad pero diferente cantidad de grupos oxigenados superficiales. Los autores concluyeron que los grupos ácidos introducidos con el tratamiento con H_2O_2 disminuyen la hidrofobicidad del carbón, favoreciendo la dispersión del metal durante la impregnación con disolución acuosa y que la presencia de los grupos oxigenados no solo favorece la dispersión del Pt, sino que además aumenta las interacciones entre el precursor metálico y el soporte, minimizando la tendencia a la sinterización del Pt.

Finalmente, el carbón activo, además del principal adsorbente, es un soporte de catalizadores plenamente consolidado en el mercado mundial. En la industria, el carbón activo se utiliza como catalizador en la síntesis de acetato de vinilo y cloruro de vinilo, además, también se emplea como soporte de metales nobles para reacciones de hidrogenación. La Guía de las Reacciones Catalíticas publicada por Jonson Matthey, unos de los principales suministradores de catalizadores a nivel mundial, recoge 9 reacciones catalizadas por metales nobles soportados sobre carbón activo [126]. Estas reacciones incluyen la hidrogenación de benceno y de compuestos nitrados tanto alifáticos como aromáticos. Sin embargo, a pesar de que existe un creciente interés, sigue siendo bajo el número de procesos catalíticos que utilizan el carbón activo como catalizador a nivel industrial. Otras reacciones donde tiene un potencial interés son la deshidratación de alcoholes para producir di-metil-eter u olefinas, la hidrodesulfonación del tiofeno o la síntesis de Fischer-Tropsch [127].

1.3.4.6. Catalizadores carbonosos a partir de lignina

La lignina es un polímero de origen natural, heterogéneo y con un alto grado de aromaticidad. Es muy abundante en plantas arbóreas y herbáceas, con una presencia sólo inferior a la de la celulosa. Aproximadamente el 25% de los materiales lignocelulósicos es lignina. Su misión fundamental es cementar las fibras de celulosa de la madera y proporcionar rigidez a las mismas. La lignina puede considerarse una red polimérica tridimensional al azar formada por unidades de fenilpropano unidas entre sí en diferentes posiciones, Figura 1.10. En cuanto al grado de polimerización, resulta difícil de establecer correctamente, dada la ruptura hidrolítica que inevitablemente sobreviene a la extracción. Lo que sí se hace evidente es el gran contenido de núcleos aromáticos, lo cual debería favorecer un mejor ordenamiento tras tratamiento térmico frente a otros polímeros naturales como la celulosa [128].

La lignina es el principal co-producto de la industria de la pulpa de celulosa. El procedimiento químico más usado por la industria papelera para la separación de la lignina es el proceso a sulfato. Como consecuencia de la digestión de la madera se obtiene la pasta de celulosa y una lejía negra o lejía kraft. En ella está disuelta la lignina. Su destino habitual es ser quemada como combustible en las plantas tras un proceso de evaporación. Este procedimiento dota a la lignina de un alto contenido de cenizas y sales, por lo que su combustión, además de proporcionar energía para la planta, también recupera las sales usadas durante el proceso. Otra vía para obtener lignina es el proceso Alcell®, el cual confiere un alto grado de pureza al material, librándolo de casi toda la materia inorgánica.

El bajo coste y la alta disponibilidad de la lignina, cuya producción anual mundial se estima cercana a las 50 millones de toneladas, de acuerdo con el “International Lignin Institute” [129], hace atractivo su uso como precursor de materiales carbonosos, gracias a que tiene un elevado contenido en carbono (básicamente como grupos aromáticos).

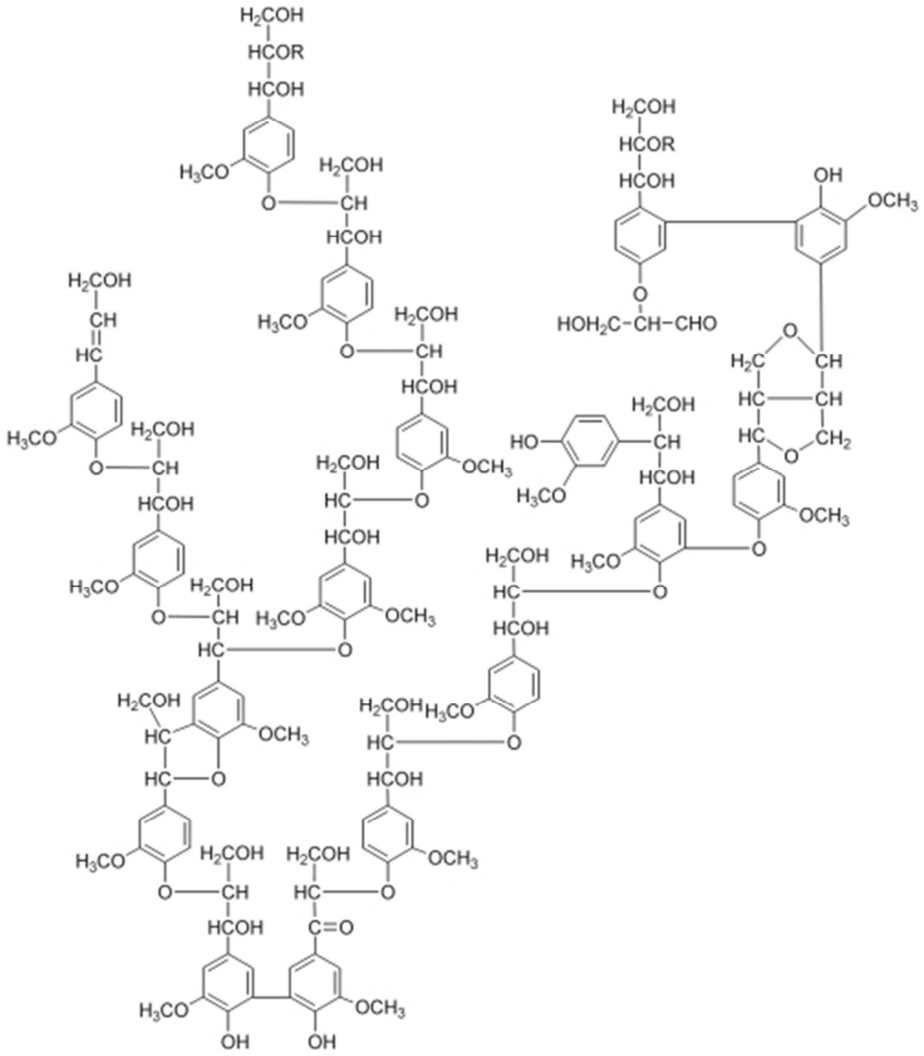

Figura 1.10. Estructura de la lignina propuesta por Adler [130].

En nuestro grupo de investigación se viene estudiando desde hace años el aprovechamiento tecnológico de la lignina vía tratamientos termoquímicos. Así, por carbonización se han obtenido unos materiales que tratados a altas temperaturas producen materiales carbonosos altamente ordenados [131]. Por gasificación parcial de los carbonizados se pueden obtener carbones activos [132] al igual que por pirólisis catalizada de la lignina con catalizadores tipo Friedel-Crafts, como $ZnCl_2$ y H_3PO_4. [133,134] También se ha empleado como precursor para la obtención de tamices moleculares de carbón por tratamiento a altas temperaturas o por deposición controlada de carbono pirolítico [135-137] y de nanofibras de carbono por la técnica de electrohilado [138,139].

1.3.5. Métodos de preparación de catalizadores másicos y soportes

Dentro de los métodos de preparación catalíticos cabe distinguir aquellos de preparación de catalizadores másicos y los soportados; los primeros están compuestos únicamente de la sustancia activa, y se siguen usando de forma masiva en la industria hoy día. Es el caso de los aluminosilicatos para craqueo de hidrocarburos, los óxidos de zinc y cromo para la conversión de gas de síntesis a metanol o los de hierro-molibdeno para la oxidación de metanol. Los impregnados se preparan dispersando, bien durante la síntesis o bien posteriormente, la fase activa sobre un material catalogado como soporte. En la industria, los catalizadores de hidrogenación e hidrotratamiento son preparados de esta manera [140]. A continuación se detallan los métodos de producción más habituales para estos soportes y catalizadores, así como los tratamientos a los que son sometidos hasta obtener el producto final.

1.3.5.1. Precipitación

El objetivo de este método es precipitar un sólido desde una disolución. La precipitación ocurre en tres pasos: supersaturación, nucleación y crecimiento. La zona de supersaturación de las curvas de solubilidad se ven afectadas por la temperatura y el pH, por lo que en la preparación de óxidos e hidróxidos se suele bajar la temperatura o subir el pH para conseguir sobresaturación. La nucleación puede suceder de forma espontánea (nucleación homogénea) o ser iniciada con materiales germinadores (nucleación heterogénea). La velocidad de nucleación se puede modificar añadiendo más germinadores. Por último, el proceso de crecimiento depende de la concentración, la temperatura, el pH y por maduración. Normalmente se obtienen materiales cristalinos, pero si la sobresaturación es muy elevada, la velocidad de agregación de partículas es mayor que la de reorientación, obteniendo sólidos amorfos. Si se quieren formar óxidos mixtos, se suelen usar carbonatos e hidróxidos de los metales deseados por su baja solubilidad y la facilidad de su descomposición térmica en aire, que además produce desarrollo de la porosidad [141].

1.3.5.2. Gelación y floculación

De forma parecida a la precipitación, la disolución de partida puede ser un coloide o “sol”, cuya gelación o floculación también produciría los catalizadores másicos o soportes requeridos. Permite un mayor contro sobre el área superficial, volumen y

distribución de tamaños de poro. Es sencillo formar soluciones coloidales hidrofílicas a partir de ácido silícico, u óxidos hidratados de aluminio o zinc. Las micelas que componen estas disoluciones se producen a partir de reacciones de polimerización y policondensación de los precursores; por ejemplo, un sol de sílica se puede obtener a partir de silicato sódico y el mineral ácido resultante de la policondensación del ácido silícico.

La reticulación de las micelas da lugar a un hidrogel, que es una red tridimensional que encierra moléculas de agua en su interior; este es el proceso conocido como gelación. Ésta se produce en cuestión de minutos a cientos de horas en función del pH principalmente, y en menor medida de la tempratura, la concentración de las micelas y la fuerza iónica del medio [142]. Es posible obtener cogeles a partir de soles que contengan dos o más especies. Además, se pueden utilizar alcóxidos como material de partida. El más conocido es el tetraetilortosilicato, muy usado para producir sílicas [143].

La floculación de las micelas se podría conseguir neutralizando su carga eléctrica, precipitando en floculados. Estos floculados son muy ricos en agua y más denso que los hidrogeles correspondientes, pero en ellos el tamaño de partícula es el de la micela original. El área superficial dependerá del tamaño de esa micela original, de la maduración y de las condiciones de secado.

1.3.5.3. Transformaciones hidrotermales

Por estos tratamientos se entiende la modificación de los precipitados, geles o floculados anteriormente descritos, usando para ello una temperatura medianamente elevada, usualmente entre 100 y 300 ºC, para madurarlos en presencia de la disolución madre. Así se consigue aumentar el tamaño del cristal o partícula, se puede cristalizar sólidos amorfos, se pueden inducir cambios de fases cristalinas o producir sinterizado del gel con disminución de su estructura porosa [144]. La nueva variable de este proceso es la presión, ya que estos tratamientos se suelen llevar a cabo en autoclaves. Los procesos hidrotermales se pueden usar para producir zeolitas y tamices moleculares, usando geles acuosos alcalinos, a temperaturas entre 70 y 300 ºC, y usando relaciones molares bien controladas de las especies que las componen.

1.3.5.4. Decantación, filtración, centrifugación y lavado.

Estas operaciones tienen por objetivo separar los sólidos a partir de las disoluciones madres. La decantación funciona bien con los precipitados, pero no tanto con los floculados, ya que tras cada lavado, al ser retirados los contraiones que neutralizan la carga de las micelas hace que los floculados reviertan a soles por peptización. Si el tamaño de la partícula es muy pequeño, en lugar de decantación se usará filtración o centrifugación. El lavado también puede usarse para intercambiar iones con la superficie del soporte o catalizador, caso de las zeolitas, en el que se intercambia los cationes sodio por amonios para obtener la forma ácida tras calcinación [145].

1.3.5.5. Secado

Esta etapa consiste en la eliminación del disolvente, usualmente agua, de los poros del sólido. Es un proceso rutinario para los materiales precipitados, pero es de importancia crítica en el caso de floculados e hidrogeles, al poder causar el colapso de la estructura porosa. Después de una primera etapa de evaporación, cuando el hidrogel tiene un contenido menor de 50% en agua comienza a contraerse, formando el xerogel correspondiente. A partir de ese punto, la velocidad de secado decae y la evaporación es controlada por fuerzas capilares. Una velocidad de evaporación más rápida que la de difusión por la red porosa causaría formación de vapor y el colapso de la estructura interna. Es posible evitar este efecto usando bajos flujos de aire, saturando ese aire con humedades relativas medias y usando temperaturas bajas [146]. Cuando el xerogel ve reducido su contenido en agua al 25-30% se suele ir a la etapa de conformado para luego calcinar en forma de pellet o extrusado.

1.3.5.6. Calcinación

Es un tratamiento térmico a elevada temperatura. Usualmente se lleva a cabo en aire, a no ser que se necesite preacondicionar el catalizador con una atmósfera especial, lo que se suele llevar a cabo in situ en el reactor al arrancar la unidad de trabajo. Durante esta etapa se producen cambios en la textura del catalizador por sinterización de los cristales, generación de nuevas fases cristalinas que pueden dar lugar a una catalíticamente activa, eliminación de agua y/o CO_2 quimisorbidos, y en general se produce la estabilización de las propiedades del sólido. Un ejemplo es la calcinación de hidróxido de aluminio a distintas temperaturas. Por encima de 300 ºC, la bohemita sufre

condensaciones de sus grupos hidroxilos y da lugar a óxidos conocidos como gamma alúmina, muy útiles como fundentes y como soportes catalíticos [147]. Además, la microporosidad se reduce al incrementar la temperatura de calcinación, incluso sin cambio de estructura cristalina.

1.3.6. Métodos de impregnación de soportes

Soportar un catalizador sobre un material poroso presenta grandes ventajas ya mencionadas con anterioridad. El principal reto de este procedimiento para producir catalizadores es conseguir una elevada dispersión de la fase activa sobre el soporte, lo que puede llevarse a cabo siguiendo los métodos listados a continuación. Una vez impregnado el soporte, es habitual un tratamiento térmico posterior para estabilizar la fase activa o incluso para formar la estructura cristalina necesaria para dotar de actividad al material.

1.3.6.1. Impregnación húmeda

Es el método tradicional. En él, el soporte es puesto en contacto con una disolución del metal o metales que componen la fase activa. Los iones metálicos difunden en la disolución dentro de los poros del soporte y se adsorben sobre sus óxidos. La actividad del catalizador puede quedar modificada en función de la fortaleza de la interacción metal-soporte. El contacto entre soporte y disolución se lleva a cabo por exceso de disolución o con aplicación repetida de la disolución, usándose para ello cantidades que corresponden al volumen total de poros del soporte [147]. Se puede utilizar diversas técnicas, como suspensiones coloidales o el empleo de tensioactivos, para producir nanopartículas con el objeto de alcanzar una mayor dispersión. Tras el contacto de la disolución con el soporte, se seca el soporte impregnado y se procede a la activación del catalizador por calcinación o reducción usando un tratamiento térmico en atmósfera adecuada. Este método se usa para cargas de catalizador bajas.

1.3.6.2. Precipitación

En ella, una disolución de la sal metálica de la fase activa se pone en contacto con el soporte para producir un hidróxido o carbonato metálico sobre la superficie del soporte. La sal escogida depende de la química superficial del soporte, añadiéndose la cantidad correspondiente a la carga de catalizador deseada. La interacción soporte- sal metálica

se ve favorecida por la presencia de grupos hidroxilos u oxigenados. Por ejemplo, los grupos silanos de la sílica interactúan con el nitrato de niquel formando hidrosilicatos en lugar de deposición de hidróxidos [148]. Este método se usa cuando la carga de catalizador deseada es igual o mayor al 15% másico.

1.3.6.3. Métodos de síntesis controlada

El auge de la nanotecnología ha facilitado el desarrollo de nuevos métodos de impregnación, en los que se aprovechan las técnicas de autoensamblaje y nanomoldeo para conseguir elevadas dispersiones de las fases activas. Algunos de estos métodos son:

- Intercambio iónico: Es un método muy usado cuando se emplean zeolitas como soporte. En este caso, los iones del metal activo se intercambian con los cationes de la estructura de la zeolita.
- Deposición química de vapor. En ella los precursores organometálicos de la fase activa se vaporizan y se depositan sobre los grupos hidroxilos del soporte, obteniéndose cargas bajas y altas dispersiones del catalizador. Este método requiere de un control exhaustivo de las temperaturas y concentraciones de los precursores para conseguir una infilitración completa del sistema poroso y así evitar problemas difusivos que favorerzcan los depósitos superficiales del catalizador, con la consiguiente pérdida de dispersión. Por esta vía se han preparado, por ejemplo catalizadores de cobalto a partir de $Co(CO)_8$ sobre sílica o de wolframio sobre alúmina a partir de $W(CO)_6$ [149,150].
- Fases embebidas: Confinando nanopartículas de metales u óxidos metálicos dentro de canales o cavidades de un sólido inorgánico permite preparar catalizadores heterogéneos de elevada actividad y estabilidad térmica [151]. Por ejemplo, es posible depositar la fase activa durante la gelación del soporte, preparando un cogel simplemente añadiendo el precursor metálico deseado como un segundo sol. La revisión de Gonzalez et al muestra las elevadas dispersiones y estabilidad térmica de los catalizadores así obtenidos [152], aunque a costa de encapsulación parcial de la fase activa, que quedaría inaccesible a reacción. También es posible preparar

catalizadores con fases embebidas mediante técnicas de microemulsión [153] y cristalización de fase sólida [154].

1.4.Experimental

Tanto la adsorción como la catálisis heterogénea son materias interdisciplinares, que requieren para su correcta aplicación de un conocimiento al menos suficiente, de química, física, matemáticas, ingeniería química y ciencia de materiales. Por ello, a lo largo de esta tesis doctoral se hace necesario el empleo de muy diversas técnicas de caracterización y análisis con el fin de esclarecer la idoneidad de los materiales propuestos como catalizadores. El desarrollo detallado de cada una de estas técnicas no cabe dentro del objeto de la tesis, por lo que se ha optado por no procurar más que una somera descripción de las mismas en cada capítulo. En cuanto a los equipos de electrospinning y las condiciones de operación impuestos en ellos, cada capítulo cuenta con la suficiente información sobre ellos.

A continuación se describen las instalaciones donde se llevaron a cabo los tratamientos posteriores a las fibras y los experimentos catalíticos.

1.4.1. Carbonización/ Calcinación.

Para la realización de los experimentos de carbonización se ha empleado una instalación como la que se muestra en la Figura 1.11 y consta de los siguientes elementos:

- Botella de nitrógeno. Proporciona el gas que mantiene la atmósfera inerte dentro del horno donde se encuentra la muestra. Para las calcinaciones, se usa una botella de aire sintético en su lugar.
- Medidor de flujo másico. Es un elemento transductor de señal (caudal-señal eléctrica). Se ubica a la salida de la botella de nitrógeno. El medidor usado es de la marca Brooks, modelo 5850 TR.
- Controlador de flujo másico. Permite controlar el flujo de gas que se introduce en el sistema para mantener la atmósfera inerte. Este dispositivo junto con el medidor de flujo másico permite fijar el caudal de gas usado en los experimentos. El controlador usado es de la marca Goosen, modelo 5878.

- Horno. El horno utilizado es de tipo tubular horizontal. Permite obtener temperaturas de hasta 1000 ºC a las que se llega con un calentamiento de 10 ºC/min. El horno utilizado es de la casa Carbolite Furnaces, modelo CFT 12/75, de 75 mm. de diámetro y 750 mm, de longitud de zona calefactada. Las muestras se introducen en el horno y se deja pasar una corriente de 150 cm^3 (STP)/min de nitrógeno (99.999%) durante 20 minutos para purgar el horno y mantener una atmósfera inerte durante la carbonización y así evitar que se queme la muestra. La velocidad de calentamiento es de 10 ºC/min desde temperatura ambiente hasta la temperatura deseada. Una vez se alcanza la temperatura final, se mantiene durante 2 horas en caso de las calcinaciones y después se deja enfriar, o directamente se procede a enfriar para las carbonizaciones, siempre manteniendo la corriente de 150 cm^3 (STP)/min de nitrógeno, con objeto de preservar la muestra de la oxidación.

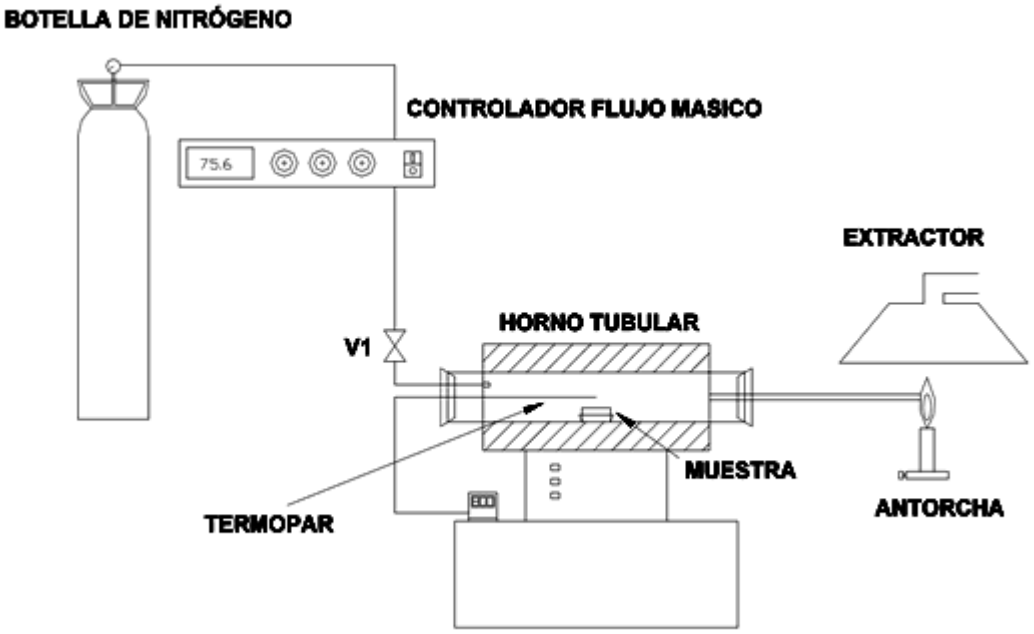

Figura 1.11. Instalación para la carbonización.

1.4.2. Lavado.

El lavado de las muestras se lleva a cabo agitando durante una hora en una disolución de HF al 49%. Pasado este tiempo se filtra con un embudo Büchner y un kitasatos, y se continúa filtrando con agua destilada, hasta pH neutro. Una vez filtrado, se deja secar en una estufa a 60 ºC durante 24 horas.

1.4.3. Reacción de descomposición de metanol

Para la realización de los experimentos de descomposición de metanol se ha empleado una instalación como la que se esquematiza en la Figura 1.12 y que consta de los siguientes elementos:

- Botellas de gases.
- Medidores de flujo másico. Elementos transductores de señal (caudalseñal eléctrica). Se ubican a la salida de las botellas de gases. El medidor usado es de la marca Brooks, modelo 5850 TR.
- Controlador de flujo másico. Este dispositivo junto con los medidores de flujo másico permite fijar el caudal de gas usado en los experimentos. El controlador usado es de la marca Goosen, modelo 5878.
- Baño termostático, para mantener los alcoholes a una temperatura conocida, y de esta forma poder controlar la cantidad del mismo que entra en el reactor.
- Refrigerador y calentador, para controlar la temperatura del baño termostático.
- Saturador, un recipiente de vidrio que permite el burbujeo de los gases a través del líquido, de esta forma a partir de la temperatura se conoce la presión parcial del líquido y por tanto se pueden ajustar las concentraciones del mismo en la corriente gaseosa al reactor.
- Cable térmico, mediante el cual se calefactan las conducciones de entrada y salida del reactor para evitar que se produzca condensación de reactivos o productos en las paredes de estas conducciones.
- Reactor, tubo de cuarzo de 4 mm de diámetro interior y una longitud de unos 40 cm, en el interior del cual se coloca el catalizador y en el que se realiza la reacción.
- Horno, para elevar la temperatura en el interior de reactor.
- Termopar, cuyo extremo se encuentra en contacto con el catalizador, para poder medir y controlar la temperatura en el interior del reactor.
- Controlador del horno, compara la temperatura del termopar con la temperatura programada y actúa en consecuencia.

- Analizadores de gases. Para poder seguir la evolución de los reactivos y productos de reacción se emplearon un espectrómetro de masas y un cromatógrafo de gases. El espectrómetro de masas es de la casa Pfeiffer Vacuum® modelo OmniStar. El cromatógrafo de gases es de la marca Perkin Elmer® modelo AutoSystem, y está equipado, caso de no ser especificado, con una columna HP-1 de 50 m de longitud y un detector de ionización de llama (FID).

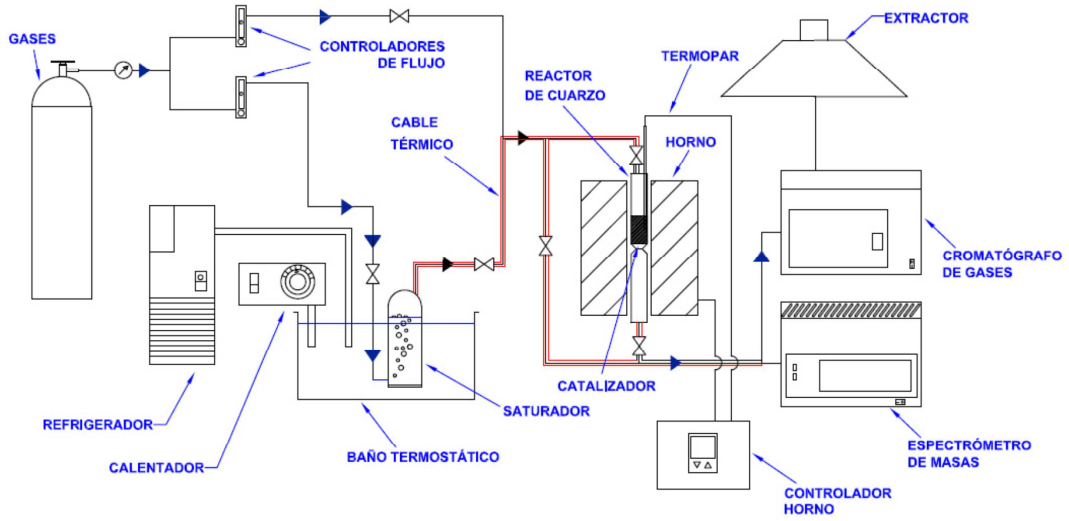

Figura 1.12. Esquema de la instalación empleada para la descomposición catalítica de metanol.

1.4.4. Reducción de NO.

En este caso, los diferentes experimentos de actividad catalítica han sido realizados a presión atmosférica en un reactor de lecho fijo de 4 mm de diámetro interno, en la instalación mostrada en la figura 1.13. El flujo total ha sido de 200 cm^3 (STP)/min, con cantidades variables de catalizador entre 80-300 mg. Las condiciones experimentales de temperatura, concentración, de diferentes especies químicas presentes en la corriente gaseosa, etc., serán presentadas en el capítulo correspondiente. La instalación usada en este caso es similar a la anterior, aunque se añaden diferentes botellas para introducir los gases de reacción y se incorpora un medidor de NOx.

El CO y CO_2 son medidos con un analizador infrarrojo no-dispersivo de la casa Siemens Ultramat 22. Para detectar tanto el NO como el NO_2 se utiliza un analizador quimioluminiscente EcoPhysics, CLD 700 AL. El N_2O, N_2 y los posibles gases que puedan obtenerse son analizados mediante un espectrómetro de masas Balzers MsCube.

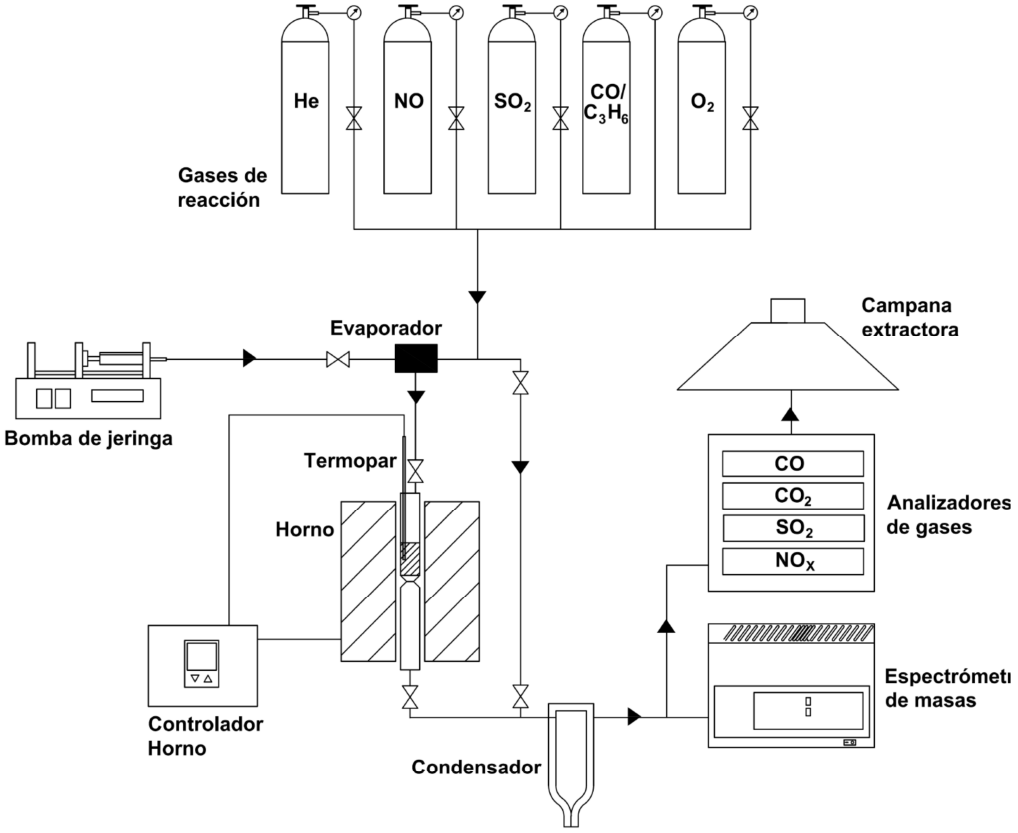

Figura 1.13. Esquema de la instalación utilizada para medir la eliminación de NO.

1.5.Referencias

1. www.hillsinc.net/arnoldtalk.shtml

2. J.G. McCulloch. The history of the development of melt blowing technology. Int. Nonwovens J, 1999; 8: 139-149.

3. A. Huczko. Template-based synthesis of nanomaterials, Appl. Phys. A, 2000; 70: 365-376.

4. J.C. Hulteen, C.R. Martin. A general template-based method for the preparation of nanomaterials. J. Mater. Chem., 1997; 7: 1075-1087.

5. T.M. Whitney, J.S. Jiang, P.C. Searson, C.L. Chien. Fabrication and Magnetic Properties of Arrays of Metallic Nanowires, Science 1993; 261: 1316-1319.

6. M. Nishizawa, K. Mukai, S. Kuwabata, C.R. Martin, H. Yoneyama. Template Synthesis of Polypyrrole-Coated Spinel LiMn2O4 Nanotubules and Their Properties as Cathode Active Materials for Lithium Batteries, J. Electrochem. Soc. 1997; 144: 1923-1927.

7. R.V. Parthasarathy, K.L.N. Phani, C.R. Martin. Template Synthesis of Graphitic Nanotubes. Adv. Mater. 1995; 7, 896-897.

8. N.K. Raman, M.T. Anderson, C.J. Brinker. Template-Based Approaches to the Preparation of Amorphous, Nanoporous Silicas. Chem. Mater., 1996, 8, 1682-1701.

9. J. Alcañiz Monge., D. Cazorla-Amorós., A. Linares-Solano, A. Oya, A. Sakamoto, K. Hoshi. Preparation of General Purpose Carbon Fibres from coal tar pitches with low softening point. Carbon 1997; 35: 1079-1087.

10. I. Mochida, S.-H. Yoon, N. Takano, F. Forti, Y. Korai, K. Yokogawa. Microstructure of mesophase pitch-based carbon fiber and its control. Carbon 1996; 34: 941-956.

11. W.M. Qiao, M. Huda, Y. Song, S.-H. Yoon, Y. Korai., I. Mochida. Carbon fibers and films based on biomass resins Energy & Fuels 2005, 19; 2576-2582.

12. S. Iijima, T. Ichihashi. Single-shell carbon nanotubes of 1-nm diameter. Nature 1993; 363: 603-605.

13. S. Iijima. Helical microtubules of graphitic carbon. Nature 1991; 354: 56-58.

14. H.M. Cheng, Q.H. Yang, C. Liu. Hydrogen storage in carbon nanotubes. Carbon 2001; 39: 1447–1454.

15. Ph. Avouris, R. Martel, V.V. Derycke, J. Appenzeller. Carbon Nanotube Transistors and Logic Circuits. Physica B 2002; 323: 6–14.

16. A.M.K. Esawi, M.M. Farag. Carbon nanotube reinforced composites: Potential and current challenges. Mater. Design 2007; 28: 2394–2401.

17. M. Penza, G. Cassano, P. Aversa, F. Antolini, A. Cusano, M. Consales, M. Giordano, L. Nicolais. Carbon nanotubes-coated multi-transducing sensors for VOCs detection. Sens. Actuators, B 2005; 111–112: 171–180.

18. C.W. Huang, Y.T. Wu, C.C. Hu, Y.Y. Li. Textural and electrochemical characterization of porous carbon nanofibers as electrodes for supercapacitors. J. Power Sources 2007; 172: 460–467.

19. T.J. Zhao, W.Z. Sun, X.Y. Gu, M. Rønning, D. Chen, Y.C. Dai, W.K. Yuan, A. Holmen. Rational design of the carbon nanofiber catalysts for oxidative dehydrogenation of ethylbenzene. Appl. Catal. A: General 2007; 323: 135–146.

20. Z. Shia, Y. Liana, X. Zhoua, Z. Gua, Y. Zhangb, S. Iijima, L. Zhou, K.T. Yue, S. Zhang. Mass-production of single-wall carbon nanotubes by arc discharge method. Carbon 1999; 37: 1449–1453.

21. T. Guo, P. Nikolaev, A.G. Rinzler, D. Tomanek, D.T. Colbert, R.E. Smalley. Self-Assembly of Tubular Fullerenes. J. Phys. Chem. 1995; 99: 10694-10697.

22. T. Guo, P. Nikolaev, A. Thess, D.T. Colbert, R.E. Smalley. Catalytic growth of single-walled nanotubes by laser vaporization. Chem. Phys. Lett. 1995; 243: 49-54.

23. M. José-Yacamán, M. Miki-Yoshida, L. Rendón, J.G. Santiesteban. Catalytic growth of carbon microtubules with fullerene structure. Appl. Phys. Lett. 1993; 62: 657-659.

24. R.S. Barhate, S. Ramakrishna. Nanofibrous filtering media: Filtration problems and solutions from tiny materials. J. Membrane Science, 2007; 296: 1-8.

25. S. Agarwal, J.H. Wendorff, A. Greiner. Progress in the Field of Electrospinning for Tissue Engineering Applications. Adv. Mater., 2009; 21: 3343-3351.

26. B. Ding, M. Wang, J. Yu, Gang Sun. Gas Sensors Based on Electrospun Nanofibers. Sensors, 2009; 9: 1609-1624.

27. S. Park, K. Park, H. Yoon, J. Son, T. Min, G. Kim. Apparatus for preparing electrospun nanofibers: designing an electrospinning process for nanofiber fabrication. Polym Int., 2007, 56, 1361-1366.

28. W. Sigmund, J. Yuh, H. Park, V. Maneeratana, G. Pyrgiotakis, A. Daga, J. Taylor, J. C. Nino. Processing and Structure Relationships in Electrospinning of Ceramic Fiber Systems. J. Am. Ceram. Soc., 2006; 89: 395-407.

29. A.K. Moghe, B.S. Gupta. Co-axial Electrospinning for Nanofiber structures: Preparation and Applications. Polymer Reviews 2008; 48: 353-377.

30. G.C. Rutledge, S.V. Fridrikh. Formation of fibers by electrospinning, Advanced Drug Delivery Reviews. 2007; 59: 1384-1391.

31. A. Formhals. Process and apparatus for preparing artificial threads. US 1,975,504, 1934.

32. www.donaldson.com

33. J. Doshi, D. Reneker. Electrospinning Process and Applications of Electrospun Fibers. J. Electrostatics 1995, 35, 151-160.

34. Y.M. Shin, M.M. Hohman, M.P. Brenner, G.C. Rutledge. Electrospinning: A whipping fluid jet generates submicron polymer fibers. Appl Phys Lett. 2001;78: 1149-1151.

35. I.G. Loscertales, A. Barrero, I. Guerrero, R. Cortijo, M. Marquez, A.M. Gañán-Calvo. Micro/nano encapsulation via electrified coaxial liquid jets. Science 2002;295:c 1695-1698.

36. O.A. Basaran. Small-Scale Free Surface Flows with Breakup: Drop Formation and Emerging Applications. AIChE Journal 2002; 48: 1842-1846.

37. W. Zuo, M. Zhu, W. Yang, H. Yu, Y. Chen, Y. Zhang. Experimental study on relationship between jet stability and formation of beaded fibers during electrospinning. Polym. Eng. Sci. 2005; 45: 704-709.

38. A.L. Yarin, S. Koombhongse, D.H. Reneker. Bending instability in electrospinning of nanofibers. J. Appl. Phys. 2001; 89: 3018-3026.

39. D.H. Reneker, A.L. Yarin, H. Fong, S. Koombhongse. Bending instability of electrically charged liquid jets of polymer solutions in electrospinning. J. Appl. Phys. 2000; 87: 4531-4547.

40. G. Riboux, A. Marín, I.G. Loscertales, A. Barrero. Whipping instability characterization of an electrified visco-capillary jet. J. Fluid Mech. 2011; 671: 226–253

41. B. Ding, H.Y. Kim, S.C. Lee, D.R. Lee, K.J.Choi. Preparation and characterization of nanoscaled poly(vinyl alcohol) fibers via electrospinning. Fiber. Polym. 2002; 3: 73-79.

42. B. Sundaray, V. Subramanian, T.S. Natarajan, R.Z. Xiang, C.C. Chang, W.S. Fann. Electrospinning of continous aligned fibers. Appl. Phys. Lett. 2004; 84: 1222–1224.

43. P.D. Dalton, D. Klee, M. Möller. Electrospinning with dual collection rings. Polymer 2005; 46: 611-614.

44. J. Kameoka, H.G. Craighead. Fabrication of oriented polymeric nanofibers on planar surfaces by electrospinning. Appl. Phys. Lett. 2003; 3: 371-373.

45. M.S. Khil, S.R. Bhattarai, H.Y. Kim, S.Z. Kim, K.H. Lee. Novel fabricated matrix via electrospinning for tissue engineering. J. Biomed. Mater. Res. B 2005; 72: 117-124.

46. S.A. Theron, E. Zussman, A.L. Yarin. Experimental investigation of the governing parameters in the electrospinning of polymer solutions. Polymer 2004; 45: 2017-2030.

47. T. Subbiah, G.S. Bhat, S. Parameswaran, S.S. Ramkumar. Electrospinning of Nanofibers. J Appl Polymer Sci 2005; 96: 557-569.

48. Y.M. Shin, M.M. Hohman, M.P. Brenner, G.C. Rutledge. Experimental characterization of electrospinning: the electrically forced jet and instabilities. Polymer 2001; 42: 9955-9967.

49. M.G. McKee, M.T. Hunley, J.M. Layman, T.E. Long. Solution Rheological Behavior and Electrospinning of Cationic Polyelectrolytes. Macromolecules 2006; 39: 575-583.

50. P.K. Baumgarten. Electrostatic spinning of acrylic microfibers. J colloid Interface Sci 1971; 36: 71-79.

51. X.H. Zong, F. Kim, D.F. Fang, S.F. Ran, B.S. Hsiao, B. Chu. Structure and process relationship of electrospun bioabsorbable nanofiber membranes Polymer 2002; 43: 4403-4412.

52. S. Ramakrishna, K. Fujihara, W.-E. Teo, T.-C. Lum, Z. Ma. An introduction to electrospinning and nanofibers, World Scientific Publishing Co. Pte. Ltd. 2005, ISBN 981-256-415-2.

53. I.G. Loscertales, A. Barrero, M. Márquez, R. Spretz, R. Velarde-Ortiz, G. Larsen. Electrically forced coaxial nanojets for one-step hollow nanofiber design. J. Am. Chem. Soc. 2004;126: 5376-5377.

54. A.B. Ripoll, A.M. Gañán-Calvo, I.G. Loscertales, R.C. Bon, M. Márquez. Production of capsules and particles for improvement of food products, US 10/627, 387, 2006.

55. Z. Sun, E. Zussman, A.L. Yarin, J.H. Wendorff, A. Greiner. Compound core-shell polymer nano fibers by co-electrospinning. Adv. Mater. 2003; 15: 1929-1932.

56. D. Li, Y. Zia. Direct fabrication of composite and ceramic hollow nanofibers by electrospinning. Nano Lett. 2004; 4: 933-938.

57. J.H. Yu, S.V. Fridikh, G.C. Rutledge. Production of submicron diameter fibers from difficult-to-process materials by two-fluid electrospinning. Adv. Mater. 2004; 16: 1562-1566.

58. J.G. Esteban-González. Generation of micro and nano-structured materials by electro-hydrodynamic techniques. Universidad de Málaga, 2010.

59. K.M. Sawicka, P. Gouma. Electrospun composite nanofibers for functional applications. J. Nanopart. Res. 2006; 8: 769–781.

60. S.A. Angadjivand, M.G. Schwartz, P.D. Eitzman, M.E. Jones. 2002. US patent 6,375,886

61. W. Wei, J.-T. Yeh, X.-L. Wang, P. Li. Removal of Cd(II) from aqueous solution by electrospun nylon 6 nanofibrous nonwoven containing attapulgite. Adv. Mater. Res. 2011; 332-334: 1295-1299.

62. X. Song, Z. Wang, Z. Li, C. Wang. Ultrafine porous carbon fibers for SO2 adsorption via electrospinning of polyacrylonitrile solution. J colloid Interface Sci. 2008; 327: 388-392.

63. G.C. Rutledge. Fibres: Superhydrophobic fibres. Advances in Textiles Technology 2008; (MAR.), 3-4.

64. Y.K. Luu, K. Kim, B.S. Hsiao, B. Chu, M. Hadjiargyrou. Development of a nanostructured DNA delivery scaffold via electrospinning of PLGA and PLAPEG block copolymers. J. Control. Release 2003; 89: 341–353.

65. H. Yoshimoto, Y.M. Shin, H. Terai, J.P. Vacanti. A biodegradable nanofiber scaffold by electrospinning and its potential for bone tissue engineering. Biomaterials 2003; 24: 2077–2082.

66. K.Y. Cai, K.D. Yao, X. Hou, Y.Q. Wang, Y.J. Hou, Z. Yang, X. Li, H. Xie. Improvement of the functions of osteoblasts seeded on modified poly(D,L-lactic acid) with poly(aspartic acid). J. Biomed. Mater. Res. 2002; 62: 283–291.

67. K. Kim, Y.K. Luu, C. Chang, D. Fang, B.S. Hsiao, B. Chu, M. Hadjiargyrou. Incorporation and controlled release of a hydrophilic antibiotic using poly(lactide-coglycolide)-based electrospun nanofibrous scaffolds. J Control Release, 2004; 98: 47-56.

68. X. Xu, X. Chen, X. Xu, T. Lu, X. Wang, L. Yang, X. Jing. BCNU-loaded PEGPLLA ultrafine fibers and their in vitro antitumor activity against Glioma C6 cells. J Control Release 2006; 114: 307-316.

69. S.Y. Chew, J. Wen, E.K. Yim, K.W. Leong. Sustained release of proteins from electrospun biodegradable fibers. Biomacromolecules, 2005; 6: 2017-2024.

70. Y.Z. Zhang, X. Wang, Y. Feng, J. Li, C.T. Lim, S. Ramakrishna. Coaxial Electrospinning of (Fluorescein Isothiocyanate-Conjugated Bovine Serum Albumin)-Encapsulated Poly(E-caprolactone) Nanofibers for Sustained Release. Biomacromolecules 2006; 7, 1049-1057.

71. H. Jiang, Y. Hu, Y. Li, P. Zhao, K. Zhu, W. Chen. A facile technique to prepare biodegradable coaxial electrospun nanofibers for controlled release of bioactive agents. J. Controlled Release 2005; 108. 237-243.

72. R. Srikar, A.L. Yarin, C.M. Megaridis, A.V. Bazilevsky, E. Kelley. Desorption-Limited Mechanism of Release from Polymer Nanofibers. Langmuir 2008; 24, 965-974.

73. R.L.V. Wal, G.M. Berger, M.J. Kulis, G.W. Hunter, J.C. Xu, L. Evans. Synthesis Methods, Microscopy Characterization and Device Integration of Nanoscale Metal Oxide Semiconductors for Gas Sensing. Sensors 2009; 9: 7866-7902.

74. H.Q. Liu, J. Kameoka, D.A. Czaplewski, H.G. Craighead. Polymeric nanowire chemical sensor. Nano Lett. 2004; 4: 671–675.

75. X.Y. Wang, Y.G. Kim, C. Drew, B.C. Ku, J. Kumar, L.A. Samuelson. Electrostatic assembly of conjugated polymer thin layers on electrospun nanofibrous membranes for biosensors. Nano Lett. 2004; 4: 331–334.

76. X.Y. Wang, C. Drew, S.H. Lee, K.J. Senecal, J. Kumar, L.A. Sarnuelson. Electrospun nanofibrous membranes for highly sensitive optical sensors. Nano Lett. 2002; 2: 1273–1275.

77. W.Z. Jia, L. Su, Y. Ding, A. Schempf, Y. Wang, Y. Lei. Pd/TiO2 nanofibrous membrane and its application in hydrogen sensing. J. Phys. Chem. C 2009; 113: 16402-16407.

78. M.Y. Song, D.K. Kim, K.J. Ihn, S.M. Jo, D.Y. Kim. Electrospun TiO2 electrodes for dye-sensitized solar cells. Nanotechnology 2004; 15: 1861-1865.

79. Y. Gu, D. Chen, X. Jiao, F. Liu. LiCoO2–MgO coaxial fibers: co-electrospun fabrication, characterization and electrochemical properties. J. Mater. Chem. 2007; 17: 1769-1776.

80. E. Formo, Z.M. Peng, E. Lee, X.M. Lu, H. Yang, Y. Xia. Direct oxidation of methanol on Pt nanostructures supported on electrospun nanofibers of anatase. J. Phys. Chem. C 2008; 112: 9970-9975.

81. J.S. Im, S. Park, T.J. Kim, Y.H. Kim, Y. Lee. The study of controlling pore size on electrospun carbon nanofibers for hydrogen adsorption. J. Colloid Interface Sci. 2008; 318: 42-49.

82. E. Formo, P.H.C. Camargo, B. Lim, M. J. Jiang, Y. Xia. Functionalization of ZrO2 nanofibers with Pt nanostructures: The effect of surface roughness on nucleation mechanism and morphology control. Chem. Phys. Lett. 2009; 476: 56-61.

83. E. Formo, E. Lee, D. Campbell, Y. Xia. Functionalization of electrospun TiO2 nanofibers with Pt nanoparticles and nanowires for catalytic applications Nano Lett. 2008; 8: 668-672.

84. D. Lin, H. Wu, R. Zhang, W. Pan. Enhanced Photocatalysis of Electrospun Ag-ZnO Heterostructured Nanofibers. Chem. Mater. 2009; 21: 3479-3484.

85. H. Jia, G. Zhu, B. Vugrinovich, W. Kataphinan, D.H. Reneker, P Wang. Enzyme-Carrying Polymeric Nanofibers Prepared via Electrospinning for Use as Unique Biocatalysts. Biotechnol. Prog., 2002; 18: 1027-1032.

86. S. Zhan, D. Chen, X. Jiao, C. Tao. Long TiO2 hollow fibers with mesoporous walls: Sol-gel combined electrospun fabrication and photocatalytic properties. J. Phys. Chem. B 2006; 110: 11199-11204.

87. M.A. Vannice. “Kinetics of Catalytic Reactions” Springer-Verlag, NY, 2005.

88. R. L. Burwell, Jr. Chemtech 1987; 17: 586.

89. U.S. Climate Change Technology Program – Technology Options for the Near and Long Term August 2005.

90. M. Boudart and G. Djega-Mariadassou, Kinetics of Heterogeneous Catalytic Reactions, Princeton University Press, Princeton, NJ, 1984.

91. B.C. Gates. Supported Metal Clusters: Synthesis, Structure, and Catalysis. Chem. Rev. 95; 1995: 511-522.

92. J. Guzman, B.C. Gates. Supported molecular catalysts: metal complexes and clusters on oxides and zeolites. Dalton Trans. 2003; 17: 3303-3318.

93. E.W. Thiele. Relation between Catalytic Activity and Size of Particle. Ind. Eng. Chem. 1939; 31: 916.

94. J. J. Carberry, ‘‘Chemical and Catalytic Reaction Engineering’’, McGraw-Hill, NY, 1976.

95. H. Matsumoto, A.Tanioka. Functionality in Electrospun Nanofibrous Membranes Based on Fiber’s Size, Surface Area, and Molecular Orientation. Membranes 2011; 1: 249-264.

96. J.-F. Lambert, M. Che. The molecular approach to supported catalyst: state of the art and future challenges. J. Mol. Catal. A: Chem. 2000; 162: 5-18.

97. L.K. Hudson, C. Misra, A.J. Perrotta, K. Wefers, F.S. Williams “Aluminum Oxide” in Ullmann's Encyclopedia of Industrial Chemistry 2002, Wiley-VCH, Weinheim.

98. J.S. Beck, C.T.-W. Chu, I.D. Johnson, C.T. Kresge, M.E. Leonowicz, W.J. Roth, J.W. Vartuli, WO Patent 91/11390, 1991.

99. A. Corma. From microporous to mesoporous molecular sieve materials and their use in catalysis. Chem. Rev. 1997; 97: 2373-2419.

100. A. Taguchi, F. Schüth. Ordered mesoporous materials in catalysis. Microporous Mesoporous Mater. 2005; 77: 1–45.

101. P. Kumar, V.V. Guliants. Periodic mesoporous organic–inorganic hybrid materials: Applications in membrane separations and adsorption. Microporous Mesoporous Mater. 2010; 132: 1–14.

102. Zeolites (natural), USGS Mineral Commodity Summaries 2011.

103. M.E. Davis, C. Saldarriaga, C. Montes, J. Garces, C. Crowder. A molecular sieve with eighteen-membered rings. Nature 1988; 331: 698-699.

104. B.J. Schoeman, J. Sterte, J.-E. Otterstedt. J. Chem. Soc. Chem. Commun. 1993; 994.

105. A.H. Janssen, A.J. Koster, K.P. de Jong. Three-Dimensional Transmission Electron Microscopy Observations of Mesopores in Dealuminated Zeolite Y. Angew. Chem. Int. Ed. 2001; 40: 1102-1104.

106. J. Levec, A. Pintar. Catalytic wet-air oxidation processes: A review. Catalysis Today 2007; 124: 172–184.

107. R.J. Davis, Z. Liu. Titania-Silica: A Model Binary Oxide Catalyst System. Chem. Mater. 1997; 9: 2311-2324.

108. B.M. Reddy, A. Khan. Recent advances on TiO2-ZrO2 mixed oxides as catalysts and catalyst supports. Cat. Rev. 2005; 47: 257-296.

109. I. Schmidt, A. Boisen, E. Gustavsson, K. Stahl, S. Pehrson, S. Dahl, A. Carlsson, C.J.H. Jacobsen. Carbon Nanotube Templated Growth of Mesoporous Zeolite Single Crystals. Chem. Mater. 2001; 13: 4416-4418.

110. M. Schneider, A. Baiker. Titania-based aerogels. Catal. Today 1997; 35: 339-365.

111. A. Tsevis, N. Spanos, P. Koutsoukos, A.J. van der Linde, J. Lyklema. Preparation and characterization of anatase powders. J. Chem. Soc. Faraday Trans. 1998; 94:295-300.

112. G.K. Chuah, S. Jaenicke. The preparation of high surface area zirconia - influence of precipitating agent and digestion. Appl. Catal. A 1997, 163: 261-273.

113. X. Song, A. Sayari, Catal. Rev. Sci. Eng. 1996; 38: 329-412.

114. A. Corma, V. Fornes, M.I. Juan-Rajadell, J.M. Lopez-Nieto. Influence of preparation conditions on the structure and catalytic properties of SO42-/ZrO2 superacid catalysts. Appl. Catal. A 1994; 116: 151-163.

115. G.D. Yadav, J.J. Nair. Sulfated zirconia and its modified versions as promising catalysts for industrial processes Microporous Mesoporous Mater. 1999; 33: 1–48.

116. T. Hosoi, S. Kitada, T. Shimizu, T. Imai, S. Nojima. Isomerisation of n-Pentane on Pt/SO4/Zr02: Role of Platinum and Reaction Mechanism. Shokubai 1990; 32: 117 see CA 113:211111b

117. M. Ozawa. Role of cerium-zirconium mixed oxides as catalysts for car pollution: A short review. J. Alloys Compd. 1998; 275: 886-890.

118. R.G. Leliveld, W.C.A. Huyben, A.J. van Dillen, J.W. Geus, D. Koningsberger: Novel hydrotreating catalysts based on synthetic clay minerals. In Hydrotreatment and Hydrocracking of Oil Fractions. Edited by Froment GF, Delmon B, Grange P. Amsterdam: Elsevier Science; 1997:137-146.

119. L.R. Radovic, F. Rodríguez-Reinoso. Chemistry and Physics of Carbons. Ed. P.A. Thrower. Marcel Dekker, Nueva York, Vol 25 1997; 243.

120. F. Rodríguez-Reinoso. Porosity in Carbons: Characterization and Applications. Ed. JW de Patrick, E Arnold. Londres. 1995; 253.

121. V Macheck, J Hanika, K Sporka, V Ruzicka, J Kunz. Coll Czech Chem Commun 1981; 46: 3270-3277.

122. F. Rodríguez-Reinoso, C. Salinas-Martínez de Lecea, A. Sepúlveda-Escribano, J.D. López-Gonzalez. Platinum catalysts supported on activated carbons : I. Preparation and characterization. J. Catal. 1986; 99: 171-183.

123. F. Derbyshire, V.H.J. de Beer, G.M.K. Abotsi, A.W. Scaroni, J.M. Solar, D.J. Skrovanek. The influence of surface functionality on the activity of carbon-supported catalysts. Appl. Catal. 1986; 27: 11-131.

124. C. Prado-Burguete, A. Linares-Solano, F. Rodríguez-Reinoso, C. Salinas-Martínez de Lecea. The effect of oxygen surface groups of the support on platinum dispersion in Pt/carbon catalysts. J. Catal. 1989; 115: 98-106.

125. C. Prado-Burguete, A. Linares-Solano, F. Rodríguez-Reinoso, C. Salinas-Martínez de Lecea. The effect of carbon support and mean Pt particle size on hydrogen chemisorption by carbon supported Pt catalysts. J. Catal. 1991; 128: 397-404.

126. L.R. Radovic, C. Sudhakar. Introduction to Carbon Technologies. Ed. H. Marsh, E.A. Heintz, F. Rodríguez-Reinoso. Secretariado de Publicaciones, Universidad de Alicante, Alicante, 1997; 107.

127. H. Jiintgen. Activated carbon as catalyst support. A review of new research results. Fuel 1986; 65: 1436-1446.

128. J. Bedia. Catalizadores Carbonosos obtenidos mediante activación química de residuos lignocelulósicos, Universidad de Málaga, Málaga, 2008; capítulo 1: 7-9.

129. http://www.ili-lignin.com

130. E. Adler. Lignin chemistry-Past, Present and Future. Wood Sci. Technol. 1977; 11: 169-218.

131. J. Rodríguez-Mirasol, T. Cordero, J.J. Rodríguez. High-temperature carbons from kraft lignin. Carbon 1995; 34: 43-52.

132. J. Rodríguez-Mirasol. Estudio de la Carbonización y Activación de Lignina kraft de Eucalipto. Tesis Doctoral, Universidad de Málaga, Málaga, 1991.

133. E. González-Serrano. Estudio de la Activación Química con ZnCl2 de la Lignina kraft. Tesis Doctoral, Universidad de Málaga, Málaga, 1996.

134. E. Gonzalez-Serrano, T. Cordero, J. Rodriguez-Mirasol, L. Cotoruelo, J.J. Rodríguez. Removal of water pollutants with activated carbons prepared from H3PO4 activation of lignin from kraft black liquors. Water Research 2004; 38: 3043–3050.

135. C. Pedrero, T. Cordero, J. Rodríguez-Mirasol, J.J. Rodríguez. Carbon molecular sieves from lignin. Carbon'99, Charleston, SC ,1999.

136. C. Pedrero, T. Cordero, J. Rodríguez-Mirasol, J.J. Rodríguez. Preparation of carbon molecular sieves by chemical vapor infiltration of lignin based microporous carbon. Carbon'01, Lexington, KEN, 2001.

137. J.M. Rosas, J. Bedia, J. Rodríguez-Mirasol, T. Cordero. Kinetics of Pyrolytic Carbon Infiltration for the Preparation of Ceramic/Carbon and Carbon/Carbon Composites. Carbon 2004; 42: 1285-1290.

138. M. Lallave, J. Bedia, R. Ruiz-Rosas, J. Rodríguez-Mirasol, T. Cordero, J.C. Otero, M. Marquez, A. Barrero, I.G. Loscertales. Filled and hollow carbon nanofibers by coaxial electrospinning of alcell lignin without binder polymers. Adv. Mater. 2007; 19: 4292–4296.

139. R. Ruiz-Rosas, J. Bedia, M. Lallave, I.G. Loscertales, A. Barrero, J. Rodríguez-Mirasol, T. Cordero. The production of submicron diameter carbon fibers by the electrospinning of lignin. Carbon. 2010; 48(3): 696-705.

140. C. Perego, P. Villa. Catalyst preparation methods. Catal. Today 34; 1997: 281-305.

141. M. U. Twigg, Editor, Catalyst Handbook, 2nd edn., Wolfe Ltd., 1989.

142. R.K. Iler, The Chemistry of Silica, Wiley, New York, 1979.

143. G.E. Doelbear, in Novel Approaches to Catalysts Preparation, Catalytica Studies Division, 1993.

144. L.L. Hech, J.K. West. The Sol-gel progress. Chem. Rev. 1990; 90: 33-72.

145. S. Bathia. Zeolite Catalysis: Principles and Applications, CRC Press, Boca Raton, FL, 1990.

146. G.M. Pajonk. Aerogel catalysts. Appl. Catal. 1991; 72: 217.

147. C.N. Satterfield. Heterogeneous Catalysis in Practice, McGraw-Hill, 1980, Chap. 4.

148. L.A.M. Hermans, J.W. Geus. Preparation of Catalysts II, Elsevier, Amsterdam, 1979, 113.

149. M. Suvanto, T.A. Pakkanen. A fluidized bed reactor for low temperature deposition. J. Mol. Catal. A 1997; 125:91-96.

150. M. Suvanto, T.A. Pakkanen. Tungsten hexacarbonyl on alumina. Controlled deposition from gas phase. Appl. Catal. A 1998; 166:105-113.

151. L. Rogatis, M. Cargnello, V. Gombac, B. Lorenzut, T. Montini, P. Fornasiero. Embedded Phases: A Way to Active and Stable Catalysts. ChemSusChem 2010; 3: 24–42.

152. R.D. Gonzalez, L. Lopez, R. Gomez. Sol-gel preparation of supported metal catalysts. Catal. Today 1997; 35:293-317.

153. G. Budroni, A. Corma. Gold-organic-inorganic high-surface-area materials as precursors of highly active catalysts. Angew. Chem. Int. Ed. 2006; 45: 3328-3331.

154. H. Morioka, Y. Shimizu, M. Sukenobu, K. Ito, E. Tanabe, T. Shishido, K. Takehira. Appl. Catal. A 2001; 215: 11-19.

2. FILLED AND HOLLOW CARBON NANOFIBERS BY COAXIAL ELECTROSPINNING OF ALCELL LIGNIN WITHOUT BINDER POLYMERS

2.0.Abstract

A study was conducted, to demonstrate a new method for obtaining solid and hollow carbon micro- and nanofibers, by co-electrospinning Alcell lignin solutions at room, without using additional polymer. The lignin micro and nanofibers were thermally stabilized and carbonized, to generate carbon nanofibers. Alcell lignin solutions that were suitable for electrospinning, were prepared in ethanol, with viscosities in the range of 350-400 cPs. The coaxial electrospinning method was also used to generate Alcell lignin hollow nanofibers (ALHFs). ALFs were stabilized ALSFs), by thermal treatment in air at 0.15 °C min^{-1} from room temperature to 200°C, which was maintained for 24 hours. Alcell lignin solid and hollow nanofibers were obtained by carbonizing at 900°C those thermostabilized, with a heating rate of 10°C min^{-1}.

2.1.Introduction

Carbon fibers have become materials that are of great technological and industrial importance because of their unique chemical, electrical, magnetic, and mechanical properties. Two types of carbon fibers are commercialized as a function of their mechanical properties: so-called high-performance carbon fibers (e.g., used in aerospace and sporting goods applications and as reinforcing components in advanced composite materials) and general purpose carbon fibers (e.g., used as activated carbon fibers and substrates for catalytic applications and for gas storage and adsorption applications). The spinning process usually employed to form both types of carbon fibers involves melt extrusion of the precursor followed by a thermal treatment to 1) stabilize the fibers of the precursor and 2) carbonize them to ultimately afford carbon fibers. The final fiber diameters typically range between 7 and 15 lm. To date, fossil pitches are the most widely investigated precursor of carbon fibers mainly because of their low cost compared to the rather expensive polyacrylonitrile (PAN). Interestingly,

renewable or recycled sources of carbon have also been considered as possible novel carbon-fiber precursors [1].

Another low-cost feedstock capable of producing general purpose carbon fibers is lignin. Lignin is the second most abundant polymer in nature after cellulose. This natural, aromatic (phenolic), heterogeneous bio-macromolecule exists in the cell wall of plants and constitutes an underutilized by-product of the papermaking industry [2]. Two types of lignin are mainly btained today. The most yielded type is the so-called Kraft lignin, which comes from the Kraft pulping process, a process that affords in this type of lignin a high content of ashes and salts (i.e., inorganic material). The second type of lignin is called Alcell lignin. In contrast to Kraft lignin, Alcell lignin contains very small amounts of inorganic materials because of the different pulping process used [3,4]. Interestingly, the Alcell pulping process exhibits higher pulp yields than the Kraft process, and it is also more environmentally friendly [5]. For these and other reasons, the Alcell process is becoming the preferred choice for the future of the paper-making industry. Kubo et al. [6] first reported the use of lignin as a precursor for carbon fibers. In order to obtain a spinnable material from lignin, these authors proposed the conversion of lignin into functional polymers by a suitable separation method from wood. The fibers, after thermal stabilization, could be carbonized to yield carbon fibers. Much more recently, several groups have reported the design of blends that contain either Kraft or Alcell lignin and synthetic polymers, suitable for melt extrusion, to produce fibers that, after a proper thermal treatment, yield carbon fibers [4,7–9]. The diameter of such fibers typically ranged from 80 to 30 lm, but smaller diameters were difficult to obtain because of inherent limitations (i.e., clogging) of the melt-extrusion process used to draw the fibers. Although this blending approach allowed lignin to be utilized to produce fibers, the need to use rather expensive polymers in the blend may be understood as a drawback, as it increases the cost of the process.

In contrast to the approach based on the use of binder polymers [10], here we present a new straightforward method for obtaining carbon micro- and nanofibers, both solid and hollow, by co-electrospinning Alcell lignin solutions at room temperature without any added polymer. The lignin micro and nanofibers were subsequently thermally stabilized and carbonized to generate carbon nanofibers. We also report the properties of these carbon nanofibers.

2.2.Experimental

The oxidative stabilization and carbonization processes were performed in a conventional horizontal furnace consisting of a 120 cm long and 7 cm inner diameter silica-glass tube heated by electrical resistance at a controlled temperature. Air and N_2 continuously flowed at 200 mL (standard temperature and pressure, STP) min^{-1}.

The surface chemistry of the nanofibers was analyzed by XPS, SEM, and TEM. XPS data for the samples were obtained using a 5700C model Physical Electronics apparatus with Mg Kα radiation (1253.6 eV). SEM and TEM images were obtained using a JEOL JSM-840 instrument at a high voltage of 20–25 kV and a PHILIPS CM-200 transmission electron microscope, respectively.

The porous structure of the nanofibers was evaluated by N_2 adsorption–desorption at –196 °C and by CO_2 adsorption at 0 °C in an Autosorb-1 apparatus (Quantachrome). Samples were previously outgassed for at least 8 h at 150 °C. From the N_2 isotherm, $A_{BET\ N2}$ was determined by applying the BET equation [11] and $V_{t\ N2}$ and $A_{t\ N2}$ were calculated using the t-method [12]. From the CO_2 adsorption data, $V_{DR\ CO2}$ and $A_{DR\ CO2}$ were calculated using the Dubinin–Radushkevich equation [13].

2.2.1. Electrospinning

We prepared solutions of Alcell lignin in ethanol (1:1 lignin/ethanol w/w) with viscosities in the range 350 to 400 cPs, which are suitable for electrospinning. A general problem when electrospinning highly concentrated solutions of rather volatile solvents, such as ethanol, is that the rapid evaporation of ethanol from the solution surface leads to the formation of a solid supernatant. This solidification eventually renders the electrospinning process unviable after a limited time because the Taylor cone (or part of it) solidifies. To overcome this problem we used a co-axial spinneret [14,15], which is shown in Figure 2.1A. The purpose of the outermost capillary needle is, in this case, to allow a thin sheath of ethanol to flow to compensate for solvent losses caused by the evaporation of the lignin solution in the Taylor cone. In fact, by controlling the sheath-to-lignin solution flow rate ratio, one can switch from steady electrospinning to steady electrospray. The electrospray produced rather monodisperse spherical lignin particles with diameters that could be varied from about one micrometer to 300 nm (not shown).

For fiber production, the sheath flow rate of ethanol is approximately 10 % of the lignin solution flow rate, although it may slightly vary depending on room conditions.

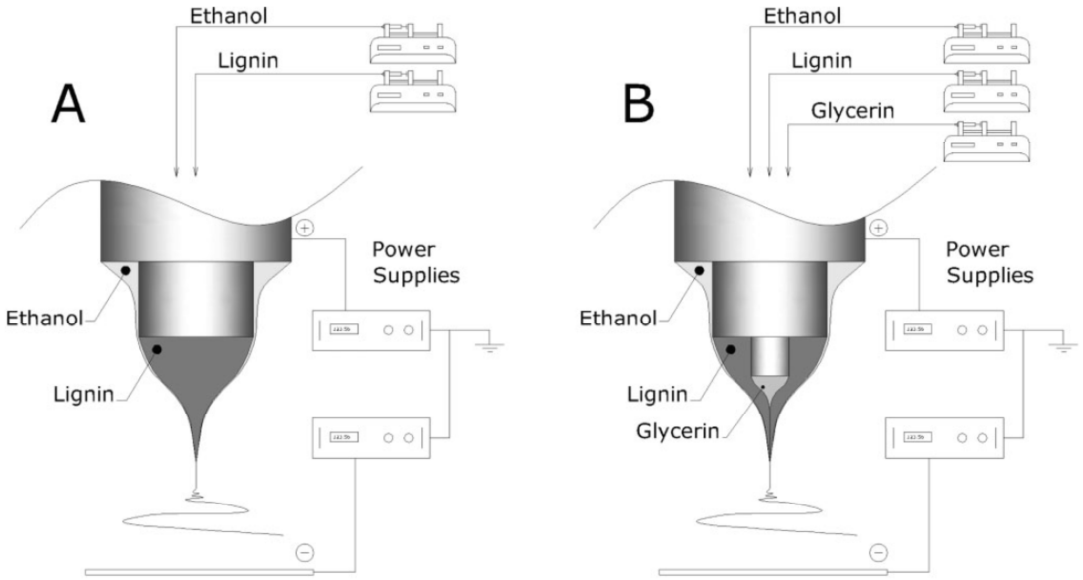

Figure 2.1. A) Coaxial needle for electrospinning with sheath. B) General set-up used in tri-axial electrospinning to produce lignin nanotubes.

To generate Alcell lignin hollow nanofibers (ALHFs), we used the coaxial electrospinning method reported in the literature[14,15] but in a tri-axial configuration to use a sheath flow of ethanol to avoid solidification of the Taylor cone; Figure 2.1B shows the tri-axial spinneret with a third needle (the innermost). This needle supplies glycerine as a template fluid. In our case, the needle outer:inner diameter ratios were 1.6/1.22, 1.1/0.8, and 0.5/0.26 mm, respectively. The flow rates through the needles ranged from 0.05/0.5/0.01 to 0.1/1/0.25 mL h^{-1} for ethanol sheath:lignin:glycerine, respectively, although the sheath flow rate varied slightly depending on ambient conditions. Typically, the flow rate of glycerine was varied in our experiments from 5 to 50 % of the flow rate of lignin.

To apply the high voltage between the spinneret and the collector, we used two high voltage power supplies: one positively polarized connected to a needle and the other negatively polarized and attached to a collector (Fig. 2.1). This configuration provided better electrostatic conditions to prevent fibers from flying to any grounded piece near the set-up, therefore facilitating the deposition of the electrospun fibers on the collector. The tip-to-collector distance was 20–25 cm, and the electrical potential

difference was 12 kV (the collector was at –6 kV and the tips at +6 kV), although this value varied depending on the collector/tip geometry.

2.3.Fiber morphology

Figure 2.2A presents a scanning electron microscopy (SEM) image of as-collected Alcell lignin electrospun nanofibers (ALFs). The fiber diameters ranged from 400 nm to 2 μm, which were much smaller than the reported 31 and 46 μm obtained for Alcell and Kraft lignin fibers, respectively, that were prepared by thermal extrusion [7]. ALFs were stabilized (ALSFs) by thermal treatment in air at 0.25 °C min^{-1} from room temperature to 200 °C, and this temperature was maintained for 24 h. The stabilization yield was 81 wt % based on the mass of the ALFs. This yield was smaller than for pitch, given that the lignin structure was already oxidized and that the condensation reaction released water, thus reducing weight [7]. No fusion was observed after stabilization, and the fibers were similar in size (diameter) to the ALFs. Alcell lignin carbon nanofibers (ALCFs) were obtained by carbonizing ALSFs at 900 °C with a heating rate of 10 °C min^{-1}. Transmission electron microscopy (TEM) images of the ALCFs are shown in Figure 2.2B. Carbon fibers with diameters as small as 200 nm were produced, and no defects were observed in the fiber surface, which seems very smooth. The carbon fiber consisted of fine carbon crystallites with a preferred orientation along the fiber axis.

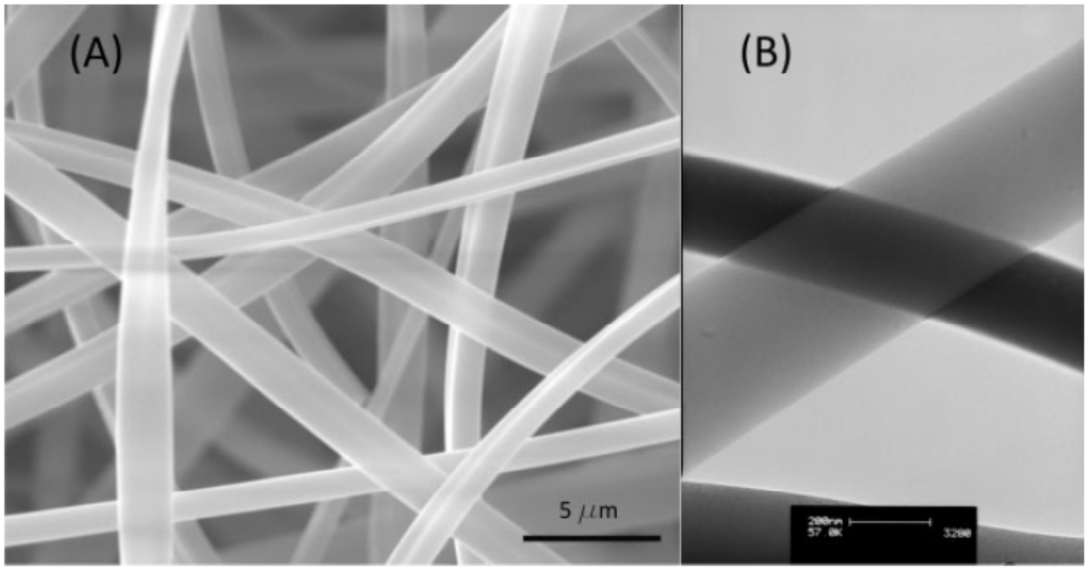

Figure 2.2 Alcell lignin fibers. A) ALFs as collected; scale bar is 5 μm. B) ALCFs; scale bar is 200 nm.

2.4.Thermogravimetric analyses

The thermogravimetric curves for the ALFs and ALCFs heated in air and for the ALSFs heat in N_2 are shown in Figure 2.3. For ALSFs, the main weight loss occurred in the temperature range 300–600 °C, a consequence of devolatilization; by 900 °C, the level was nearly constant. Similar results were reported for ground Kraft lignin [16]. The carbonization yield was 39 wt % based on the ALSF mass, with a total yield value for the carbon nanofibers of 31.6 wt % based on the initial nanofiber (ALF).

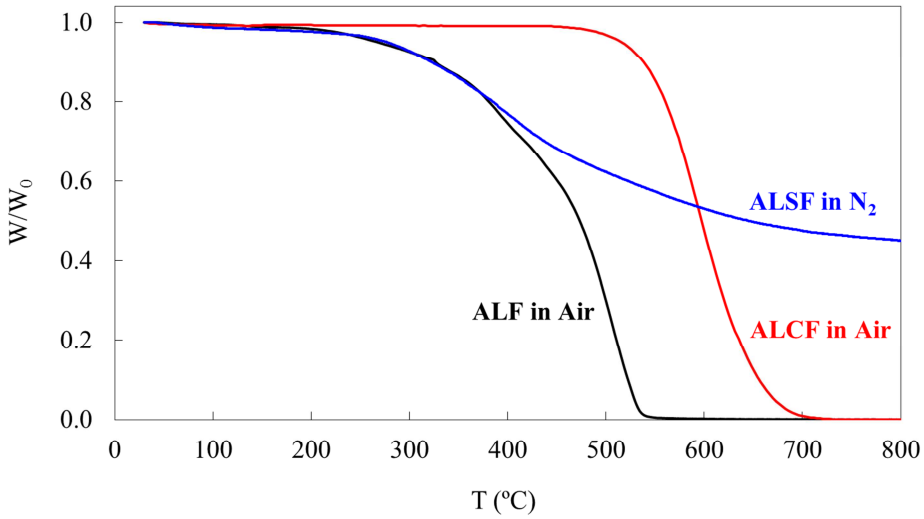

Figure 2.3. Thermogravimetric curves for ALFs and ALCFs in air and for ALSFs in N_2.

2.5.Elemental composition

The heat treatment to 900 °C reduced the oxygen content of the ALSFs, giving rise to a more condensed polynuclear structure with an increase in the carbon content of the ALCFs to 94.3 wt % (Table 2.1), which is comparable to values obtained for Kraft lignin heat-treated under similar conditions [17,18]. The elemental analyses for the ALFs and the ALSFs are shown in Table 2.1. The lignin nanofibers had a slightly higher carbon content (and lower oxygen percentage) than their precursor. Oxidative stabilization of the lignin fibers increased, as expected, the oxygen content of the fiber.

Table 2.1. Elemental analyses of Alcell lignin and lignin-based fibers.

	C (%)	H (%)	O (%)
AL	66.2	6.2	27.6
ALF	68.7	6.3	24.9
ALSF	62.1	3.8	34.1
ALCF	94.3	1.0	4.7

2.6.Surface chemistry

X-ray photoelectron spectroscopy (XPS) analyses were performed to study the chemical composition of the surfaces of the ALFs, ALSFs, and ALCFs. Figure 2.4 presents the C1s spectral region for these nanofibers. The ALFs show a wide band from 288 to 282 eV, centered at approximately 285 eV. The binding energy of 286 eV is associated with C–O bonds of surface functional groups, such as hydroxyl and/or ether moieties, and the main peak at ca. 285 eV corresponds to C–C and C=C groups [19]. The broadening of this band toward lower binding energies may be due to a significant contribution of the C–H bonding in the lignin [20]. The ALSF spectrum shows an increase in the band at 286 eV and a new band centered at 288.6 eV with a small tail near 290 eV. These two binding energies are related to C=O bonds with –COO– bond characteristics of anhydride, carboxylic, and/or ester groups, respectively [19]. The oxygen atomic surface concentration increased with stabilization from 20.2 % in ALFs to 25 % in ALSFs (Table 2.2). These results suggest that stabilization of lignin-based nanofibers produced crosslinking reactions that incorporated carbonyl, carboxylic, anhydride, and ester groups into the structure of the nanofibers [21], which seem to be responsible for maintaining the fibers in the glassy state ($Tg > T$) [7].

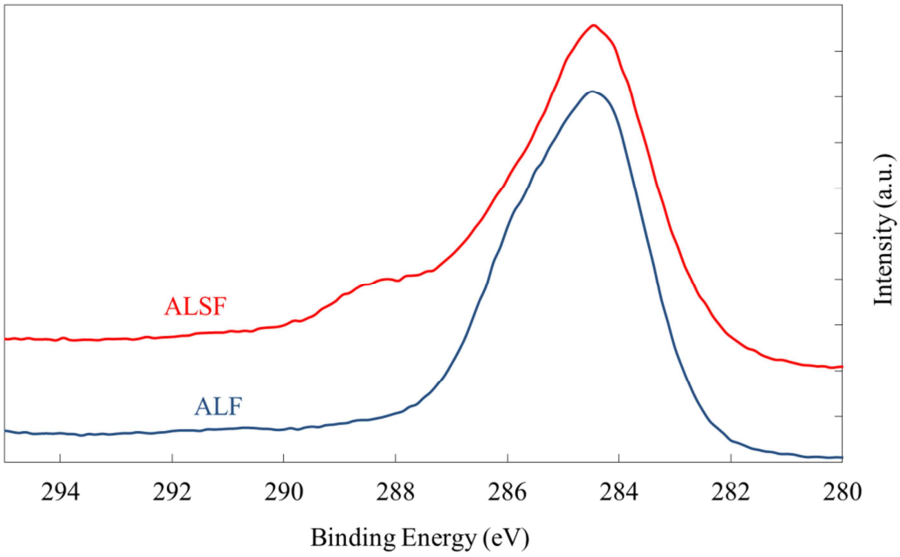

Figure 2.4. XPS C 1s region for ALFs and ALSFs.

Table 2.2. Atomic surface concentration obtained from XPS quantitative analysis for lignin-based fibers.

	C (%)	O (%)
ALF	79.8	20.2
ALSF	75.0	25.0
ALCF	93.1	6.9

2.7.Structural order

Figure 2.5 presents the Raman spectrum of ALCFs. In a previous Raman study with heat-treated carbon obtained from Kraft lignin, the ratio of the intensity of the band in the 1350 cm^{-1} region to the band corresponding to the E_{2g} line I_{1350}/I_{E2g}) decreased significantly as the treatment temperature increased from 1100 to 2800 °C, indicating a lower contribution of structural disorder in the higher-temperature carbons [22]. The I_{1350}/I_{E2g} ratio of 0.85 obtained for ALCFs and the fact that the frequency of the E_{2g} line of 1585 cm^{-1} observed for these carbon nanofibers is in the vicinity of the 1582 cm^{-1} value found for graphite suggests an onset of structural organization in the carbon nanofiber [23], although some disordered carbon is still present.

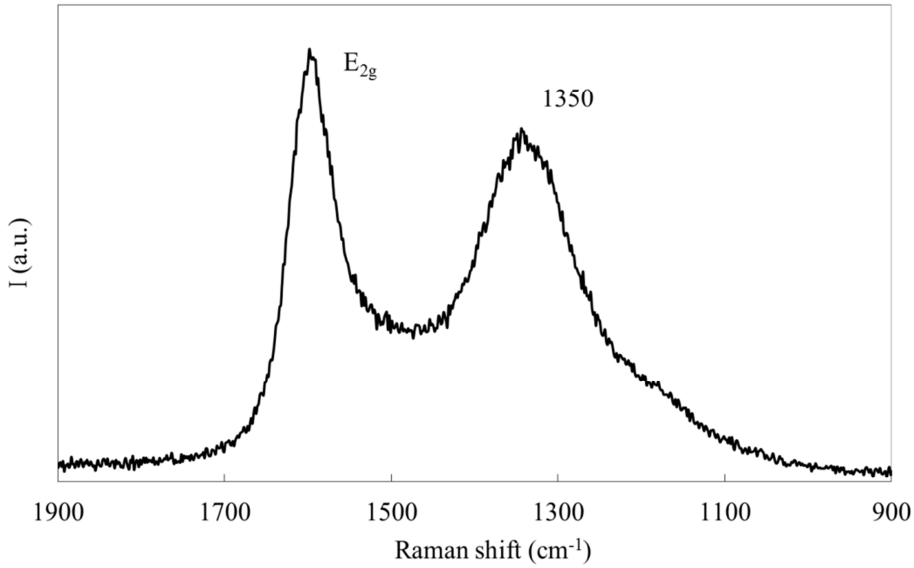

Figure 2.5. Raman spectrum of ALCFs.

2.8.Textural properties

In order to study the porous structure of the carbon nanofiber, N_2 adsorption and desorption and CO_2 adsorption studies were performed. Figure 2.6 represents the adsorption–desorption isotherm of N_2 for ALCFs. The isotherm can be characterized as type I, which is typical of microporous solids (pore sizes smaller than 2 nm). Table 2.3 summarizes the pore structure parameters for the ALCFs, such as Brunauer–Emmett–Teller (BET) specific surface area, $A_{BET\ N2}$, the external surface area, $A_{t\ N2}$, the micropore volume calculated from the N_2 isotherm and the micropore volume, $V_{DR\ CO2}$, and the micropore surface area, $A_{DR\ CO2}$, calculated from the CO_2 isotherm. The CO_2 isotherm covered the relative pressure range up to 0.03, where only narrow micropores of < 0.7 nm were filled. Adsorption of N_2 and CO_2 on the ALFs and ALSFs was almost negligible, indicating that these nanofibers are nonporous solids. The process of carbonization at 900 °C develops narrow microporosity in the fiber structure as a consequence of devolatilization. This behavior was also reported for ground Kraft and Alcell lignins [17,24]. The ALCFs have a BET surface area value of 1200 $m^2\ g^{-1}$ and a micropore volume of 0.488 $cm^3\ g^{-1}$. These values are similar to values obtained for PAN-derived carbon nanofibers prepared by electrospinning [25]. The high values observed for the CO_2 surface area and micropore volume (Table 2.3) indicate that there is a large contribution of micropores smaller than 0.7 nm in the ALCF porous structure.

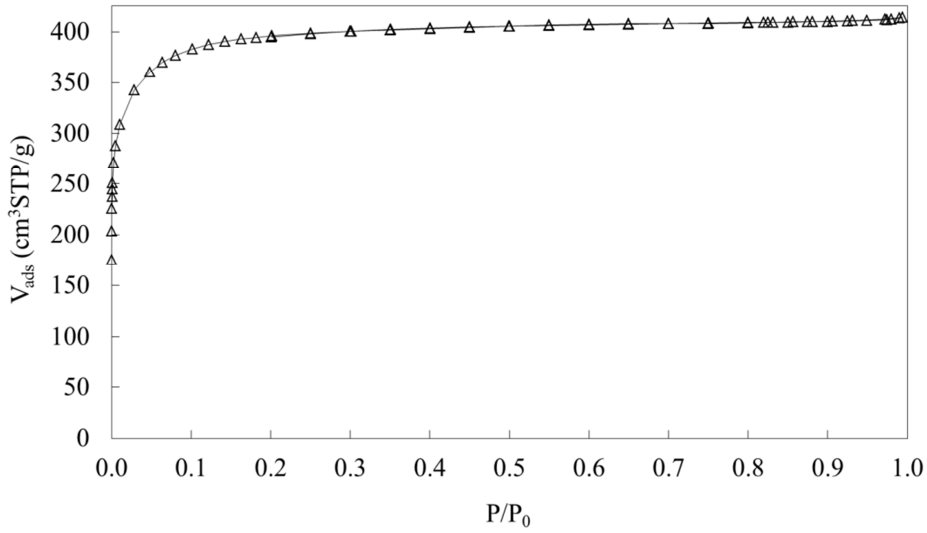

Figure 2.6. N_2 adsorption–desorption isotherm at –196 °C for ALCFs.

Even though ALCF is highly microporous, the thermal treatment at 900 °C improved the oxidation resistance of the fibers. It can be seen from Figure 2.3 that oxidation of the ALCFs began at 550 °C, nearly 300 °C higher than for ALFs. High surface areas and oxidation resistance are key features for many applications, such as catalysis, filtration, adsorption, fuel cells, solar cells, batteries, and tissue engineering [26,27].

2.9.Secondary morphology: carbon nanotubes

To produce Alcell lignin hollow nanofibers (ALHFs), we used the tri-axial spinneret (see Fig. 2.1B). The thermal treatment to produce the Alcell lignin hollow carbon nanofibers (ALHCFs) was optimized to avoid melting; the hollow nanofibers were stabilized by heating at 0.05 °C min^{-1} from room temperature to 200 °C. Carbonization of the stabilized nanotubes occurred at a heating rate of 10 °C min^{-1} from room temperature to 900 °C. Figure 2.7 shows an example of the ALHCFs obtained from this procedure.

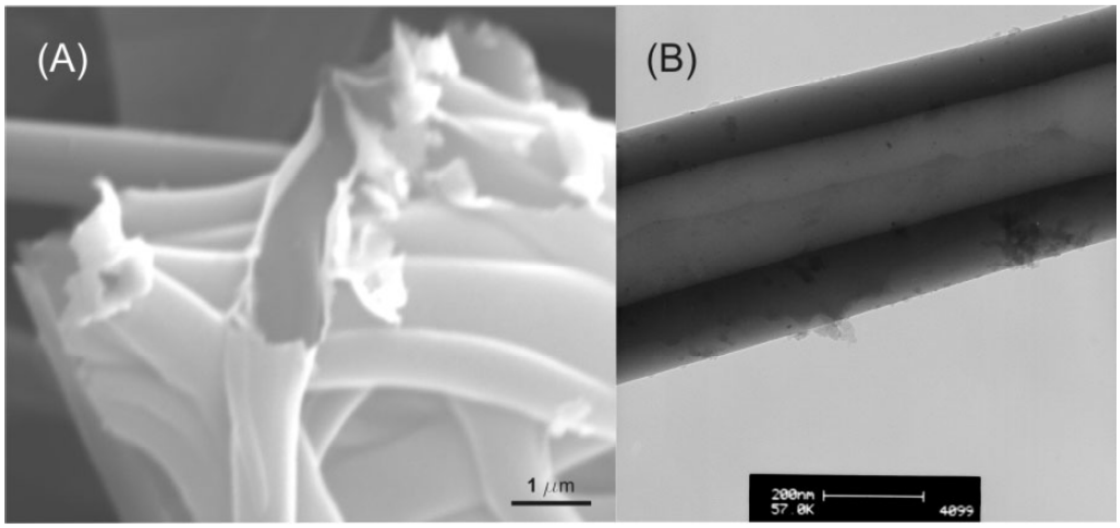

Figure 2.7. Examples of ALHCFs. A) SEM of mechanically broken hollow fibers. B) TEM of one of the hollow carbon fibers

Shape of the hollow channel and wall of these tubes can be controlled just selecting templates oils with different viscosity. Figure 2.8 presents ALHCFs prepared using as template sunflower oil, which has lower viscosity than the previously tested. If the motion of the driving liquid is dominated by surface tension more than by viscosity, recirculating flows appear inside the Taylor cone. Thus, the outer liquid will not totally pull the inner liquid toward the tip, producing dripping flow mode in the inner liquid.

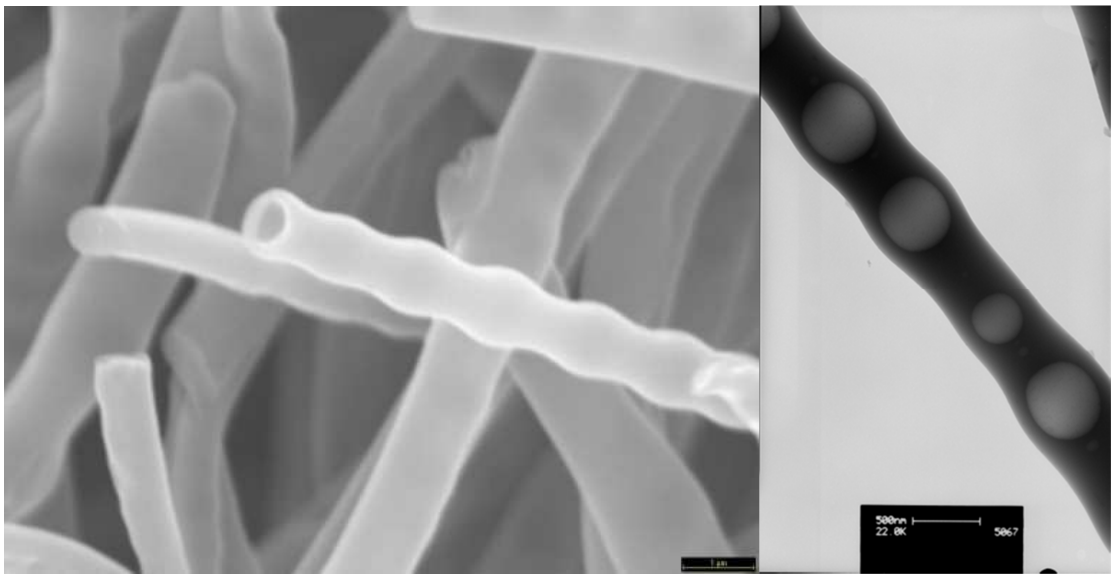

Figure 2.8. ALHCFs prepared with low viscosity oil as template. A) SEM of beaded carbon hollow fibers. Scale bar: 1µm B) TEM of one of the beaded carbon hollow fibers. Scale bar: 500 nm

The size of the wall and the hollow channel are also a tunable feature. Modification of such parameters is possible carefully selecting suitable values of template feed rate to the needle. Figure 2.9 shows ALHCFs prepared with synthetic oil in increased oil flow rates. It is easy to notice how the size of the hollow channel and the fiber diameter increases when higher oil feed rate is set, whereas the lignin shell width is reduced.

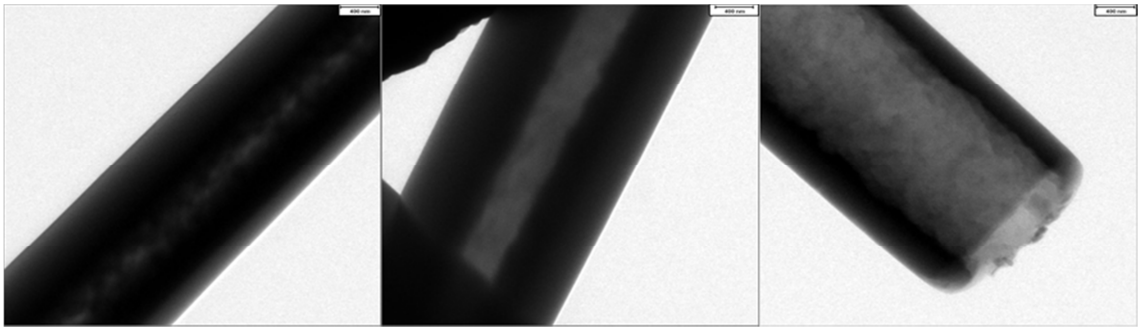

Figure 2.9. ALHCFs obtained at different synthetic oil flow rates. A) Q= 0.2 mL/h B) Q=0.4 mL/h. C) Q=0.6 mL/h. Scale bars: 400 nm

2.10.References

1. W.M. Qiao, M. Huda, Y. Song, S.-H. Yoon, Y. Korai, I. Mochida. Carbon Fibers and Films Based on Biomass Resins. Energy Fuels 2005; 19: 2576-2582.

2. J.H. Lora, W.G. Glasser. Recent industrial applications of lignin: A sustainable alternative to nonrenewable materials. J. Polym. Environ. 2002; 10: 39-48.

3. M. Funaoka. Lignin: its functions and successive flow. Macromol. Symp. 2003; 201: 213-222.

4. S. Kubo, J.F. Kadla. Poly(Ethylene Oxide)/Organosolv Lignin Blends: Relationship between Thermal Properties, Chemical Structure, and Blend Behavior. Macromolecules 2004; 37: 6904-6911.

5. D. Yawalata, L. Paszner. Cationic effect in high concentration alcohol organosolv pulping: The next generation biorefinery. Holzforschung 2004; 58: 7-13.

6. S. Kubo, Y. Uraki, Y. Sano. Preparation of carbon fibers from softwood lignin by atmospheric acetic acid pulping. Carbon 1998; 36: 1119-1124.

7. J.F. Kadla, S. Kubo, R.A. Venditti, R.D. Gilbert, A.L. Compere, W. Griffith. Lignin-based carbon fibers for composite fiber applications. Carbon 2002; 40: 2913-2920.

8. S. Kubo, J.F. Kadla. Effect of Polymer Blending on the Properties of Lignin-based Carbon Fibers. J. Polym. Environ. 2005; 13: 97-105.

9. J.F. Kadla, S. Kubo. Lignin-based polymer blends: analysis of intermolecular interactions in lignin–synthetic polymer blends. Compos. A 2004; 35: 395-400.

10. Although a picture of electrospun fibers from a mixure of Kraft liginin and poly(ethylene oxide) PEO is shown at http://www.cfr.ncsu.edu/wps/pp/Gradprograms/dfafbm_details.htm, which is a report of the Department of Wood and Paper Science. Fiber and Wood Engineering Fellows Program, North Carolina State University, we have not found any published paper disclosing such results.

11. S. Brunauer, P.H. Emmett, E. Teller. Adsorption of Gases in Multimolecular Layers. J. Am. Chem. Soc. 1938; 60: 309-319.

12. B.C. Lippens, J.H. de Boer. Studies on pore systems in catalysts: V. The t method. J. Catal. 1965; 4: 319-323.

13. M.M. Dubinin, E.D. Zaverina, L.V. Radushkevich. Russ. J. Phys. Chem. 1947; 21: 1351-1362.

14. I.G. Loscertales, A. Barrero, I. Guerrero, R. Cortijo, M. Marquez, A. M. Gañan-Calvo. Micro/Nano Encapsulation via Electrified Coaxial Liquid Jets. Science 2002; 295: 1695-1698.

15. I.G. Loscertales, A. Barrero, M. Márquez, R. Spretz, R. Velarde-Ortiz, G. Larsen. Electrically Forced Coaxial Nanojets for One-Step Hollow Nanofiber Design. J. Am. Chem. Soc. 2004; 126: 5376-5377.

16. E. González-Serrano, T. Cordero, J Rodríguez-Mirasol, J.J. Rodríguez. Development of Porosity upon Chemical Activation of Kraft Lignin with ZnCl2. Ind. Eng. Chem. Res. 1997, 36, 4832-4838.

17. J. Rodríguez-Mirasol, T. Cordero, J.J. Rodríguez. CO2-Reactivity of eucalyptus wood chars. Carbon 1993; 31: 53-61.

18. J. Rodríguez-Mirasol, T. Cordero, J.J. Rodríguez. Preparation and characterization of activated carbons from eucalyptus kraft lignin. Carbon 1993; 31: 87-95.

19. H. Darmstadt, C. Roy, S. Kaliagune. ESCA characterization of commercial carbon blacks and of carbon blacks from vacuum pyrolysis of used tires. Carbon 1994; 32: 1399-1406.

20. J.F. Kadla, S. Kubo. Miscibility and hydrogen bonding in blends of poly(ethylene oxide) and kraft lignin. Macromolecules 2003; 36: 7803-7811.

21. J.L. Braun, K.M. Holtman, J.F. Kadla. Lignin-based carbon fibers: Oxidative thermostabilization of kraft lignin. Carbon 2005; 43: 385-394.

22. J. Rodríguez-Mirasol, T. Cordero, J. J. Rodríguez. High-temperature carbons from kraft lignin. Carbon 1996; 34: 43-52.

23. P. Lespade, A. Marchand, M. Couzi, F. Cruege. Characteristics of carbon materials by Raman microspectrometry. Carbon 1984; 22: 375-385.

24. C. Pedrero, T. Cordero, J. Rodríguez-Mirasol, J. J. Rodríguez, in Proc. of the 6th Int. Symp. on the Characterization of Porous Solids (Eds. F. Rodríguez-Reinoso, B. McEnaney, J. Rouquerol, K. K. Unger), Elsevier Science, New York 2002.

25. W.G. Shim, C. Kim, J.W. Lee, J. J. Yun, Y. I. Jeong, H. Moon, K.S. Yang. Adsorption characteristics of benzene on electrospun-derived porous carbon nanofibers. J. Appl. Polym. Sci. 2006; 102: 2454-2462.

26. D. Li, Y. Xia. Electrospinning of Nanofibers: Reinventing the Wheel? Adv. Mater. 2004; 16: 1151-1170.

27. J.T. McCann, B. Lim, R. Ostermann, M. Rycenga, M. Marquez, Y. Xia. Carbon nanotubes by electrospinning with a polyelectrolyte and vapor deposition polymerization. Nano Lett. 2007; 7: 2470-2474.

3. THE PRODUCTION OF SUBMICRON DIAMETER CARBON FIBERS BY THE ELECTROSPINNING OF LIGNIN

3.0.Abstract

Lignin fibers with and without platinum were synthesized in a single step by electrospinning of lignin/ethanol/platinum acetyl acetonate and lignin/ethanol solutions, respectively. The fibers obtained were stabilized in air at low temperature to avoid fiber fusion during the subsequent carbonization process. The effect of the carbonization temperature (600-1000 ºC) on surface chemistry, morphology, textural properties and oxidation resistance of the final carbon fibers was studied. The carbonization process decreased the oxygen content of the fibers, increasing the carbon and surface platinum proportion and producing a well developed microporous structure. Carbon fibers with and without platinum with apparent surface areas of 1178 and 1195 m^2/g, respectively, and micropore volumes of around 0.52 cm^3/g were obtained. The diameter of the carbon fibers obtained is in the range of 400 nm to 1 µm. Carbon fibers with surface platinum of 0.6% in weight were obtained. The carbon fibers with and without platinum showed high oxidation resistance despite their highly developed porous structure.

3.1. Introduction

Carbon fibers have become materials that are of great technological and industrial importance because of their unique chemical, electrical, magnetic, and mechanical properties [1,2].Fossil pitches and polyacrylonitrile (PAN) are widely used as precursors for the carbon fiber production and their choice is dictated by the end application of the carbon fiber. PAN-based carbon fibers exhibit the highest tensile strengths whereas pitch-based carbon fibers exhibit high modulus and high thermal conductivity. Renewable sources of carbon have also been studied as carbon-fiber precursors [3]. Lignin is the second most abundant polymer in nature after cellulose. This natural, aromatic (phenolic), heterogeneous bio-macromolecule exists in the cell wall of plants. It is obtained, also, as a co-product of the papermaking industry [4].The low cost and high availability of lignin have brought interest on its use as precursor of carbonaceous materials like activated carbons [5,6,7,8] carbon catalysts [9] or composite materials [10,11].

The use of lignin as a precursor for carbon fibers has been previously reported [12,13]. The lignin glass transition temperature is much lower than the decomposition temperature, as it happens with most of carbon fiber precursors, thus a pretreatment must be performed to avoid fiber softening and fusion. Braun et al [14] suggested air oxidation at low heating rates as a simple and low cost method of thermostabilization. After the thermal stabilization, the fibers are usually carbonized to yield carbon fibers. The use of blends that contain lignin and synthetic polymers improved melt extrusion to produce fibers. These blends after a proper thermal treatment yielded carbon fibers with sizes ranged from 80 to 30 μm [15]. Smaller diameters were difficult to obtain because of the inherent limitations (i.e., clogging) of the melt-extrusion process used to draw the fibers and to the particulate impurities present in the lignin.

An interesting application of the carbon fibers is their use as support of metal active catalysts (i.e. platinum) for catalytic oxidation [16], hydrogenation and dehydrogenation [17] reactions and hydrogen storage for fuel cell applications [18]. Incipient wetness is a conventional way to deposit the metal phase on the carbon fiber surfaces. However, the closure of the micropores by the deposition of the metal particles and the insufficient penetration of the precursor solution in the inner of the micropores are significant drawbacks of this method. Besides, additional thermal treatment steps are usually necessary to assure the anchorage of the metal phase to the carbon fiber surface [19].

In this work we present a simple and straightforward experimental method [20] for obtaining lignin submicrofibers with and without platinum by co-electrospinning lignin solutions at room temperature without any added polymer and in a single step. The lignin submicrofibers were thermally air stabilized and carbonized to generate carbon submicrofibers. We also report the effect of the carbonization temperature on surface chemistry, morphology, textural properties and oxidation resistance of the carbon submicrofibers obtained.

3.2. Experimental

3.2.1. Electrospinning

Alcell® lignin was used as precursor of the carbon fibers. In contrast to Kraft lignin, Alcell lignin contains very small amounts of inorganic materials because of the different pulping process (organosolv process) used. In this process ethanol is used as the delignifying agent and lignin solvent, and lignin is obtained as a sulfur-free, fine, brown powder [21]. Alcell lignin fibers (ALF) and Alcell lignin fibers doped with platinum (ALFPt) were synthesized by electrospinning of Alcell lignin solutions [20]. For ALF a spinnable solution of lignin and ethanol with weight ratio 1:1 was used, whereas for ALFPt spinnable solutions of lignin, ethanol and platinum acetyl acetonate with weight ratios 1:1:0.002 and 1:1:0.004 were prepared. The action of the electric field over a drop forming at the tip of a capillary change its shape into a charged conical meniscus known as the Taylor cone [22]. In our configuration while the solution comes through the central capillary tip, pure ethanol flows by the outermost, feeding the Taylor cone with enough solvent to compensate losses due evaporation and avoiding the solidification of the Taylor cone. Parameters such as viscosity, flow, concentration of electrospun solution or applied voltage control diameter and length of fibers. In fact, it is possible to switch between steady electrospray and electrospinning controlling rate flow between outer and inner solutions, which allows encapsulating of core liquid [23,24]. Ethanol and lignin solution flow rates were 0.06 and 0.8 mL/h, respectively. To apply the high voltage between the spinneret and the collector, two high voltage power supplies were used: one positively polarized connected to the needle and the other negatively polarized attached to a collector. This configuration provided better electrostatic conditions to prevent fibers from flying to any grounded piece near the set-up, therefore facilitating the deposition of the electrospun fibers on the collector. The tip-to-collector distance was 20–25 cm, and the electrical potential difference was 12 kV (the collector was at –6 kV and the tips at +6 kV), although this value varied depending on the collector/tip geometry.

3.2.2. Thermostabilization and carbonization

The Alcell lignin fibers with and without Pt (ALFPt and ALF, respectively) were thermostabilizied in a tubular furnace under an oxidizing atmosphere (150 cm^3 STP/min of air). The fibers were heated from room temperature up to 200 ºC at a heating rate of 0.05 ºC/min, maintaining the final temperature (200 ºC) for 36 hours. The stabilized fibers with and without Pt (ALFSPt and ALSF, respectively) were subsequently carbonized in the same tubular furnace with a flow of N_2 (150 cm^3 STP/min, Air Liquide, Alphagaz® 1, purity of 99.999%, with amounts of oxygen and water lower than 2 and 3 ppm, respectively) at different temperatures, from 600 to 1000 ºC. The heating rate in the carbonization stage was 10 ºC/min. Carbon fibers obtained with and without Pt were denoted by ALCFPt and ALCF, respectively, followed by the carbonization temperature in degrees Celsius. The carbon fibers with higher platinum load, those obtained by electrospinning of a more concentrated lignin/ethanol/platinum acetyl acetonate solution with weight ratio 1:1:0.004 and carbonized at 900 ºC, are denoted as ALCFPt-900b.

3.2.3. Characterization

Carbonization of the Alcell lignin fibers was studied in a thermogravimetric system (CI Electronics). The amounts of CO and CO_2 evolved from the carbonization experiments were monitored by NDIR analyzers (Siemens; ULTRAMAT 22 model). A mass spectrometer (OmnistarTM, Pfeiffer Vacuum) was used to analyze the evolved gas concentrations of H_2 and H_2O. The surface morphology was studied by scanning electron microscopy (SEM) using a JSM 840 JEOL microscope working at 25 KV voltage and by transmission electron microscopy (TEM) in a Philips CM200 microscope at an accelerating voltage of 200 kV. Particle size distribution of the fibers with high platinum content was obtained by counting between 100 and 200 particles. The size distribution was fitted to a normal distribution. From the size distribution, we determined the number average diameter $d_n = \sum n_i d_i / \sum n_i$ [25]. Platinum particle size (supposing spherical particles) and dispersion (D) are related by $D = 108/d_n$ (nm) [26]. Raman spectra were recorded with a RENISHAW micro-Raman system using an Ar^+ laser at 514 nm as the excitation source with a spectral resolution of 2 cm^{-1}.

The porous structure was characterized by N_2 adsorption-desorption at -196 ºC and by CO_2 adsorption at 0 ºC, carried out in a Micromeritics ASAP2020 and a Quantachrome Autosorb-1 apparatus, respectively. Samples were previously outgassed for 8 hours at 150 ºC under vacuum. From the N_2 adsorption/desorption isotherm, the apparent surface area (A_{BET}) was calculated by applying the BET equation, and the micropore volume (V_t) and the external surface area (A_t) were calculated using the t-method. The narrow micropore volume (V_{DR}) was estimated using the expression of the Dubinin-Radushkevich adsorption isotherm, as well as characteristic energy (E_0) and optimized Dubinin-Astakhov exponent (n) of the Dubinin-Astakhov equation. The three parameters were obtained from the CO_2 adsorption isotherm.

The surface chemistry of the samples was studied by X-ray photoelectron spectroscopy (XPS) analysis. XPS analyses of the carbons were obtained using a 5700C model Physical Electronics apparatus with MgKα radiation (1253.6 eV). For the analysis of the XPS peaks, the C1s peak position was set at 284.4 eV and used as reference to locate the other peaks. The fitting of the XPS peaks was done by least squares using Gaussian-Lorentzian peak shapes. The oxidation resistance of the carbon fibers was evaluated using thermogravimetric analysis (TG) performed in a CI Electronics MK2 balance under N_2 and air flow (150 cm^3 STP/min) from room temperature to 900 ºC at a heating rate of 10 ºC/min with a sample weight of about 10 mg.

3.3. Results and Discussion

3.3.1. Preparation yields

Table 3.1 reports the yields of the stabilization and carbonization stages of the Alcell lignin fibers with and without platinum. Both fibers show very similar stabilization yields. Weight loss can be ascribed to condensation and dehydration reactions involved in the cross-linking between lignin polymeric chains and to evaporation of occluded ethanol while heating. In a lesser extent it can also be due to elimination reactions which involve release of CO and CO_2. Taking into account that lignin presents an already oxidized structure, a low oxygen gain is expected during the stabilization step. Carbonization yields decrease with increasing carbonization

temperature, due to the progressive loss of volatile matter and are slightly higher for the fibers without platinum than those with platinum.

Table 3.1. Yields of the stabilization and carbonization treatments.

Sample	Stabilization treatment (w%)	Carbonization treatment (w%)			
		600 ºC	800 ºC	900 ºC	1000 ºC
ALF	76.0	47.8	41.2	39.0	36.1
ALFPt	76.8	46.3	40.8	38.7	34.3

3.3.2. Carbonization products

Lignin presents aromatic rings with a wide range of activity due to the different chemical bonds, which results in a wide decomposition temperature range [27]. The main weight-loss for ALSF takes place within a relatively narrow temperature range (250-450 ºC), with the maximum mass loss rate at about 380 ºC (see information in Supplementary Material). The amounts of H_2O, CO, CO_2 and H_2 desorbed from the fibers during heating are represented in Figure 3.1. The amount of H_2O, CO and CO_2 is due to the decomposition of the large amount of hydroxyl groups and oxygen atoms present in lignin polymers. The H_2O profile ranges from about 100 up to 600 ºC, indicating the multiple origin of water. The H_2O desorbed at low temperatures is related to the loss of humidity of the samples, whereas the water evolved at higher temperatures is associated to the decomposition of the hydroxyl groups of the polymeric constituents [28]. The CO_2 release can be formed probably through the release of COOH groups or the rupture C-O groups during the lignin degradation, producing also H_2O [27,29]. The broad curve of CO up to high temperatures can be related to the char formation reactions [28] and to the cracking of carbonyl (C-O-C) and carboxyl (C=O) groups [27]. Release of H_2 at high temperatures is observed probably due to the depolymerization of the abundant phenyl groups of the lignin or the secondary reactions between heavy molecular hydrocarbon liquids and the light hydrocarbon gases in the evolving volatiles [30].

3.3.3. Fiber morphology

Figures 3.2a to d show SEM micrographs of ALFPt, ALSFPt, ALCFPt-600 and ALCFPt-900, respectively. The electrospun fibers diameter is between 800 nm and 3

µm. The stabilization stage avoided fiber fusion without modification of the fiber size as clearly seen in Figure 3.2b. In contrast, fiber size decreases with increasing carbonization temperature. The diameter of the fiber carbonized at 900 ºC is in the range of 400 nm to 1 µm (Figure 3.2d). The behavior of the Alcell lignin fibers without platinum is very similar [20].

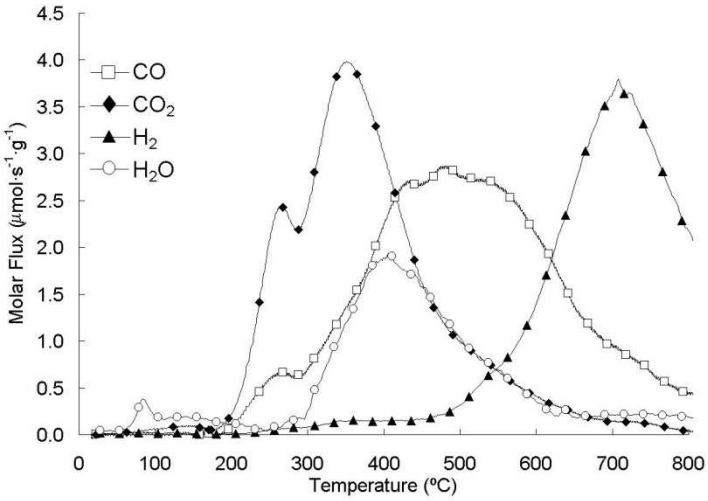

Figure 3.1. Amounts of H_2O, CO, CO_2 and H_2 desorbed from ALSF fibers during heating in inert atmosphere.

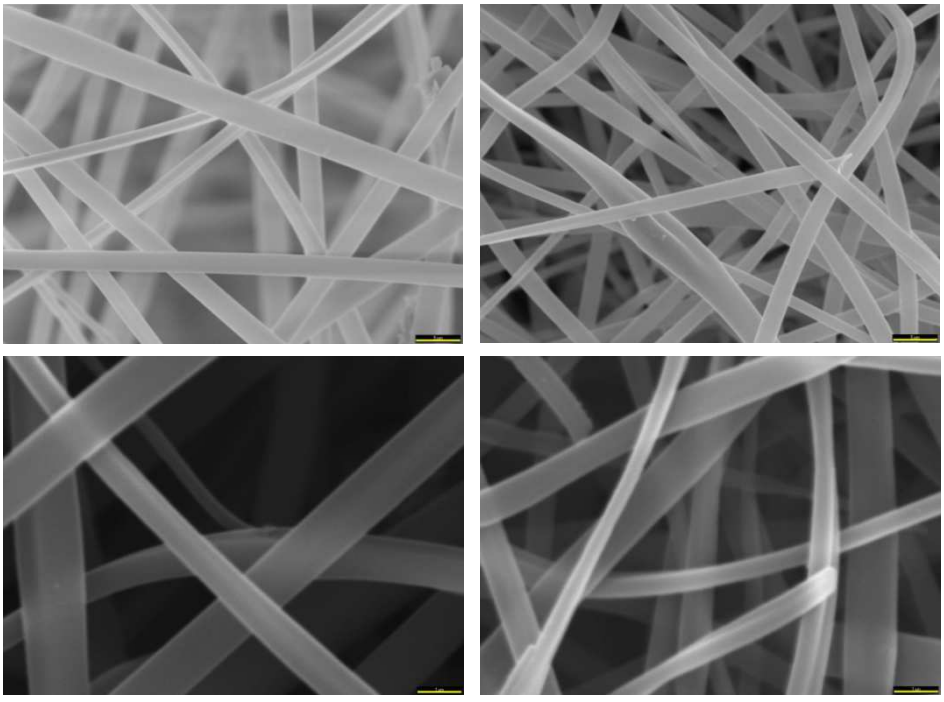

Figure 3.2. SEM micrographs of (a) ALFPt (bar length: 5 µm), (b) ALSFPt (bar length: 5 µm), (c) ALCFPt-600 (bar length: 1 µm) and (d) ALCFPt-900 (bar length: 1 µm).

Figures 3.3a to c represent TEM images of ALCF-900, ALCF-1000 and ALCFPt-900b, respectively. The fibers show an apparent smooth surface with absence of defects. The fiber without platinum carbonized at 900 ºC shows a diameter of around 500 nm (Figure 3.3a). Figure 3.3b shows a more detailed image of the ALCF-1000. No defects were observed in the fiber surface, which seems very smooth. TEM micrograph of ALCFPt-900b (Figure 3.3c) shows well dispersed platinum particles with sizes in the range of less than 10 nm to about 25 nm. The platinum particle size distribution of the carbon fibers with high platinum content have been fitted to a normal distribution with mean μ = 10.25 ± 0.54 nm and standard deviation σ = 2.95 ± 0.26, resulting in a platinum dispersion of 10.53 %.

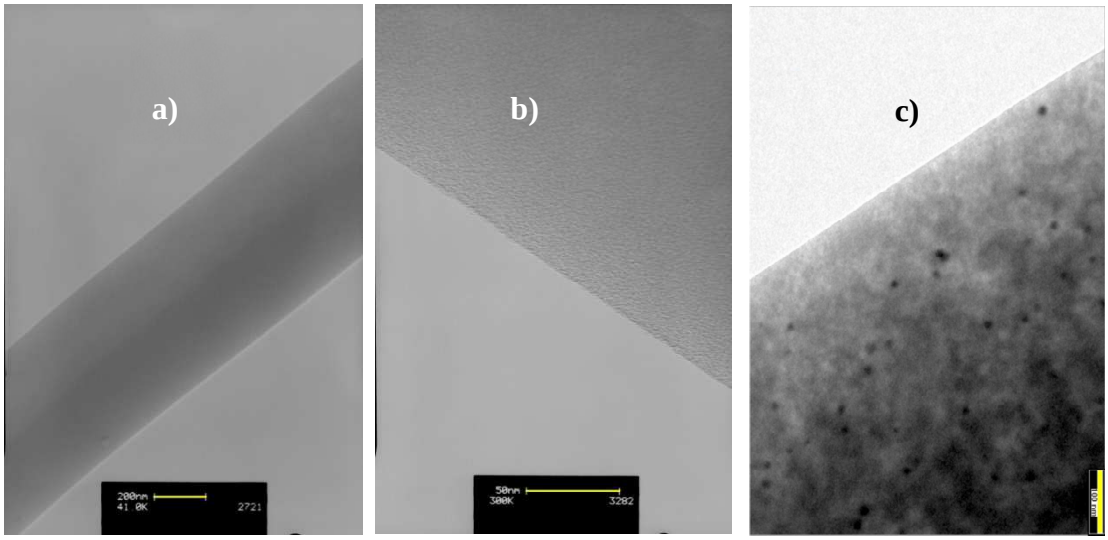

Figure 3.3. TEM images of (a) ALCF-900 (bar length: 200 nm), (b) ALCF-1000 (bar length: 50 nm) and (c) ALCFPt-900b (bar length: 100 nm).

3.3.4. Surface chemistry

X-ray photoelectron spectroscopy (XPS) analyses were performed to the different fibers to study their surface chemical composition (Results are shown in the Supplementary Material). The stabilization process increases the amount of all oxygen surface groups by the oxidation of the fiber surface, especially those corresponding to carbonyl groups. The carbonization process, however, produces a decrease in the amount of the oxygen surface groups, which evolve as CO and mainly as CO_2 (Figure 3.1). Lignin fiber carbonized at 600 ºC, ALCF-600, shows still a significant amount of carboxylic acid groups with lower amounts of phenol and carbonyl groups. However, an

increase of the carbonization temperature results in a clear reduction of the amount of surface oxygen groups of the carbon fibers.

Figure 3.4 displays the Pt 4f spectra for the Pt containing stabilized and carbonized fibers. The Pt 4f region of the spectra for these fibers presents a doublet corresponding to Pt $4f_{7/2}$ and Pt $4f_{5/2}$ [31]. The separation between Pt $4f_{7/2}$ and Pt $4f_{5/2}$ peaks, due to spin orbital splitting, is a quantized value of 3.33 eV. The Pt $4f_{7/2}$ peak lying at around 71.5 eV can be attributed to Pt^0 (metallic Pt), while the Pt $4f_{7/2}$ peak located at around 73.0 eV is related to Pt^{2+} (electrodeficient platinum) [31]. The stabilized fibers present most of the platinum in form of Pt^{2+}, probably due to the oxidation of the platinum species during the stabilization treatment in air at 200 ºC. The carbonization process produces an increase and a shift of the peaks to lower binding energies, which indicate the presence of a higher contribution of Pt in form of Pt^0 on the surface of the carbonized fibers. This result suggests that during carbonization of the stabilized fibers electrodeficient platinum is reduced to metallic platinum by the carbon surface.

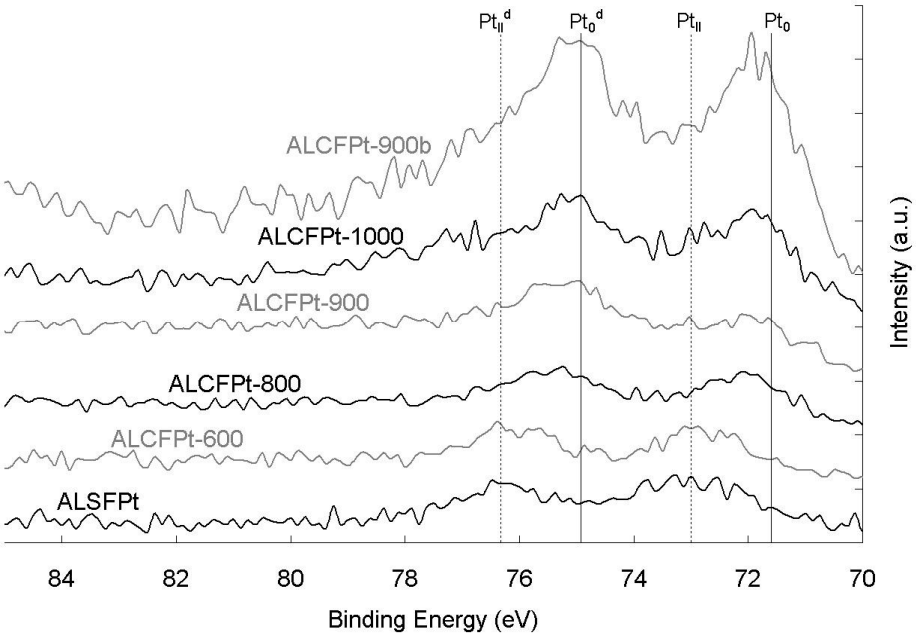

Figure 3.4. Pt 4f spectra for the stabilized and carbonized fibers with platinum.

Table 3.2 summarizes the mass surface concentration obtained by XPS and the ultimate analysis of the different lignin-derived fibers analyzed in this work. The stabilization process, as expected, increased the oxygen content of the fibers due to the

oxidation reaction that produces carbonyl, carboxylic, anhydride and ester groups on the fiber surface [14], which seem to be responsible of maintaining the fibers in the glassy state ($T<T_g$) [12]. Carbonization of the stabilized fibers produces an increase of the carbon proportion. Higher carbonization temperatures yielded fibers with higher carbon and lower oxygen percentages. The amount of hydrogen decreased with the carbonization temperature due to the aromatic condensation process [32]. The amount of surface Pt also increased with the carbonization. Amounts of surface Pt up to 0.32% were obtained for the fibers carbonized at 1000 ºC. Table 3.2 summarizes (in brackets) the estimated global amount of platinum of the stabilized and carbon fibers obtained from the amount of platinum used in the formulation of the lignin fibers and taking into account the carbonization yield. As can be seen, there is a good correlation between the amount of surface platinum obtained by XPS and the estimated global amount of platinum. This suggests that platinum is homogeneously dispersed on the surface of the carbon fibers. The maximum amount of platinum is obtained for ALCFPt-900b, which shows about twice surface platinum than ALCFPt-900, obtained at the same carbonization temperature. The content of platinum measured by EDAX (not show) is 0.5% for ALCFPt-900b, very similar to that obtained by XPS and that calculated based in the amount of platinum used in the formulation of the fibers.

Table 3.2. Mass surface concentration obtained by XPS quantitative analysis and ultimate analysis of the different fibers.

	XPS			Ultimate analysis			
Sample	C (%)	O (%)	Pt (%)	C (%)	H (%)	N (%)	O (%)
ALF	72.9	27.1	--	71.2	5.2	0.3	23.3
ALSF	67.4	32.6	--	63.3	2.8	1.2	32.8
ALCF-600	91.5	8.5	--	87.1	1.4	0.5	11.0
ALCF-800	93.9	6.1	--	90.2	1.1	0.6	8.1
ALCF-900	94.8	5.2	--	94.3	1.0	0.5	4.2
ALCF-1000	96.2	3.8	--	95.0	0.7	0.7	3.6
ALFPt	74.3	25.6	0.1 (0.10)	65.0	5.7	0.2	27.7
ALSFPt	67.4	32.5	0.1 (0.10)	59.4	4.0	0.5	35.6
ALCFPt-600	93.0	6.8	0.2 (0.21)	89.8	2.2	0.6	7.4
ALCFPt-800	94.4	5.4	0.2 (0.24)	90.8	1.1	0.6	8.6
ALCFPt-900	95.5	4.3	0.2 (0.26)	92.5	0.9	0.3	6.3
ALCFPt-1000	96.5	3.2	0.3 (0.29)	94.7	0.8	0.5	4.0
ALCFPt-900b	94.8	4.7	0.6 (0.63)	--	--	--	--

3.3.5. Structural order

The first order Raman spectra of carbonized fibers with and without platinum are represented in Figure 5S of Supplementary Material. The spectra show the typical features of carbon materials with two broad and overlapping bands at about 1340 cm^{-1} and 1590 cm^{-1}, the former being associated to the E_{2g} vibration mode of the a ideal graphitic lattice, and the latter being usually referred as D band, which is characteristic for disordered carbon [33,34]. The relationship between both bands intensities is largely employed in literature as a measure of structural order. More band parameters, like the width of the D or G band, are also correlated to the structural disorder [35,36]. Deconvolution of the spectra reveals the presence of other bands on the vicinity of 1170 and 1515 cm^{-1}, which are ascribed to oxygen superficial groups and/or ions impurities, i.e. platinum, and interstitial defects, respectively [35,36]. They are clearly visible on the deconvoluted spectra of lignin fiber carbonized at 900ºC, presented in Figure 3.5.

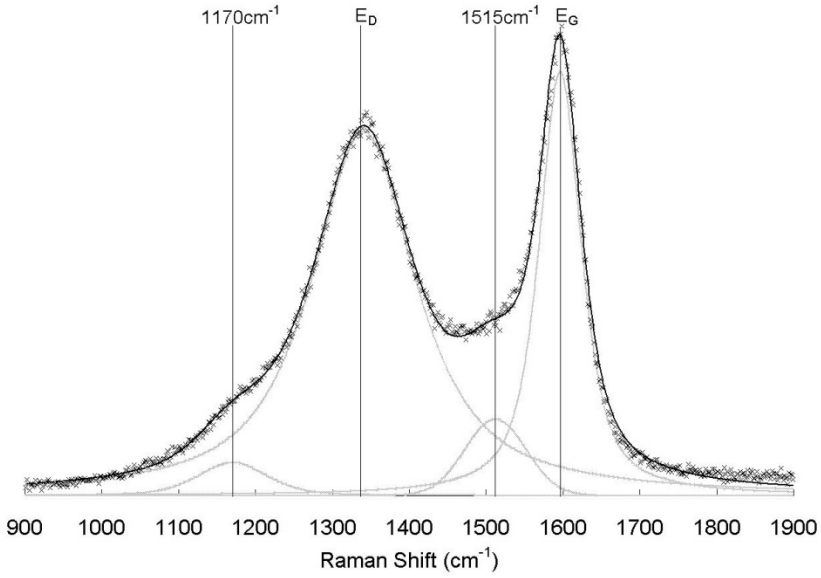

Figure 3.5. First order Raman deconvoluted spectra of ALCF-900 lignin fiber.

Table 3.3 compiles the intensity of G (I_G) and 1170 cm^{-1} (I_{1170}) bands related to the total integrated intensity of the spectra (I_T), and the full width at half maximum of D and G bands, W_D and W_G, respectively, for all carbonized fibers. The increase of the carbonization temperature from 600 to 900 ºC for the fibers without platinum causes a narrowing of D and G band, accompanied by a more intense G band signal. These facts suggest a lower contribution of structural disorder for the carbons fibers obtained at

higher carbonization temperatures [37]. The degree of structural organization on these samples is superior to those reported for pitch-based carbon fibers prepared at similar temperatures [36]. Platinum carbon fibers follow the same trend with temperature, but show higher values of W_D and a lesser intense G band signal than those carbon fibers prepared at the same temperature. It has to be pointed out the low differences in structural ordering between fibers with and without platinum. The presence of well dispersed Pt particles on the structure of the fibers could hinder the orientation of the graphene layers during the carbonization process. The slightly higher total amount of oxygen in carbon fibers containing platinum may also results in a lower structural ordering than that corresponding to the platinum free carbon fibers. As expected, the carbon fibers with the most platinum, ALCFPt-900b and ALCFPt-1000, show the most intense 1170 cm^{-1} band.

Table 3.3. Parameters obtained from deconvolution of first order Raman spectrum of carbon fibers.

Sample	I_G/I_T (%)	I_{1170}/I_T (%)	W_D (cm^{-1})	W_G (cm^{-1})
ALCF-600	24.0	2.2	239.5	75.6
ALCF-800	25.0	2.4	218.1	77.7
ALCF-900	30.2	3.8	162.5	65.5
ALCF-1000	27.9	3.1	196.3	74.6
ALCFPt-600	23.5	2.9	239.5	78.1
ALCFPt-800	25.5	2.8	226.4	78.0
ALCFPt-900	25.5	3.3	211.3	72.5
ALCFPt-900b	25.8	5.6	197.2	71.2
ALCFPt-1000	26.5	4.5	162.1	65.1

3.3.6. Textural properties

Figures 3.6 a and b show the N_2 adsorption-desorption isotherms at -196 ºC for the fibers carbonized at different temperatures without and with platinum, respectively. The fresh and the stabilized lignin fibers, with and without platinum, adsorbed a negligible amount of N_2 indicating very poor developed porous structures. Regarding the other carbon fibers, all of them exhibit isotherms essentially of type I, typical of microporous solids, with a sharp increase of N_2 uptake at very low relative pressures

and the appearance of a plateau at higher relative pressures [38]. Desorption branch of all samples follows the corresponding adsorption curve at low relative pressures, pointing out the absence of irreversible adsorption, typical of constrained microporosity. The carbonization process produces a substantial microporosity development, as a consequence of the loss of volatile matter. The amount of N_2 adsorbed increased in the range of low relative pressure with carbonization temperature except for the fiber without platinum carbonized at 1000 ºC, which shows a significant decrease in the amount of N_2 adsorbed if compared to that of the fiber carbonized at 900 ºC. This high carbonization temperature could produce a solid reorganization resulting in a shrinkage of the porous structure of the carbon fiber [37,39]. ALCFPt-1000 is the only sample that shows a small hysteresis loop beyond 0.4 relative pressures, indicating the presence of some mesoporosity. The knee at low relative pressures broadened as carbonization temperature increases, indicating a widening of the microporosity. The carbon fiber with the higher platinum content, ALCFPt-900b, shows a similar adsorption-desorption isotherm than that observed for the carbon obtained at the same carbonization temperature with a lower amount of platinum, ALCFPt-900. This suggests that the increase in the amount of platinum of the fiber has limited influence on the porous structure development.

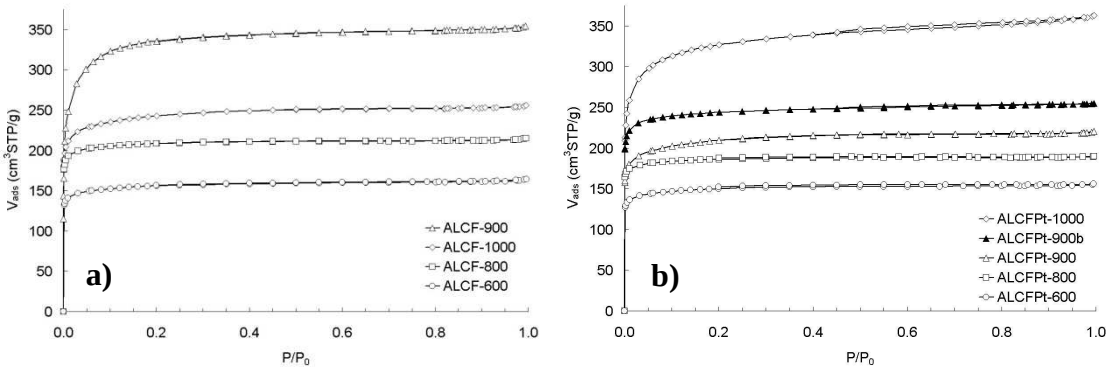

Figure 3.6. N_2 adsorption-desorption isotherms at -196 ºC for the carbonized fibers (a) without platinum and (b) with platinum.

Table 3.4 reports the porous structural parameters of the carbon fibers obtained from the N_2 adsorption-desorption isotherms and from the CO_2 adsorption isotherms. Alcell lignin fibers, ALF, have a very low A_{BET}. However, these fibers present adsorption of CO_2 at 0 ºC, from which a micropore volume of 0.027 cm^3/g, is obtained. This result indicates the presence of narrow microporosity inaccessible to N_2 at -196 ºC,

but accessible to CO_2 at 0 ºC that adsorbs only in narrow micropores of size lower than 0.7 nm [40]. Stabilization of lignin fibers increases the narrow micropore volume, V_{DR}^{CO2}, with no noticeable increase of the A_{BET}. This increase could be associated to the oxidation of the lignin fiber during the stabilization process in air. Despite the stabilization is performed at low temperature (up to 200 ºC), thermogravimetric analyses of Alcell lignin fibers previously reported [20] have shown that these fibers begin to oxidize at temperatures as low as 200 ºC, resulting in a slight oxidation of the lignin fibers. Furthermore, at the low temperature, oxidation reaction is chemically controlled rather than diffusionally controlled. This way, oxygen molecules could diffuse to the narrow micropore surface, where the gasification takes place, increasing the narrow micropore volume. The apparent surface area is significantly increased during the carbonization step, with values of 1195 and 1178 m^2/g obtained for ALCF-900 and ALCFPt-1000, respectively. It is noticeable the high surface areas and micropore volumes obtained for these fibers, comparable to those of commercial activated carbon products and certainly much greater than that observed for chars not submitted to an activation process. The high oxygen content of the lignin fibers after the stabilization process (about 33%w according to the ultimate analysis) could act as activating agent during the subsequent carbonization process, producing a large development of porosity. The low A_t/A_{BET} ratio values observed for all samples indicate the lack of mesoporous structure. The n value reflects the width of the energy distribution and is related to the pore size distribution. Values of n between 1 and 4 are characteristic of most carbon adsorbents, values of $n>2$ are related to molecular sieve carbons or carbon adsorbents with highly homogeneous and small micropores, whereas $n<2$ is found for strongly activated carbons and heterogeneous micropore carbons [41]. The carbon fibers obtained shown values higher than 2 at low carbonization temperatures and lower than 2 at high carbonization temperatures. This indicates that the increase of the carbonization temperature results in carbon with a more heterogeneous narrow micropore structure. In general trend, the E_0 value decreases with the carbonization temperature due to the enlargement of the narrow microporosity with the carbonization temperature.

Table 3.4. Porous structural parameters of the carbon fibers.

Sample	N_2 isotherm				CO_2 isotherm		
	A_{BET} (m^2/g)	A_t (m^2/g)	V_t (cm^3/g)	$V_{0.995}$ (cm^3/g)	V_{DR} (cm^3/g)	E_0 (kJ/mol)	n
ALF	<1	<1	--	--	0.027	--	--
ALFS	<1	<1	--	--	0.085	--	--
ALCF-600	524	11	0.239	0.254	0.227	34.87	2.44
ALCF-800	699	6	0.322	0.333	0.349	31.21	2.16
ALCF-900	1195	21	0.523	0.548	0.443	16.18	1.32
ALCF-1000	821	12	0.380	0.396	0.389	29.76	1.97
ALFPt	<1	<1	--	--	--	--	--
ALFSPt	<1	<1	--	--	--	--	--
ALCFPt-600	505	6	0.233	0.241	0.273	35.76	2.55
ALCFPt-800	535	2	0.243	0.298	0.276	36.66	2.44
ALCFPt-900	722	13	0.325	0.341	0.366	30.22	1.95
ALCFPt-1000	1178	61	0.520	0.592	0.429	19.37	1.52
ALCFPt-900b	818	12	0.371	0.394	0.381	26.99	1.02

3.3.7. Oxidation resistance

Figures 3.7 a and b compare the non-isothermal oxidation profiles of fresh lignin fiber (non-stabilized) and different lignin-derived carbon fibers without and with platinum as a function of temperature in air atmosphere. The non-stabilized lignin fibers, ALF and ALFPt, start to oxidize at a significant reaction rate at temperatures of around 250 ºC. In contrast, the carbon fibers show a high oxidation resistance, in spite of the high developed porous structure of these fibers (Table 3.4) and even those containing platinum (ALFPt serie). The Pt only slightly decreases the oxidation resistance of the carbon fibers at the beginning of the reaction probably due to the low amount of Pt in the carbon fibers. Once a significant burn-off is reached, the differences are larger due to the higher relative amount of Pt in the carbon fiber. The carbon fibers carbonized at low temperature (600º C) start to oxidize at temperatures higher than 400 ºC and the fibers carbonized at high temperatures (900ºC) at temperatures higher than 500 ºC

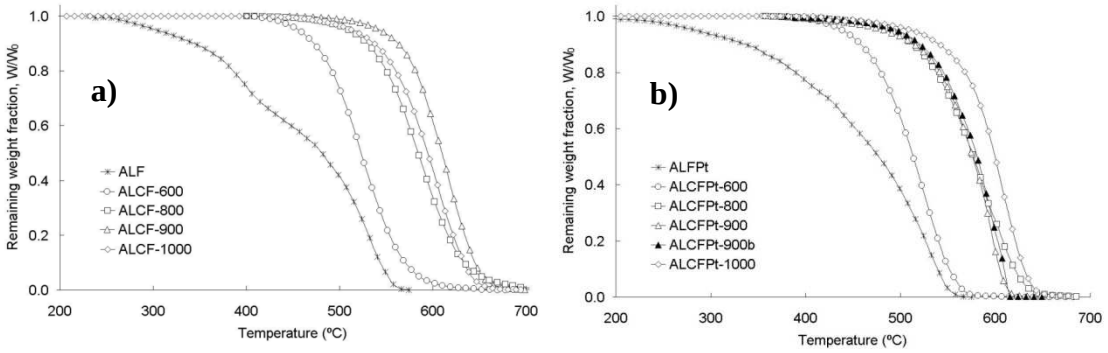

Figure 3.7. Oxidation resistance profiles of electrospun and lignin-derived carbon fibers (a) without platinum and (b) with platinum.

The Raman spectra of the lignin-derived carbon fibers (Figure 5S of Supplementary Material) suggest an onset of the structural organization in the carbon fibers, although disordered carbon was present. The presence of certain carbon ordered structures [42] and the lack of superficial defects (Figures 3.2 and 3.3) are responsible of the high starting oxidation temperatures of the carbon fibers obtained. Figure 3.8 shows that there seems to be a correlation between the starting oxidation temperature (established as that measured at 5% of weight loss) and the structural order of the lignin-derived carbon-fibers, measured by means of E_D band width. In general, the heat treatment causes an improvement on crystalline organization of the carbon fibers, which leads to higher oxidation resistance. For a similar structural order the presence of platinum produces a slightly lower oxidation resistance. This trend is also manifested for the case of ALCFPt-900b that shows a TG curve similar to ALCFPt-900.

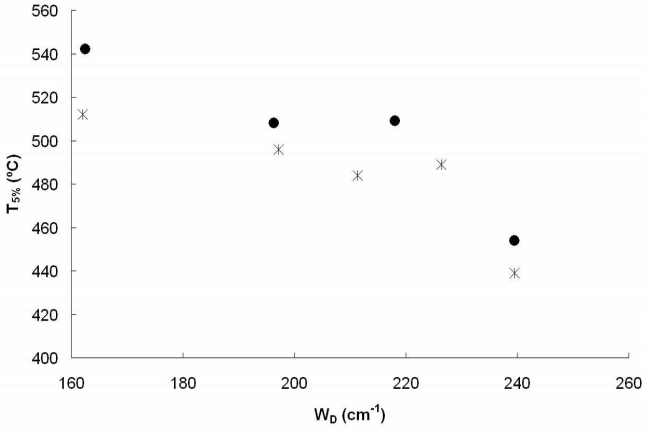

Figure 3.8. Temperature at 5% weight loss of carbonized fibers during oxidation TG analysis E_D line width. Dots: ALCF serie; Asterisks: ALCFPt serie.

The evolution of the morphology and size of ALCF-900 and ALCFPt-900b submitted to several isothermal oxidation runs at 525ºC is shown in Figure 9. The runs stopped when remaining weight of 50%, 30% and 10% were achieved for both fibers. The partially oxidized ALCF-900 fibers show a decrement of their diameter and preserve a rather smooth surface, Figure 9.c, e and g. The observed diameters seems to follow those predicted by a shinkring core model that assumes constant density of the fibers while oxidation takes place at their surface, thus making their radii at different burn-offs proportional to the square root of the remaining weight ($R = R_0 \cdot \sqrt{W/W_0}$). The oxidation reaction seems to proceed mainly over the external fiber surface. In the case of the fibers near complete oxidation (90% BO) the diameter is larger than that expected from the model, probably due to the effect of oxidation on the inner surface of the fibers.

For the fibers with platinum (ALCFPt-900b), an initial shrinkage of the fibers during the first steps of oxidation (50% BO) is observed, comparable to that for ALCF-900 (Figures 3.9 c and d). Beyond 50% of burn-off (Figures 3.9.f and h) the diameter of the carbon fibers with platinum is higher than that predicted by the shrinking core model and some defects on the external surface of the fiber are observed. As deduced from the XPS analyses (Table 3.2) platinum seems to be homogeneously distributed on the surface of the fibers. The presence of platinum enhances the widening of the micropore structure during the first steps of oxidation, which results in a more homogeneous oxidation of the surface fibers (external and internal) at high burn-offs. The platinum particles size increases (from around 10 nm on original carbon fibers to 20-30 nm at 90% of burn-off) with burn-off due to sintering during oxidation reaction.

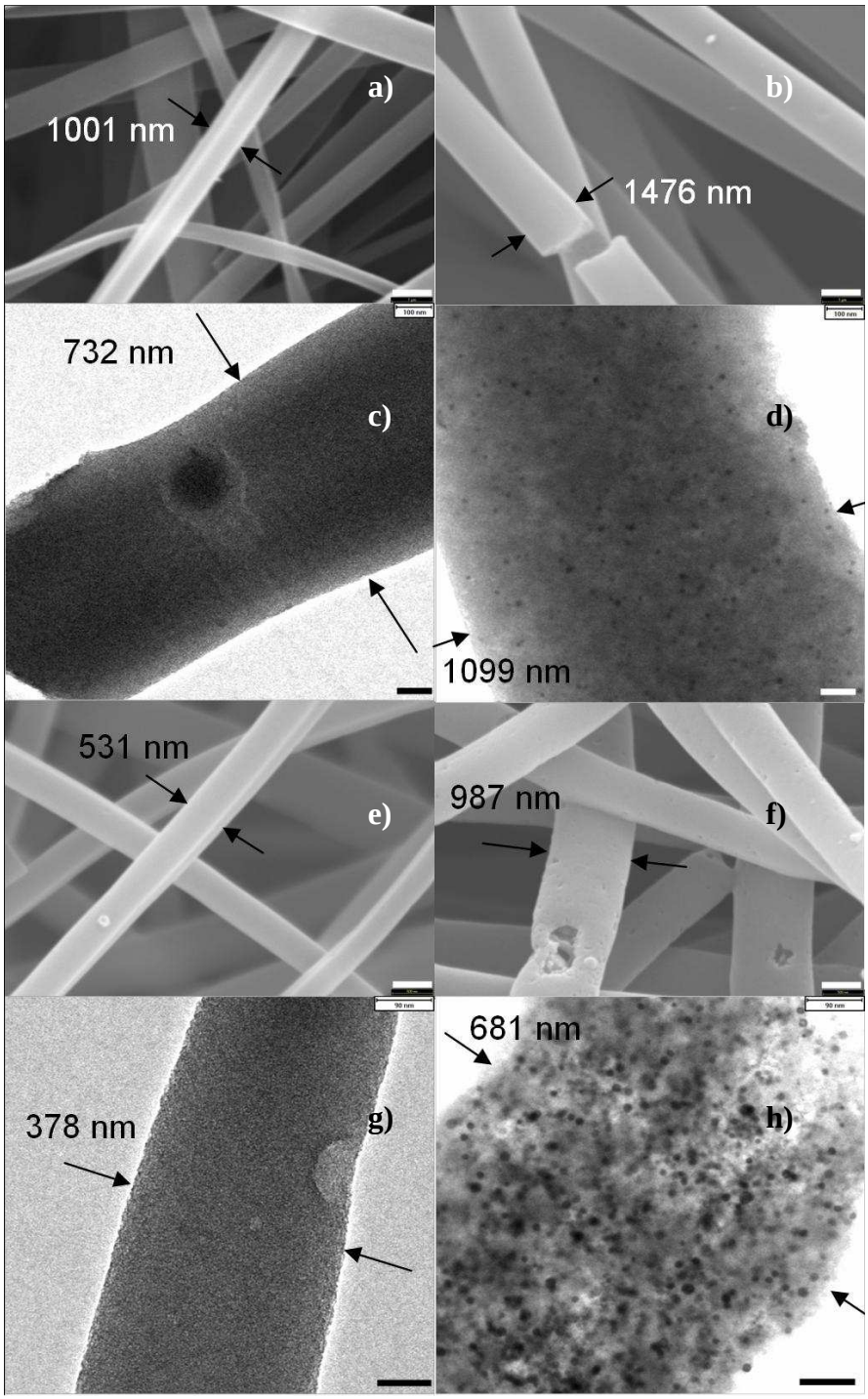

Figure 3.9. SEM and TEM images of ALCF-900 (left) and ALCFPt-900b (right) at several burn-offs (BO); (a & b) original carbon fibers (bar lengths: 1000 nm); (c & d) 50% BO (bar lengths: 100 nm); (e & f) 70% BO (bar lengths: 500 nm); (g & h) 90% BO (bar lengths: 90 nm)

3.4. Conclusions

Lignin fibers with and without platinum were synthesized by a straightforward experimental method in a single step by electrospinning of a lignin/ethanol/platinum acetylacetonate and lignin/ethanol solutions, respectively. The fibers obtained were stabilized by an air oxidation process in order to avoid fiber fusion during the subsequent carbonization step. The stabilization stage increases the oxygen content of the fibers. The stabilized fibers were carbonized at different temperatures between 600 and 1000 ºC. The increase of the carbonization temperature decreased the oxygen content of the fibers, increasing the carbon and surface platinum proportion, as well as result in fibers with a higher structuralder. Carbon fibers with surface platinum of 0.6% in weight were obtained. All the carbon fibers obtained present an essentially microporous structure. The increase of carbonization temperature produces a development of the porous structure of the carbon fibers. Carbon fibers with and without platinum with apparent surface areas of 1178 and 1195 m^2/g, respectively, and micropore volumes of 0.52 cm^3/g were obtained. The thermal treatment of the lignin-based stabilized fibers produced a decrease of the final carbon fibers diameters. TEM micrographs show carbon fibers with no defects, very smooth surface and size in the range of 400 nm to 1 µm. The carbon fibers obtained present a high oxidation resistance, probably due to a certain degree of structural order and to the lack of surface defects. The presence of platinum slightly reduces the oxidation resistance of the lignin-based carbon fibers.

3.5.References

1. P. Morgan. Carbon fibers and their composites. Taylor & Francis Groups, Boca Ratón, FL, 2005.

2. J.B. Donnet, S. Rebouillats, T.K. Wang, J.C.M. Perry. Carbon fibers. 3rd ed, Marcel Dekker, New York, 1998.

3. W.M. Qiao, M. Huda, Y. Song, S.-H. Yoon, Y. Korai, I. Mochida. Carbon fibers and films based on biomass resins. Energy Fuels 2005; 19: 2576-2582.

4. J.H. Lora, W.G. Glasser. Recent industrial applications of lignin: a sustainable alternative to non-renewable materials. J. Polym. Environ. 2002; 10: 39-48.

5. Suhas, P.J.M. Carrott, M.M.L. Ribeiro Carrott. Lignin - from natural adsorbent to activated carbon: A review. Bioresour. Technol. 2007; 98: 2301-2312.

6. J. Hayashi, A. Kazehaya, K. Muroyama, A.P. Watkinson. Preparation of activated carbon from lignin by chemical activation. Carbon 2000; 38: 1873-1878.

7. J. Rodríguez-Mirasol, T. Cordero, J.J. Rodríguez. Activated carbons from CO2 partial gasification of eucalyptus Kraft lignin. Energy Fuels 1993; 7: 133-138.

8. J. Bedia, J. Rodríguez-Mirasol, T. Cordero. Water vapour adsorption on lignin-based activated carbons. J. Chem. Technol. Biotechnol. 2007:82:548-557.

9. J. Bedia, J.M. Rosas, J. Márquez, J. Rodríguez-Mirasol, T. Cordero. Preparation and characterization of carbon based acid catalysts for the dehydration of 2-propanol. Carbon 2009; 47: 286-294.

10. B. Kosikova, V. Demianova, M. Kacurakova. Sulfur-free lignins as composites of polypropylene films. J. Appl. Polym. Sci. 1993:47:1065-1074.

11. W. Thielemans, E. Can, S.S. Morye, R.P. Wool. Novel applications of lignin in composite materials. J. Appl. Polym. Sci. 2002; 83: 323-331.

12. S. Kubo, Y. Uraki, Y. Sano. Preparation of carbon fibers from softwood lignin by atmospheric acetic acid pulping. Carbon 1998; 36: 1119-1124.

13. J.F. Kadla, S. Kubo, R.A. Venditti, R.D. Gilbert, A.L. Compere, W. Griffith. Lignin-based carbon fibers for composite fiber applications. Carbon 2002; 40: 2913-2920.

14. J.L. Braun, K.M. Holtman, J.F. Kadla. Lignin-based carbon fibers: Oxidative thermostabilization of kraft lignin. Carbon 2005; 43: 385-394.

15. S. Kubo, J.F. Kadla. Effect of polymer blending on the properties of lignin-based carbon fibers. J. Polym. Environ. 2005; 13: 97-105.

16. H.X. Huang, S.X. Chen, C. Yuan. Platinum nanoparticles supported on activated carbon fiber as catalyst for methanol oxidation. J. Pow. Sour. 2008; 175: 166-174.

17. S.R. De Miguel, J.L. Vilella, E.L. Jablonski, O.A. Scelza, C. Salinas-Martinez de Lecea, A. Linares-Solano. Preparation of Pt catalysts supported on activated carbon felts (ACF). Appl. Catal. A: Gen 2002; 232: 237-246.

18. 18.J. Ozakia, W. Ohizumia, A. Oya, M.J. Illan-Gomez, M.C. Roman-Martinez, A. Linares-Solano. Comparison of hydrogen adsorption abilities of platinum-loaded carbon fibers prepared using two different methods. Carbon 2000; 38: 778-780.

19. Z.-M. Wang, N. Shindo, Y. Otake, K. Kaneko. Enhancement of NO adsorption on pitch-based activated carbon fibers by dispersion of Cu-doped α-FeOOH fine particles. Carbon 1994; 32: 515-521.

20. M. Lallave, J. Bedia, R. Ruiz-Rosas, J. Rodríguez-Mirasol, T. Cordero, J.C. Otero, et al. Filled and hollow carbon nanofibers by coaxial electrospinning of Alcell lignin without binder polymers. Adv. Mater. 2007; 19: 4292-4296.

21. E.K. Pye, J.H. Lora. The Alcell process: a proven alternative to Kraft pulping, Tappi J. 1991; 74: 113–118.

22. G. Larsen, R. Velarde-Ortiz, K. Minchow, A. Barrero, I.G. Loscertales. A Method for Making Inorganic and Hybrid (Organic/Inorganic) Fibers and Vesicles with Diameters in the Submicrometer and Micrometer Range via Sol-Gel Chemistry and Electrically Forced Liquid Jets. J. Am. Chem. Soc. 2003; 125: 1154–1155.

23. J.E. Díaz, A. Barrero, M. Marquez, I.G. Loscertales. Controlled Encapsulation of Hydrophobic Liquids in Hydrophylic Polymer Nanofibers by Co-electro-spinning. Adv. Func. Mater. 2006; 16: 2110-2116.

24. I.G. Loscertales, A. Barrero, I. Guerrero, R. Cortijo, M. Márquez, A.M. Gañán-Calvo. Micro/nano encapsulation via electrified coaxial liquid jets. Science 2002:295:1695-1698.

25. M.A. Vannice. Kinetics of Catalytic Reactions. Springer-Verlag, NY, 2005; 20.

26. R.J. Farrauto, C.H. Bartholomew. Fundamentals of Industrial Catalytic Processes. B lackie Academic & Professional, NY, 1997.

27. H. Yang, R. Yan, H. Chen, D.H. Lee, C. Zheng. Characteristics of hemicellulose, cellulose and lignin pyrolysis. Fuel 2007; 86: 1781-1788.

28. C.J. Gómez, E. Mészáros, E. Jakab, E. Velo, L. Puigjaner. Thermogravimetry/mass spectrometry study of woody residues and an herbaceous biomass crop using PCA techniques. J. Anal. Appl. Pyrol. 2007; 80: 416-426.

29. M.C. Blanco López, C.G. Blanco, A. Martínez-Alonso, J.M.D. Tascón. Composition of gases released during olive stones pyrolysis. J. Anal. Appl. Pyrol. 2002; 65: 313-322.

30. K.H. Van Heek, W. Hodek. Structure and pyrolysis behavior of different coals and relevant model substances, Fuel 1994; 73: 886–896.

31. J.F. Moulder, W.F. Stickle, P.E. Sobol, K.D. Bomben, in: J. Chastain, R.C. King Jr. (Eds), Handbook of X-ray Photoelectron Spectroscopy, Physical Electronics, Inc., Eden Prairie, MN, 1995.

32. M. Jagtoyen, F. Derbyshire. Activated carbons from yellow poplar and white oak by H3PO4 activation. Carbon 1998; 36: 1085-1087.

33. M. Nakamizo, R. Kammereck, P.L. Walker. Laser raman studies on carbons. Carbon 1974; 12: 259-267.

34. P. Lespade, A. Marchand, M. Couzi, F. Cruege. Caracterisation de materiaux carbones par microspectrometrie Raman. Carbon 1984; 22: 375-385.

35. A. Sadezky, H. Muckenhuber, H. Grothe, R. Niessner, U. Poschl. Raman micro spectroscopy of soot and related carbonaceous materials: Spectral analysis and structural information. Carbon 2005; 43: 1731–1742.

36. A. Cuesta, P. Dhamelincourt, J. Laureyns, A. Martínez-Alonso, J.M.D. Tascón. Raman microprobe studies on carbon materials. Carbon 1994; 32: 1523-1532.

37. J. Rodríguez-Mirasol, T. Cordero, J.J. Rodríguez. High-temperature carbons from kraft lignin. Carbon 1996; 34: 43-52.

38. S.J. Gregg, K.S.W. Sing. Adsorption, surface area and porosity. 2nd ed. Academic Press, New York, 1982, 195-248.

39. I. Martín-Gullón, J.P. Marco-Lozar, D. Cazorla-Amorós, A. Linares-Solano. Analysis of the microporosity shrinkage upon thermal post-treatment of H3PO4 activated carbons. Carbon 2004; 42: 1339-1343.

40. D. Cazorla-Amorós, J. Alcañiz-Monge, M.A. de la Casa-Lillo, A. Linares-Solano. CO2 as an adsorptive to characterize carbon molecular sieves and activated carbons. Langmuir 1998; 14: 4589-4596.

41. F. Carrasco-Marin, M.A. Alvarez-Merino, C. Moreno-Castilla. Microporous activated carbons from a bituminous coal. Fuel 1996; 75: 966-970.

42. J. Rodríguez-Mirasol, P.A. Thrower, L.R. Radovic. On the oxidation resistance of carbon-carbon composites: Importance of fiber structure for composite reactivity. Carbon 1995; 33: 545-554.

4. PREPARATION OF CARBON/CERAMIC COMPOSITE SUBMICROFIBERS BY ELECTROSPINNING

4.0.Abstract

Electruspun alumina or silice-lignin microfibers have been obtained using a coaxial electrospinning setup and sol-gel technique. Preparation of composite electrospun fibers allows the encapsulation of lignin inside an alumina or silica shell allows that can be carbonized saving time and energy in the stabilization step. The presence of a ceramic coating the lignin does not hinder the great development of porosity that lignin-based electrospun carbon fibers have previously show when carbonized at 900 ºC. The obtained lignin/ceramic composite submicrofibers can also be properly treated to prepare alumina/silica tubes or carbon fibers by oxidizing the lignin core or by washing the carbonized hybrid fibers with hydrofluoric acid, respectively. These pure carbon fibers are highly microporous and present more than 1000 m^2/g of apparent surface area and surface acidity, which enable their use as heterogeneous catalysts among other applications.

4.1. Introduction

Electrospinning is one of the most suitable methods for preparing very thin fibrilar structures from ceramics and polymers precursors [1]. This flexible technique allows generating continuous tubes and fibers with sizes under the micron, and it is rather promising in terms of achieving large scale production [2]. The small sizes, the surface topology, the rich variety of possible precursors along with the easiness to cast composite or supported materials provide valuable structural, thermal, chemical and electrical properties to the resulting electrospun fibers. These properties enable the use of such materials on a wealth of applications so diverse that can include fuel cells [3], protein immobilization [4], filters [5], catalysis [6], energy storage [7], supercapacitors [8], drug delivery [9] among many others.

Carbon fibers can be obtained by this approach if a carbon source is used as precursor. To the date, the rather expensive polyacrylonitrile (PAN) is the preferred precursor [8,10,11], though other polymers [12,13] and even isotropic pitch [14] have also been used. Some of the carbon fibers prepared by electrospinning showed a well-

developed porous structure, which provides the key parameter for using them as adsorbent for pollutant removal [15], being well supported by their fine fiber size and adequate surface chemistry. Lignin could be a good alternative to those relatively high cost precursors. It is one of the most abundant polymers in nature, being mainly obtained as a co-product of the papermaking industry. Lignin has been proved to serve as raw material for preparation of activated carbons [16], highly ordered carbons [17] and carbon fibers [18]. Its properties as carbon precursor, low cost and high availability motivated two previous works where it was reported the production of carbon submicrofibers with high specific surface areas due to a well-developed microporosity by coaxial electrospinning of Alcell lignin solutions, without needing to use any binder [19,20]. The main drawback of this method is the necessity of a slow stabilization step in order to change the thermoplastic character of lignin to thermostable [21,22], thus avoiding the fusing of fibers in the ongoing carbonization step.

On the other hand, the possibility to combine the chemical and thermal stability of inorganic materials and the precise control of the structure, a distinctive of the electrospinning technique, in a micro or nanoscale size range has drawn several advances in the preparation of ceramic fibers. Capability of electrospinning combined with sol-gel chemistry for production of ceramic hollow fibers has been reported several years ago [23]. More specifically, several papers have reported works that have successfully produced alumina and silica fibers, along with titania in their formulation to cast composites for photocatalysis applications [24-26]. Other authors have proposed several approaches to produce macroporous electrospun ceramic hollow fibers, with inner diameters ranging from 100 nm to more than a micron [27-32]. Three approaches are postulated to achieve the tube shape; playing with the miscibility of the gel that is condensing inwards on the external wall of the electrospun fiber and the alcohol solvent that carries the sol [27]; using polymer electrospun fibers as a template to deposit the ceramic precursor over it, followed by its removal [28,29]; and finally, coaxial electrospinning has also been successfully used to encapsulate polymer cores inside inorganic shells to produce hollow fibers [30,31]. In this technique, two spinnable solutions are pumped into two needles which are displayed coaxially one inside the other [32]. An immiscible liquid, usually oil, can be injected in the inner needle, whereas the solgel precursor flows through the outer one. The oil is later removed producing the hollow channel inside the fiber. This method provides an opportunity to

combine the advantages of inorganic materials, such as high chemical and thermal resistance, with the large porosity obtained when polymeric fibers are carbonized, and has been successfully used for preparing silica/PAN fibers [33].

In this work, the electrospinning of lignin and alumina or silica precursors using a co-axial needle configuration is proposed to obtain lignin/ceramic composites fibers. The coated lignin fibers could be carbonized saving time and energy in the stabilization step, as an alternative pathway to the already published lignin-based carbon fiber process [19]. Removal of the ceramic shell or oxidation of the lignin core would result in pure carbon or hollow ceramic fibers, respectively.

4.2.Experimental

4.2.1. Electrospinning set-up

The precursor lignin solution was made adding Alcell ® lignin to an ethanol (CH_3CH_2OH ≥99.5%, sigma Aldrich) at a weight ratio of 1:1. The viscosity of the solution ranged between 350 and 400 cPs, making it suitable for electrospinning.

Sol-gel process for preparation of spinnable ceramic xerogels is a well-known technique which has been readily adopted in electrospinning [34]. Alkoxide precursor solutions can be previously aged [31] or directly spun for on-course hydration [27]. In both cases, the inorganic oxide is formed from the hydrated form via condensation:

$$C(OR)_x + xH_2O \Longrightarrow C(OH)_x + xROH \quad \text{(hydration)}$$

$$2 \cdot C(OH)_xO \Longrightarrow (O)_{x-1}C - O - C(O)_{x-1} + H_2O \quad \text{(condensation)}$$

Where *C* stands for aluminum or silicon in this work and *R* is the corresponding hydrocarbon radical of the alcohol. The alumina precursor is prepared from aluminum s-butoxide bis-ethylacetoacetate (CAS. 93918-06-0). In a typical synthesis, 20 mL of ethanol are added to 32 g of alkoxide solution. Then, 4 ml of 10 M HCl are slowly added to the mixture. Solution is placed in a closed flask, stirred vigorously and heated up to 80 ºC for 2 hours. Afterwards, flask is removed from heat, opened and let evaporate until viscosity increases until obtaining spinnable solution. This solution is expected to get hydrolyzed during electrospinning. On the other hand, the silica starting

sol-gel material is Tetraethyl orthosilicate (TEOS, CAS. 78-10-4), which is subjected to a polymerization/ageing process during 4 days. The resulting sol-gel is then added to an acetone mixture in a 1:1 weight ratio in order to reduce its viscosity and thus avoiding the stop of the electrospinning process due to an early solidification of the sol-gel at the tip of the nozzle, in the so-called Taylor cone.

The electrospinning device used in the preparation of the lignin-ceramic composite is schemed in Figure 4.1. The precursor mixtures were placed into two syringes. Syringe pumps delivered the liquids to the spinneret at a constant flow rate. The lignin solution was feed to the inner needle using a flow rate of 4 mL/hour, which is fast enough to avoid the formation of supernatants in the Taylor cone due to rapid evaporation of the solvent. Additionally, the sol-gel was poured into the outer needle at a flow rate of 0.5 mL/hour for casting the alumina composite. It was raised to 0.8 mL/hour when preparing the silica-lignin fiber. The purpose of feeding the ceramic sol-gel through the outer capillary needle is to dispose a thin sheath of the ceramic over the lignin fiber, resulting in the preparation of a ceramic-shell/lignin-core composite. Two high voltage supplies, one positively charged and the other negatively polarized and connected to the collector, were used to apply the high voltage between the nozzle and the collector. The electrical potential difference was 16 kV, being the collector at -8 kV and the spinneret at +8 kV. This electrostatic configuration helped to prevent fibers flying to nearing grounded pieces. Finally, the tips of the needles were displayed at a distance of 25 cm above the collector.

4.2.1. Characterization of the fibers

The porous structure of each sample was characterized by N_2 adsorption–desorption at −196 °C and CO_2 adsorption at 0 °C. The analyses were performed in an ASAP 2020 apparatus (Micromeritics). All the fibers were previously outgassed for 8 h at 150 °C at a relative pressure of 10^{-5}. From the N_2 isotherm, the apparent surface area (A_{BET}) was calculated applying the BET equation, whereas the micropore volume (V_t) and the external surface area (A_t) were determined using the t-method. The mesopore volume (V_{mes}) was estimated as the difference between adsorbed volume at a relative pressure of 0.95 and the previously stated V_t. From the CO_2 adsorption data, the narrow micropore volume (V_{DR}) and apparent surface area (A_{DR}) were calculated using the Dubinin–Radushkevich equation.

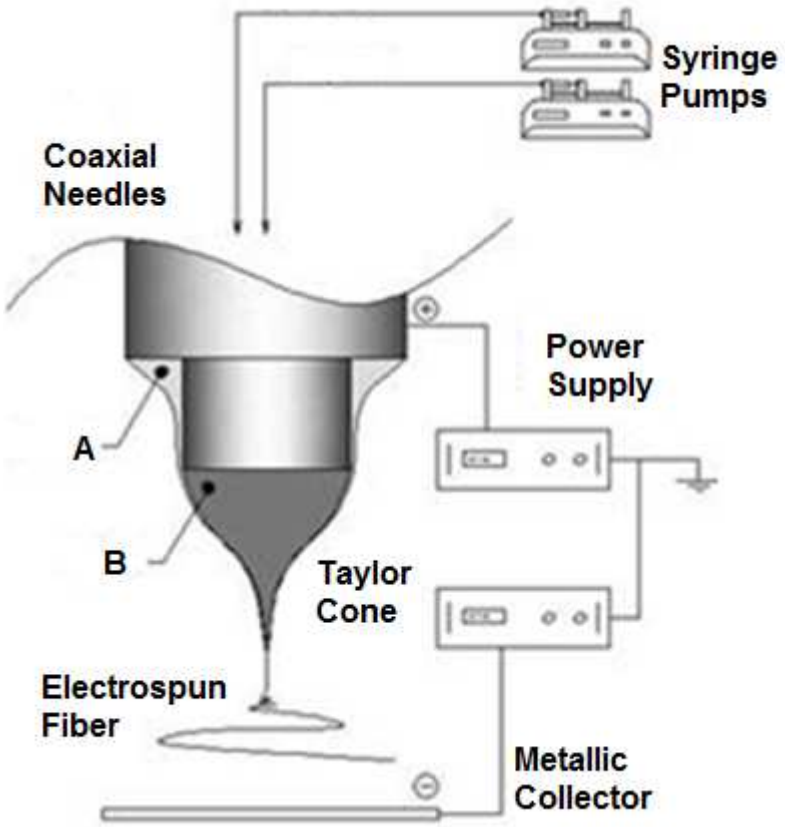

Figure 4.1. Coaxial needle spinneret set-up used in the co-electrospinning of alumina or silica (through A needle) and lignin (B needle) solutions.

The surface chemistry of the samples was studied by means of X-ray photoelectron spectroscopy (XPS). XPS analyses of the samples were obtained using a 5700C model Physical Electronics apparatus with Mg Kα radiation (1253.6 eV). For the analysis of the XPS peaks, the C1s peak position was set at 284.5 eV and used as reference to locate the other peaks. The fitting of the XPS peaks was done by least squares using Gaussian–Lorentzian peak shapes. The full width at half maximum (FWHM) was fixed at approximately 2.0 eV and the position of the peak center was allowed to vary within±0.2 eV of the reported value. The intensity values of XPS spectra shown in this work are proportional to the corresponding atomic concentration; for that, first the area behind the spectra is normalized to one, and then each point of the spectrum is multiplied by the atomic concentration of their respective element.

Non-isothermal thermogravimetric (TG) analyses were carried out in a gravimetric thermobalance system, CI electronics. Experiments were carried out in inert

atmosphere (N_2), and in air atmosphere, for a total flow rate of 150 cc (STP)/min. A small piece of each fiber cloth was cut and placed inside the apparatus. The sample mass was approximately 7 mg. The sample temperature was increased from room temperature up to 900 ºC at a heating rate of 10 ºC/min. The TG profiles were then derived to obtain DTG curves.

The morphology of the fibers was studied by scanning electron microscopy (SEM). The micrographs were obtained using a JEOL JSM-840 instrument, working at a voltage of 20–25 kV. Additionally, the inner texture of the samples was characterized by transmission electron microscopy (TEM). Transmission electron micrographs were carried out by a Philips CM200 instrument at high voltage of 100-200 kV. In order to untangle the fiber cloth and thus making easier taking micrographs from isolated fibers, the fibers were finely dispersed in a pure ethanol solution and were ultrasonically treated for 1 hour. Small droplets of the dispersion were deposited onto a holey carbon film supported by a copper grid. The elemental analysis was performed with energy dispersive system (EDS, EDAX) attached to the microscope. The analysis probe allowed scanning the composition of the fibers in axial or radial directions.

The acidity of some catalysts was determined by adsorption–desorption of pyridine carried out in a thermogravimetric system (CI Electronics) at 100 ◦C. The inlet partial pressure of the organic base, 0.02 atm, was achieved saturating He with the organic base in a saturator at controlled temperature. After saturation of the sample, desorption is carried out at the adsorption temperature in Helium flow.

4.2.2. Preparation of composites fibers

The as-spun hybrid fibrous composite, whether it has been casted with alumina (noted by A) or silica (S) precursors, were recovered from the collector as a thin, non-woven cloth of yellowish brown color. Those electrospun composites have been used to generate different composite or pure materials. For clarity's sake, Figure 4.2 shows the scheme followed for producing all the materials presented in this work.

First, as-spun fibers were thermal treated under N_2 atmosphere. This carbonization process was carried out with about 200 mg of fiber cloth pieces, in crucibles (Alsint 99.7%) located in the isothermal region of a horizontal tubular furnace. The required inert atmosphere was set under constant nitrogen flow of 150 cm^3/min

(STP) that was maintained for 30 minutes before heating the furnace to the selected temperature. The heating rate was 10 ºC/min and two different final temperatures, 600 and 900 ºC, were set to study the effect of the treatment temperature on the textural and chemical surface properties of the composites. The furnace was then let cooled overnight to room temperature, obtaining carbon-alumina/silica composite fibers. The carbonization temperature is added at the end of the acronym to distinguish between the treatment at 600 and the treatment a 900 Celsius degree.

On the other hand, lignin-ceramic composites were also placed inside an oven for air oxidative stabilization at 200 ºC for different times. Stabilized fibers were denoted by the stabilization time in hours preceding the name of the parent as-spun composite. Moreover, the air stabilized composites were also carbonized using the same conditions detailed earlier. The resulting composites were denoted by their previously shown acronym followed by their carbonization temperatures.

The air stabilized and carbonized composites were also acid washed for etching the ceramic content. A sample of around 150mg was inserted in a flask with 50 mL of hydrofluoric acid (48%, ACS reagent) and subjected to continuous stirring for one hour. The washed material was named as the parent fiber acronym followed by W.

The as-spun lignin-ceramic composite fibers were also used as raw material to prepare hollow ceramic fibers. In that sense, small quantities of each A and S fiber cloth were heated under air atmosphere up to 600 ºC and keep at that temperature for 1 hour looking for a total removal of lignin, obtaining CA and CS ceramic hollow fibers.

Finally, textural and chemistry surface properties of lignin powder and carbon fibers from electrospun lignin fibers prepared in previous works [19,20] are also mentioned along the work for the sake of comparison. In those cases, they are named as L or LF for lignin powder or fiber, respectively, preceeded by the air stabilization time and followed by the carbonization temperature.

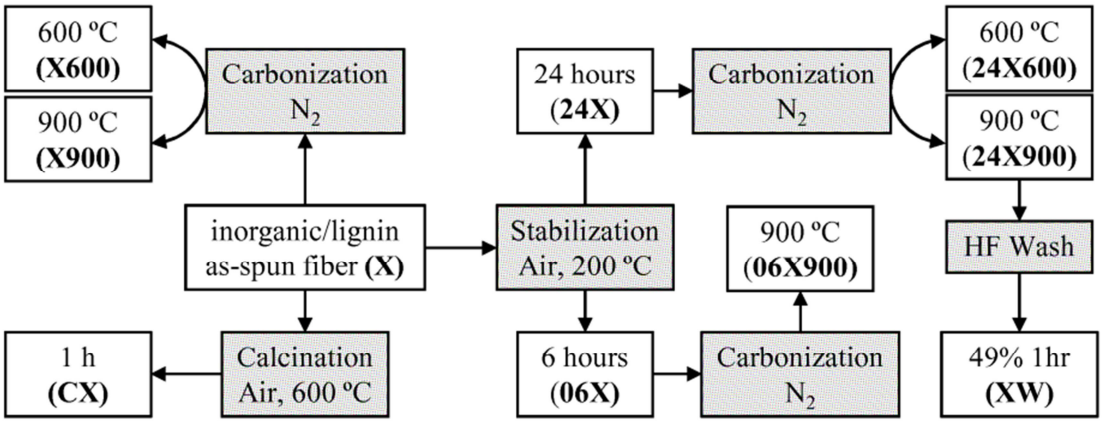

Figure 4.2. Fiber composite's production scheme. Boxes related to treatments are filled in grey.

4.3.Results and Discussion

4.3.1. Yields

The yield in each stage and for the overall production process was estimated in dry basis from furnace experiments. It is shown in Table 4.1. Significant weight loss occurred in the carbonization process, being much lower during thermostabilization. Weight loss increased with stabilization time probably due to further condensation and dehydration of lignin oxygen groups [20,21]. Yield for the thermostabilization process in case of lignin powder seems to be higher than for A and S composites. Differences can be accountable to incomplete hydrolysis/condensation of the alkoxides in composites. The S composite showed lesser weight losses after thermostabilization, which can be connected to the long gelation time of the TEOS precursor solution, producing fibers with a ceramic layer which is hydrolyzed and condensed in a higher extent than alumina-lignin ones.

Carbonization of powdered lignin used in the formulation of the fibers yielded similar weights than those reported for pyrolysis of alcell lignin [39]. Carbonization yields for the fibers are higher, due to the alumina or silicon fraction of the composite fibers, which is thermally stable. On the other hand, a previous thermostabilization stage induces a higher carbonization yield. The air stabilization process increases the molecular weight of lignin as a result of formation of anhydride and ether linkages between lignin polymeric chains [21,22]. The thermosetting polymer probably has a

lower volatile fraction. Overall (thermostabilization plus carbonization) yield is higher when composites are produced avoiding thermostabilization, especially when it lasted for 24 hours in A composite. Dissimilarities cannot be assessed to elimination reaction of oxygen groups from lignin, as the differences in carbonization yield are greater in composite fibers (5%) than for powdered lignin (2%), which can be taken as a baseline. This can be better explained by the complete hydrolysis/condensation of the ceramic layer in air stabilized samples. The organic ligands of remaining alkoxide molecules in as-spun fibers, which only decompose to dibuthylether at temperatures higher than 600 ºC in nitrogen atmosphere, could be pyrolized in the presence of nascent surface acid sites from the silica or the alumina surface in a similar manner than cracking volatiles from polymer degradation in infiltrated zeolites [40], producing a higher carbonization yield.

Table 4.1. Yields for each process step in the production of composite carbonized fibers (wt.%)

	Stabilization		**Carbonization**		**Global**
Sample	**time (hrs)**	**yield**	**600 ºC**	**900 ºC**	**900**
A	No	--	52.8	48.1	48.1
	6	92.3	X	49.9	46.0
	24	86.6	56.7	49.1	42.5
S	No	--	--	47.4	47.4
	24	89.1	--	50.0	44.5
L	No	--	45.0	42.1	42.1
	6	92.8	--	45.5	42.2
	24	90.8	50.9	43.8	39.8

4.3.2. Air stabilization of electrospun fibers

When studying the oxidative thermostabilization of lignin fibers, Kadla and Kubo found that temperatures in the range of 200-250 ºC are optimal for avoiding excessive weight loss due to elimination reactions and for favoring lignin polymer C-O-C cross-linking bridges, which turns to be a key factor to raise the glass transition temperature of lignin [21,22]. This step was necessary to avoid fusion in the production of carbon nanofibers from electrospun lignin fibers. In two previous works electrospun pure lignin fibers have been stabilized in air at 200 ºC for more than 30 hours using low heating rate values of 0.05-0.10 ºC/min [19,20]. In that sense, the heat treatment took

about 60 hours. Aiming to reduce the treatment time, two modifications were taken. First, the oven temperature for the air treatment of the composite fibers was directly set to 200 ºC, avoiding the slow heating ramp used in the previously mentioned papers. Second, stabilization time at 200 ºC was reduced. At such a high temperature, evaporation of remnant solvent occurred at beginning of the stabilization, which was confirmed by fast weight loss of 8% for A composite after the first hour. Evaporation is followed by weight loss rate of 0.3% per hour which slowly decays until weight reaches near steady value of 85% after 54 hours.

Hydration and condensation of the alkoxide layer during ageing or electrospinning process could have result in formation of amorphous oxide shell previously to the air stabilization step. In this sense, several works have already reported production of amorphous silica or alumina electrospun fibers from alkoxide precursor [27,31]. The aluminum or silicon oxide layer is expected to be solid enough to keep enclosed the molecules of lignin, but permeable to diffusion of carbonization gaseous products (H_2, H_2O, CO, CO_2) leaving from the fiber core. This way, ceramic/carbon composite fibers would be obtained despise incomplete thermosetting or even avoding it.

The effect of oxidative thermostabilization time on surface chemistry was studied by means of XPS analyses. It is important to take into account that this technique provides information only of the outermost 5-10 nm of the exposed solid surface. Thus, the wider silica layer (observed in TEM micrographs for S fibers, see section 4.3.7) hinders any effect of air oxidation or carbonization in the lignin core behind it, and therefore A fiber were chosen for this study. XPS spectra for the as-spun and air-thermosetted A fibers at 200 ºC and different times are shown in Fig. 4.3. The Al2p region of the spectra, Figure 4.3a, presents a maximum lying at 74.0 eV, which shifted to 74.3 eV after air thermostabilization for 6 hours. This displacement can be related to hydrolysis of aluminum alkoxide [35], producing higher contribution to XPS signal from Al_2O_3 (Al-O-Al bond, at 74-74.5 eV [36]) respect to that of aluminum s-butoxide (C-O-Al bond, located at 73.0 eV). This result suggests that, after electrospun of the composite fibers, the remaining alkoxide is hydrolyzed during the air stabilization. Longer stabilization times just resulted in slightly higher Al2p peak intensity.

The changes in spectra in C1s and O1s photoemission region, Figures 4.3b & c, confirmed the oxidative thermosetting of lignin fiber. As-spun fibers O1s spectrum shows a nearly symmetric peak lying around 532.0 eV, which is product of convolution of C-O-R, C=O and Al-O signals at 532.6, 530.8 and 529.3 eV respectively [37]. The stabilization process produces an increase of oxygen content and displacement of the maximas to higher binding energies, which is associated to higher presence of C-O-R groups. Deconvolution of C1s spectrum show three different peaks; (i) at 284.5 eV associated to C-C and C-H bonds; (ii) at 286.1 eV that could be related to C-OH groups, widely represented in liginin monomer; (iii) and at 288.5 eV associated to carbonyl and C-O-C groups [38]. While C-OH contribution seems to remain almost constant, the C-C/C-O-C ratio seems to diminish from A to 24A fiber, being even lower in the case of 54A spectra. As aforementioned, condensation reactions between adjacent carboxylic or phenyl groups, increasing glass transition temperature of lignin, are expected during air treatment at 200ºC and can be causing higher C-O-C contribution, whereas longer time exposures to air produces increases in total oxygen content and lower C-C/C-O-C ratios due to insertion of more phenyl, carbonyl and carboxyl groups and condensation of carboxilic groups.

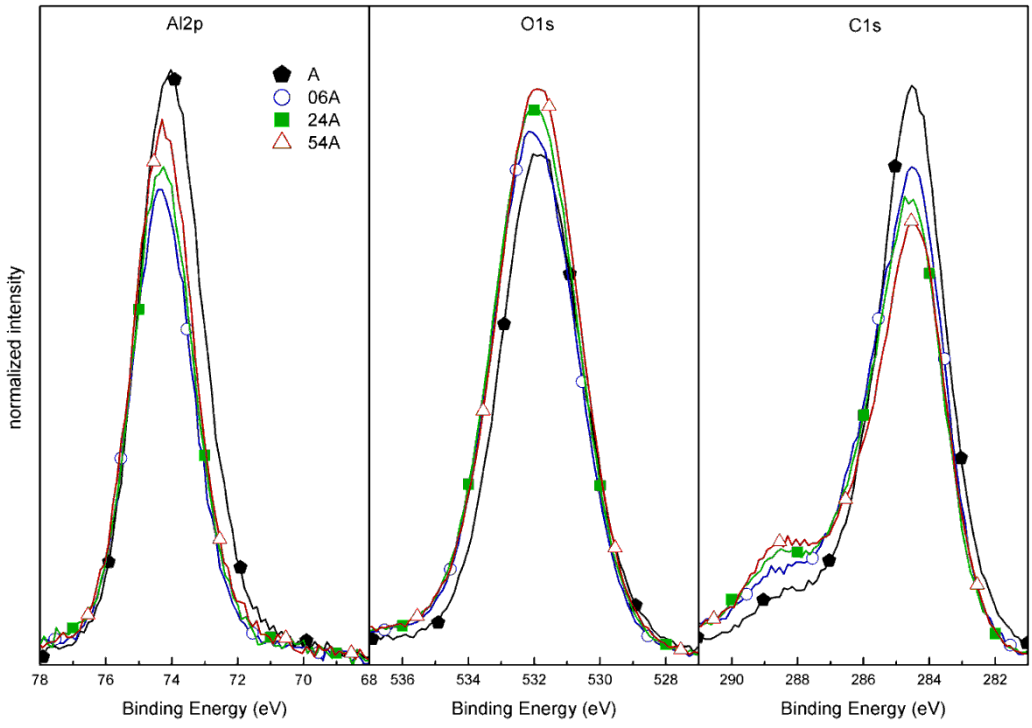

Figure 4.3. Normalized Al2p, O1s and C1s regions of XPS spectra from as-spun and air-stabilized A composite fibers.

It can be concluded that the shell-core arrangement of the composite do not difficult the oxidation of lignin because of restricted diffusion of oxygen through the alkoxide/ceramic layer. On the other hand, the oxygen groups inserted in this step can cause changes in the chemical or structural properties of the final composites, so short and long time stabilized composites, i.e. air stabilization times of 6 and 24 hours respectively, were further used for carbonization and confronted with direct carbonized fiber composites.

4.3.3. Thermogravimetric analyses

Figure 4.4.a depicts the weight loss of as-spun A and S fibers as well as solely lignin fibers during an air calcination run at 10 ºC/min. Residual ethanol or organic solvent, which accounted for 5-8% wt. and evaporate at temperatures under 100 ºC, are discounted from the TG profiles. All the fibers started losing weight at 150 ºC. The S and L fibers were completely burnt at 600 ºC, while aluminum-lignin fiber still lost a minor weight quantity up to 650 ºC. The DTG profiles of both composites show a similar pattern than pure lignin fibers, having two main peaks which are endorsed to combustion of lignin, the principal component of all fibers. Faster weight loss rates for both composites can be observed between 100 and 400 ºC. Those mass losses can be associated to condensation of the hydrous ceramic layer and decomposition of the organic part of remnant alkoxides, which is removed in air below 500 ºC [41].

Differences on the carbonization process of lignin in composites fibers were also studied using nitrogen thermogravimetric analyses. Figure 4.4.b depicts the resulting TG and DTG profiles. S and L DTG curves seem to be similar, exception made of the differences at T~150 ºC, where condensation of silicic acid to form silicon dioxide proceeds with water elution, and the slightly superior weight loss at T>600 ºC, which is related to decomposition of remnant TEOS to form silicon dioxide and di-ethyl-ether. It can be said that pyrolysis of lignin is not affected by the presence of the ceramic layer. On the other hand, differences in thermal devolatilization onset temperature and remaining weight at 900 ºC are observed between S and 24S composites. The devolatilization of the latter fiber seems to be delayed to higher temperature, and proceeds in a lesser extent, as pointed out by its higher remaining weight at 900 ºC. This is related to condensation and, though less likely, elimination reactions of oxygen surface groups that take place during the air stabilization of lignin [21].

Thermostabilization also inserted C=O groups, as revealed by XPS analyses. Considering that Figuereido et al. [42] stated that ethers and anhydrides surface groups evolves from activated carbon surfaces at temperatures between 600 and 800ºC in form of CO and CO/CO_2 respectively, the higher weight loss for 24S at 600 ºC can be related to removal of the inserted C=O groups and C-O-C bridges formed during the air stabilization stage.

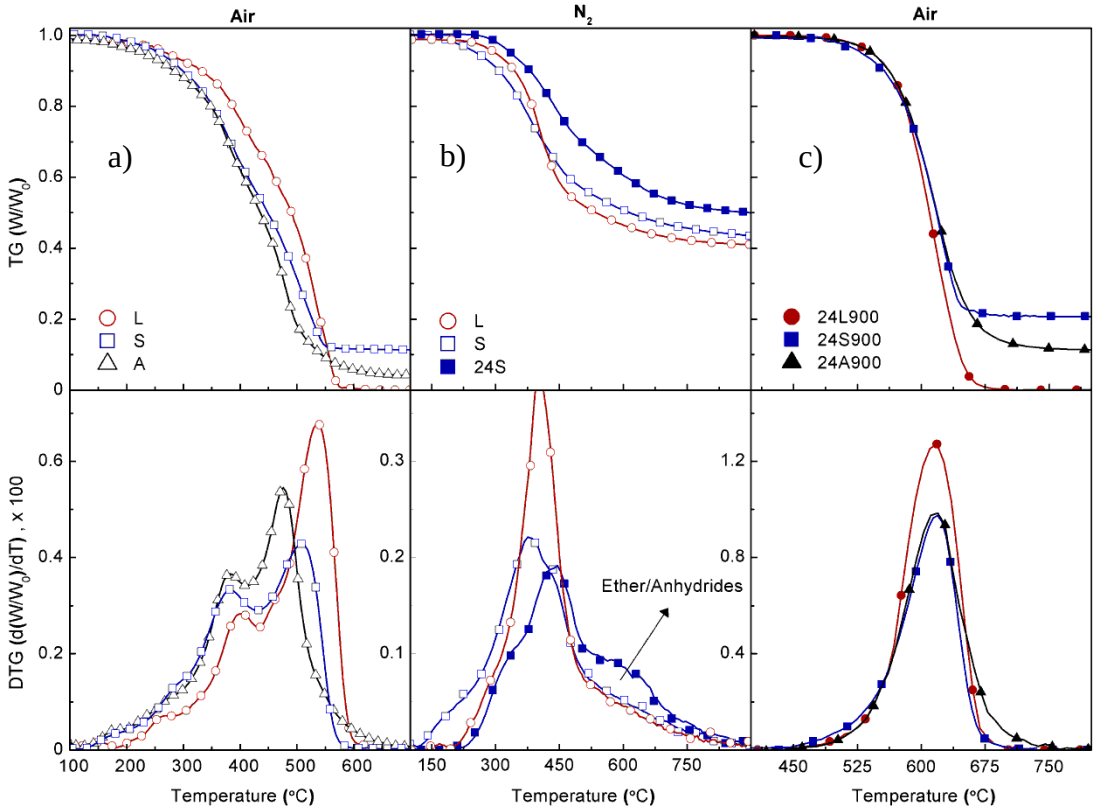

Figure 4.4. TG and DTG profiles of lignin and as-spun fiber composites in air (a), lignin and S fiber before and after air stabilization for 24 h in nitrogen (b), carbonized lignin and stabilized fiber composites in air (c).

Air TGs in Figure 4.4.c studies the effect of the ceramic layer on the oxidation resistance of carbonized lignin fibers. For this purpose, it is also shown a TG profile of a carbonized fiber from slowly air stabilized lignin fiber, LF900 [19]. 24S900 and 24A900 were chosen because they have been subjected to the most similar air stabilization treatment. All three fibers show a remarkable oxidation resistance. The silicon or aluminum oxide presence did not improve the oxidation onset temperature,

probably due to the expected ceramic layer being porous or not closed, with the carbon core being partially exposed.

On the other hand, weight after calcination at 900 ºC is 10.0±0.4 for S and 3.1±0.2 % for A fibers, calculated from the respective Air-TG of S. Theoretical calcination yields can be estimated taking into account the appropriate alkoxide/lignin electrospun pumping feed ratio from the formulation of the electrospun fiber plus the ratio between the SiO_2 or $AlO_{1.5}$ molecular weight and that of their respective precursor, i.e. TEOS and aluminum sec-butoxide. Therefore, expected yield for production of CA is 16.67% x 0.1425· = 1.58%, whereas CS yield means to be 28.6% x 0.2885= 4.81%. The higher experimental values can be endorsed to the hydrolysis and condensation of the alkoxide during solidification of the jet in electrospinning and to the ageing step for the TEOS solution. Calcination yield if the external layer of the as-spun fibers is considered as hydrous silica and alumina would be 10.42% and 7.26%. The similar yield value for the production of CS is pointing out that TEOS solution was mostly hydrolyzed, whereas the experimental yield value obtained from calcination of A fiber points out the aluminum alkoxide layer is only partially hydrolyzed in them.

4.3.4. SEM and TEM analyses

4.3.4.1. Production of electrospun composites

The SEM micrographs compiled in Figure 4.5 depict the as-spun aluminum and silicon/lignin composite fibers (A & S). The A mat proved to be compound by long fibers with a high distribution of sizes, ranging from 200 nanometers up to 4 microns in diameter. They also showed a circular cross-section. The regular appearance of the tip of broken fibers, as can be seen in some of the fibers of Figure 4.5.a, indicated that the core of the fiber is solid. The absence of ill formed fibers and the rather smooth surfaces pointed out that the electrospinning process was working adequately at the chosen combination of operation conditions. The electrospinning of the S composite performed in a similar fashion, but this material showed a more homogeneous distribution of the fiber size.

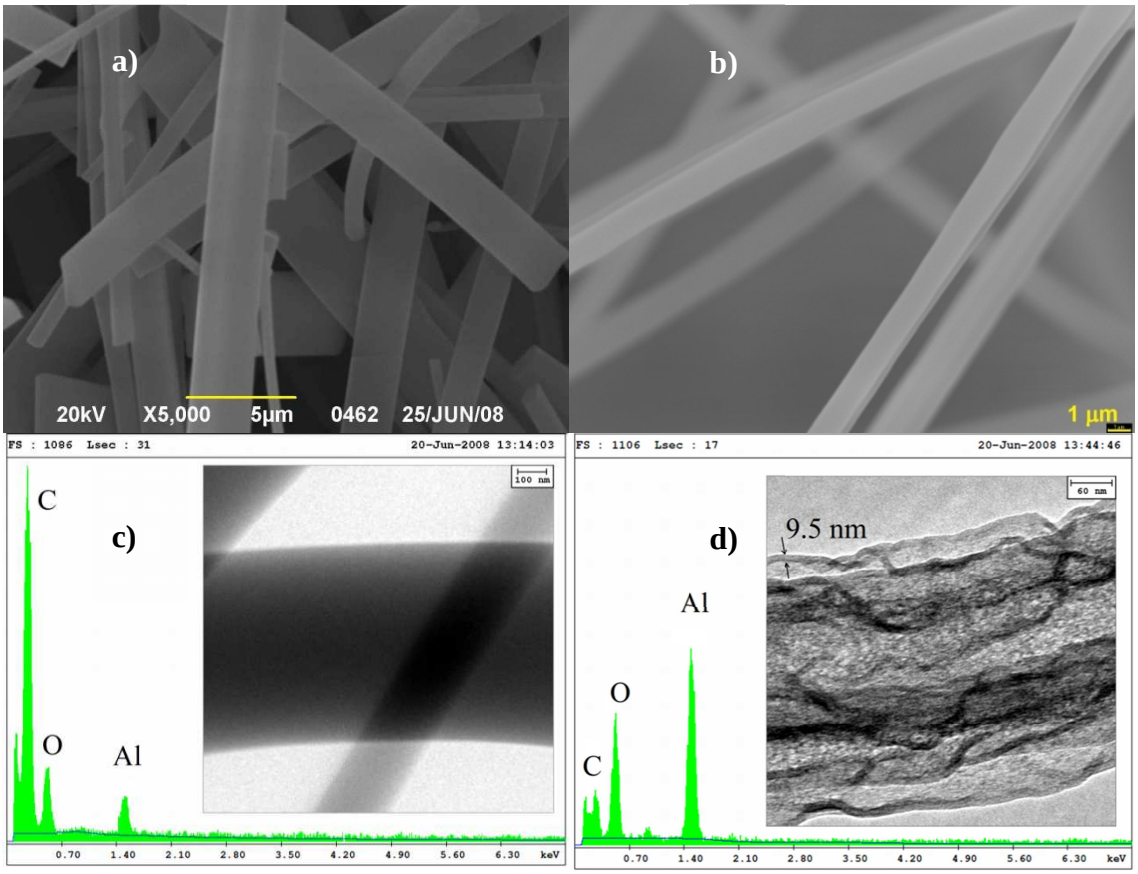

Figure 4.5. SEM images of a) aluminum alkoxide/lignin composites and b) silica alkoxide/lignin composite fibers. TEM images and EDAX spectrum of A fiber when c) directly submitted to TEM or d) stirred in ethanol and ultrasonically treated for 30 minutes. Bar length: 100 and 60 nm respectively.

The inner structure of the composite was studied by means of transmission electron microscopy. Figure 4.5.c confirmed that the core of the freshly electrospun fiber is solid and homogeneous. The main elements found by EDAX are carbon, oxygen and aluminum. The outer surface did reveal neither a gradual interphase nor a less dense, dissimilar sheath, so lignin could be infiltrating the shell and concealing the ceramic layer. The last image in Figure 4.5 corresponds to ethanol-cleansed A composite. EDAX composition reveals the resulting mat consists mostly in aluminum oxide tubes. It seems that ethanol diluted the lignin from the core of the composite. TEM image reveals an irregular and less dense core with long and denser strings that run sinuously along the fiber axis. The darker strings seem to be a transversal slit of the alumina shell. When those striations are seen in the middle of the fiber, is because the wrinkled topology of the external surface, which is probably due to ceramic shell

having partially collapsed inwards. The layer is rather thin, showing a width of around 10 nm.

4.3.4.2.Inorganic oxide tubes

Once the electrospun lignin-ceramic composite fibers have been successfully casted, they could be used as the starting material for the production of hollow inorganic oxide fibers. The formation of the ceramic tube requires the removal of the lignin core and the production of the alumina or silica layer from the matching alcoxide if it is not completely gelated. The most straightforward method to achieve both goals is the calcination of the original composite. The calcination temperature to produce the inorganic tubes was set to 600 ºC, and was maintained for one hour to ensure entire calcination of the organic compounds of the fiber, whis was verified by the hollow structure observed in TEM images, Figure 4.6.

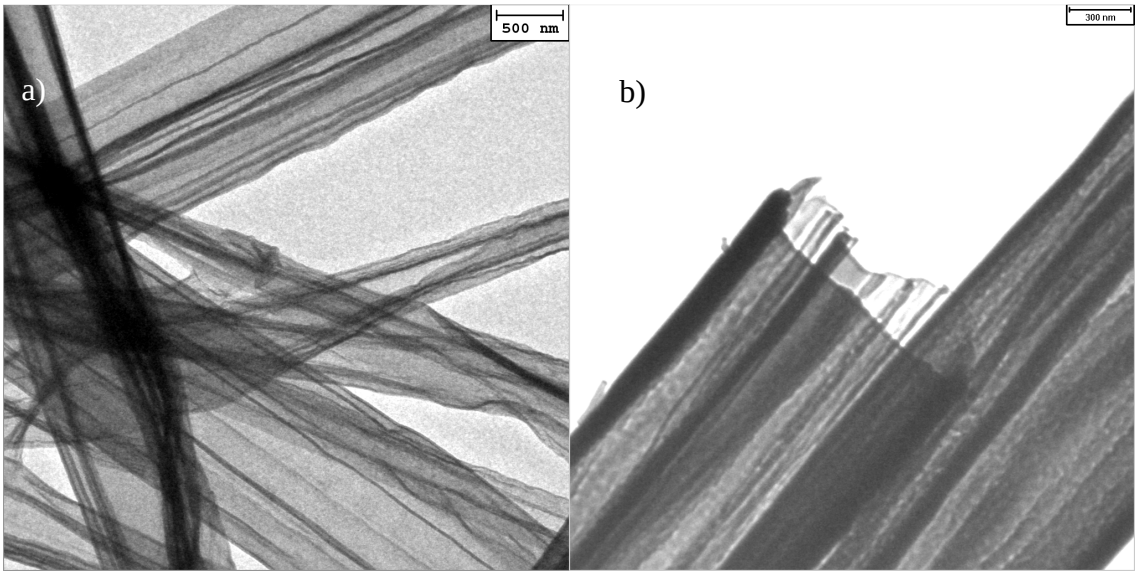

Figure 4.6. TEM images and EDAX spectrum of calcined fibers. (a) CA fiber. Bar length: 500 nm. (b) CS fiber. Bar length: 300 nm

These tubes have external sizes to some extent lower than those detected for the composite fibers (200-2000 nm for A and 400-1200 nm for S), probably due to shrinkage during the polymer core removal in the oxidation process. Their surface aspect is more regular that those obtained by lignin removal by ethanol washing, as the remaining alkoxide and hydroxides over the fiber surface turns into amorphous alumina or silica prior lignin oxidation, hardening the ceramic layer. Evidences of the

morphological changes caused by the higher sol-gel flow rate in the production of S fiber are clearly provided by the transmission images on Figure 4.6.a and b. The width of the silica wall is two-three times higher of that measured for the alumina tubes. The higher width of the silica wall in CS corroborates the correlation between the feed rate of the sol-gel to the nozzle and the size of the ceramic tubes' wall. They also showed lesser cracks and defects and a more rigid and linear fiber structure than their alumina counterpart.

4.3.4.3. Production of carbon-ceramic fiber composites

The controlling step of time production of carbon fibers is usually the stabilization step. The feed rate of the ceramic shell precursor is going to be a critical parameter if the composite stabilization procedure is to be improved. This is supported by SEM and TEM results. Figure 4.7.a & b follows the morphology of A fiber after stabilization and posterior carbonization. Figure 4.7.a supports the absence of fused fibers when as-spun fibers are directly thermostabilized at 200 ºC, despite the lower glass transition temperature of lignin. The presence of the alumina shell has greatly shorten the thermostabilization treatment time required for obtain lignin-based carbon electrospun fibers. The stabilized composite fibers seem to be fairly similar in size to the electrospun composite. Carbonization at 900 ºC of alumina-lignin stabilized composite fiber proved to produce stable alumina-carbon composite fibers with smooth surfaces and lack of fusion points, as supported by the scanning image on Figure 4.7.b. Figure 4.7.c and d shows SEM and TEM images from respective A and S composites submitted to direct carbonization. In the pictures from the A900 composite, Figure 4.7.c, it can be seen fibers sharing fused cross-sections with nearby fibers. It seems that the alumina layer is not wide or rigid enough to effectively encapsulate the lignin inside it. Consequently, lignin is able to diffuse through the ceramic layer when carbonized, causing fusion of the fiber with nearby fibers. On the other hand, when the ceramic-lignin composite fiber was prepared using a higher flow rate and aged solution, as in the case of S fiber, the SEM images showed lesser evidences of fused fibers, Figure 4.7.d. No cross-linkage is detected, although some fibers are seen to get stuck and run in pairs for some hundreds of microns before getting apart. Their surfaces are also rough, probably related to the softening of the inner lignin core before getting carbonized,

giving the fibers a relaxed appearance. Nevertheless, direct carbonization of this composite keeping fibrile form seems to be possible thanks to the wider ceramic layer.

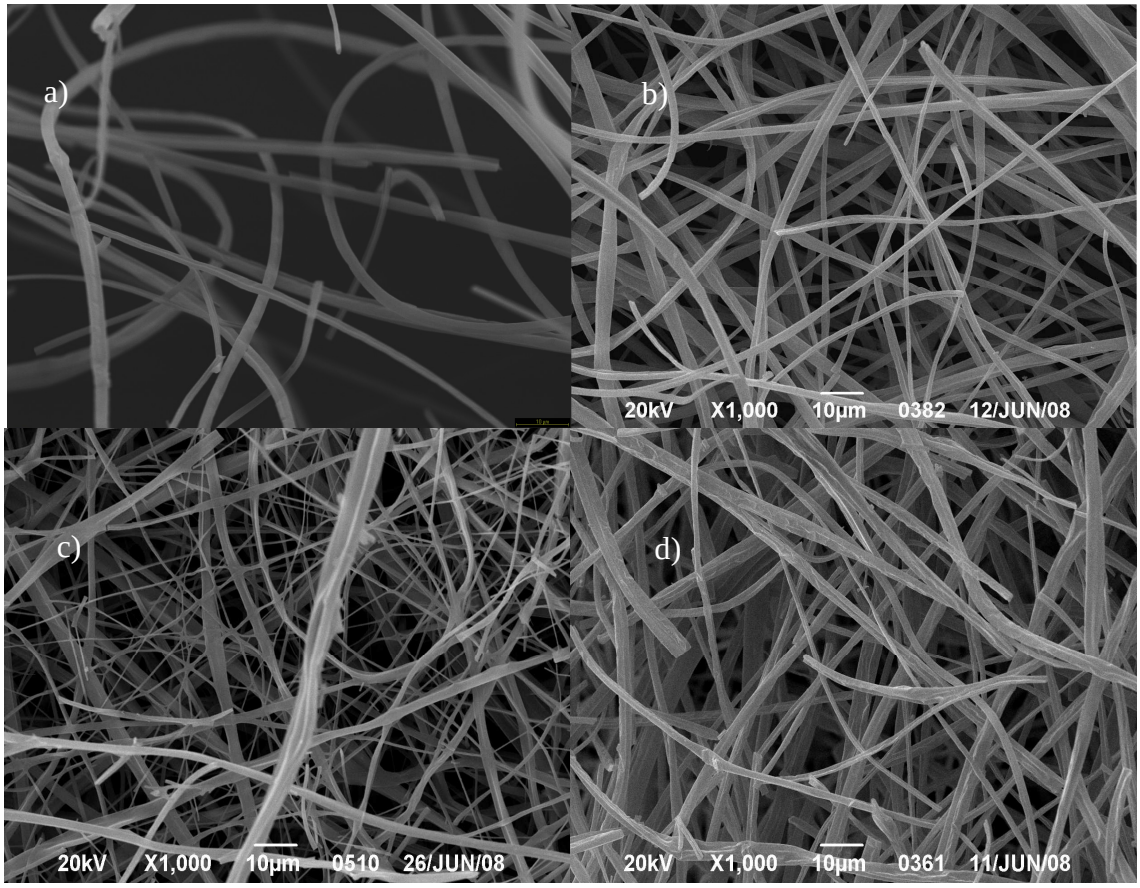

Figure 4.7. SEM images of carbonized composites. a) 06A, b) 06A900, c) A900, d) S900. Bar length: 10 µm

Further information about the condition of the ceramic sheath after carbonization of composite fibers can be obtained from TEM images. Figures 4.8.a and c presents direct carbonized and carbonized after stabilization alumina-lignin fibers, respectively. It is easy to notice the occurrence of a less dense sheath in the outer region of 06A900, which is unnoticed in fibers from A900 sample. It seems air stabilization helped to tight the alumina shell and to establish a vivid interphase with the carbon core. The composition of that coat is studied in Figure 4.8.d. EDAX of C, O and Al K lines were registered along the radial axis (following the black arrow) of the fiber presented in Figure 4.8.c. Carbon signal takes the form of a plateau, whereas aluminum has two strong peaks at both ends of the fiber, where the dark coat is located, and keeps a low intensity profile along the rest of the fiber. Oxygen seems to follow a similar trend than aluminum. From these results it can be said alumina is covering the whole lignin core,

being located at the surface of the fiber. Lastly, Figure 4.8.b shows a S900 fiber which was subjected to partial oxidation (30% burn off) under air atmosphere at 600 ºC. The silica coat at the outer surface of the fiber is clearly identified, while a less dense region appears just under it. It seems that the oxidation of the carbon core proceeds radially, which points out that the silica layer over the composite fiber is permeable to oxygen diffusion.

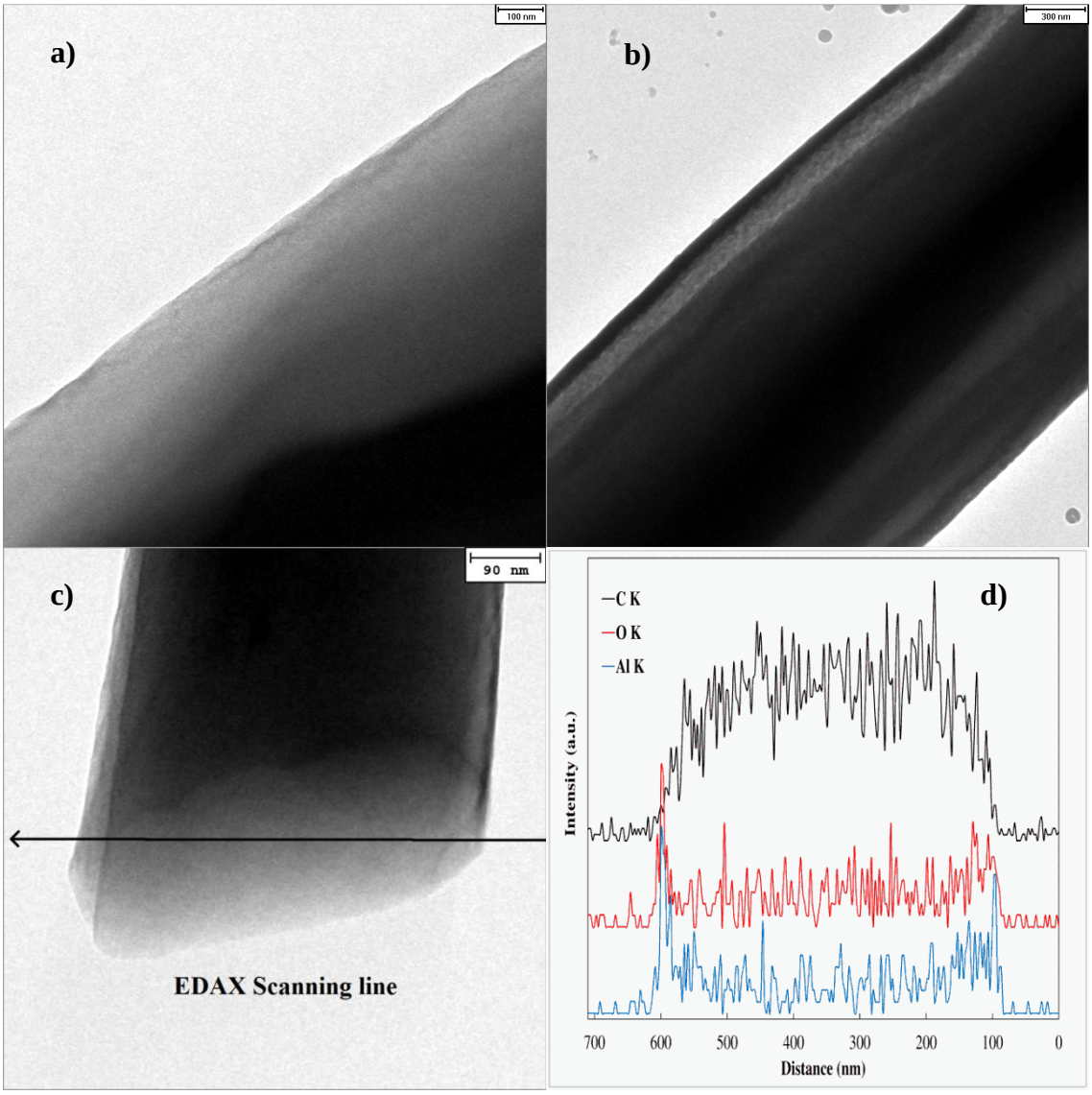

Figure 4.8. TEM images and EDAX spectrum of lignin and carbon alumina composites. a) A900 fiber; line bar: 100 nm. b) S900 fiber, 30% burn off; line bar: 300 nm c) 06A900 fiber line bar: 90 nm d) 06A900 EDAX linear scanning spectra.

4.3.4.4. Production of carbon fibers

Figure 4.9 displays SEM and TEM images from 24A900 composite cloth that has been rinsed in a hydrofluoric acid wash for one hour. SEM images showed the fibril morphology of the material have not been compromised, thus the scrubbing of the ceramic material on the fiber have not damage the fiber, although the surface of the fibers is now more rough, as can be seen in Fig. 4.9.b. The fiber diameter seems to be smaller, probably due to the removal of some of the carbon core linked to the ceramic layer. EDAX of carbon fiber core in Figure 4.9.b reveals that it is mostly made of carbon, confirming utter removal of silicon dioxide. Fluorine presence reveals that some of the etching agent seems to be retained in the porosity of the fiber.

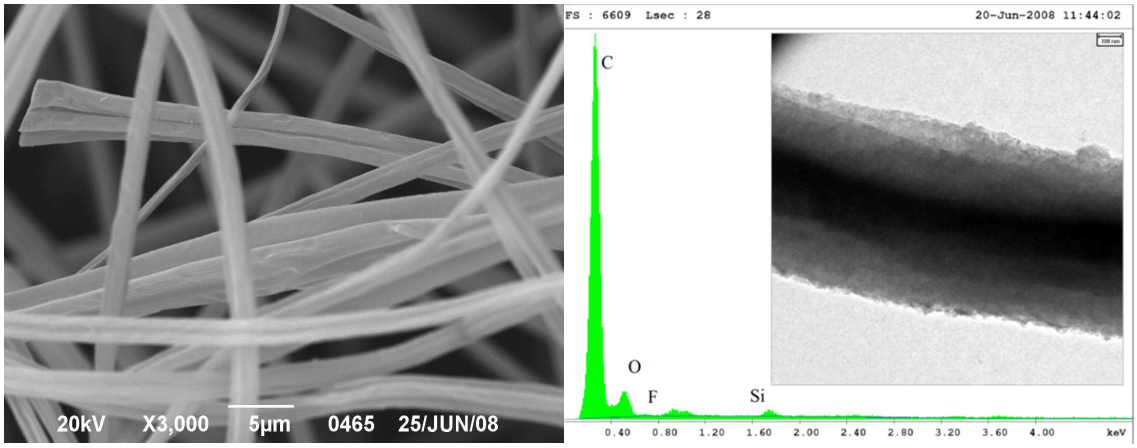

Figure 4.9. SEM and TEM/EDAX images of 24S900 fiber washed in 49% HF for 1 hr.

4.3.5. XPS analyses

Table 4.2 Reports XPS quantitative analysis results for ceramic-carbon composite fibers at different preparation stages. Results for lignin powder are also included to establish a baseline. From the results of S series, it can be concluded that the expected O/Si surface atomic ratio is slightly higher than 2 (silica) in as-spun fibers, as some TEOS and silicic acid still remains to be hydrolyzed and condensed to form SiO_2. The O/Si ratio gets closer to 2 after carbonization and matches the silica value in carbonized fibers after stabilization and in CS calcined fibers.

On the other hand, O/Al ratio in A as-spun fiber is 3.2, far from the 1.5 belonging to alumina. As commented in Section 4.3.2, oxygen amount increases after air oxidative stabilization and with longer time for fiber exposure. Carbonization of the

fibers lowers the O/Al ratio to approx. 2.5 at 600 ºC and near 1.6 at 900 ºC. The O/Al ratio of 24A600 is higher than expected due to oxygen contribution from oxygen surface groups of carbonized lignin under the alumina layer. The incomplete hydrolysis of oxygen-rich aluminum sec-butoxide, which decomposes to alumina and dibuthylether higher than 600ºC, is exposed by the even higher O/Al ratio value observed in A600 fiber. CA tubes show low carbon content and match the O/Al ratio of alumina. Higher carbon content is detected for direct carbonized composites, probably due to the lignin core getting fused and mixed with the incomplete-condensed alumina layer. On the other hand, carbon content is unaltered in carbonized composites prepared from the air stabilized fibers.

Table 4.2. XPS quantitative analyses on lignin powder and alumina-lignin and silica-lignin composite fibers.

Series	**Silicon-lignin fibers (at%)**			**Aluminum-lignin fibers (at%)**			**Powdered Lignin (at%)**	
Sample	**C**	**O**	**Si**	**C**	**O**	**Al**	**C**	**O**
X	29.5	48.8	21.7	57.0	32.7	10.3	87.5	12.5
06X	--	--	--	55.7	35.1	8.6	85.6	14.4
24X	34.1	46.8	19.1	53.7	36.0	9.2	83.6	16.4
X600	--	--	--	85.3	10.9	3.8	92.5	7.5
24X600	--	--	--	59.3	29.7	11.0	93.6	6.4
X900	26.4	49.0	24.6	73.0	16.6	10.4	93.1	6.9
06X900	--	--	--	60.6	24.1	15.3	94.3	5.7
24X900	18.5	54.0	27.5	59.9	25.6	15.5	96.1	3.9
CX	7.3	61.1	31.6	15.1	52.6	32.3	--	--
XW	82.8	15.8	0.6	88.8	10.8	0.4	--	--

Finally, XPS results allow ruling out the presence of silicon or aluminum in AW and SW carbon fibers. HF acid washing seems to effectively etch the ceramic layer in both A and S composites fibers. The remaining carbon core is richer in oxygen than carbonized lignin powders and lignin-base carbon microfibers [20]. The presence of oxygen surface groups could be of interest for catalytic applications.

4.3.6. N_2 & CO_2 adsorption analyses

Figure 4.10 depicts the nitrogen adsorption-desorption isotherms for A composite fiber series. As-spun fibers seem to be a non-porous material, showing

negligible nitrogen uptakes before and after thermostabilization in air. Incipient porosity is developed in the fibers after carbonization at 600 ºC. Air stabilization seems to neither compromise nor improve the micropores formation at this preparation point. After carbonization at 900 ºC, all mats increases notoriously nitrogen adsorption capacity and show type I adsorption isotherms, characteristics of strictly microporous materials. The absence of hysteresis loop, as nitrogen desorption branch seems to follow adsorption one, allow discarding the presence of mesopores in these fibers. Although a variation in nitrogen uptake is registered when carbonizing fibers after air stabilization at quite long times (54 hours), increasing near 20% the nitrogen adsorption amount, it can be also seen that fibers which were carbonized after small and medium stabilization times show similar and even lower nitrogen uptake than directly carbonized fibers (see 06A900 & 24A900 vs A900).

This particular discordance between medium and long stabilization times can be better explained appealing to textural properties obtained from CO_2 adsorption at 0 ºC. Comparison between micropores volume measured using both techniques allow to assess activated diffusion problems and discerning between supermicropores, which are not filled at the low relative pressure range covered by adsorption at 0 ºC of CO_2 at atmospheric pressure, and micropores with sizes under 0.7 nm, which are narrow pores where CO_2 can readily adsorb at 0ºC, while nitrogen has huge diffusional constraints to reach and get adsorbed in them at -196ºC [43]. In that sense, Table 4.3 reports the textural properties derived from the N_2 and CO_2 adsorption isotherms at 77 K and 273K, respectively. LF900 carbon lignin-based fiber and silica-carbon composite 24S900 are also included for comparison sake. The eminently microporous character of all samples are confirmed by the low A_t/A_{BET} ratios. The low micropore volumes measured by N_2 adsorption in stabilized fibers and carbonized fibers at 600 ºC are now confronted by CO_2 micropore volumes of 0.072 and circa 0.200 cm^3/g respectively. It seems that 24A fibers developed a nascent and quite close porosity during the air stabilization process, being further developed on devolatilization of lignin at 600 ºC. Raising the carbonization temperature to 900 ºC improves the development of the porosity, widening the pore size and thus allowing the diffusion of nitrogen into them, obtaining similar N_2 and CO_2 micropore volumes. Although in carbonized fibers prepared at 900ºC a clear trend is not observed between N_2 micropore volume development and air

stabilization time, CO_2 micropore volume does correlate with higher time for oxidation at 200 ºC, obtaining increases of microporosity around 30% in the best case.

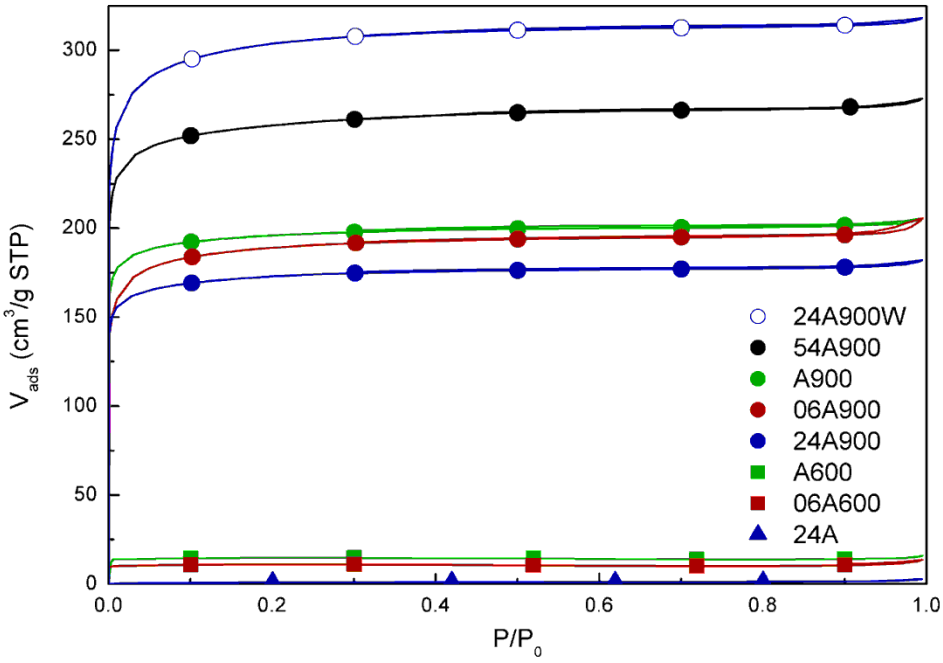

Figure 4.10. N_2 adsorption-desorption isotherms at -196 ºC of as-spun, air stabilized, carbonized and HF-cleansed alumina-lignin composites fibers.

When the alumina shell of the carbonized composite is removed (24A900W), the BET area and micropore volume turn to be very close to those reported for LF900 [20]. Highly porous carbon nanofibers could be used as supercapitors or in hydrogen storeage. It is noteworthy the specific internal area of these carbon fibers are much higher than those reported for porous carbon nanofibers from etching with HF electrospun polyacrylonitrile/SiO_2 [7], higher to those of PAN-based carbon nanofibers chemically activated using 2 M NaOH at 750 ºC [44] and similar to those of physically activated at 750 ºC with 30 vol. % of steam for 30 minutes [8]. The amorphous alumina usually has a much lower porosity and specific areas than porous carbon materials, and consequently removal of alumina shell is expected to produce a raise in microporosity. But observed differences cannot be accountable just to etching of a non-porous part of the fiber, which would produce BET area of 667/0.685=972 m^2/g. The additional developed porosity could be obtained because occluded porosity by alumina particles in the carbon core is getting available for adsorption. Furthermore, the alumina layer accounts for only 6% of total weight of the fiber, whereas the weight loss in HF treatment is more than 30%, so it could be possible that removal of part of the carbon

core is opening new porosity. Another option is partial mixing of alumina precursor and lignin during elecrospinning. Ji et al. reported the production of porous carbon nanofibers from electrospun Polyacrylonitrile (PAN)/SiO_2 composite nanofibers. After using hydrofluoric acid as etching agent, SiO_2 nanoparticles and agglomerates are removed from the carbon matrix, releasing new porosity inside them [7]. In a similar way, small droplets of alumina inside the carbon core could act as template for formation of new porosity when they are removed during HF washing.

Table 4.3. Textural properties of composite fibers

Sample	N_2 Adsorption				CO_2 Adsorption	
	A_{BET} (m^2/g)	A_t (m^2/g)	V_t (cm^3/g)	V_{meso} (cm^3/g)	V_{DR} (cm^3/g)	A_{DR} (m^2/g)
A	3	1	0.001	0.003	0.023	68
54A	4	1	0.002	0.002	0.072	213
A600	48	1	0.024	0.002	0.204	510
06A600	40	1	0.018	0.003	0.203	509
A900	715	13	0.342	0.015	0.268	667
06A900	710	10	0.296	0.020	0.253	625
54A900	996	19	0.400	0.016	0.376	938
24A900	667	10	0.298	0.014	0.313	781
24A900W	1126	18	0.473	0.013	0.406	1017
LF900	1195	21	0.523	0.025	0.443	1109
24S900	886	12	0.354	0.008	[a]n.m.	n.m.

[a]: not measured

4.3.7. Pyridine adsorption

Chemisorption of basic molecules such as pyridine (Py) is frequently used to determine the surface acidity of solids [45]. The lone electron pair at the nitrogen atom and availability to accept protons in pyridine allow interaction with Lewis and Brønsted acidic sites. Fig. 4.11 displays the adsorption and desorption kinetics of Py at 100 ◦C on alumina-carbon composite fiber carbonized at 600 ºC and 900 ºC, as well as activated carbon catalyst HA2800 (BET area: 1043 m^2/g; A^t: 475 m^2/g). A600 shows a low Py uptake before and after desorption. HA2800 have adsorbed more reversible pyridine than A900, while the amount of Py irreversibly adsorbed on boths samples are very similar (approximately 1.0 mmol/g after desorption for 20 h). Reversible or physisorbed pyridine adsorption depends on specific surface area and porosity size, therefore the lower physisorption in carbon-alumina fibers is probably related to a lower specific area

and a more constricted porosity than HA2800 carbon. On the other hand, the amount of Py retained after the desorption process (irreversible chemisorbed Py) has been related to the acidity of HA2800, which have been proven to act as catalysts for alcohol dehydrogenation [46,47]. Therefore, similar irreversible pyridine uptake on HA2800 and A900 confirms the presence of surface acidity in the alumina-carbon composites that could be useful in heterogeneous catalysis. Their use as catalysts will be further studied in a subsequent work.

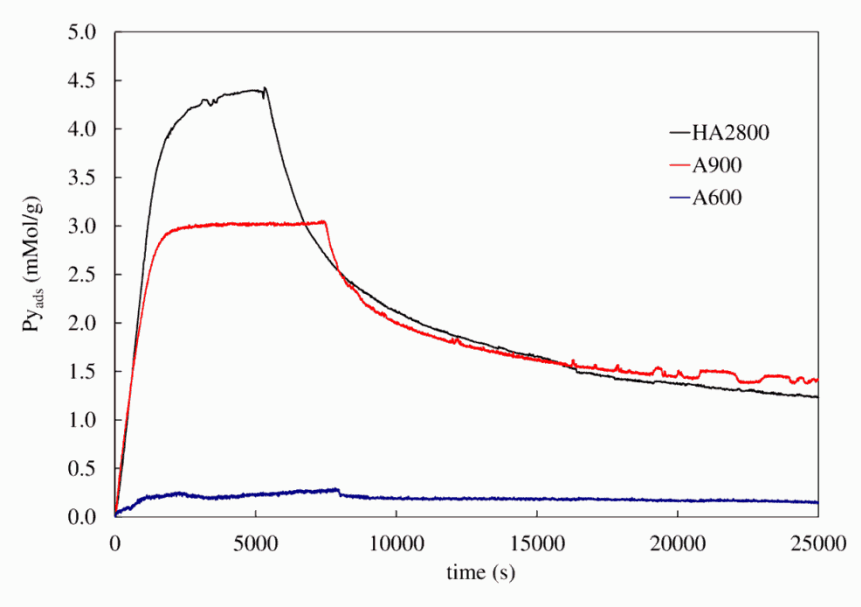

Figure 4.11. Adsorption and desorption kinetics of pyridine at 100 ◦C on A600, A900 composite fibers and HA2-800 carbon.

4.4.Conclusions

Alumina or silica-lignin fibers with sizes between 500 and 2000 nm in shell-core arrangement can be casted using coaxial electrospinning of an alkoxide precursor, not necessary aged, through the outer needle of the spinneret. Six hours of air thermostabilization at 200 ºC or carbonization at temperatures higher than 600 ºC is required to form the ceramic shell if alkoxide has not been gelified. The alkoxide precursor rate allows controlling the width of the ceramic shell. The ceramic shell allows diffusion of oxygen and other gases, but it does not allow the thermoplastic lignin diffusing outside it when fibers are heated. In consequence, these fibers can be directly carbonized if the ceramic shell is properly formed, saving a great time in the air

thermostabilization step, which is the time-controlling step in carbon fiber production. The obtained carbon/alumina composite fibers are thermally stable in air and can also be treated to prepare alumina tubes oxidizing the carbon core or carbon fibers by washing the carbonized fibers with hydrofluoric acid. These carbon fibers are highly porous, showing a narrow microporosity that gets broadened with carbonization temperature, achieving BET areas from 600 to 1100 m^2/g at 900 ºC. Moreover, XPS demonstrated that air stabilization introduces oxygen surface groups that seem to be related to an increase in porosity of about 30% in the best case. In addition, pyridine adsorption results show that the remaining functional groups after carbonization at 900 ºC are acid enough to be used as heterogeneous catalysts.

4.5.References

1. G. Larsen, R. Velarde-Ortiz, K. Minchow, A. Barrero, I.G. Loscertales. A Method for Making Inorganic and Hybrid (Organic/Inorganic) Fibers and Vesicles with Diameters in the Submicrometer and Micrometer Range via Sol−Gel Chemistry and Electrically Forced Liquid Jets. J .Am. Chem. Soc. 2003; 125: 1154-1155.

2. Y. Dzenis. Spinning continuous fibers for nanotechnology. Science 2004; 304: 1917-1919.

3. S.W. Hoi, Y.-Z. Fu, Y.R. Ahn, S.M. Jo, A. Manthiram. Nafion-impregnated electrospun polyvinylidene fluoride composite membranes for direct methanol fuel cells, J. Power Sources 2008; 180: 167-171.

4. J. Xie, Y.-L. Hsieh. Ultra-high surface fibrous membranes from electrospinning of natural proteins: Casein and lipase enzyme. J. Mater. Sci 2003; 38: 2125-2133.

5. C. Shin, G.G. Chase, D.H. Reneker. Recycled expanded polystyrene nanofibers applied in filter media. Colloid Surfaces A 2005; 262: 211-215.

6. S. Madhugiri, B. Sun, P.G. Smirniotis, J.P. Ferraris, K.J. Balkus Jr. Electrospun mesoporous titanium dioxide fibers. Micropor. Mesopor. Mat. 2004; 69: 77-83.

7. L. Ji, Z. Lin, A.J. Medford, X. Zhang. Porous carbon nanofibers from electrospun polyacrylonitrile/SiO2 composites as an energy storage material. Carbon 2009; 47: 3346-3354.

8. C. Kim, K.S. Yang. Electrochemical properties of carbon nanofiber web as an electrode for supercapacitor prepared by electrospinning. Appl. Phys. Let. 2003; 83: 1216-1218.

9. J. Zeng, X. Xu, X. Chen, Q. Liang, X. Bian, L. Yang, X. Jing. Biodegradable electrospun fibers for drug delivery. J. Control. Release 2003; 92: 227-231.

10. C. Kim, Y.J. Cho, W.Y. Yun, B.T.N. Ngoc, K.S. Yang, D.R. Chang, J.W. Lee, M. Kojima, Y.A. Kim, M. Endo. Fabrications and structural characterization of ultra-fine carbon fibres by electrospinning of polymer blends. Solid State Commun. 2007; 142: 20–23.

11. Y. Wang, J.J. Santiago-Aviles. Conductivity measurement of electrospun PAN-based carbon nanofiber, J. Mater. Sci. Lett. 2002; 21: 1055-1057.

12. M. Rose, E. Kockrick, I. Senkovska, S. Kaskel. High surface area carbide-derived carbon fibers produced by electrospinning of polycarbosilane precursors. Carbon 2010; 48: 403–407.

13. C. Kim, S.-H. Park, W.-J.Lee, K.-S. Yang. Characteristics of supercapaitor electrodes of PBI-based carbon nanofiber web prepared by electrospinning. Electrochim. Acta 2004; 50: 877–881.

14. S.-H. Park, C. Kim, K.-S. Yang. Preparation of carbonized fiber web from electrospinning of isotropic pitch. Synthetic Met. 2004; 143: 175–179.

15. X. Song, C. Wang, D. Zhang. Surface structure and adsorption properties of ultrafine porous carbon fibers. Appl. Surf. Sci. 2009; 255: 4159–4163.

16. J. Rodríguez-Mirasol, T. Cordero, J.J. Rodríguez. Preparation and characterization of activated carbons from eucalyptus kraft lignin. Carbon 1993; 31: 87-95.

17. J. Rodríguez-Mirasol, T. Cordero, J.J. Rodríguez. High-temperature carbons from kraft lignin. Carbon 1996; 34: 43-52.

18. W.M. Qiao M. Huda, Y. Song, S.-H. Yoon, Y. Korai, I. Mochida. Carbon fibers and films based on biomass resins. Energ. Fuels 2005; 19: 2576-2582.

19. M. Lallave, J. Bedia, R. Ruiz-Rosas, J. Rodríguez-Mirasol, T. Cordero, J.C. Otero, M. Márquez, A. Barrero, I.G. Loscertales. Filled and hollow carbon nanofibers by coaxial electrospinning of Alcell lignin without binder polymers. Adv. Mat. 2007; 19: 4292-4296.

20. R. Ruiz-Rosas, J. Bedia, M. Lallave, I.G. Loscertales, A. Barrero, J. Rodriguez-Mirasol, T. Cordero. The production of submicron diameter carbon fibers by the electrospinning of lignin. Carbon 2010; 48: 696-705.

21. J.L. Braun, K.M. Holtman, J.F. Kadla. Lignin-based carbon fibers: oxidative thermostabilization of kraft lignin. Carbon 2005; 43: 385–394.

22. J.F. Kadla, S. Kubo, R.A. Venditti, R.D. Gilbert, A.L. Compere, W. Griffith. Lignin based carbon fibers for composite fiber applications. Carbon 2002; 40: 2913-2920.

23. I.G. Loscertales, A. Barrero, M. Márquez, R. Spretz, R. Velarde-Ortiz, G. Larsen. Electrically forced coaxial nanojets for one-step hollow nanofiber design. J Am Chem Soc 2004; 126: 5376-5377.

24. A.-M. Azad. Fabrication of transparent alumina (Al2O3) nanofibers by electrospinning, Mater. Sci. Eng. A 2006; 435:468-473.

25. Y. Liu, S. Sagi, R. Chandrasekar, L. Zhang, N.E. Hedin, H. Fong. Preparation and characterization of electrospun SiO2 nanofibers. J. Nanosci. Nanotechno. 2008; 8: 1528-1536.

26. S. Zhan. D. Chen, X. Jiao. Y. Song. Mesoporous TiO2/SiO2 composite nanofibers with selective photocatalytic properties. Chem. Commun. 2007; 20: 2043-2045.

27. V. Maneeratana, W.M. Sigmund. Continuous hollow alumina gel fibers by direct electrospinning of an alkoxide-based precursor. Chem. Eng. J. 2008; 137: 137-143.

28. Q. Peng, X.-Y. Sun, J.C. Spagnola, G.K. Hyde, R.J. Spontak, G.N. Parsons. Atomic layer deposition on electrospun polymer fibers as a direct route to Al2O3 microtubes with precise wall thickness control. Nano Lett. 2007; 7: 719-722.

29. Y. Cheng, J. Zhang, Y. Zhang, X. Chen, Y. Wang, H. Ma, X. Cao. Preparation of hollow carbon and silicon carbide fibers with different cross-sections by using electrospun fibers as templates. Eur. J. Inorg. Chem. 2009; 28: 4248-4254.

30. I.G. Loscertales, A. Barrero, M. Marquez, R. Spretz, R. Velarde Ortiz, G. Larsen. Electrically forced coaxial nanojets for one-step hollow nanofiber design, J. Am. Chem. Soc. 2004; 126: 5376-5377.

31. S. Zhan, D. Chen, X. Jiao. Co-electrospun SiO2 hollow nanostructured fibers with hierarchical walls, Journal of Colloid and Interface Science 2008; 318: 331-336.

32. I.G. Loscertales, A. Barrero, I. Guerrero, R. Cortijo, M. Marquez, A.M. Gañán-Calvo. Micro/nano encapsulation via electrified coaxial liquid jets. Science 2002; 295: 1695-1698.

33. L. Ji, X. Zhang. Ultrafine polyacrylonitrile/silica composite fibers via electrospinning. Material Letters 2008; 62 :2161–2164.

34. D. Li, Y. Xia. Electrospinning of Nanofibers: Reinventing the Wheel? Adv. Mater. 2004; 16: 1151–1170.

35. J.J. Pireaux, M. Chtaib, Q.T. Le, R. Caudano. Caractérisation de l'interface Mylar / Al par analyses angulaires en spectroscopie de photoélectron ESCA. Le Vide, les Couches Minces 1991; 258: 86-88.

36. I.V. Plyuto, A.P. Shpak, J. Stoch, L.F. Sharanda, Y.V. Plyuto, I.V. Babich, M. Makkee, J.A. Moulijn. XPS characterisation of carbon-coated alumina support. Surf. Interface Sci. 2006; 38: 917-921.

37. J.F. Moulder, W.F. Stickle, P.E. Sobol, K.D. Bomben. In: Chastain J, King Jr RC, editors.Handbook of X-ray photoelectron spectroscopy. Eden Prairie, MN: Physical Electronics Inc.; 1995. p. 4872–4875.

38. S. Biniak, G. Szymanski, J. Siedlewski, A. Swiatkowski. The characterization of activated carbons with oxygen and nitrogen surface groups. Carbon 1997; 35: 1799–1810.

39. G. Jiang, D.J. Nowakowski, A. Bridgwater. A systematic study of the kinetics of lignin pyrolysis. Thermochim. Acta 2010; 498: 61-66.

40. P. Enzel, T. Bein. Poly(acrylonitrile) chains in zeolita channels: Polymerization and pyrolysis. Chem. Mater. 1992; 4: 819-824.

41. I. Szczygieł, A. Matraszek, J. Chęcmanowski, B. Szczygieł. Thermal behaviour of mixed alumina–silica gels obtained from alkoxides: Phase formation and morphology of powders, J. Non-Cryst. Solids 2010; 356: 2824-2830.

42. J.L. Figuereido, M.F.R. Pereira, M.M.A. Freitas, J.J.M. Órfão. Modification of the surface chemistry of activated carbons. Carbon 1999; 37: 1379–1389.

43. F. Rodríguez-Reinoso, J. Garrido, J.M. Martín-Martínez, M. Molina-Sabio, R. Torregrosa. The combined use of different approaches in the characterization of microporous carbons. Carbon 1989; 27: 23-32

44. J.S. Im, S.-J. ParkJ, Y.-S. Lee. Superior prospect of chemically activated electrospun carbon fibers for hydrogen storage. Mater. Res. Bull. 2009; 44: 1871-1878.

45. H.A. Benesi. Determination of proton acidity of solid catalysts by chromatographic adsorption of sterically hindered amines. J. Catal. 1973; 28: 176–178.

46. J. Bedia J, R. Ruiz-Rosas, J. Rodríguez-Mirasol, T. Cordero. A kinetic study of 2-propanol dehydration on carbon acid catalysts J. Catal. 2010; 271: 33–42.

47. J. Bedia, R. Barrionuevo, J. Rodríguez-Mirasol, T. Cordero. Ethanol dehydration to ethylene on acid carbon catalysts. App Catal B: Environ 2011; 103: 302–310.

5. METHANOL DECOMPOSITION ON ELECTROSPUN ZIRCONIA NANOFIBERS

5.0. Abstract

Electrospinning has been used for the preparation of pvp-zirconium acetate nanofibers. The obtained non-woven cloths have been calcined at different temperatures (200-1000 ºC) and used as heterogeneous catalysts in the gas phase decomposition of methanol. The X-ray diffraction spectra of the zirconia nanofibers show the onset of a semicrystalline tetragonal structure for the fibers calcined at 400ºC. Transformation from tetragonal to monoclinic zirconia starts at a calcination temperature between 600 and 800 ºC. SEM and TEM images of the zirconia nanofibers show fibers with a high aspect ratio and sizes as thin as 200 nm. The increase of the calcination temperature results in zirconia fiber catalysts with lower methanol steady state conversions, probably due to changes in the crystalline phase and crystal sintering. The fibers calcined at 500 ºC yielded the highest methanol conversion and selectivities to dimethyl ether. In general trend, methanol dehydrates to dimethyl ether at the lower reaction temperatures and decomposes to hydrogen and carbon monoxide at the higher reaction temperatures. Deactivation of the catalyst is observed only at the highest reaction temperature, being probably related to deposition over the fiber surface of pyrolitic carbon from cracking reaction of dimethyleter.

5.1. Introduction

Zirconia exhibits advantageous physical and chemical properties such as excellent thermal and chemical stability, high strength and fracture toughness, low thermal conductivity, high corrosion resistance and both acidic and basic properties. These advantages make zirconia materials suitable for applications in structural materials, thermal barrier coatings, oxygen sensors, fuel cells, catalysts and catalytic supports and as a gate dielectric in metal oxide-semiconductor (MOS) devices [1,2].

Nanostructured materials such as nanofibers or nanowires show interesting physical and chemical properties, which make them promising materials for applications in semiconductor, energy storage, biomedicine or catalysis fields and play an important role in fundamental research as well as industrial application [3-6]. Pore

diffusion resistance is significant in pellet shaped catalysts, while powdered catalysts, as was the practice in most laboratory-scale studies could cause problems of high pressure drop in industrial size reactors. Therefore, the use of novel forms of catalyst supports, as fiber catalysts, is a key point for many catalytic industrial processes. Fibers as catalyst supports are easy to handle, may be packed or constructed in the best form to fit the particular use and show very small resistance to diffusion and lower pressure drop [7]. In the technical literature, zirconia nanofibers or nanowires are obtained from porous anodic alumina oxide templates [8], sol-gel deposition procedures [9] or solution routes [10]. In contrast to these methods, electrospinning is a simple and straightforward method that has been used to obtain carbon and polymer fibers in the submicro and nanoscale [11-14]. In the electrospinning process, a polymer solution held by its surface tension at the end of a capillary tube is subjected to an electric field. When the applied electric field reaches a critical value, the repulsive electrical forces overcome the surface tension forces. Eventually, a charged jet of the solution is ejected from the tip of the charged conical meniscus known as the Taylor cone and a rapid, unstable whipping of the jet occurs in the space between the capillary tip and collector which leads to evaporation of the solvent, leaving a polymer fiber behind [11]. Parameters such as viscosity, flow, concentration of electrospun solution or applied voltage control diameter and length of fibers. In fact, it is possible to switch between steady electrospray and electrospinning controlling rate flow between outer and inner solutions, which allows encapsulating of core liquid [15,16].

The intensive use of biomass, especially of biomass waste, as a renewable source of energy and high added valued products could reduce significantly the dependency of the fossil fuels and decrease the carbon dioxide emissions [17]. The use of biofuels offers advantages over the fossil fuels in terms of (a) availability of renewable sources; (b) representing CO_2 cycle in combustion; (c) environmentally friendly; and (d) biodegradable and sustainable [18].

(Bio)methanol is used as source of a high amount of very valuable products by means of different catalytic processes such as, methanol to hydrocarbons [19-21] or methanol to olefins [22,23]. It has also attracted worldwide attention for onsite or onboard hydrogen production from methanol, since hydrogen is inconvenient for transporting and storage. Unlike gasoline or diesel fuel, liquid methanol can be readily

produced from biomass, it is easily adaptable to the current infrastructure, it is easily transported and stored, and finally it has a high hydrogen density [24].

One of the most promising candidates to be directly used as fuel in compression-ignition engines is dimethyl ether (DME). In the last decades the most important application of DME is its use as clean alternative fuel in diesel engines [25-27]. DME is produced by the conversion of various feedstock such as natural gas, coal, oil residues and bio-mass. Although the most interesting raw material would be bio-mass, natural gas is arguably the economically most viable feedstock at the present [28]. DME production methods consist essentially in dehydration of methanol or direct conversion from synthesis gas (syngas). In the latter case, the first step is usually production of syngas from the carbonaceous feedstock, then methanol synthesis using a copper-based catalyst, while the third step is the dehydration of methanol to DME using alumina- or zeolite-based catalysts. For the former case, second and third steps can occur simultaneously in one reactor using appropriate catalysts. A final step of purification of the product would be needed, as it may also contain some methanol and water [28]. Besides the aforementioned application as bioethanol, DME is also used to obtain many chemical products as methyl acetate, dimethyl sulphate and in propellant formulations, replacing chlorofluorocarbons (CFC) that destroy the ozone layer [29-31]. The catalytic dehydration of methanol to DME has been widely studied in the literature [32-34]. Dimethyl ether can be produced by methanol dehydration over acidic porous materials, which usually yield non desirable hydrocarbons as by-products [35]. Moreover, the methanol dehydration produces a fast deactivation of the catalysts due to the coke deposition [36,37]. To avoid the coke deposition and to increase the selectivity to DME, the strength of the acid sites should be decreased [29].

In this study we have synthesized zirconia nanofibers by the electrospinning technique. The zirconia nanofibers were further calcined at different temperatures between 200 and 1000 ºC and characterized. The calcined zirconia nanofibers have been used as heterogeneous catalysts in the gas phase catalytic dehydration and decomposition of methanol.

5.2. Experimental

5.2.1. Zirconia fibers preparation

A zirconium solution was prepared from a zirconium acetate solution diluted in acetic acid (Sigma-Aldrich, CAS 7585-20-8, $Zr^{+x} \cdot xCH_3COOH$, Zr ~16% wt.) mixed with 6%wt. of polyvinylpyrrolidone, PVP (CAS 9003-39-8, Mw = 1300000). In order to turn it spinnable, viscosity is increased shaking the mixture for 10 hours up to transparency. Figure 5.1 represents the single electrospinning setup for the preparation of the fibers. The flow rate through the spinneret of zirconium solution ranges between 0.1 and 0.4 mL/h, depending on the tip to collector electric potential difference. To apply the high voltage between the spinneret and the collector (Figure 1), two high voltage power supplies were used: one positively polarized connected to the needle and the other negatively polarized attached to a collector. This configuration provided better electrostatic conditions to prevent fibers from flying to any grounded piece near the set-up, therefore facilitating the deposition of a non-woven cloth of electrospun fibers on the collector. In a usual run, the tip-to-collector distance was 15 cm, and the electrical potential difference was 10 kV (the collector was at –5 kV and the tips at +5 kV).

Finally, the electrospun fibers were recovered in form of non-woven cloth and calcined in air at different temperatures between 200 and 1000 ºC for 2 hours in a muffle furnace, in order to eliminate solvent and stabilize the zirconia fibers.

5.2.2. Characterization

Thermogravimetric analysis (TG) and differential thermogravimetric analyses (DTG) were performed to the electrospun fibers (not calcined) in a CI Electronics MK2 balance under air flow (150 cm^3 STP/min) from room temperature to 900 ºC at a heating rate of 10 ºC/min with a sample weight of about 10 mg. X-ray diffraction patterns (XRD) of the fibers calcined in air at different temperatures were recorded in the region of 2θ = 5-80º on a Philips X'Pert PRO MPD diffractometer using CuKα monochromatic radiation (operation value 45 kV and 40 mA), using a step size of 0.017° (2θ) and counting time of 712 s/step. The monoclinic and tetragonal fractions, x_M and x_T respectively, were calculated from the XRD patterns using the following equations:

$$x_M = \frac{I_M(1\ 1\ 1) + I_M(1\ 1\ \bar{1})}{I_M(1\ 1\ 1) + I_M(1\ 1\ \bar{1}) + I_T(0\ 1\ 1)}$$

$$x_T = 1 - x_M$$

where I_M and I_T are the integrated intensities of the monoclinic and tetragonal phases, respectively [38]. The average crystallite size of the samples size was calculated from the peak $(11\bar{1})$ for the monoclinic phase and from the (011) for the tetragonal one using the Scherrer equation [39]:

$$D = \frac{k \cdot \lambda}{\beta \cdot \cos\theta}$$

where D is the crystallite size (nm), λ is the radiation wavelength (0.15406 nm), θ is the diffraction peak angle, β is the corrected half-width at half-maximum intensity (FWHM) in radians and k is a crystallite shape constant, here taken as 0.9.

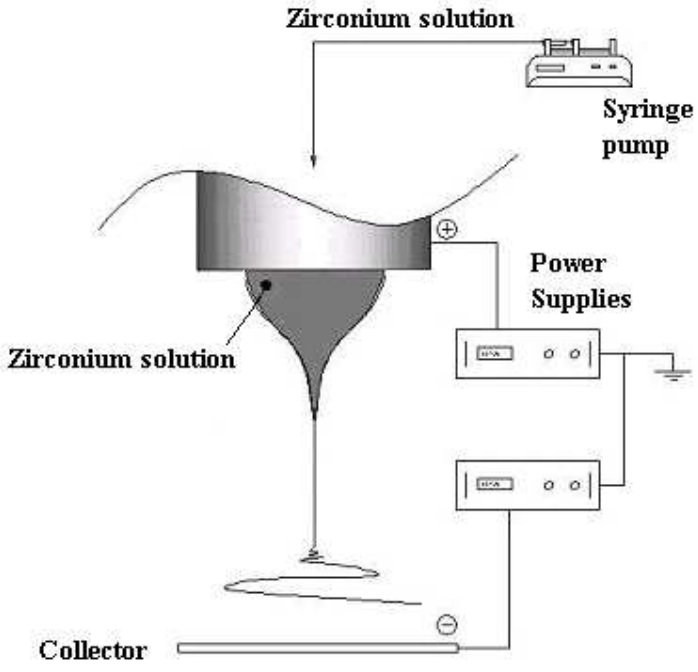

Figure 5.1. Electrospinning set up.

The porous structure was characterized by N_2 adsorption-desorption at -196 ºC and by CO_2 adsorption at 0 ºC, carried out in a Micromeritics ASAP2020 apparatus. Samples were previously outgassed for 8 hours at 150 ºC under vacuum. From the N_2 adsorption/desorption isotherm, the specific surface area (A_{BET}) was calculated by applying the BET equation. The surface chemistry of the samples was studied by X-ray photoelectron spectroscopy (XPS) analysis, using a 5700C model Physical Electronics apparatus with MgKα radiation (1253.6 eV). For the analysis of the XPS peaks, the C1s peak position was set at 284.8 eV and used as reference to locate the other peaks. The fitting of the XPS peaks was done by least squares using Gaussian-Lorentzian peak shapes.

FTIR were obtained using a Bruker Optics Tensor 27 FT-IR spectrometer by adding 256 scans in the 4000-400 cm^{-1} spectral range at 4 cm^{-1} resolution. Pressed KBr pellets at a sample/KBr ratio of around 1:250 were used. The type of surface acidity (Brönsted or Lewis) was studied by FTIR analysis of the sample with chemisorbed pyridine. The inlet partial pressure of the pyridine was 0.02 atm and it was established by saturating a stream of He with the organic base in a saturator at controlled temperature. The pellets were exposed to the probe molecule, pyridine, at 100 ºC and a pressure of 0.02 atm for 120 min. The wafer was then evacuated during 1 hour at the adsorption temperature and then the spectrum was recorded.

The surface morphology was studied by scanning electron microscopy (SEM) using a JSM 840 JEOL microscope working at 25 kV and by transmission electron microscopy (TEM) in a Philips CM200 microscope at an accelerating voltage of 200 kV.

5.2.3. Methanol decomposition

The zirconia nanofibers were used as catalysts in the dehydration and decomposition of methanol at atmospheric pressure in a fixed bed microreactor (i.d. 4 mm) placed inside a vertical furnace with temperature control. In a typical experiment 80 mg of zirconia fibers were used as catalyst. Helium was saturated with methanol (Sigma–Aldrich, >99.9%) vapor by contact in a saturator at controlled temperature resulting in partial pressures from 0.01 to 0.04 atm and space times between 0.027 and 0.107 $g \cdot s/\mu mol$ (GHSV from 1770 to 7000 $m^3_{gas} \cdot h^{-1} \cdot m^{-3}_{catalyst}$). To avoid the

condensation of any reactant or product, all the lines from the saturator to the gas chromatograph were heated above 120 ºC.

The concentrations of methanol and products in the outlet gas stream were analyzed by gas chromatography (Perkin-Elmer, Autosystem GC) using an auto-sampling valve with a methyl silicone capillary column (HP-1, 50 m) and a flame ionization detector. A mass spectrometer (OmnistarTM, Pfeiffer Vacuum) was used to analyze the outlet gas concentrations of CO_2, CO, H_2 and H_2O. In all the cases carbon and hydrogen mass balances were closed with errors lower than 5%. The methanol conversion is defined as the molar ratio of methanol converted to methanol fed to the reactor. The selectivity is defined as:

$$S_i = \frac{C_i}{\sum_i C_i}$$

where C_i is the molar flow of i product in the outlet stream. The carbon-containing products detected in the decomposition of methanol catalyzed by the zirconia nanofibes were methane, ethylene, propylene, butenes, dimethyl ether, carbon monoxide and carbon dioxide. Hydrogen-containing products were hydrogen and water.

5.3. Results and discussions

5.3.1. Fiber characterization

5.3.1.1. Characterization by SEM, TEM and EDAX

Figure 5.2.a presents a SEM image of the as-spun zirconium acetate nanofibers. The fibers show a high aspect (length to diameter) ratio, and no fused zones or beads were found. Fiber size is quite uniform, ranging from 300 to 500 nm and mean diameter of 350 nm. After calcination at 500 ºC, the resultant zirconia fibers are able of retain the cylindrical shape and high aspect ratio of electrospun fibers, while thermal decomposition of zirconium acetate causes a diameter shrinkage of about 30%, Figure 5.2.b. Zirconia fibers with sizes lower than 200 nm are produced, showing an average diameter of 240 nm. Higher calcination temperatures do not render any further diameter reduction. Size of as-spun fibers is similar to those obtained from electrospinning of

mixtures of PVP and zirconia suspensions [40], although shrinkage after calcination was not detected in this case because only PVP is removed during the heat treatment.

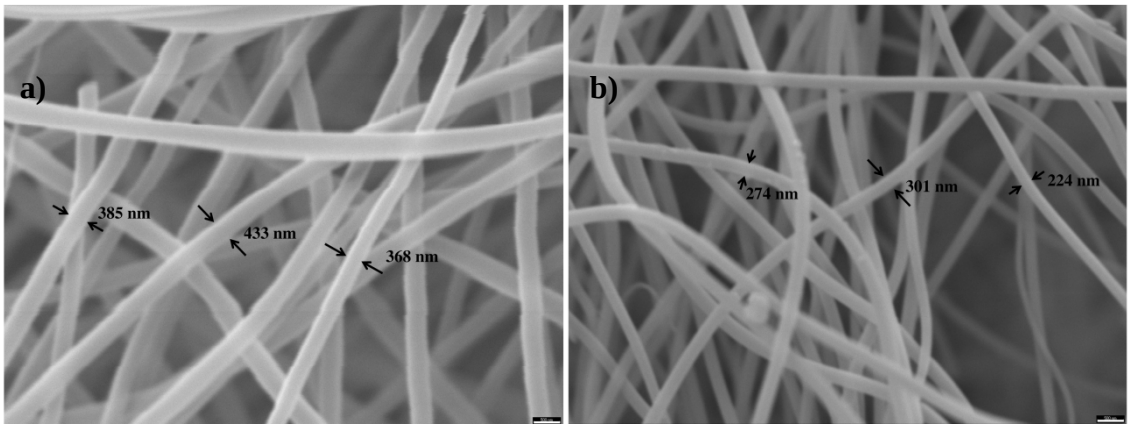

Figure 5.2. Scanning electron micrographs of (a) as-spun zirconium acetate nanofibers (b) zirconia nanofibers calcined at 500 ºC (bar lengths, 500 nm).

Figure 5.3 displays a collection of TEM images of zirconia nanofibers calcined at 500 and 1000 ºC. Fibers calcined at 500 ºC, Figure 5.3.a, show the onset of a crystalline structure. Small ordered regions with sizes around 10-20 nm appears inside the amorphous zirconia core of the fiber. When calcination temperature is raised to 1000 ºC, fiber surfaces gets intensely roughened, Figure 5.3.b. Zirconia grains with sizes of 30 nm are found arraying firmly against each other. These grains seem to be deformed prisms with parallelepiped sides, Figure 5.3.c. Figure 5.3.d. details the inner structure of those grains. The stacks of ordered zirconia layers observed in the upper grain of the micrography point out the crystalline nature of the grains that compose the nanofibers.

Figure 5.3.e shows four selected-area electron diffraction pattern (SAED) of fibers calcined at increasing temperatures. The microstructure evolution after heat treatment at increasing temperatures is clearly proved. At 200 ºC, no diffraction pattern is obtained. On raising calcination temperature to 500ºC (Figure 5.3.e), SAED verified the presence of crystalline ZrO_2 displaying characteristic diffuse electron diffraction rings. The continuous diffraction rings in nanofibers calcined at 500 ºC indicate that the crystals have random orientation, whereas the absence of rings in dotted SAED image taken from fibers calcined at 800 and 1000 ºC remarks the higher crystallinity and long-range order attained at temperatures beyond 600 ºC.

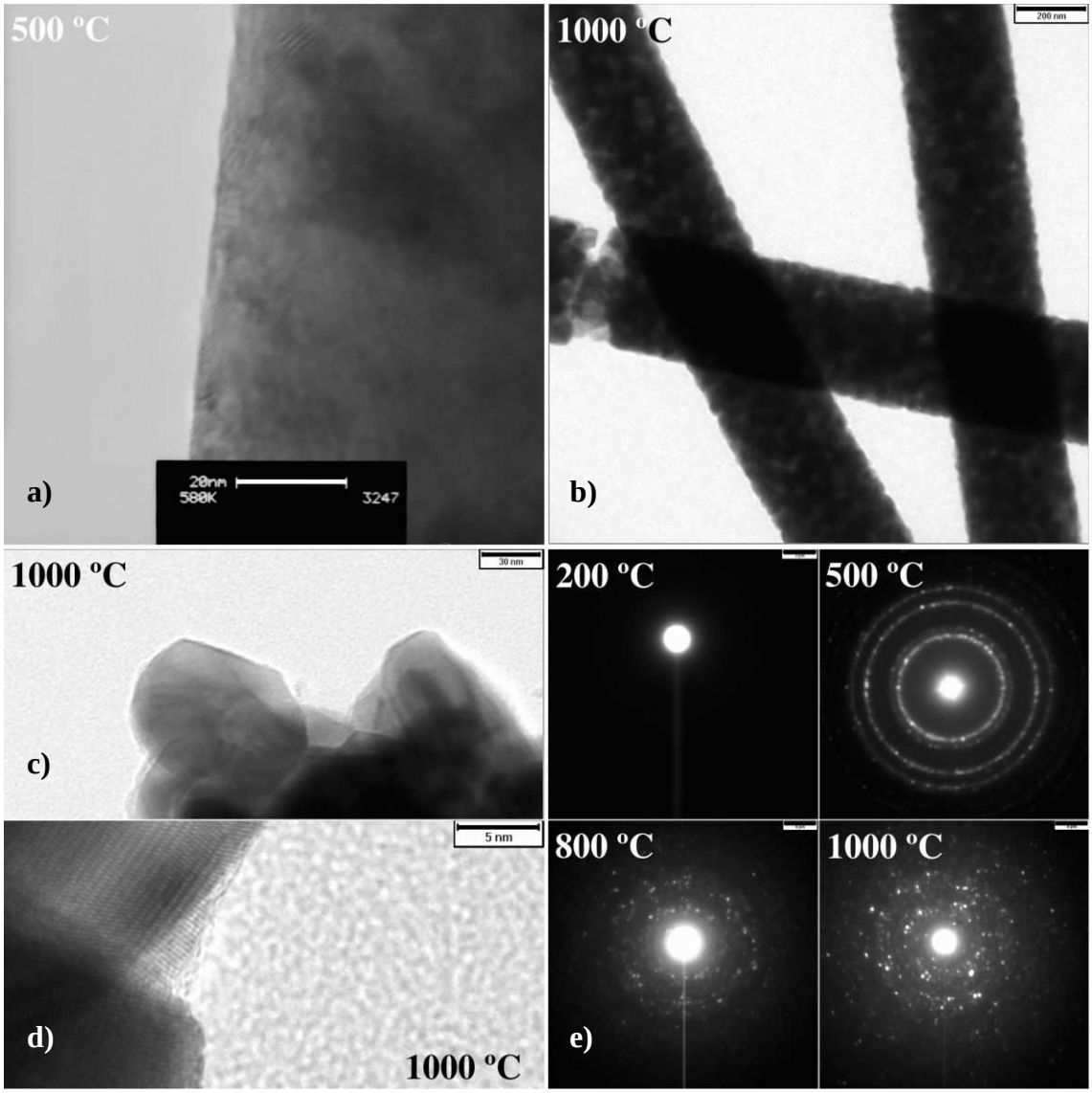

Figure 5.3. TEM and SAED images of zirconia nanofibers calcined at different temperatures. Bar lengths: (a) 20 nm (b) 200 nm (c) 30 nm (d) 5 nm.

Figure 5.4 represents the energy dispersive X-ray spectroscopy analysis (EDAX) of the fibers calcined at 200 and 800 ºC. The fibers calcined at 200 ºC show a clear peak associated to carbon indicating that the solvents used in the formulation of the fibers are not completely removed. However, EDAX of fibers calcined at 800 ºC displays no carbon peak which suggests a correct removal of both PVP and carbonate and acetate ligands during the calcination process.

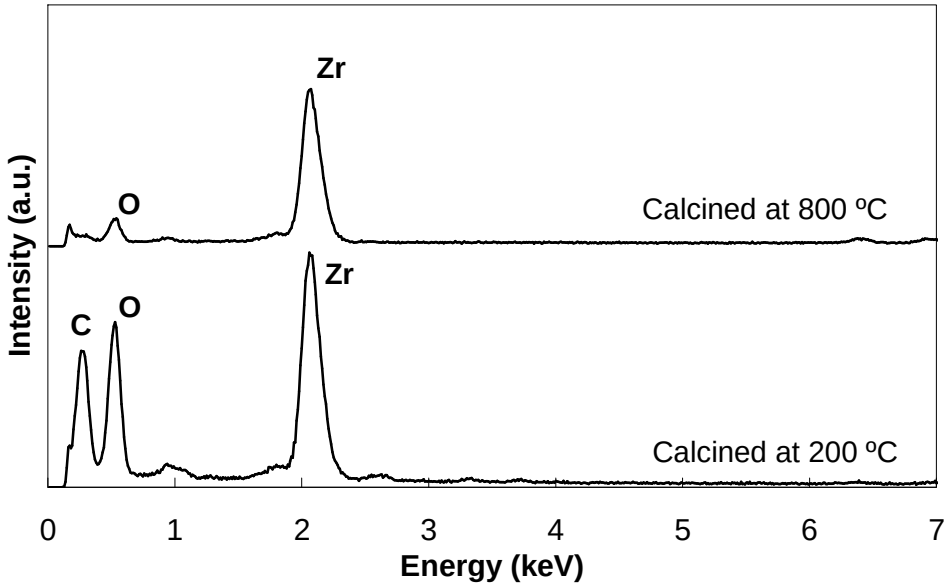

Figure 5.4. Energy dispersive X-ray spectroscopy analysis (EDAX) of the fibers calcined at 200 and 800 ºC.

5.3.1.2. Characterization by TG-MS

Figure 5.5 represents the weight loss (TG) and the derivative of the weight loss (DTG) as a function of temperature, from room temperature to 900 ºC at 10 ºC/min. The outlet calcination products where monitored using a mass spectroscopy (MS). The TG plot shows three major weight loss zones at 56, 340 and 678 ºC. The DTG peak at low temperature corresponds to evaporation of moisture. The remaining solvent from the zirconium acetate precursor used in the formulation of the spinable solution (mainly acetic acid and ammonia from ammonium zirconium carbonate), also evolved to 200-250 ºC. Together they sum up 20.8% of the total weight of electrospun fibers. The mass loss registered around 300-400 ºC is about 30.4% and can be related to the decomposition of the PVP polymer, as the oxidation temperature of the polymer fits in that range. The zirconium-PVP mixture used as precursor solution has in its formulation 20.3% of equivalent ZrO_2 and 5.7% of PVP. The remaining fiber cloth weight after calcination at 900 ºC is 45.2%, where fiber is expected to be composed mostly of ZrO_2. PVP amount can be then estimated from the aforementioned starting composition, if we consider no PVP losses during the preparation process, to be 12.5%. Therefore, the remaining 17.9% mass reduction at 300-400 ºC is thus attributed to decomposition of acetate ligands and dehydroxilation of hydrated zirconia in the as-spun fiber. The third peak observed in the DTG plot, with the maximum located at 678.5 ºC is coupled to

evolution of CO_2, thus is associated to decomposition of the zirconia carbonate. The small and continuous mass loss beyond that temperature is mainly related to oxidation of decomposition products from acetate ligands and further dehydroxilation reactions, as suggests the presence of CO_2 and small amount of H_2O, detected by MS in the outlet gas at those temperatures.

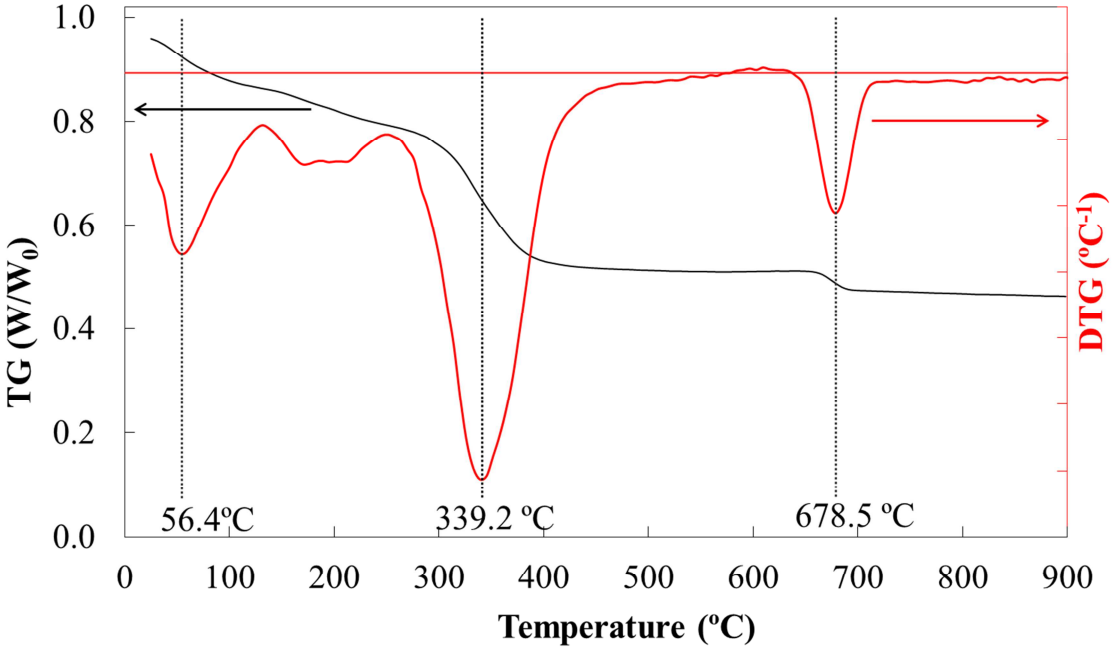

Figure 5.5. TG (a) and DTG (b) profiles of the electrospun zirconia fibers.

5.3.1.3. Characterization by XRD

The X-ray diffraction spectra of the zirconia nanofibers calcined at different temperatures from 200 and 1000 ºC are shown in Figure 5.6. The zirconia fibers calcined at 200 ºC show amorphous structure. The onset of a semicrystaline tetragonal (T) structure is observed for the fibers calcined at 400ºC. It seems the initial crystal phase right after the start of crystallization depends on sample preparation methods, although it is stated that usually tetragonal form is the preferential phase during crystallization of amorphous zirconia [41]. Transformation of tetragonal to monoclinic (M) zirconia starts at a calcination temperature around 600 ºC. Calcination at temperatures higher than 800 ºC results in sharpening and increasing intensity of the monoclinic peaks and a further decrease of tetragonal zirconia. The percentage of tetragonal phase and the crystallite size obtained by the Scherrer equation for the

zirconia fibers calcined at different temperatures are reported in Table 5.1. The similar cristal size of fibers calcined at 500 and 600 ºC seems to point out the hindering effect of residual carbonate on the crystallization process. The increase in calcination temperatures from 600 to 1000 ºC was accompanied by enlargement of the crystallite size. For the fibers calcined at 1000 ºC most of the zirconia is in monoclinic phase.

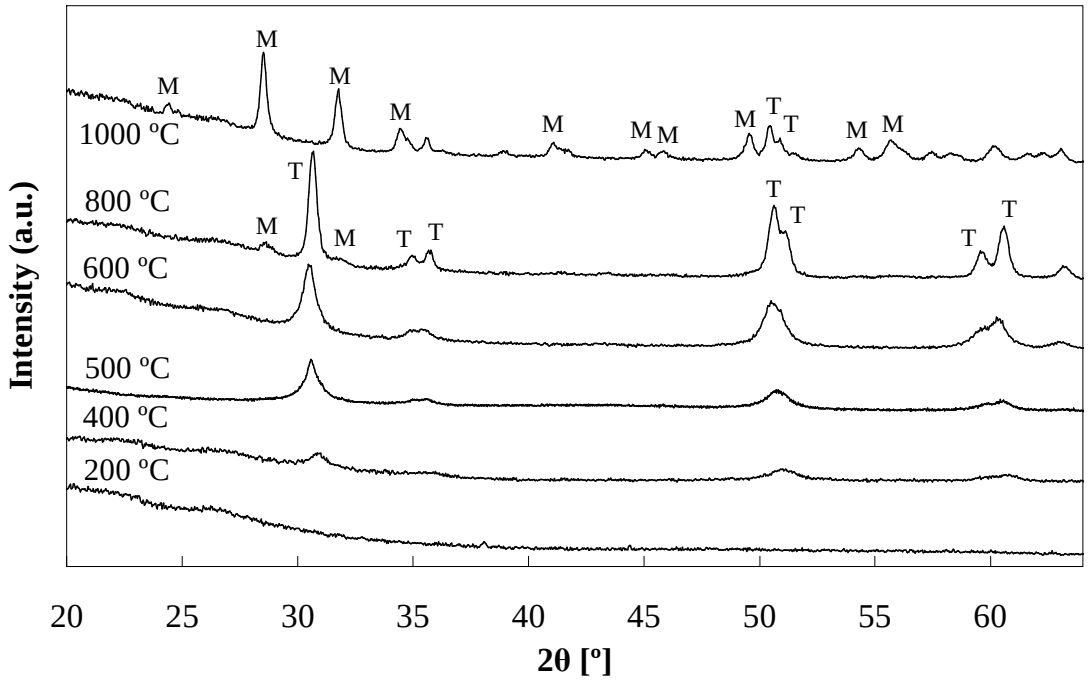

Figure 5.6. XRD patterns of zirconia fibers calcined at temperatures between 200 and 1000 ºC.

Table 5.1. Percentage of tetragonal phase and the crystallite size of the zirconia fibers calcined at different temperatures.

Calcination temperature (ºC)	% Tetragonal phase	Crystallite size (nm)
200	--	Amorphous
400	--	Poorly crystalline
500	100	14.5
600	100	14.9
800	88.5	19.8
1000	14.6	26.9*

* Obtained from peak at 2·θ at 28.54º

5.3.1.4. Characterization by N_2 adsorption

The porous structure of as-collected and calcined zirconia fibers at 500 ºC has been analyzed by N_2 adsorption-desorption isotherms at -198 ºC. Both as spun and calcined fibers at 500 ºC show very low N_2 adsorption resulting in BET areas of 3.4 and 5.9 m^2/g, and external surface areas of 2.5 and 3.5 m^2/g, respectively. The expected external surface area of the fiber can be estimated, assuming cylindrical shape of fiber, taking into account the mean fiber radio and zirconia density from the expression, $A = \frac{2 \cdot R^2}{\rho}$, which results in values of 2.0 and 2.9 m^2/g for as-spun and calcined fiber, respectively. Reversing the expression is possible to estimate mean fiber radio, which is 290 nm for as-spun and 200 nm for calcined fiber. The small difference observed between the calculated values taking into account the former equation and those obtained from the N_2 isotherms can be explained by external roughness of fiber surface being evidently unaccounted or by uncorrected assessment of mean diameter of fiber, probably related to a non-symetric size distribution with lower side deviations.

5.3.1.5. Characterization by XPS

Table 5.2 summarizes the atomic surface concentrations obtained from the numerical integration of the XPS peaks for the zirconia nanofibers not calcined and calcined at different temperatures. The freshly electrospun zirnonia nanofibers show a high amount of carbon due to the presence of PVP polymer and carbonate ligand of the zirconia precursor used in the formulation of the fibers. The presence of a low but significant amount of surface nitrogen in these fibers is due to the utilization of the PVP polymer as binder, as sample preparation for XPS analysis forces removal of residual ammonia,as well as moisture and acetic acid. The detected amount of surface zirconia is higher than that calculated from the PVP/zirconia ratio and using the molecular formulas of the binder polymer and the two possible zirconium species after electrospinning: zirconium carbonate or zirconium acetate (7.6 for the latter and 8.9% at. for the former). On the other hand, nitrogen content is lower than expected (2.0 and 2.8% for carbonate and acetate zirconia, respectively), therefore differences are assessed to zirconium-containing species being primarily displayed in fiber surface. Calcined nanofibers at 500 ºC and higher temperatures do not show nitrogen amount, and they have a much lower carbon content than the freshly electrospun fibers. This seems to be

in agreement to the TG analysis (Figure 5.5), where PVP decomposition finishes at temperatures around 500 ºC, whereas carbonates are removed at temperatures higher than 650 ºC, explaining the slightly higher surface carbon and oxygen contents in fibers calcined at 500 ºC. That content seems to be unaltered at temperatures higher than 800 ºC. The calcination evidently increases the surface oxygen and zirconia content, which show an atomic ratio (O/Zr) value close to 2.

Table 5.2. Atomic surface concentration (%) of zirconia fibers determined by XPS quantitative analysis.

	%C	**%N**	**%O**	**%Zr**	**O/Zr**
Freshly electrospun	50.9	1.7	37.5	9.9	3.79
Calcined at 500 ºC	19.5	--	54.0	26.5	2.04
Calcined at 800 ºC	17.7	--	54.2	28.1	1.93
Calcined at 1000 ºC	17.9	--	54.3	27.8	1.95
Calcined at 500 ºC (after reaction at 600ºC)	82.7	--	11.6	5.7	2.04

Figure 5.7 show the C1s deconvoluted spectra, for the freshly electrospun and C1s spectra for the calcined (500 ºC) zirconia fibers. The C1s deconvoluted spectrum show three different peaks (i) at 284.8 eV associated to C-C and C-H bonds, (ii) at around 287.6 eV that could be related to the aldehyde group of the PVP polymer and (iii) at approximately 288.6 eV associated to carboxyl groups from the carbonates and maybe to acetate ligands from acetic acid used as solvent for the fiber formulation [42]. In contrast, the C1s spectra of the fibers calcined at 500 ºC presents a main peak located at 284.8 eV, less intense than that observed for the freshly fibers, probably due to aliphatic carbon. A low photoemission in the carboxyl region is still detected for the calcined fibers, probably related to the presence of carbonates that are not fully removed at the current calcination temperature.

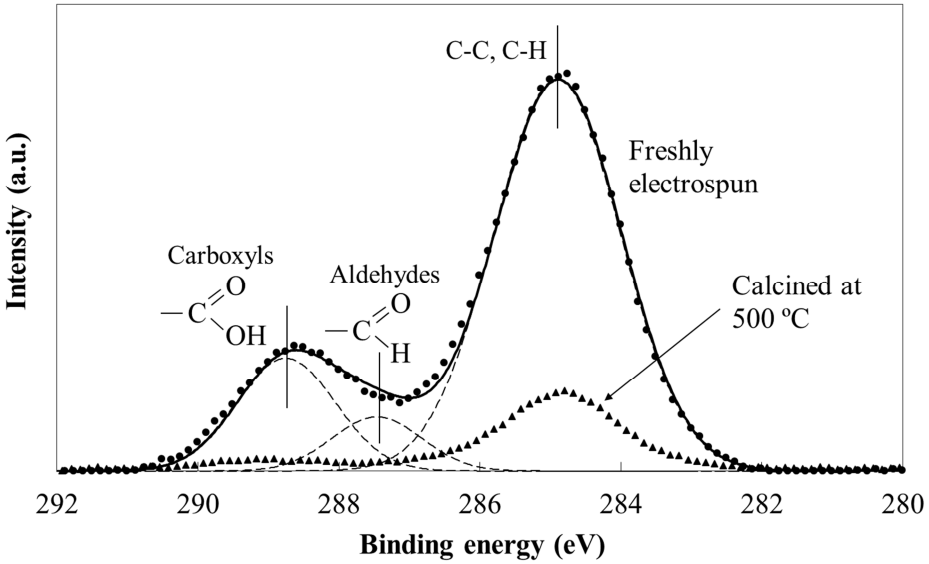

Figure 5.7. C 1s spectra of the freshly elesctrospun (deconvoluted) and calcined at 500 ºC zirconia fibers.

Figure 5.8 represents the Zr3d spectra of as-spun and the calcined (500, 800 and 1000 ºC) zirconia fibers. The Zr3d region of the spectra for all the catalysts present a doublet corresponding to $Zr3d_{5/2}$ and $Zr3d_{3/2}$ [42]. The separation between Zr $3d_{3/2}$ and Zr $3d_{5/2}$ peaks, due to spin orbital splitting, is a quantized value of 2.2 eV. The $Zr3d_{5/2}$ peak maximum is close to 182 eV for all samples, being attributed to Zr^{4+}. Nevertheless, it can be noticed a shift of the maxima towards lower photoemission energies when calcination temperature was increased. This could be a consequence of the different coordination environments of zirconium and oxygen in zirconia polymorphs. In the tetragonal lattice the Zr^{4+} cation is octacoordinated and the O^{2-} anion is tetracoordinated. Whereas in the monoclinic lattice the Zr^{4+} cation is heptacoordinated and the O^{2-} anion is either tri- or tetracoordinated [43]. Furthermore, the high-temperature annealing favors the removal of hydroxyls of terminal Zr-OH, which was also seem in O1s spectra (not shown), producing more oxygen defects [44]. This would render a somehow lower oxidation state for monoclinic zirconia, which is the most available crystalline phase of ZrNF-1000.

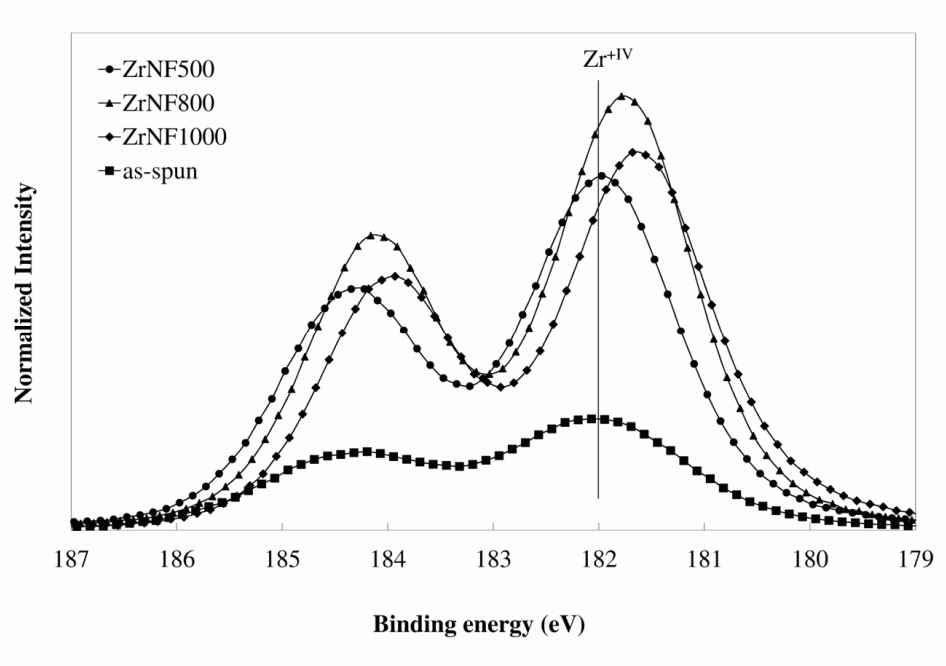

Figure 5.8. Zr 3d spectra of the freshly elesctrospun and calcined zirconia fibers.

5.3.1.6. Characterization by pyridine adsorption

Adsorption of pyridine (Py) on the surface of acid solids is frequently used for the characterization of the surface acidity. The use of IR spectroscopy to analyze adsorbed pyridine also allows discriminating between the different acid sites. The coordination of Py molecules to the surface is indicative of exposure on the surface of coordinatively unsaturated metal sites, i.e. Lewis acid sites. On the other hand, protonation of Py molecules into pyridinium ions are indicative of the availability of Brönsted acid sites (bridging or multicentered OH groups and coordinated H_2O molecules) [45]. Occurrence of both acid sites is likely to happen in crystalline zirconia. Figure 5.9 represents the FTIR spectra of ZrNF-500 before and after pyridine chemisorption over the frequency range of ring breathing modes of vibration. The band at 1635 cm^{-1} in the ZrNF-500 spectrum is attributed to the flexion vibration of the O-H band of terminal hydroxyl groups. The presence of a band at 1620 cm^{-1} could be associated to the υ_{8a} vibration mode of pyridine and suggests the presence of Lewis acid sites, which is supported by the peak at 1441 cm^{-1}, related to the υ_{19b} vibration mode of pyridine on Lewis acid sites [45]. On the other hand, appearance of protonated pyridine species over Brönsted acid sites could not be undoubtedly concluded. In our case, it is clearly seen a peak at 1540 cm^{-1}, which is assessed to υ_{19b} vibration mode of pyridine on

Brönsted acid sites; however, the υ_{8a} vibration mode (1640–1630 cm^{-1}) is not clearly resolved [45]. Nonetheless, the presence of –OH groups in terminal positions in the crystalline framework which could work as Brönsted acids was confirmed by XPS O1s and Zr3d spectra, along with Lewis acidity detected on surface, makes conceivable further use of these fibers as catalyst in methanol dehydration.

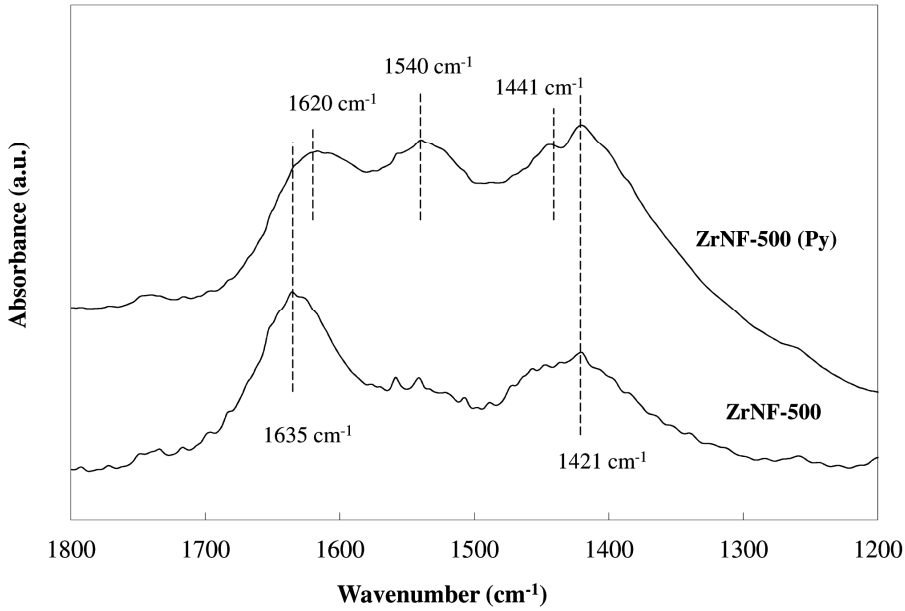

Figure 5.9. FTIR spectra of ZrNF-500 sample without and with chemisorbed pyridine [ZrNF-500 (Py)].

5.3.2. Methanol decomposition

5.3.2.1. Methanol decomposition over calcined zirconia nanofibers

Figure 5.10.a represents steady state methanol conversions as a function of reaction temperature at an inlet methanol vapor pressure of 0.02 atm and space time of 0.214 g·s/µmol for zirconia fibers calcined at different temperatures, 500, 800 and 1000 ºC. ZrNF-500 shows a similar performance (conversion and selectivity) to that reported for grounded (20-42 mesh) pure zirconia catalyst pre-conditioned at 550 ºC in air for 3.5 hours, working at higher methanol partial pressure (P_{MeOH}= 0.15 atm and space time of 0.077 g·s/µmol) [27]. The highest calcination temperatures analyzed, 1000 ºC, results in a catalyst with the lowest methanol steady state conversion values. Li et al. [46] observed changes in the selectivity of the CO hydrogenation reaction for monoclinic

and tetragonal zirconia and Stichert et al. [47] stated that the activity of monoclinic sulfate zirconia is lower by a factor of 2–5 compared to that of tetragonal sulfated zirconia for n-butane isomerization in a fixed bed reactor.

Differences in activity could be associated to the crystal size and surface properties of the fibers by changing from tetragonal to monoclinic phase, or to differences in surface acidity, i.e. nature, strength and amount of acid sites, which happens to be related to crystalline properties and calcination temperature. Brönsted acid sites or Lewis acid–base pair sites are believed to play a role in methanol dehydration and, generally, the stronger the acid sites the more active the catalysts. As far as Brönsted sites are involved, their strength and the reaction temperature should be controlled if hydrocarbons formation is to be avoided. The reaction mechanism based on Lewis acidity, on the other hand, requires an adjacent acid–base pair sites to provide the reaction between the adsorbed alcohol molecule on an acidic site and an adsorbed alkoxide anion on a basic site [48-50]. Fibers calcined at high temperatures have faced a more pronounced dehydroxilation, rendering lower number of Brönsted acid sites than ZrNF-500. For the fibers calcined at 1000 ºC, although in monoclinic zirconia high-temperature annealing favors the production of more oxygen defects, i.e. Lewis sites [44], the number of those acid sites available for methanol adsorption is lower, as sintering leads to higher crystal size which reduces the surface/bulk zirconia amount ratio.

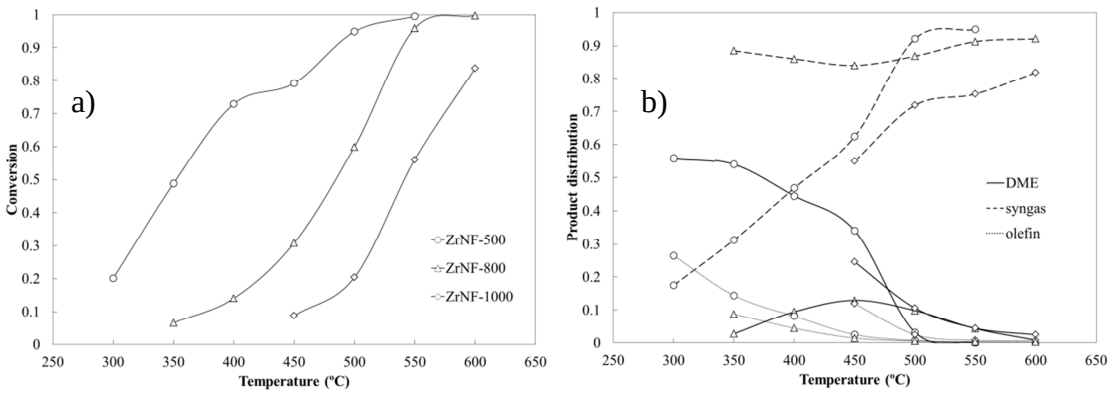

Figure 5.10. Steady state methanol conversions (a) and distribution of carbon products for ZrNF-500 (circles), ZrNF-800 (triangle), ZrNF-1000 (diamond) (b) as a function of reaction temperature. Inlet methanol vapor pressure of 0.04 atm, space time of 0.214 $g \cdot s \cdot \mu mol^{-1}$.

Figure 5.10.b represents the distribution of carbon products as a function of reaction temperature for the zirconia nanofibers calcined at 500, 800 and 1000ºC. DME, CO, H_2, H_2O were the main products found by GC/MS at reactor exit. Propene and small amounts of C4 hydrocarbons, named olefins for brevity sake, were also found at low temperatures. Secondary products were methane and CO_2 at T>500ºC, showing distribution values lower than 10%. H_2O/(DME +olefin/2) molar ratio values were found to be close to 1, whereas H_2/CO ratio values were near 2, which suggest that syngas is produced from methanol rather than for DME, being differences accountable to hydrogen formed in methanation of methanol. Small traces of ethane were found for ZrNF-500 at 550ºC. The low amount of ethene obtained in our study is in agreement with the previously reported by Gayubo et al [37] for the methanol-to-olefins process over a SAPO-18 catalyst. In general trend, at low-intermediate reaction temperatures methanol is mainly dehydrated to dimethyl ether and olefins (propylene or butenes), while at high reaction temperatures methanol begins to decompose to CO and hydrogen, with small participation of methanation [26,27,51]. Finally, the carbon dioxide could be produced by water-gas shift, the methane/CO_2 ratio observed, close to a value of 1, suggests that it is probably formed as a side product of methanol methanation and perhaps in Boudart reaction (2CO ➔ C + CO_2). Selectivity values to DME for the different catalysts followed the order ZrNF-500>ZrNF-800>ZrNF-1000. In consequence, the kinetics of methanol dehydration was studied in ZrNF-500; although the ones calcined at 800 and 1000 ºC render high selectivity to syngas, which could be of interest for catalyst support in hydrogen production from methanol.

5.3.2.2. Catalyst deactivation

Experiments conducted at 550 ºC with time on stream longer than 18 hours over ZrNF-500 did not show relevant decrease in conversion. For higher reaction temperatures, deactivation of the catalysts takes place in about 6 hours of time on stream. The temperature at which the deactivation begins increases with the calcination temperatures of the zirconia fibers from around 580 ºC for the ZrNF-500 to 650 ºC for ZrNF-1000. This change in deactivation temperatures could be related to the lower activity of the catalyst, due to a lower number of acid sites with increasing calcination temperatures, as previously discussed. Table 5.2 shows the atomic surface concentration of the fibers calcined at 500 ºC after reaction at high temperatures. A significant

increase of the atomic concentration of carbon for the wasted catalyst is observed, suggesting the deposition of pyrolytic carbon during the methanol decomposition reaction. Figure 5.11 represent TEM micrographs of zirconia nanofibers calcined at 500 ºC after reaction with methanol at 600ºC for 6 hours. Micrograph in Fig 5.11.a shows a thin layer of 5-20 nm of deposited pyrolytic carbon over the zirconia fiber. Figure 5.11.b presents a higher magnification micrograph of this layer, in which two different structures are observed. The inner one is constituted by regular zirconia crystals, in which the ordered planes of the zirconia are observed. The exterior one seems to consist in a layer of pyrolytic carbon –composition confirmed by EDAX- covering the external boundary of the zirconia. These facts point out that deactivation of catalyst probably proceeds by pyrolytic carbon formation by means of cracking or Boudart reaction, blocking the access to the active sites. Air-TG of wasted catalyst shown that the amount carbon pyrolitic deposited was around 2.5% wt. Carbonaceous deposits were burnt-off at 400 ºC, but further experiments over the regenerated nanofiber are required to verify recovery of activity.

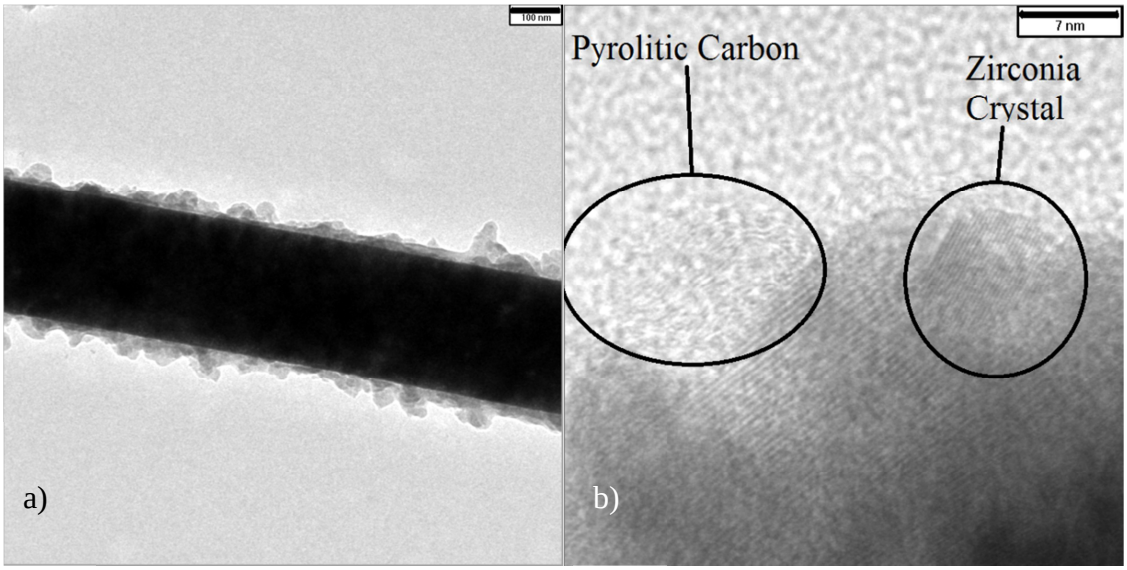

Figure 5.11. Transmission electron micrographs of the ZrNF-500 after reaction with methanol at 600 ºC bar lengths: (a) 100 nm (b) 7 nm.

5.3.2.3. Mechanism for methanol consumption

In the proposed reaction mechanism, adsorbed methanol is first dehydrated to dimethyl ether. DME and methanol then interacts to produce light olefins. Side reactions for decomposition of methanol to hydrogen and CO runs in parallel. Lastly, at

high temperatures, adsorbed methanol undergoes methanation, producing methane and carbon dioxide. It is generally accepted that the dehydration of methanol to dimethyl ether over solid acid catalysts goes through an intermediate protonated surface methoxyl, which is subjected to a nucleophilic attack by methanol [51]. However, in the literature, there is no agreement for the reaction mechanism responsible of the formation of the C-C bond of the olefins from the C1 reactants (methanol and dimethyl ether). A summary of the most relevant proposed mechanisms for this step are reported by Stöker [26]. On the other hand, water is believed to block active sites for methanol consumption through competitive adsorption with methanol on the catalyst surface [21]. An experiment over the same catalyst and operating conditions, just adding water in methanol equimolar amount to gas inlet, proved to delay 30 ºC methanol conversion onset temperature. In this sense, the following reaction scheme is proposed:

$$CH_3OH + l \overset{Km}{\leftrightarrow} CH_3OH - l \qquad (1)$$

$$CH_3OH - l + CH_3OH \xrightarrow{k_{DME}} DME - l + H_2O \qquad (2)$$

$$DME - l \overset{1/K_{DME}}{\longleftrightarrow} DME + l \qquad (3)$$

$$H_2OH + l \overset{Kw}{\leftrightarrow} H_2O - l \qquad (4)$$

$$DME - l + CH_3OH \xrightarrow{kole} C_3H_6 + 2H_2O + l \qquad (5)$$

$$CH_3OH - l \xrightarrow{ksyn} CO - l + 2H_2 \qquad (6)$$

$$CO - l \xrightarrow{1/K_{CO}} CO + l \qquad (7)$$

$$2CO - l \xrightarrow{kbou} C - l + CO_2 \qquad (8)$$

$$C_3H_6 - l \xrightarrow{kcra} 3H_2 + C_3 - l(coke\ deposition) \qquad (9)$$

$$CH_3OH - l + CH_3OH - l \xrightarrow{kmet} CH_4 + CO_2 + 2H_2 \qquad (10)$$

The proposed mechanism accounts for methanol being first adsorbed over acid active sites, *l* (1). DME is formed over the active site by reaction between the adsorbed

methanol, which at current temperatures studied in this work could be probably in form of protonated methoxyl, and gas methanol by Eley-Rideal mechanism (2,3). The water formed in this dehydration reaction competes with methanol for adsorption in the active site (4). Adsorbed DME can react with gaseous methanol to produce propylene or higher olefins (5). On the other hand, the methoxyl intermediate can produce and adsorbed formaldehyde intermediate that can decomposes to syngas at higher temperatures (6,7) [52]. At temperatures higher than 580 ºC, retained CO or olefins produces coke deposition through Boudart reaction or cracking (8,9). Methanation from intermediates producing equimolar amount of CO_2 and CH_4 occurs at high temperatures (10).

It should be noted that in these set of equations, k_i accounts for kinetic rate constant, while K_i stands for adsorption equilibrium constants. Both of them depend on temperature following the Arrhenius and Van't Hoff laws, respectively:

$$k_i = k_{0,i} \cdot \exp\left(\frac{-E_{a,i}}{R \cdot T}\right) \qquad (11)$$

$$K_i = K_{0,i} \cdot \exp\left(\frac{-\Delta H_i}{R \cdot T}\right) \qquad (12)$$

Now k_o and K_0 are the preexponential factor, R is the universal gas constant, T is the temperature, E_a is the activation energy and ΔH the enthalpy of adsorption.

For the proposed kinetic model it is assumed that CO formed in the decomposition reaction is probably desorbed rapidly to the gas phase. Moreover, Boudart and cracking reactions for formation of pyrolitic carbon does not reach notorious extend until temperatures beyond the scope of the kinetic model. Consequently, Eqn. 7 to 9 are not considered. Besides, in all the adsorption steps a quasi-equilibrium state is supposed to be reached. Taking these considerations into account, the kinetic rate expression for the formation of each product can be drawn from the above reaction scheme.

$$r_{CO} = k_{syn} \cdot C_{l-CH3OH} = \frac{k_{syn} \cdot K_M \cdot P_{CH3OH}}{1 + K_M \cdot P_{CH3OH} + K_w \cdot P_w + K_{DME} \cdot P_{DME}} \qquad (12)$$

$$r_{met} = k_{met} \cdot C_{l-CH3OH}{}^2 = k_{met} \cdot \left(\frac{K_M \cdot P_{CH3OH}}{1 + K_{ads} \cdot P_{CH3OH} + K_w \cdot P_w + K_{DME} \cdot P_{DME}}\right)^2 \qquad (13)$$

$$r_{ole} = k_{ole} \cdot P_{CH3OH} \cdot C_{l-DME} = \frac{k_{ole} \cdot K_M \cdot P_{CH3OH} \cdot P_{DME}}{1 + K_M \cdot P_{CH3OH} + K_w \cdot P_w + K_{DME} \cdot P_{DME}} \quad (14)$$

$$r_{DME} = k_{DME} \cdot P_{CH3OH} \cdot C_{l-CH3OH} - r_{ole} = \frac{k_{DME} \cdot K_M \cdot P_{CH3OH}^2 - k_{ole} \cdot K_M \cdot P_{CH3OH} \cdot P_{DME}}{1 + K_M \cdot P_{CH3OH} + K_w \cdot P_w + K_{DME} \cdot P_{DME}} \quad (15)$$

Finally, the following suppositions were assumed: the reactor is considered as a plug flow integral reactor, homogeneous distribution of active sites on the catalyst surface, catalyst operates at steady-state conditions, diffusional constraints and transport limitations were negligible (theoretically proven from Damköhler and Thiele modulus), and changes in temperature and pressure within the reactor were neglected. All these suppositions have been checked in previous work on alcohol dehydration using the same experimental procedure [53,54]. They allow considering plug flow integral for the interpretation of the experimental data. To this purpose the reactor mass balance equation (16) was numerically integrated to calculate the exit conversion of methanol as well as product yields:

$$\frac{dX_i}{d(W/F)} = r_i \quad (16)$$

where *W/F* is the ration between catalyst weight and the methanol molar flow rate, i.e. the space time, and X_i is the methanol conversion or product yield (methanol conversion x product selectivity). Thus, combining molar balances, rates equations and stoichiometrics relationships, a system of differential equations is obtained. The kinetic parameters involved in the differential equations system were calculated using the Runge-Kuta method, implemented in Matlab 2010a software, by minimizing the objective function (O.F.):

$$O.F. = \left(\sum_j \sum_i \left(Xcal_{i,j} - Xexp_{i,j}\right)^2\right)/i \cdot (j - n) \quad (17)$$

where $Xexp_{i,j}$ represents the value of the conversion of reactant or product *i* in experiment *j*, obtained experimentally, and $Xcal_{i,j}$ the calculated value, being *n* the number of kinetic parameters, 14. The optimization routine was based in the Levenberg-Marquart algorithm. 52 experiments at different temperatures, space times and methanol partial pressures were considered. Solution of the optimization problem gave a OF value of $1.36 \cdot 10^{-3}$. The good agreement between calculated and experimental conversion and yields is illustrated in next section.

5.3.2.4. Kinetic study

Table 5.3 summarizes the values of the activation energy or enthalpy of adsorption and the preexponential factors (k_o, K_o) for all the implied reactions and equilibriums. The values obtained for methanol dehydration, k_{dme}, and decomposition, k_{syn}, are within range to those reported by Mastalir et al [55] on $Cu/ZrO_2/CeO_2$ catalysts with different copper loadings (75-143 kJ/mol) and by Croy et al [56] using bimetallic Pt-M catalysts, with M = Au, Pd, Ru, Fe, supported on ZrO_2 (59-96 kJ/mol). Activation energies for olefin production and methanation are slightly higher than those reported by Gayubo et al. in the kinetic modeling of methanol-to-olefin process a SAPO18 catalyst (57 and 127 kJ/mol respectively) [37].

Table 5.3. Kinetic parameters for methanol conversion.

	$E_a/\Delta H$ (kJ/mol)	**K_o/k_o ($L\cdot mol^{-1}$, $g\cdot s\cdot mol^{-1}$)**
K_{ads}	-17.8	672.0
K_w	-25.5	854.7
K_{dme}	-30.3	44.74
k_{dme}	69.8	475.2
k_{syn}	134.5	3136
k_{met}	156.7	$1.567\cdot10^5$
k_{ole}	77.7	1179

Figures 5.12.a and b illustrate the steady-state methanol conversion and product yields to main products of ZrNF-500 at constant space time and different methanol inlet pressures. The results predicted by the model are shown in solid lines for comparison sake. It can be noted the good agreement in methanol conversion between experimental and estimated values. Increase of Methanol pressure did not modify substantially conversion, though DME kinetic rate, eqn. 14, depends on gas methanol pressure, and consequently greater yields of this product were achieved at high methanol partial pressure. In general, the results for all products were successfully reproduced, with the exception of those for the yield to olefins, especially at low temperatures. A possible explanation for the difference observed between the experimental and calculated olefin yields is that methane could be produced from the olefins pool rather than from

methanol, so olefin kinetic rate could be raised to satisfy low yield requirements, while olefin yield would be lowered at high temperatures.

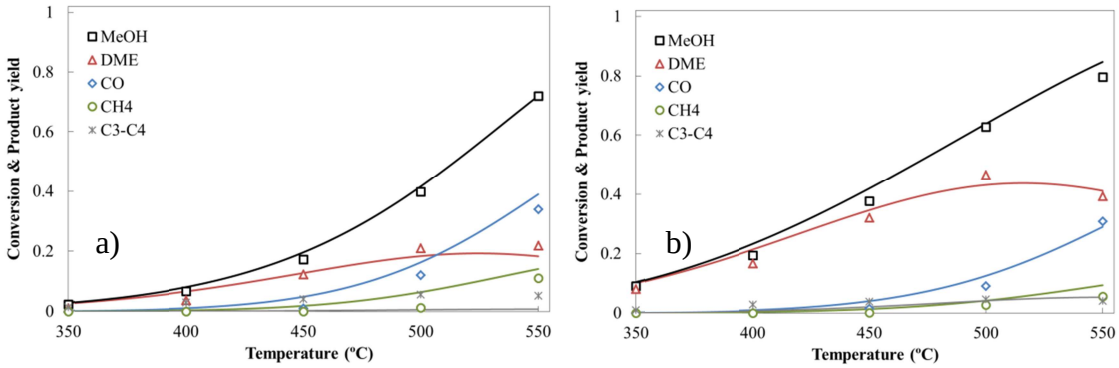

Figure 5.12. Experimental and simulated steady state methanol conversions and selectivities to main products as a function of reaction temperature for ZrNF-500. Methanol space time: 0.107 g·s·µmol^{-1}. P_{MEOH}= 0.01 atm (a) 0.04 atm (b)

Figure 5.13.a represents the steady state methanol conversions as a function of space time at reaction temperature of 500 ºC and different inlet methanol partial pressures from 0.01 to 0.04 atm for ZrNF-500 catalyst. Solid lines represent the simulated conversion profile. It is noteworthy the good agreement between experimental and calculated values provided by the kinetic model. Figure 5.13.b displays the steady state methanol conversions as a function of reaction temperature at a inlet methanol partial pressures of 0.02 atm and different space times, from 0.027 to 0.107 g·s/µmol for zirconia fibers calcined at 500 ºC. Steady state methanol conversion increases with the inlet methanol partial pressures, although this effect is no longer observed for methanol partial pressures higher that 0.02 atm. This could be due to the high affinity of methanol for zirconia and a relatively low active site concentration. Hence, at the highest partial pressure most of the catalysts active sites are covered by methanol, and therefore a further increase in the methanol inlet vapor pressure does not result in a significant increase of the methanol rate conversion. At higher reaction temperatures, saturation seems to be readily reached at methanol partial pressure of 0.02 atm.

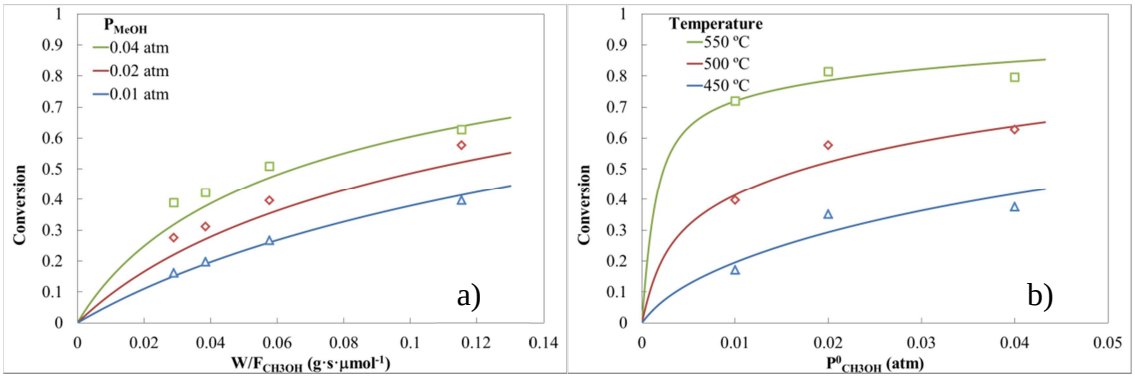

Figure 5.13. Steady state methanol conversions for ZrNF-500. Space time influence at given temperature = 500ºC and different methanol partial pressures (a). Partial pressure influence at given space time = 0.107 g·s·μmol^{-1} and different reaction temperatures (b).

5.4. Conclusions

Zirconia nanofibers, obtained by electrospinning technique, have been calcined at different temperatures and used as heterogeneous catalyst in the gas phase dehydration of methanol. SEM and TEM images of the electrospun nanofibers show uniform and no sintering fibers with a high aspect ratio and sizes around 400 nm. Calcination at 500 ºC produces shrinkage of about 30%, whereas increasing calcination temperature confers the fiber surface a granulose aspect due to crystallization of zirconia. As a consequence of the crystal sintering, the resulting nanofibers shown low BET areas similar to the exposed surface area per gram of the fibers. The X-ray diffraction spectra of the zirconia nanofibers show the onset of a semicrystaline tetragonal structure for the fibers calcined at 400ºC. Transformation of tetragonal to monoclinic zirconia starts at a calcination temperature of 600 ºC. Calcination at temperatures higher than 800 ºC results in monoclinic crystal size growth. The catalytic results have shown that increase of the calcination temperature results in zirconia fiber catalysts with lower steady state conversion values, probably due to a change of the surface acidity of the zirconia fibers because the higher extend of dehydroxilation. For reaction temperatures higher than 580 ºC, a deactivation of the catalysts takes place probably due to the cracking reaction of reaction products that blocks with pyrolytic carbon the active sites responsible of the methanol decomposition reaction. The fibers calcined at 500 ºC show significantly higher selectivities to dimethyl ether, probably due to the higher strength and number of acid sites of the catalyst prepared at lower

calcination temperature, whereas the monoclinic crystalline nanofiber are more selective towards syngas production. The kinetic study carried out over the zirconia nanofiber calcined at 500ºC allowed assessing the influence of temperature and methanol partial pressure in conversion and selectivity to DME. Selectivity and yield to this product has been proven to increase with increasing methanol pressure, while methanol conversion increased with space time and temperature, although at temperatures higher than 500 ºC syngas production started to compete with DME. Additionally, it was also showed that methanol conversion and product yields can be accurately predicted by the proposed kinetic model.

5.5. References

1. A.H. Heuer, L.W. Hobbs, Sciences and Technology of Zirconia, Advances in Ceramics, vol. 3, American Ceramic Society, Columbus, OH, 1981.

2. T. Yokoyama, T. Setoyama, N. Fujita, M. Nakajima, T. Maki, K. Fujii. Novel direct hydrogenation process of aromatic carboxylic acids to the corresponding aldehydes with zirconia catalyst. Appl. Catal. A 1992; 88: 149-161.

3. C.M. Lieber. Nanoscale science and technology: Building a big future from small things. MRS Bull. 2003; 28: 486-491.

4. J. Xiang, W. Lu, Y.J. Hu, Y. Wu, H. Yan, C.M. Lieber. Ge/Si nanowire heterostructures as high-performance field-effect transistors. Nature 2006; 441: 489-493.

5. M. Law, J. Goldberger, P.D. Yang. Semiconductor nanowires and nanotubes. Annu. Rev. Mater. Res. 2004; 34: 83-122.

6. Y.N. Xia, P.D. Yang, Y.G. Sun, Y.Y. Wu, B. Mayers, B. Gates, Y.D. Yin, F. Kim, Y.Q. Yan. One-dimensional nanostructures: Synthesis, characterization, and applications. Adv. Mater. 2003; 15: 353-389.

7. Y. Matatov-Meytal, V. Barelko, I. Yuranov, M. Sheintuch. Cloth catalysts in water denitrification. I. Pd on glass fibers. Appl. Catal. B 2000; 27: 127-135.

8. H.Q. Cao, X. Qiu, B. Luo, Y. Liang, Y.H. Zhang, R.Q. Tan, M.J. Zhao, Q.M. Zhu. Synthesis and room-temperature ultraviolet photoluminescence properties of Zirconia nanowires. Adv. Funct. Mater. 2004; 14: 243-246.

9. H. Xu, D.H. Qin, Z. Yang, H.L. Li. Fabrication and characterization of highly ordered zirconia nanowire arrays by sol–gel template method. Mater. Chem. Phys. 2003; 80: 524-528.

10. W.-S. Dong, F.-Q. Lin, C.-L. Liu, M.-Y. Li. Synthesis of ZrO2 nanowires by ionic-liquid route J. Colloid Interface Sci. 2009; 333: 734–740.

11. I.G. Loscertales, A. Barrero, M. Márquez, R. Spretz, R. Velarde-Ortiz, G. Larsen. Electrically Forced Coaxial Nanojets for One-Step Hollow Nanofiber Design. J. Am. Chem. Soc. 2004; 126: 5376-5377.

12. G. Larsen, R. Velarde-Ortiz, K. Minchow, A. Barrero, I.G. Loscertales. A Method for Making Inorganic and Hybrid (Organic/Inorganic) Fibers and Vesicles with Diameters in the Submicrometer and Micrometer Range via Sol-Gel Chemistry and Electrically Forced Liquid Jets. J. Am. Chem. Soc. 2003; 125: 1154–1155.

13. M. Lallave, J. Bedia, R. Ruiz-Rosas, J. Rodríguez-Mirasol, T. Cordero, J.C. Otero, et al. Filled and hollow carbon nanofibers by coaxial electrospinning of Alcell lignin without binder polymers. Adv. Mater. 2007; 19: 4292-4296.

14. R. Ruiz-Rosas, J. Bedia, M. Lallave, I. G. Loscertales, A. Barrero, J. Rodríguez-Mirasol, T. Cordero. The production of submicron diameter carbon fibers by the electrospinning of lignin. Carbon 2010; 48: 696-705.

15. I.G. Loscertales, A. Barrero, I. Guerrero, R. Cortijo, M. Márquez, A.M. Gañán-Calvo. Micro/nano encapsulation via electrified coaxial liquid jets. Science 2002:295:1695-1698.

16. J.E. Díaz, A. Barrero, M. Marquez, I.G. Loscertales. Controlled Encapsulation of Hydrophobic Liquids in Hydrophylic Polymer Nanofibers by Co-electro-spinning. Adv. Func. Mater. 2006; 16: 2110-2116.

17. P. Mckendry. Energy production from biomass (part 1): Overview of biomass. Bioresour. Technol. 2002; 83: 37–46.

18. D. Puppan. Environmental evaluation of biofuels. Period Polytech Ser. Soc. Man. Sci. 2002; 10: 95–116.

19. M. Stöcker. Methanol-to-hydrocarbons: Catalytic materials and their behavior. Micropor. Mesopor. Mat. 1999; 29: 3-48.

20. F.J. Keil. Micropor. Mesopor. Mat. 1999; 29: 49-66.

21. A.G. Gayubo, P.L. Benito, A.T. Aguayo, M. Olazar, J. Bilbao. J. Chem. Technol. Biotechnol. 1996; 65: 186-192.

22. A.T. Aguayo, A.G. Gayubo, R. Vivanco, M. Olazar, J. Bilbao. Relationship between surface acidity and activity of catalysts in the transformation of methanol into hydrocarbons. Appl. Catal. A 2005; 283: 197-207.

23. A.G. Gayubo, A.T. Aguayo, A.E. Sánchez del Campo, A.M. Tarrío, J. Bilbao. Relationship between surface acidity and activity of catalysts in the transformation of methanol into hydrocarbons. Ind. Eng. Chem. Res. 2000; 39: 292-300.

24. J. Agrell, K. Hasselbo, K. Jansson, S.G. Järas, M. Boutonnet. Production of hydrogen by partial oxidation of methanol over Cu/ZnO catalysts prepared by microemulsion technique. Appl. Catal. A 2001; 211: 239-250.

25. A.M. Rouhi. Amoco, haldor topsoe develop dimethyl ether As alternative diesel fuel. Chem. Eng. News 1995; 73: 37-39.

26. N. Inoue, Y. Ohno. A view of future synthetic fuel oil - 5. Dimethyl ether synthesis technology. Petrotech 2001; 24: 319-322.

27. M. Xu, J.H. Lunsford, D.W. Goodman, A. Bhattacharyya. Synthesis of dimethyl ether (DME) from methanol over solid-acid catalysts. Appl. Catal. A 1997; 149: 289-301.

28. C. Arcoumanis, C. Bae, R. Crookes, E. Kinoshita. The potential of di-methyl ether (DME) as an alternative fuel for compression-ignition engines: A review. Fuel 2008; 87: 1014–1030.

29. D.M. Brown, B.L. Bhatt, T.H. Hsiung, J.J. Lewnard, F.J. Waller. Novel technology for the synthesis of dimethyl ether from syngas. Catal. Today 1991; 8: 279-304.

30. W.W. Kaeding, S.A. Butter. Production of chemicals from methanol. I. Low molecular weight olefins. J. Catal. 1980; 61: 155-164.

31. G. Cai, Z. Liu, R. Shi, C. He, L. Yang, C. Sun, Y. Chang. Light alkenes from syngas via dimethyl ether. Appl. Catal. A 1995; 125: 29-38.

32. S.D. Kim, S.C. Baek, Y.-J. Lee, K.-W. Jun, M.J. Kim, I.S. Yoo. Effect of γ-alumina content on catalytic performance of modified ZSM-5 for dehydration of crude methanol to dimethyl ether. Appl. Catal. A 2006; 309: 139–143.

33. T.A. Semelsberger, K.C. Ott, R.L. Borup, H.L. Greene. Role of acidity on the hydrolysis of dimethyl ether (DME) to methanol. Appl. Catal. B 2005; 61: 281–287.

34. V. Vishwanathan, K.-W. Jun, J.-W. Kim, H.-S. Roh. Vapour phase dehydration of crude methanol to dimethyl ether over Na-modified H-ZSM-5 catalysts. Appl. Catal. A 2004; 276: 251–255.

35. T. Takeguchi, K. Yanagisawa, T. Inui, M. Inoue. Effect of the property of solid acid upon syngas-to-dimethyl ether conversion on the hybrid catalysts composed of Cu-Zn-Ga and solid acids. Appl. Catal. A 2000; 192: 201-209.

36. A.G. Gayubo, A.T. Aguayo, M. Olazar, R. Vivanco, J. Bilbao. Kinetics of the Irreversible Deactivation on the HZSM-5 Zeolite Catalyst in the MTO. Process Chem. Eng. Sci. 2003; 58: 5239-5249.

37. A.G. Gayubo, A.T. Aguayo, A. Alonso, A. Atutxa, J Bilbao. Reaction Scheme and Kinetic Modelling for the MTO process over a SAPO-18 Catalyst. Catal. Today 2005; 106: 112-117.

38. H. Toraya, M. Yoshimura, S. Somiya. Quantitative Analysis of Monoclinic-Stabilized Cubic ZrO2 Systems by X-Ray Diffraction. J. Am. Ceram. Soc. 1984; 67: C183-C184.

39. P. Scherrer, Goettinger Nachrichten 1918; 2: 98-100.

40. L. Li, P. Zhang, J. Liang, S.M. Guo. Phase transformation and morphological evolution of electrospun zirconia nanofibers during thermal annealing. Ceramics International 2010; 36: 589–594.

41. G.-Y. Guo, Y.-L. Chen. Unusual structural phase transition in nanocrystalline zirconia. Appl. Phys. A 2006; 84: 431-437.

42. J.F. Moulder, W.F. Stickle, P.E. Sobol, K.D. Bomben, in: J. Chastain, R.C. King Jr. (Eds), Handbook of X-ray Photoelectron Spectroscopy, Physical Electronics, Inc., Eden Prairie, MN, 1995.

43. K.-H. Jacob, E. Knözinger, S. Benfer. Adsorption sites on polymorphic zirconia. J. Mater. Chem. 1993; 3: 651-657.

44. J.A. Wang, M.A. Valenzuela, J. Salmones, A. Vázquez, A. García-Ruiz, X. Bokhimi. Comparative study of nanocrystalline zirconia prepared by precipitation and sol-gel methods. Catal. Today 2001; 68: 21–30.

45. M.I. Zaki, M.A. Hasan, F.A. Al-Sagheer, L. Pasupulety. In situ FTIR spectra of pyridine adsorbed on SiO2-Al2O3, TiO2, ZrO2 and CeO2: General considerations for the identification of acid sites on surfaces of finely divided metal oxides. Colloid Surface Physicochem. Eng. Aspect 2001; 190: 261–274.

46. W. Li, Y. Yin, R. Gao, R. Hou, J. Mol. Catal. (China) 1999; 13: 186-192.

47. W. Stichert, F. Schüth, S. Kuba, H. Knözinger. Monoclinic and tetragonal high surface area sulfated zirconias in butane isomerization: CO adsorption and catalytic results. J. Catal. 2001; 198: 277-285.

48. H. Knözinger, K. Kochloeft, W. Meye. Kinetics of the bimolecular ether formation from alcohols over alumina. J. Catal. 1973; 28: 69.

49. H. Knözinger, D. Dautzenberg. Influence of steric and inductive effects on product distributions in the dehydration of secondary alcohols on alumina. J. Catal. 1974; 3: 142-144.

50. F.S. Ramos, A.M. Duarte de Farias, L.E.P. Borges, J.L. Monteiro, M.A. Fraga, E.F. Sousa-Aguiar, L.G. Appel. Role of dehydration catalyst acid properties on one-step DME synthesis over physical mixtures. Catal. Today 2005; 101: 39–44.

51. C.D. Chang, in: D.M. Bibby, C.D. Chang, R.F. Howe, S. Yurchak (Eds.), Methane Conversion, Elsevier, Amsterdam, 1988, p. 127.

52. S.T. Korhonen, M.A. Bañares, J.L.G. Fierro, A.O.I. Krause. Adsorption of methanol as a probe for surface characteristics of zirconia-, alumina-, and zirconia/alumina-supported chromia catalysts. Catal. Today 2007; 126: 235–247.

53. J. Bedia, R. Ruiz-Rosas, J. Rodríguez-Mirasol, T. Cordero. A kinetic study of 2-propanol dehydration on carbon acid catalysts. J. Catal. 2010; 271: 33-42.

54. J. Bedia, R. Ruiz-Rosas, J. Rodríguez-Mirasol, T. Cordero. Kinetic study of the decomposition of 2-butanol on carbon-based acid catalyst. AIChE Journal 2010; 56: 1557–1568.

55. A. Mastalir, B. Frank, A. Szizybalski, H. Soerijanto, A. Deshpande, M. Niederberger, R. Schomäcker, R. Schlögl, T. Ressler. Steam reforming of methanol over Cu/ZrO2/CeO2 catalysts: A kinetic study. J. Catal. 2005; 230: 464–475.

56. J.R. Croy, S. Mostafa, L. Hickman, H. Heinrich, B. Roldan Cuenya. Bimetallic Pt-Metal catalysts for the decomposition of methanol: Effect of secondary metal on the oxidation state, activity, and selectivity of Pt. Appl. Catal. A: Gen. 2008; 350: 207–216.

6. ELECTROSPINNING OF SILICA SUB-MICROTUBES WITH PLATINUM NANOPARTICLES FOR CATALYTIC NO REDUCTION

6.0.Abstract

The preparation of sub-microstructured fiber catalysts with well dispersed metal nanoparticles is currently of great interest. In this work, we present the preparation and characterization of silica sub-microtubes with and without platinum nanoparticles obtained by electrospinning (in co-axial configuration) of silica sol-gel followed by a calcination process. The silica sol was prepared from TEOS, ethanol, distilled water, and HCl using platinum (II) acetylacetonate as the catalyst metal precursor. The electrospinning process allows the preparation of one-dimesional structured materials with well dispersed platinum particles by a simple and straightforward method. The silica tubes obtained are very uniform, showing a high aspect ratio with external/internal diameters of around 350/125 nm and well dispersed platinum nanoparticles of around 2 nm in size on the surface. The sub-microtubes with platinum were used as catalysts for the NO reduction reaction. This catalyst shows a high NO conversion, with very high selectivity to N_2 at moderate conditions when using C_3H_6 as reducing agent in the presence of oxygen. When CO was used as reducing agent, NO conversion was negligible, probably due to the strong chemisorption of CO on the catalyst active sites.

6.1.Introduction

One dimensional nano- and sub-microstructured materials, such as fibers, wires or tubes show novel and interesting physical and chemical properties, which make them promising materials for applications in semiconductor, energy storage, sensor, optics or catalysis and play an important role in fundamental research [1-4]. In catalytic processes, pore diffusion resistance is significant in pellet shaped catalysts, while powdered catalysts, as is the practice in most laboratory-scale studies could cause problems of high pressure drop in industrial size reactors. Therefore, novel forms of catalyst supports, as sub-microtubes catalysts, which are easy to handle, may be packed or constructed in the best form to fit the particular use and show very small resistance to diffusion [5], represent a key research issue for many catalytic industrial processes.

In this sense, electrospinning is a simple technique that has been used to obtain polymer and carbon fibers and tubes in the submicro- and nanoscale [6-11], in which a solution held in a capillary tube by its surface tension is subject to an electric field that stretched the electrified jet due to the electrostatic repulsions between the surface charges and the evaporation of the solvent. The action of the electric field over a drop, forming at the tip of a capillary, changes its shape into a charged conical meniscus known as the Taylor cone [9]. Parameters such as viscosity, flow rate, concentration of electrospun solution or applied voltage control the diameter and length of fibers/tubes. Moreover, using a co-axial electrospinning setup makes possible to switch between steady electrospray (droplets) and electrospinning (fibers/tubes) just controlling rate flow between outer and inner solutions. It also allows encapsulating of core liquid and the production of tubes [12,13]. The sol-gel technique has been widely studied for the preparation of different forms including monoliths, powders, coatings, and fibers [14,15]. In the case of silica forms, the typical sol-gel method consist of the hydrolysis and condensation of tetraethyl orthosilicate (TEOS), $Si(OCH_2CH_3)_4$.

Co-electrospinning technique, i.e., adding a second compound to the spinnable solution in order to cast both of them together, presents the advantage to allow an easily deposition of metal catalysts on fiber/tubes by simple solution of the metal precursor in the spinnable solution [11]. The presence of metal nanoparticles on the electrospun fiber/tube displays a huge potential in the area of heterogeneous catalysis. Specifically, among noble metals, platinum could be very active for selective catalytic reduction of NOx with hydrocarbons (HC-SCR) at low temperature ($T < 300$ ºC). The platinum particle size and the support properties play an important role in the NOx reduction mechanism through the hydrocarbon activation [16,17]. Therefore, the preparation of one-dimensional microstructured catalysts with well dispersed metal nanoparticles can be currently of great interest.

In this work, we present the preparation and characterization of silica sub-microtubes with and without platinum nanoparticles using a sol-gel method followed by an electrospinning process. This way, we are able to obtain one-dimesional structured materials with well dispersed platinum particles by a simple and straightforward method. The sub-microtubes with platinum were used as catalysts for the NO reduction reaction in the presence of oxygen.

6.2.Experimental Procedures

6.2.1. Catalyst preparation.

The silica sol was prepared from TEOS, ethanol, distilled water, and HCl. The sol composition in molar ratio was 1:2:2:0.025 (TEOS:ethanol:water:HCl). First, the HCl was mixed with water. Once diluted, ethanol was added to the solution. This solution is added to the TEOS. The acid catalyzes the hydrolysis reaction, which is strongly exothermic, and the TEOS is dissolved. The mixture, stirred vigorously, was heated up to 80 ºC for 1 h and then cooled down to 60 ºC. In the case of the tubes containing platinum, platinum (II) acetylacetonate is added to the solution at 60 ºC in a molar ratio to TEOS of 0.006. The solutions (with and without platinum) were maintained at this temperature under stirring for approximately 48 h in order to evaporate the alcohols formed during the condensation phase of the sol gel and to reach the proper viscosity for the electrospinning process. Silica sub-microtubes were generated by using the coaxial electrospinning method reported in the literature [12] in a co-axial configuration, with the sol gel coming through the external capillary tip and synthetic oil flowing by the central one (Figure 6.1). This central needle supplies the synthetic oil that acts as a template fluid and that after its removal produces the tube configuration. The flow rates through the needles ranged from 1.0/0.2 to 2.0/1.0 $mL \cdot h^{-1}$ for sol gel/synthetic oil, respectively. To apply the high voltage between the spinneret and the collector (Figure 6.1), two high voltage power supplies are used: one positively polarized connected to the needle and the other negatively polarized attached to a collector. This configuration provided better electrostatic conditions to prevent tubes from flying to any grounded piece near the set-up, therefore facilitating the deposition of the electrospun tubes on the collector. The tip-to-collector distance was 20–25 cm, and the electrical potential difference was 10 kV (the collector was at –5 kV and the tips at +5 kV), although this value could varied depending on the collector/tip geometry. The electrospun tubes with and without platinum are denoted as SiT-Pt and SiT, respectively. Finally, the electrospun tubes were calcined at 500 ºC for 2 hours in a muffle furnace, in order to eliminate the solvents and the synthetic oil and stabilize the silica tubes. The stabilized (calcined) electrospun tubes with and without platinum are denoted as SSiT-Pt and SSiT, respectively.

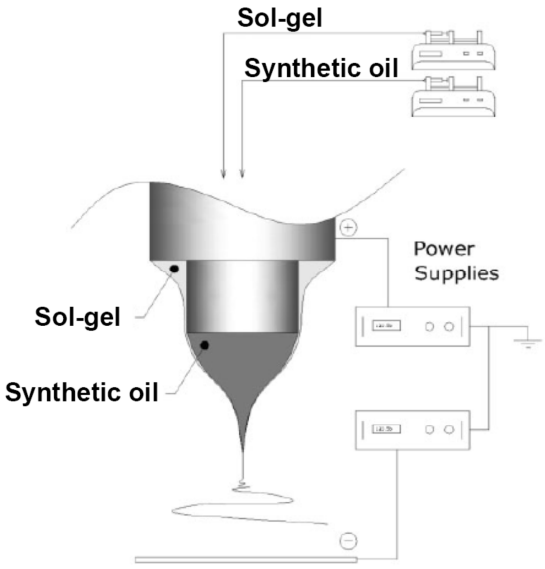

Figure 6.1. Electrospinning set up.

6.2.2. Catalyst characterization.

Thermogravimetric analysis (TG) were performed in a CI Electronics MK2 balance under air flow (150 cm^3 STP/min) from room temperature to 900 ºC at a heating rate of 10 ºC/min with a sample weight of about 10 mg. X-ray diffraction patterns (XRD) were recorded in the region of 2θ = 5-80º on a Philips X'Pert PRO MPD diffractometer using CuKα monochromatic radiation (operation value 45 kV and 40 mA).

The porous structure was characterized by N_2 adsorption-desorption at -196 ºC and by CO_2 adsorption at 0 ºC, carried out in a Micromeritics ASAP2020 apparatus. Samples were previously outgassed for 8 hours at 150 ºC under vacuum. From the N_2 adsorption/desorption isotherm, the apparent surface area (A_{BET}) was calculated by applying the BET equation and from the CO_2 adsorption isotherm the narrow micropore surface area (A_{DR}) was obtained by applying the Dubinin-Raduskevich equation [18]. The surface chemistry of the samples was studied by X-ray photoelectron spectroscopy (XPS) analysis, using a 5700C model Physical Electronics apparatus with MgKα radiation (1253.6 eV). For the analysis of the XPS peaks, the C1s peak position was set at 284.5 eV and used as reference to locate the other peaks. The fitting of the XPS peaks was done by least squares using Gaussian-Lorentzian peak shapes. Fourier transform infrared (FTIR) spectra were obtained using a Bruker Optics Tensor 27 FT-IR

spectrometer by adding 256 scans in the 4000-400 cm^{-1} spectral range at 4 cm^{-1} resolution. Pressed KBr pellets at a sample/KBr ratio of around 1:250 were used.

The surface morphology of the tubes was studied by scanning electron microscopy (SEM) using a JSM 840 JEOL microscope working at 25 KV voltage and by transmission electron microscopy (TEM) in a Philips CM200 microscope at an accelerating voltage of 200 kV. Platinum size distribution of the SSiT-Pt sample was obtained by counting between 100 and 200 particles. The size distribution was fitted to a normal distribution. From the size distribution, we determined the number average diameter $d_n = \sum n_i \cdot d_i / \sum n_i$ [19]. Platinum particle size (assuming spherical particles) and dispersion (D) are related by $D = 108/d_n$ (nm) [20].

6.2.3. NO reduction experiments

The NO reduction experiments were performed in a quartz fixed bed microreactor (4 mm i.d.) at atmospheric pressure. Experiments were carried out with 80 mg of stabilized tubes (SSiT or SSiT-Pt). The inlet flow rate used was 200 cm^3 STP/min, with NO concentration of 200 ppm, resulting in a space time of $W/F_{NO} = 2.88$ g·s/µmol. The concentrations of other inlet gases were 1500 ppm of C_3H_6 or 1% CO and 3% of O_2. A chemiluminiscent analyzer (EcoPhysics, CLD 700 AL model) was used to measure the outlet gas concentrations of NO and NO_2. The CO and CO_2 outlet concentrations were analyzed by means of a non-dispersive infra-red analyser (Ultramat 22, Siemens model). C_3H_6, H_2O, N_2, N_2O and O_2 concentrations were measured by a mass spectrometer analyzer (Balzers MsCube).

6.3. Results and Discussion

6.3.1. Catalyst characterization

Figure 6.2 represents the weight loss of the silica tubes with and without platinum and of the synthetic oil used as template in the electrospinning process as a function of temperature, from room temperature to 900 ºC, at a heating rate of 10 ºC/min in air atmosphere. TGA results revealed different steps in the degradation of the template oil under oxygen atmosphere, probably corresponding to decomposition of unsaturated and saturated fatty acids which are the main component of oils [21] and also

the oxidation of carbon residue. In the case of the tubes, the mass loss begins at temperatures lower than 100 ºC probably due to the evaporation of the solvents used in the formulation of the silica tubes. The TG profiles for the tubes show a significant mass loss at around 300 ºC, coinciding with those of the synthetic oil used as template and, therefore, associated to the decomposition and oxidation of the oil remaining in the inner of the non stablized silica tubes. This mass loss is more pronounced and starts at lower temperature for the SiT-Pt tubes than for the SiT ones, probably as a consequence of the catalytic effect of the platinum in the decomposition and oxidation reaction. The weight loss of the tubes slowly continues with increasing temperature up to around 800 ºC, probably as a consequence of the evaporation of the water molecules formed during the self-condensation reaction of the silanol groups [22].

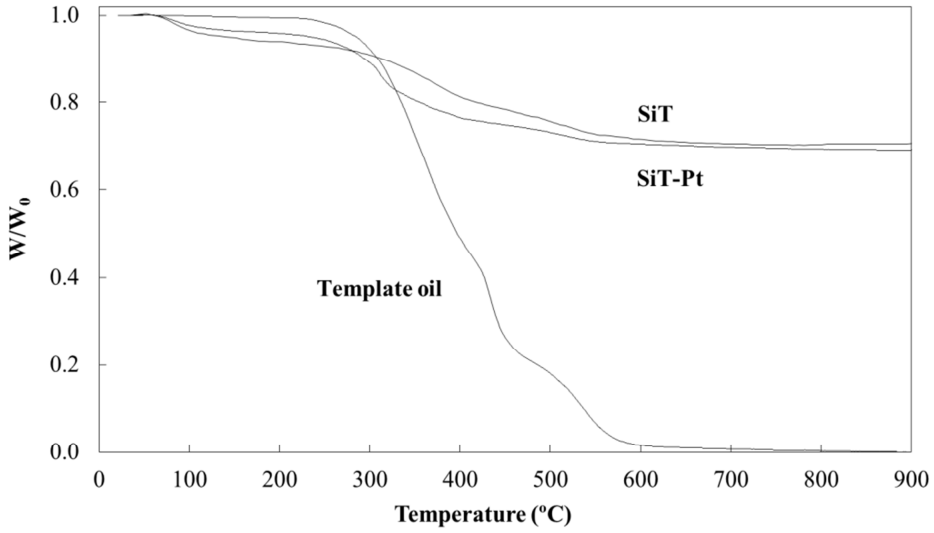

Figure 6.2. TG profiles of the silica sub-microtubes with and without platinum and of the synthetic oil used as template in the electrospinning process in air atmosphere.

The crystalline structure of the silica tubes was investigated by X-ray diffraction analysis. Figure 6.3 represents the XRD patterns of the non stabilized and stabilized tubes with and without platinum, which exhibit the characteristics of amorphous silica [23]. XRD patterns of the silica tubes with and without platinum calcined and not calcined show the same characteristics. In the case of the platinum containing samples, the peaks associated to the platinum crystal planes are not observed, probably as a consequence of well dispersed platinum in very small crystal sizes.

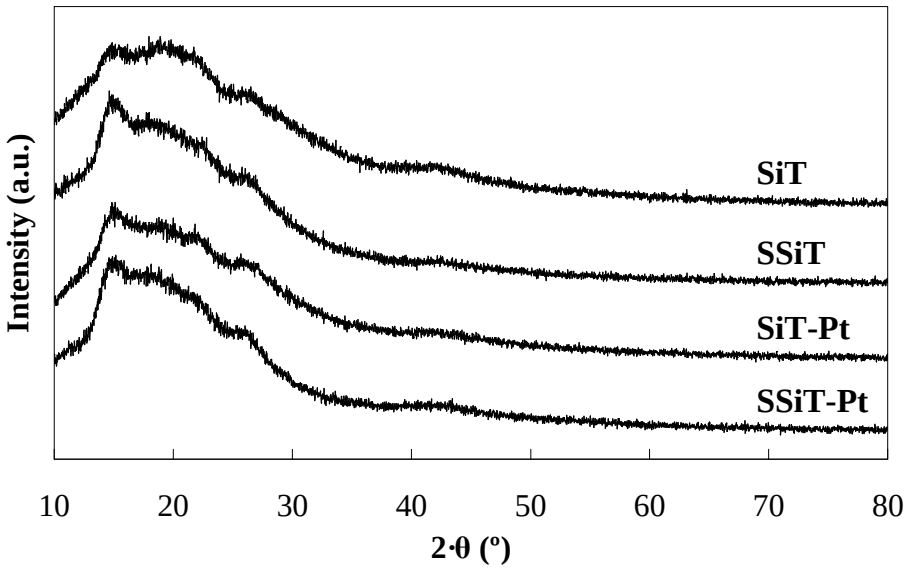

Figure 6.3. XRD patters for different sub-micro silica tubes.

Figure 6.4 represents the FTIR spectrum of the non stabilized and stabilized tubes with and without platinum. Broad absorption bands between 4000 and 3000 cm^{-1} are observed which correspond to the fundamental stretching vibrations of different types of hydroxyl groups [24]. The spectra show clearly two bands at 795 and 950 cm^{-1} associated to Si-O vibration in silanol groups (Si-OH). The bands at 1082 cm^{-1} are related to Si-O-Si groups. These groups are formed due to the hydrolysis and condensation of TEOS and, as the calcination temperature increases, a gradual decrease in the Si-OH band and an increase in the Si-O-Si band are observed due to the complete condensation of hydrolyzed silica precursor (Si-OH) to silica (SiO_2) [25]. The band at 1625 cm^{-1} could be related to the combination of the SiO_2 vibrational modes. It should be noted the low intensity of the bands related to CH_3 or CH_2 located at around 2800-3000 and 1400-1800 cm^{-1}, respectively. This indicates that there is a low contribution of methyl (CH_3) or methylene (CH_2) of ethoxy groups ($-OCH_2CH_3$), suggesting that most of the TEOS is hydrolyzed.

The bands associated to the methyl (CH_3) or methylene (CH_2) of ethoxy groups ($-OCH_2CH_3$) are even smaller in the spectra of the stabilized fiber, probably due to the decomposition and oxidation of the organic compounds (solvents and template oil) of the tubes during the calcination process.

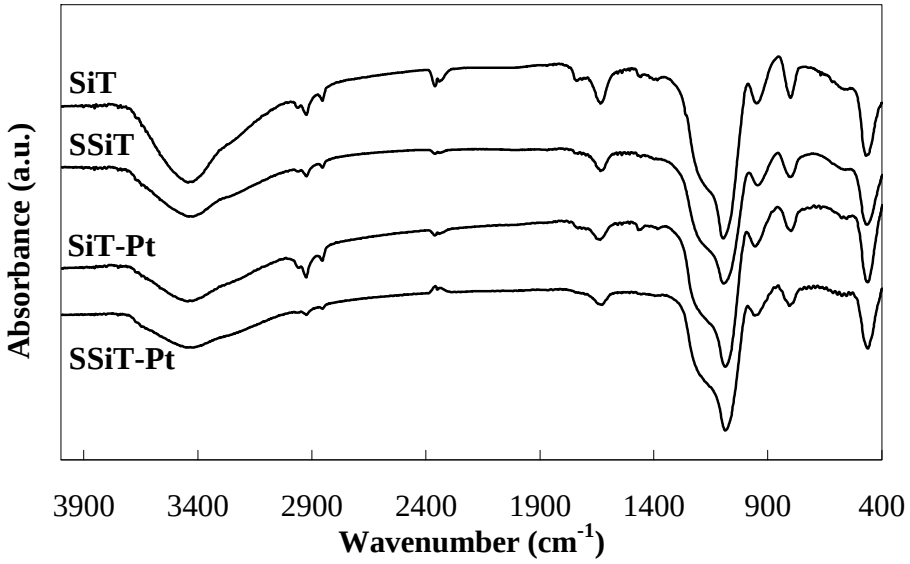

Figure 6.4. IR spectra of different sub-micro tubes with and without platinum.

The porous structure of the different tubes was analyzed by N_2 adsorption-desorption isotherms at -196 ºC and CO_2 adsorption at 0 ºC, and the results are shown in Table 6.1. The electrospun tubes with and without platinum, SiT-Pt and SiT respectively, show very low or negligible BET areas, indicative of very poorly developed porous structures. In contrast, the narrow micropore surface areas, A_{DR}, obtained from the CO_2 adsorption isotherms are 228 and 121 m^2/g, respectively. The results of apparent surface area for the electrospun tubes, obtained from the N_2 and CO_2 adsorption isotherms, with $A_{DR} >> A_{BET}$, are characteristics of solids with a narrow microporosity [26].

The calcination process of the SiT seems to produce the shrinkage of this narrow microporosity. However, the presence of platinum in the calcination process results in a development of wide microporosity, measured with N_2 adsorption, resulting in tubes with total BET surface area of 144 m^2/g. Lin et al. [27] reported that the addition of low Pt salt concentrations to the electrospinning of polyacrylonitrile/platinum acetylacetonate solution could increase the fiber diameters, due to the formation of polymer–salt– solvent interactions, which changed the balance among the viscosity, surface tension, and conductivity of the synthesis solutions. They did not analyze the influence of the Pt salt on the fibers porosity. However, it can be plausible to associate the porosity increase of the tubes to the addition of the Pt salt to the solution. In this sense, these results can be also related to the decomposition of the platinum salt. Ji et al.

reported the production of porous carbon nanofibers from electrospun polyacrylonitrile (PAN)/SiO_2 composite nanofibers. After using hydrofluoric acid as etching agent, SiO_2 nanoparticles and agglomerates are removed from the carbon matrix, releasing new porosity inside them [28]. In a similar way, small droplets of platinum salt inside the SiO_2 tubes' wall can act as template for formation of microporosity when the organic acetate ligands are removed during calcination, probably producing a more developed porous structure than in solely silica tubes.

Table 6.1. Porous structural parameters of different sub-microtubes with and without platinum obtained from N_2 and CO_2 isotherms.

	A_{BET} (m^2)	V_t (cm^3/g)	A_t (m^2)	A_{DR} (m^2)	V_{DR} (cm^3/g)
SiT	3	--	2	228	0.087
SSiT	7	0.001	4	135	0.051
SiT-Pt	--	--	--	121	0.046
SSiT-Pt	144	0.056	13	273	0.104

Table 6.2 summarizes the atomic surface concentrations obtained from the numerical integration of the XPS peaks for the different silica tubes. The as-spun silica tubes show a high amount of carbon, due mainly to the organic compounds present in the synthetic oil used as template and, in a lower extent, to remaining ethoxy groups of TEOS and solvents used in the formulation of the tubes. The amount of surface silicon is much lower than that of carbon and oxygen for the non stalilized tubes. The stabilized (calcined) samples show much lower carbon content than that of the non stabilized tubes, as a consequence of the oxidation of organic compounds of the synthetic oil and to the decomposition of the ethoxy groups and solvents present in the spinnable solution. Therefore, the calcination process reduces the carbon content and increases the surface oxygen and silicon content of the tubes, which show an atomic ratio (O/Si) as that of silica. In the case of the tubes that contains platinum, the amount of platinum increases with the stabilization process, as a consequence of the decomposition and oxidation of the organic compound used in the formulation of the tubes. The platinum/silicon atomic ratio keeps constant at 0.004, which is lower than the value of 0.006 corresponding to the Pt/Si atomic ratio of the $Pt(AcAc)_2$/TEOS initial solution, so platinum particles seems to be imbued in the internal surface of the tubes. The stabilized silica tubes with platinum show an atomic surface concentration of surface platinum of

0.12% which corresponds to a weight surface concentration of 1.20%, very close to the theoretical value from the tubes formulation, 1.04%.

Table 6.2. Atomic surface concentration (%) of different sub-microtubes with and without platinum determined by XPS quantitative analysis.

	%C	%O	%Si	%Pt
SiT	48.6	35.5	15.9	--
SSiT	11.0	60.5	28.5	--
SiT-Pt	57.7	31.7	10.6	(0.04)
SSiT-Pt	9.8	60.1	30.0	0.12

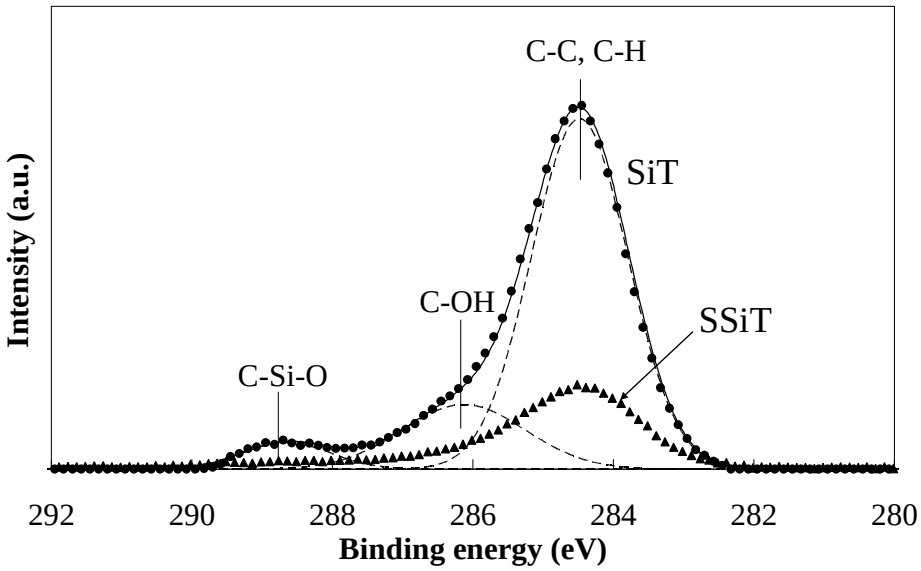

Figure 6.5. C 1s spectra of the non stabilized (deconvoluted), SiT, and stabilized, SSiT, silica tubes.

Figure 6.5 shows the C1s spectra for the non stablized and stabilized silica tubes. The deconvolution of C1s spectrum of non stabilized tubes is also represented in Figure 5. The presence of platinum does not modify significantly the C1s spectra. The deconvoluted spectrum show three different peaks, (i) at 284.5 eV associated to C-C and C-H bonds [29], (ii) at around 286.1 eV that could be related to C-OH groups [29] present in the ethanol used in the precursor solution and produced by the hydrolysis reaction of TEOS and (iii) at approximately 288.7 eV associated to the C-Si-O groups [24] from the TEOS used in the tube formulation. The calcination process removes

almost totally all the carbon groups due to the decomposition of the ethanol and to the oxidation of organic compounds present in the remaining synthetic oil used as template of the tube. Thus, the C1s spectra of the stabilized tubes presents a main peak located at 284.5 eV and probably due to adventitious carbon since at the calcination temperature, 500 ºC, most of the carbon should have been oxidized.

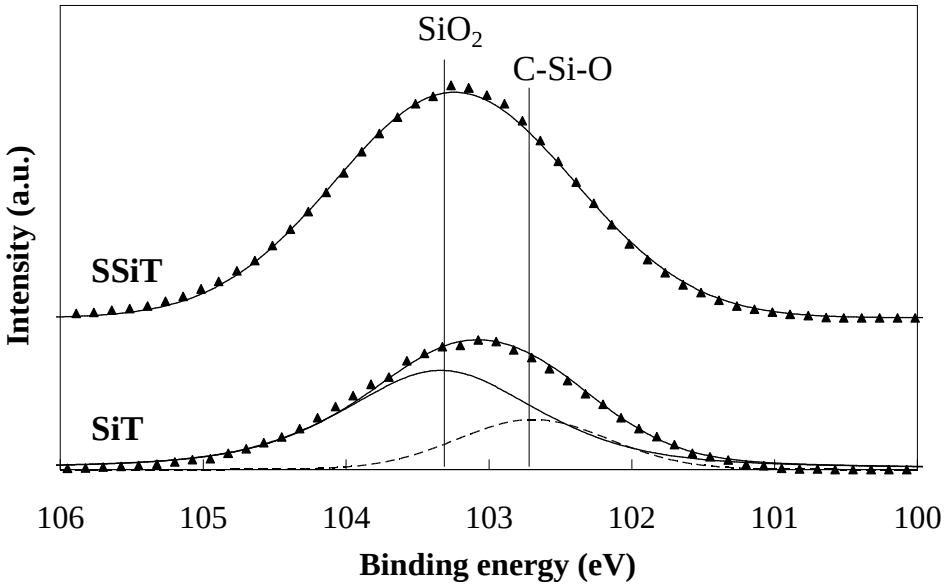

Figure 6.6. Deconvoluted Si 2p spectra of SiT and SSiT samples.

The deconvoluted Si 2p spectra of SiT and SSiT tubes are represented in Figure 6.6. The spectrum of the non stabilized tubes show a shift to lower binding energies probably as a consequence of the presence of carbon atoms bonded to silicon. In SiO_2, which has a tetragonal structure, the Si atom is bonded to four neighboring oxygen atoms. The chemical shift in the Si 2p photoelectron signal is mainly induced by the number of oxygen atoms bound to a Si atom. When introducing carbon atoms into SiO_2, some of the four oxygen atoms bonded to the silicon are replaced by carbon atoms and the Si 2p spectra shifts to lower binding energy values [30,31]. This suggests that, prior to stabilization, part of the TEOS remains not hydrolyzed and, therefore, Si-O-C is observed in the XPS of SiT sample. After stabilization, the organic matter has been removed and all the silicon is in form of SiO_2. Furthermore, a slight asymmetry of the spectrum of as-spun tubes is observed. According to Ingol el al. [32], it could be adscribed to the presence of Si-O-CH_2CH_3 bonds from the precursor solution and disappears when the sol-gel materials are subjected to air thermal treatments at temperatures higher than 400°C.

Figure 6.7 displays the Pt 4f spectra for the Pt containing non-stabilized and stabilized tubes. The Pt 4f region of the spectra for these tubes presents a doublet corresponding to Pt $4f_{7/2}$ and Pt $4f_{5/2}$ [29]. The separation between Pt $4f_{7/2}$ and Pt $4f_{5/2}$ peaks, due to spin orbital splitting, is a quantized value of 3.33 eV. The Pt $4f_{7/2}$ peak lying at around 71.0 eV can be attributed to Pt^0 (metallic Pt), while the Pt $4f_{7/2}$ peak located at around 72.8 eV is related to Pt^{2+} (electrodeficient platinum) [29]. The non stabilized tubes present most of the platinum in form of Pt^{2+}, in agreement with the oxidation state of platinum in the precursor (platinum acetylacetonate). The stabilization process produces an increase and a shift of the peaks to lower binding energies, which indicate the presence of a higher contribution of platinum in form of Pt^0 on the surface of the stabilized tubes. This result suggests that during the stabilization of the tubes electrodeficient platinum is reduced to metallic platinum. Probably, during the calcination process most of the organic compounds are oxidized producing, among other gases, CO which is a reductive gas. In this sense, Cavaliere et al. [33] reported the elaboration of Pt loaded titania nanofibres and they also observed the presence of metallic Pt. They associated these results to the alcohol present as traces of solvent, or formed during the hydrolysis of the TiO_2 precursor, which reduces the Pt^{2+} in the presence of PVP, leading directly to metallic Pt nanoclusters, without the need for a subsequent reduction step [34]. However, they did not exclude that C or CO produced during the thermal decomposition of ethanol and PVP participates in reduction of Pt^{2+}.

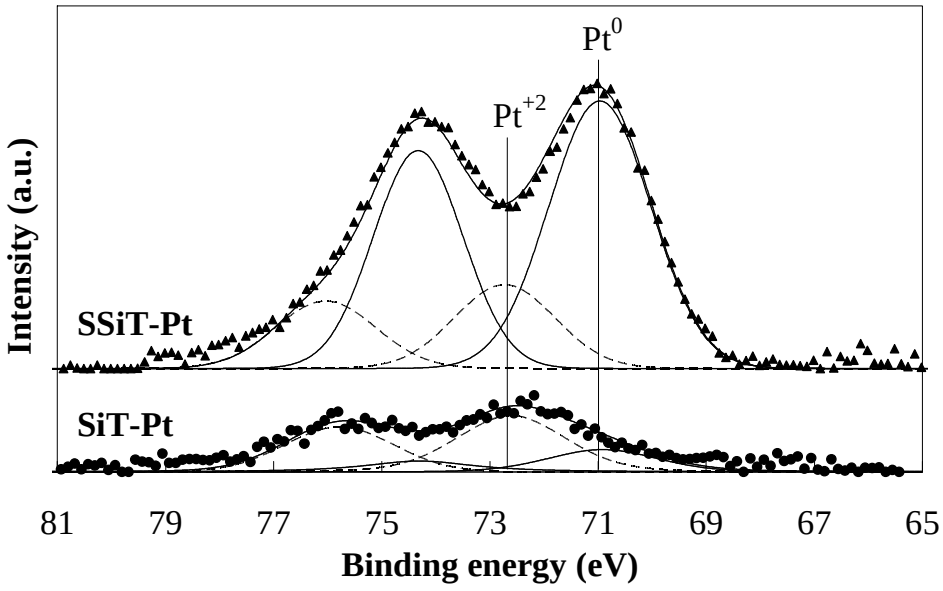

Figure 6.7. Deconvoluted Pt 4f spectra of SiT-Pt and SSiT-Pt samples.

Figures 6.8 a to d show SEM images of the SiT, SSiT and SSiT-Pt. The tubes obtained were very uniform and no sintering or beads were found. Furthermore, the tubes show a high aspect ratio (ratio between the length and the diameter of the fiber), with tubes sizes clearly lower than 1 µm. Neither the calcination process nor the introduction of platinum show any influence on the morphology or size of the resulting tubes. In the Figure 6.8 d it is clearly seen the inner hollow at the tip of some broken tubes.

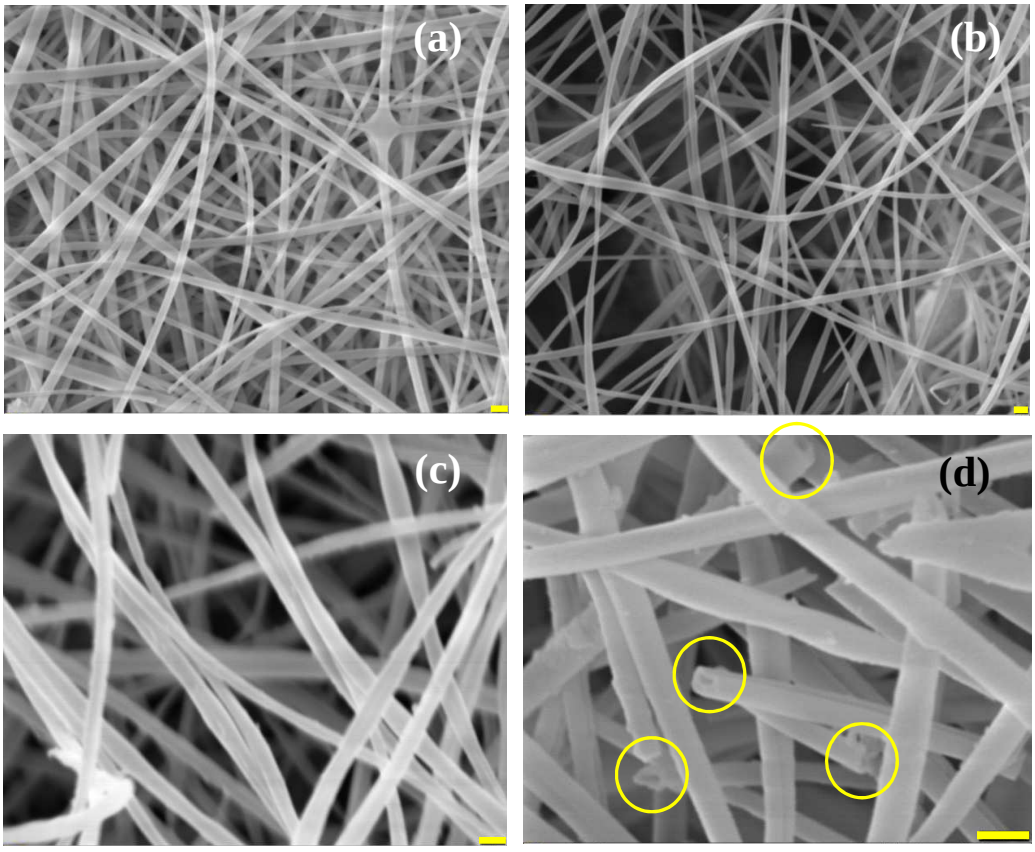

Figure 6.8. SEM images of (a) SiT, (b) SSiT, (c) and (d) SSiT-Pt (bar lengths: 1 µm)

Figure 6.9 displays TEM images of SSiT, (a and b) and SSiT-Pt (c and d). Figure 6.9 a shows non stabilized silica tubes with external diameters of approximately 350 nm and internal diameter sizes of around 125 nm. The tubes show no structural defects. Figure 6.9 b represents a higher magnification TEM image of a stabilized silica tube. This tube shows likewise an external diameter of 346 nm and a hollow size of 122 nm. The selected-area electron diffraction pattern (SAED) of the stabilized tubes (detail in Figure 6.9 b) shows no diffraction patterns supporting the amorphous structure of the silica tubes.

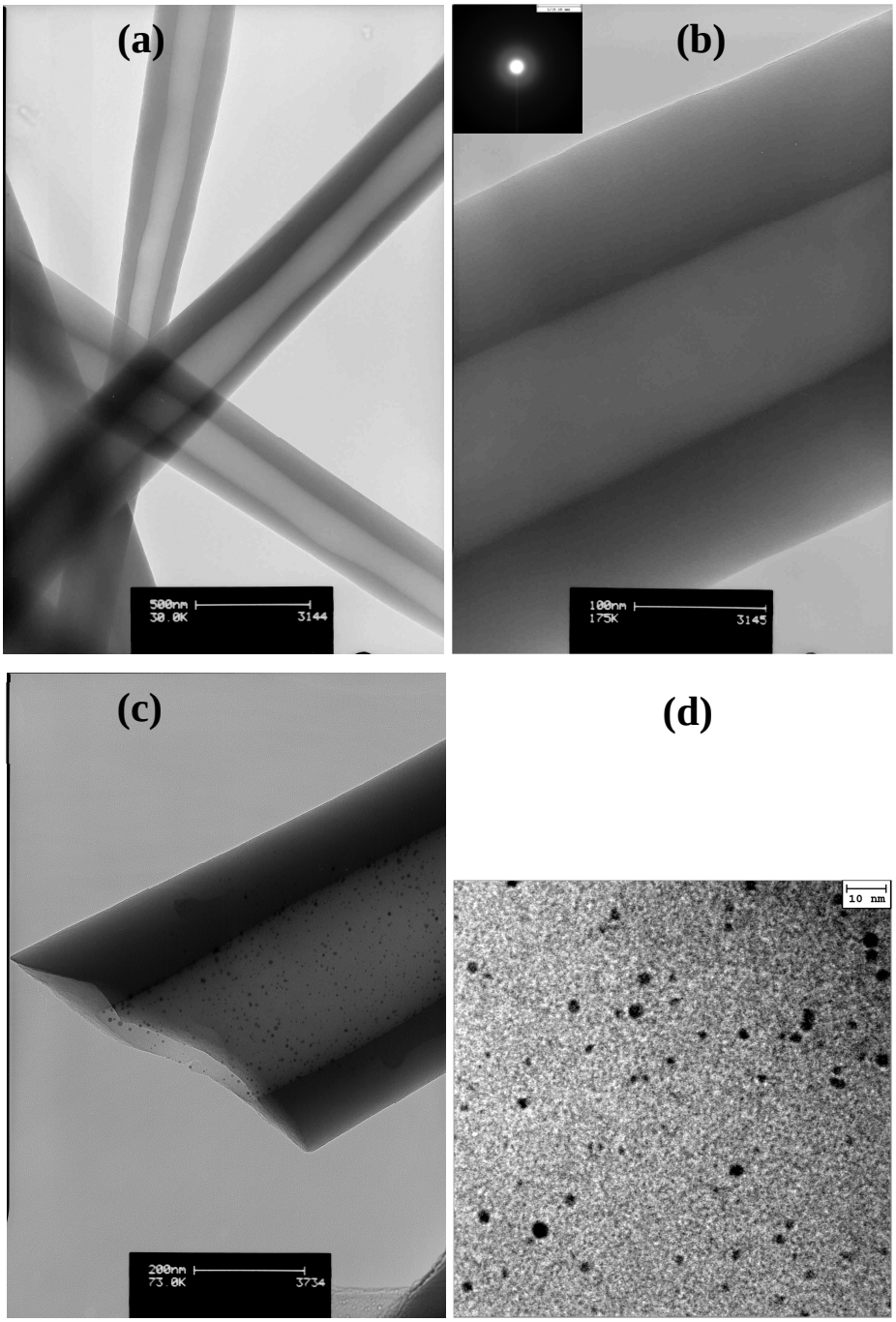

Figure 6.9. TEM images of (a) SSiT (bar length: 500 nm), (b) SSiT (bar length:100 nm), (c) SSiT-Pt (bar length: 200 nm) and (d) SSiT-Pt (bar length: 10 nm)

Figure 6.9 c represents a transmission electronic micrograph of a stabilized tube with platinum. In this case the tube presents a higher size, with an external diameter of 540 nm and an internal diameter size of around 280 nm, showing well dispersed platinum nanoparticles. Figure 6.9 d shows a higher magnification TEM image of a stabilized tube with platinum. As can be seen, the tubes present platinum particles, showed as darker spots, which seem to be well dispersed and essentially spherical, with

sizes between 0.5 and 4 nm. Figure 6.10 represents the platinum particle size distribution histogram. The particles size distributions have been fitted to a normal distribution with mean μ and standard deviation σ. Based on this measurement, the average diameter size was 1.8 nm and the dispersion of the platinum is as high as 59.3%.

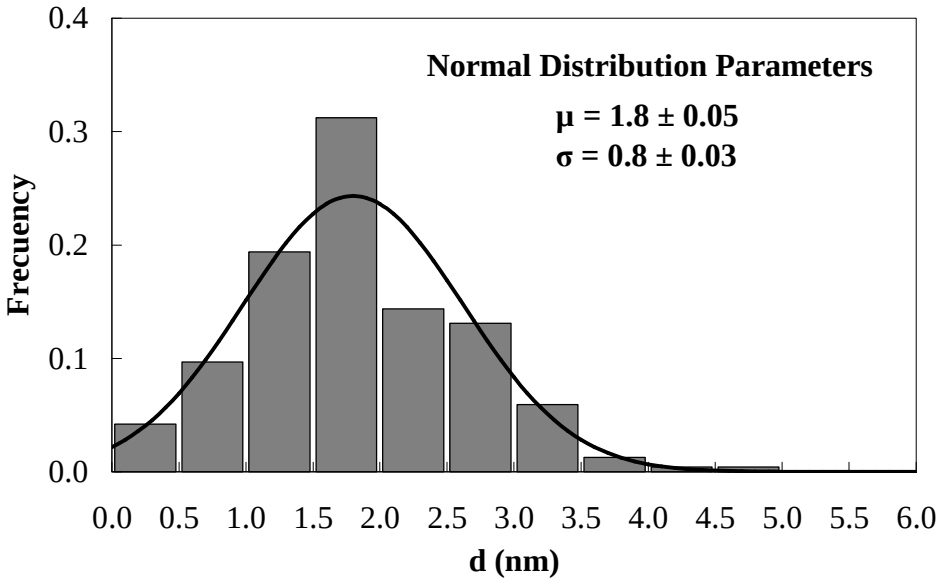

Figure 6.10. Platinum particle size distribution histogram of the SSiT-Pt sample.

6.3.2. Catalytic NO reduction.

The catalytic reduction of NO in the presence or absence of C_3H_6 or CO as reductant gases and in the presence or absence of O_2 was studied for the two different stabilized tubes with and without platinum, SSiT-Pt and SSiT respectively. SSiT showed no catalytic effect for reduction of NO. However, SSiT-Pt have shown a considerably NO conversion depending on the reaction conditions.

Figure 6.11 represents the evolution of outlet gas concentration as a function of the reaction time for SSiT-Pt catalyst at a reaction temperature of 200 ºC. The inlet gases were changed sequentially. Initially, only NO diluted in He (200 ppm, W/F_{NO} = 2.88 g·s/μmol) was introduced in the inlet gas stream, after approximately 40 min O_2 (3% vol) was added to the inlet stream, and finally, at about 120 min of reaction time CO (1% vol) was introduced. In the first part of the experiment, when the inlet gas is NO diluted in He, there is a decrease in the outlet NO concentration compared to the

inlet concentration as a consequence of the NO adsorption. The presence of oxygen results in a partial NO oxidation to NO_2, probably due to the presence of platinum, a well-known oxidation catalyst. Nevertheless, the addition of CO produces an increase in the NO outlet concentration. This behavior could be due to a strong competition between NO and CO molecules for the catalyst active sites, as previously reported by Hao et al. [35]. In this case, it seems that CO adsorption is favored with respect to NO adsorption and, therefore, the adsorption and oxidation of NO are practically negligible, in the presence of CO. When NO was not added to the gas inlet, partial oxidation of CO was observed to proceed in a similar fashion than in presence of NO.

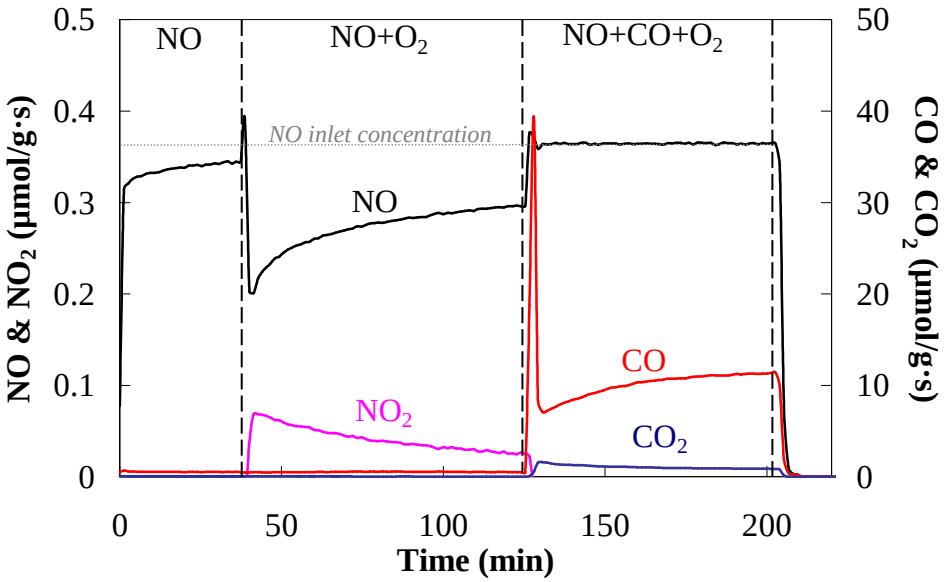

Figure 6.11. Evolution of outlet gas concentration as a function of the reaction time for SSiT-Pt catalyst at a reaction temperature of 200 ºC using 1%v CO as reductant and 3% O_2.

Figure 6.12 represents the evolution of outlet gas concentration as a function of the reaction time for SSiT-PT catalyst at a reaction temperature of 190 ºC. The inlet gases were again changed sequentially. Initially, only NO diluted in He (200 ppm, W/F_{NO} = 2.88 g·s/µmol) was introduced in the inlet gas stream, after around 10 min C_3H_6 (1500 ppm) was added to the inlet stream, and finally, at around 62 min of reaction time O_2 (3% vol) was introduced. In the first step only a low adsorption of NO was observed and no reaction products were detected. With the addition of propylene to the inlet stream, NO was partially desorbed, probably due to a competitive adsorption on the active sites between NO and C_3H_6 molecules. However, with the addition of O_2,

an important increase of the NO conversion and the complete conversion of propylene were observed. Furthermore, in this stage, N_2, CO_2 and H_2O were detected in the outlet gas stream, indicating that most of the NO was reduced to N_2 while all the C_3H_6 was oxidized to CO_2 and H_2O. It is important to point out that one of the main drawbacks reported in the literature for the platinum catalysts is the significant selectivities towards N_2O [36-38]. However, in our conditions, the formation of N_2O was not detected. NO conversion reached a steady-state value of about 90%, with total selectivity to N_2. This catalyst, SSiT-Pt, shows much better behavior that others reported in the literature, using a similar platinum content [32,33], which showed comparable conversion values at analogous reaction conditions, but with a much lower selectivity to N_2.

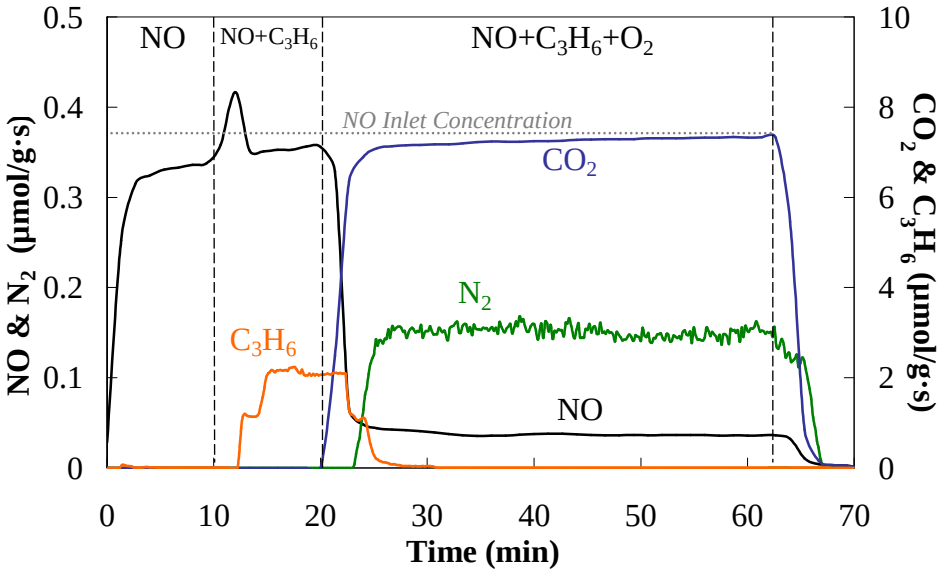

Figure 6.12. Evolution of outlet gas concentration as a function of the reaction time for SSiT-Pt catalyst at a reaction temperature of 190 ºC using 1500 ppm C_3H_6 as reductant and 3% O_2.

The technical literature proposes two main reaction pathways for selective catalytic reduction of NO on Pt catalysts. The first one involves production of molecular nitrogen through NO dissociative adsorption via a redox mechanism [39,40]. This mechanism assumes that NO is adsorbed on the Pt surface and decomposes to yield adsorbed nitrogen and oxygen atoms, which desorb in the form of molecular N_2 and N_2O. According to this scheme, the role of the reductant is to react with oxygen atoms and regenerate the active sites. Other mechanisms propose that the activation of the hydrocarbon, which plays an important role in the lean-deNO_x reaction, occurs through

adsorbed NO_2 or other intermediates, such as organo-nitro and related species [41]. In our case, although additional work is necessary to elucidate most plausible reaction mechanism, in a first approximation, it seems that the dissociative adsorption of NO can be disregarded, given that this is the main reaction pathway to produce N_2O (not detected with our catalyst). Furthermore, we have observed, in the absence of a reductant agent, the oxidation of NO to NO_2, which suggests that the formation of adsorbed NO_2 specie is probably necessary for the final NO reduction. This fact would explain why in the presence of CO, reduction of NO is not observed.

6.4.Conclusions

One-dimensional microstructured catalysts with well dispersed metal nanoparticles have been obtained and used as catalysts in the NO reduction reaction. The tubes have been obtained by electrospinning of a sol-gel prepared from TEOS, ethanol, distilled water, and HCl using platinum (II) acetylacetonate as metal precursor, followed by a calcination process. We have obtained silica tubes with external/internal diameters of around 350/125 nm, respectively, and with well dispersed platinum nanoparticles of about 1.8 nm in size. The sub-microtubes with platinum were used as catalysts for the NO reduction reaction. This tubes show a high NO conversion with total selectivity to N_2 at moderate conditions when using C_3H_6 as reducing agent, comparing quite well with other catalyst reported in the literature. When using CO as reducing agent there was no NO conversion, probably due to the competition between NO and CO for the catalyst active sites.

6.5. References

1. C.M. Lieber. Nanoscale science and technology: Building a big future from small things. MRS Bull. 2003; 28: 486-491.

2. J. Xiang, W. Lu, Y.J. Hu, Y. Wu, H. Yan, C.M. Lieber. Ge/Si nanowire heterostructures as high-performance field-effect transistors. Nature 2006; 441: 489-493.

3. M. Law, J. Goldberger, P.D. Yang. Semiconductor nanowires and nanotubes. Annu. Rev. Mater. Res. 2004; 34: 83-122.

4. Y.N. Xia, P.D. Yang, Y.G. Sun, Y.Y. Wu, B. Mayers, B. Gates, Y.D. Yin, F. Kim, Y.Q. Yan. One-dimensional nanostructures: Synthesis, characterization, and applications. Adv. Mater. 2003; 15: 353-389.

5. Y. Matatov-Meytal, V. Barelko, I. Yuranov, M. Sheintuch. Cloth catalysts in water denitrification. I. Pd on glass fibers. Appl. Catal. B 2000; 27: 127-1135.

6. D.H. Reneker, I. Chun. Nanometre diameter fibres of polymer, produced by electrospinning. Nanotechnology 1996, 7, 216.

7. Z.-M. Huang, Y.-Z. Zhang, M. Kotaki, S. Ramakrishna. A review on polymer nanofibers by electrospinning and their applications in nanocomposites. Comp. Sci. Technol. 2003, 63, 2223-2253.

8. I.G. Loscertales, A. Barrero, M. Márquez, R. Spretz, R. Velarde-Ortiz, G. Larsen. Electrically Forced Coaxial Nanojets for One-Step Hollow Nanofiber Design. J. Am. Chem. Soc. 2004; 126: 5376-5377.

9. G. Larsen, R. Velarde-Ortiz, K. Minchow, A. Barrero, I.G. Loscertales. A Method for Making Inorganic and Hybrid (Organic/Inorganic) Fibers and Vesicles with Diameters in the Submicrometer and Micrometer Range via Sol-Gel Chemistry and Electrically Forced Liquid Jets. J. Am. Chem. Soc. 2003; 125: 1154–1155.

10. M. Lallave, J. Bedia, R. Ruiz-Rosas, J. Rodríguez-Mirasol, T. Cordero, J.C. Otero, et al. Filled and hollow carbon nanofibers by coaxial electrospinning of Alcell lignin without binder polymers. Adv. Mater. 2007; 19: 4292-4296.

11. R. Ruiz-Rosas, J. Bedia, M. Lallave, I. G. Loscertales, A. Barrero, J. Rodríguez-Mirasol, T. Cordero. The production of submicron diameter carbon fibers by the electrospinning of lignin. Carbon 2010; 48: 696-705.

12. I.G. Loscertales, A. Barrero, I. Guerrero, R. Cortijo, M. Márquez, A.M. Gañán-Calvo. Micro/nano encapsulation via electrified coaxial liquid jets. Science 2002:295:1695-1698.

13. J.E. Díaz, A. Barrero, M. Marquez, I.G. Loscertales. Controlled Encapsulation of Hydrophobic Liquids in Hydrophylic Polymer Nanofibers by Co-electro-spinning. Adv. Func. Mater. 2006; 16: 2110-2116.

14. R.D. Gonzalez, T. Lopez, R. Gomez. Sol—Gel preparation of supported metal catalysts, Catal. Today 1997; 35: 293-317.

15. R. Ruiz-Rosas, J. Bedia, J.M. Rosas, M. Lallave, I.G. Loscertales, J. Rodríguez-T. Cordero. Methanol decomposition on electrospun zirconia nanofibers. Catalysis Today. DOI: 10.1016/j.cattod.2011.10.031.

16. G. Garrigós-Pastor, S. Parres-Esclapez, A. Bueno-López, M.J. Illán-Gómez, C. Salinas-Martínez de Lecea. Appl. Catal. A: Gen. 2009; 354: 63-71.

17. P.A. Kumar, H.P. Ha. Synthesis and Dispersion of Dendrimer-Encapsulated Pt Nanoparticles on γ-Al2O3 for the Reduction of NOx by Methane. Catal. Lett. 2010; 136: 177-184.

18. S.J. Gregg, K.S.W. Sing. Adsorption, surface area and porosity, 2nd edition, Academic Press, London, 1982.

19. M.A. Vannice. Kinetics of Catalytic Reactions. Springer, New York, USA, 2005; 20.

20. R.J. Farrauto, C.H. Bartholomew. Fundamentals of Industrial Catalytic Processes. Blackie Academic & Professional, NY, 1997.

21. J. C. O. Santos, I. M. G. Santos, M. M. Conceição, S. L. Porto, M. F. S. Trindade, A. G. Souza, S. Prasad, V. J. Fernandes, A. S. Araújo. Thermoanalytical, kinetic and rheological parameters of commercial edible vegetable oils. J. Therm. Anal. Calorim. 2004; 75: 419-428.

22. W.L. Huang, S.H. Cui, K.M. Liang, Z.F. Yuan, S.R. Gu. Evolution of pore and surface characteristics of silica xerogels during calcining. J. Phys. Chem. Solids 2002; 63: 645-650.

23. S.S. Choi, S.G. Lee, S.S. Im, S.H. Kim, Y.L. Joo. Silica nanofibers from electrospinning/sol-gel process. J. Mater. Sci. Lett. 2003; 22: 891-893.

24. R.S. McDonald. Surface functionality of amorphous silica by infrared spectrometry. J. Am. Chem. Soc. 1958; 62: 1168-1178.

25. A.C. Patel, S. Li, C. Wang, W. Zhang, Y. Wei. Electrospinning of Porous Silica Nanofibers Containing Silver Nanoparticles for Catalytic Applications. Chem. Mater. 2007; 19: 1231-1238.

26. F. Rodríguez-Reinoso, J. Garrido, J.M. Martín-Martínez, M. Molina-Sabio, R. Torregrosa. Different approaches in the characterization of microporous carbons. Carbon 1989; 27: 23-32.

27. Z. Lin, M.D. Woodroof, L. Ji, Y. Liang, W. Krause, X. Zhang. Effect of platinum salt concentration on the electrospinning of polyacrylonitrile/platinum acetylacetonate solution. J. Appl. Polymer Sci. 2010; 116: 895-901.

28. L. Ji, Z. Lin, A.J. Medford, X. Zhang. Nanofibers from electrospun polyacrylonitrile/ SiO2 composites as an energy storage material. Carbon 2009; 47: 3346-3354.

29. J.F. Moulder, W.F. Stickle, P.E. Sobol, K.D. Bomben in: Chastain, J.; King Jr., R. C. (Eds), Handbook of X-ray Photoelectron Spectroscopy, Physical Electronics, Inc., Eden Prairie, MN, 1995.

30. R.J.P. Corriu, D. Leclercq, P.H. Mutin, A. Vioux. super (29) Si NMR and XPS investigation of the structure of silicon oxycarbide glasses derived from polysiloxane precursors. Mater. Res. Soc. Symp. Proc. 1994; 346: 351-356.

31. G.D. Sorarù, G. D'Andrea, A. Glisenti. XPS characterization of gel-derived silicon oxycarbide glasses. Mat. Lett. 1996, 27, 1-5.

32. G.M. Ingo, C. Riccucci G. Bultrini, S. Dirè, G.J. Chiozzini. Thermal and Microchemical Characterisation of Sol-Gel SiO2, TiO2 and xSiO2–(1–x)TiO2 Ceramic Materials. Thermal. Anal. Calorim. 2001; 66: 37.

33. S. Cavalieri, S. Subianto, L. Chevallier, D.J. Jones, J. Rozière. Single step elaboration of size-tuned Pt loaded titania nanofibres. Chem. Commun., 2011; 47: 6834–6836.

34. N. Toshima. Macromol. Symp. 1996; 105: 111.

35. X. Hao, B. Shan, J. Hyun, N. Kapur, K. Fujdala, T. Truex, K. Cho. Experimental and Theoretical Study of CO Oxidation on PdAu Catalysts with NO Pulse Effects. Top. Catal. 2009; 52: 1946-1950.

36. J.M. García Cortés, M.J. Illán Gómez, C. Salinas Martínez de Lecea. The selective reduction of NOx with propene on Pt-beta catalyst: A transient study. Appl. Catal. B: Environ. 2007; 74: 313-323.

37. S.-C. Shen, J. Kawi. Mechanism of selective catalytic reduction of NO in the presence of excess O2 over Pt/Si-MCM-41 catalyst. J. Catal. 2003; 213: 241-250.

38. P. Denton, A. Giroir-Fendler, H. Praliaud, M. Primet. Role of the Nature of the Support (Alumina or Silica), of the Support Porosity, and of the Pt Dispersion in the Selective Reduction of NO by C3H6 under Lean-Burn Conditions. J. Catal 2000; 189: 410-420.

39. R. Burch, J.A. Sullivan. A Transient Kinetic Study of the Mechanism of the NO/C3H6/O2Reaction over Pt–SiO2Catalysts: Part I: Non-Steady-State Transient Switching Experiments. J. Catal. 1999; 182: 489-496.

40. R. Burch, P.J. Millington, A.P. Walker. Mechanism of the selective reduction of nitrogen monoxide on platinum-based catalysts in the presence of excess oxygen. Appl. Catal. B: Environ. 1994; 4: 65-94.

41. A. Obuchi, A. Ogata, H. Takahashi, J. Oi, G.R. Bamwenda, K. Mizuno. Selective reduction of nitrogen oxides with various organic substances on precious metal catalysts under a high GHSV condition. Catal. Today 1996; 29: 103-107.

7. GENERAL CONCLUSIONS AND FUTURE WORKS

Electrospun fibers seem to be suited for catalytic uses. Preparation of highly porous carbon nanofibers from lignin, in composite or pure fibers rise as an easy method to produce microporous supports with feasible applications in energy storage systems. Alumina, silica or zirconia catalysts, which are profusely documented as acid solid catalyst, can be also casted as nanofibers through this method. Moreover, the co-electrospinning casting method for supporting active phase over the nanofiber micropores has proven to be effective in achieving high dispersed catalyst without compromising the textural, physical and chemistry properties of electrospun fibers.

But there is still more work to do.

- Platinum carbon nanofibers as those shown in chapter 3 are to be tested in electrochemical storage of hydrogen.
- We are currently developing the most viable mechanism of NO reduction over platinum-doped silica tubes from chapter 6.
- Although pyridine adsorption-desorption tests point out the high amount of surface acidity in composite alumina-carbon and silica-carbon fibers from chapter 4, those composite mats are still to be tested as solid acid catalysts.
- The co/tri-axial electrospinning device is being tested with a modification on the coelectrospinning of active phase precursor. Instead of depositing the metal in the core of the fiber, the metallic salt can be dissolved in the outer liquid, so active phase is deposited mainly over the external surface of the fiber.
- In the same sense, in tri-axial electrospinning the active phase precursor can be added to the innermost fluid, so the active phase will be displayed over the inner wall of the tubes. This way, a catalyst with two different active phases can be casted avoiding possible sintering of metals into different crystalline phases.

As a preliminary result, Figure 7.1 shows a transmission image of one electrospun silica nanotube. It was prepared as detailed in experimental section of

chapter 6, but now Pt(AcAc)2 is added to oil template solution. This time, platinum nanoparticles seem to lie over the inner surface of tube wall.

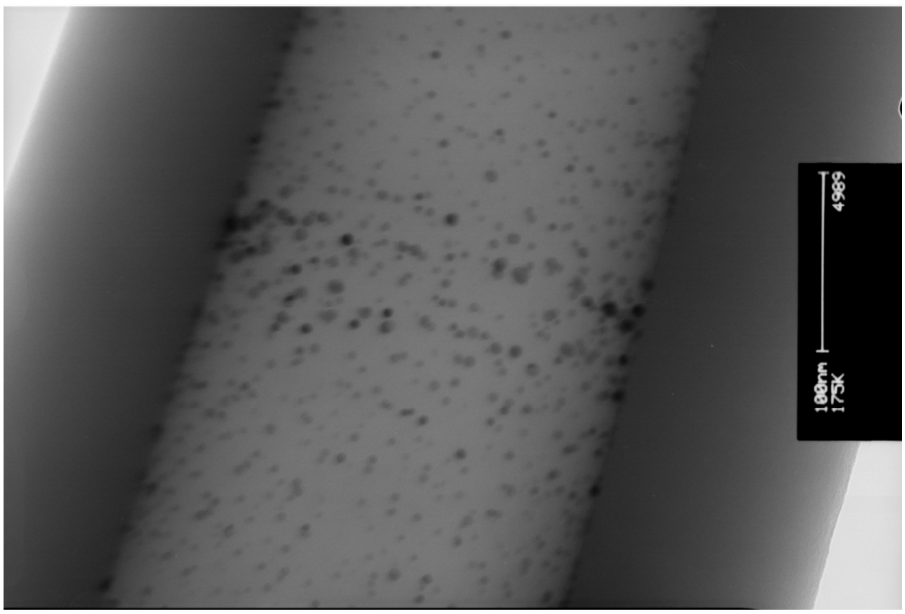

Figure 7.1. Platinum doped silica nanotubes. Metal nanoparticles seem to be deposited over the inner surface of the nanotubes.